

# Ligand Design for Heterometallic 3d Metallacrown Complexes

## Dissertation

zur Erlangung des akademischen Grades

Doktor der Naturwissenschaften

im Promotionsfach Chemie  
der  
Johannes Gutenberg-Universität Mainz  
vorgelegt von

Christoph Gamer

geboren am 30. Mai 1989

Mainz, den 31.10.2018



---

Die vorliegende Arbeit wurde in der Zeit von Juli 2015 bis Oktober 2018 am Institut für Anorganische und Analytische Chemie der Johannes Gutenberg-Universität Mainz unter der Betreuung von Frau Prof. Dr. [REDACTED] angefertigt.

Ich versichere, dass ich diese Arbeit selbstständig verfasst und keine anderen als die angegebenen Quellen und Hilfsmittel benutzt habe.

---

Datum und Ort

---

Christoph Gamer

Dekan:

Prof. Dr. [REDACTED]

Erste Berichterstatterin:

Prof. Dr. [REDACTED]

Zweite Berichterstatterin:

Prof. Dr. [REDACTED]

Prüfer:

Prof. Dr. [REDACTED]

Tag der mündlichen Prüfung:

D77



## Abstract

Two decades of research on *single molecule magnets* (SMMs) led to multiple concepts to reach one of the most ambitious goals in molecular magnetism, a high energy barrier ( $U_{eff}$ ) for the magnetization reversal of a single molecule. This energy barrier is dependent on the spin ground state ( $S$ ) and the axial magnetoanisotropy ( $D$ ) of the molecule. Previous research projects led to complexes with remarkably high  $S$  or  $D$  values but only few combining both. Up to now, a systematical manipulation and control of  $S$  and  $D$  on a molecular scope has not been accomplished yet. Herein, a systematic approach to obtain a high spin ground state accompanied with high molecular magnetic anisotropy is presented using the versatile compound class of metallacrowns (MCs).

The *magnetic director approach* has proven to effectively yield 12-MC-4 structures with high spin ground states. In addition, the planar crown scaffold represents an ideal framework to align the Jahn-Teller axes of ring forming metal ions with high single ion anisotropy. Prerequisites for an effective use of both concepts are the ability of the central guest ion to take part in strong magnetic exchange coupling and a tuneable anisotropic electron distribution of the ring forming metal ions. Hence, 3d transition metal ions express themselves as the optimal choice.

Systematic synthesis of heterometallic MCs requires varying selectivity of the central and the ring coordination pockets. To fulfill this condition, two distinct ligand optimizations were followed in this work. The donor atoms on apical coordination sites of the crown metal ions were varied yielding to a different binding affinity according to Pearson's HSAB concept. Moreover, additional coordinating functionalities were introduced in established MC ligand systems, like amidoximes, in order to adjust the whole coordination environment of the crown forming metal ions.

According to these approaches, several new 3d MC compounds were synthesized and analyzed using infrared spectroscopy, single crystal X-ray diffraction and SQUID magnetometry. Synthesis and the use of 2-methylmercaptobenzohydroxamic acid led to the isolation of the very first cadmium(II) metallacrown opening new perspectives for an improvement of the luminescence properties of this compound class. To highlight some of the results, a mixed valent cobalt(II/III) MC, double decker and a discrete Cu(II) MC and even two manganese double decker MCs are reported in this work.



## Kurzzusammenfassung

Nach über zwei Jahrzehnten der Forschung an Einzelmolekülmagneten (engl.: *single molecule magnets* - SMMs) sind verschiedene Konzepte bekannt, das bislang anspruchsvollste Ziel des molekularen Magnetismus, eine möglichst große effektive Energiebarriere für die Umkehr der Magnetisierung eines einzelnen Moleküls, zu erreichen. Diese Energiebarriere zeigt eine Abhängigkeit vom Spingrundzustand ( $S$ ) und der axialen, magnetischen Anisotropie ( $D$ ) des Moleküls. Bisherige Forschungsprojekte bezüglich dieser Systeme führten zu Komplexverbindungen mit bemerkenswert hohen  $S$  oder  $D$  Werten, aber nur wenige weisen beides auf. Bis jetzt konnte die systematische Manipulation und Kontrolle von  $S$  und  $D$  auf molekularer Ebene nicht zufriedenstellend ermöglicht werden. In dieser Arbeit wird ein systematisches Konzept vorgestellt, einen hohen Spingrundzustand sowie hohe magnetische Anisotropie mit Hilfe der vielfältigen Verbindungsklasse der Metallakronen (engl.: *metallacrowns* - MCs) in einem Molekül zu vereinen.

Mit dem *magnetic director approach* wurde bereits eindrucksvoll gezeigt, wie ein hoher Spingrundzustand in einer 12-MC-4 Struktur gezielt zu generieren ist. Zudem weist die planare Kronenstruktur eine ideale Koordinationsumgebung auf, um die Jahn-Teller Achsen von Ringmetallionen mit hoher Einzelionenanisotropie parallel zueinander auszurichten. Bedingungen für die effektive Anwendung dieser beiden Konzepte sind die Fähigkeit des zentralen Gastions an starken magnetischen Austauschwechselwirkungen teilzunehmen, sowie eine beeinflussbare anisotrope Elektronenverteilung der Ring-bildenden Metallionen. Daher präsentieren sich 3d Übergangsmetallionen als die optimale Wahl für diesen Ansatz.

Die Synthese von heterometallischen MCs erfordert verschiedene Selektivitäten der zentralen gegenüber der im Ring befindlichen Koordinationstasche. Um diese Bedingung zu erfüllen, wurden zwei verschiedene Ligandoptimierungen in dieser Arbeit verfolgt. Die Donoratome in apikaler Koordinationsumgebung der Ringmetallionen wurden variiert, was zu einer veränderten Bindungsaffinität entsprechend des HSAB Konzepts nach Pearson führt. Zudem wurden zusätzliche koordinierende Funktionalitäten in bereits etablierte MC Ligandensysteme, wie die Amidoxime, eingeführt, um die Koordinationsumgebung den Kronenbildenden Metallionen anzupassen.

Diesen Konzepten folgend konnten mehrere neue 3d MC Verbindungen hergestellt und mittels Infrarotspektroskopie, Einkristallröntgendiffraktometrie und SQUID Magnetometrie charakterisiert werden. Die Synthese und Verwendung von 2-Methylmercaptobenzoehydroxamsäure führte zur erstmaligen Isolierung einer Cadmium(II) basierten Metallakrone und damit zu einer neuen Perspektive bezüglich einer Verbesserung der Lumineszenzeigenschaften dieser Verbindungsklasse. In dieser Arbeit werden eine gemischtvalente Kobalt(II/III) MC, Doppeldecker sowie eine isolierte Cu(II) MC und zwei Mangan(II/III) Doppeldecker MCs vorgestellt, um nur einige der Ergebnisse hervorzuheben.

---



---

## Danksagung

[Redacted text block]

[Redacted text block]

[Redacted text block]

[Redacted text block]

[Redacted text block]

[Redacted text block]

[Redacted text block]

[Redacted text block]



---

# Contents

|  |           |
|--|-----------|
| <b>1. Introduction</b>   | <b>1</b>  |
| <b>2. Aim of this work</b>   | <b>16</b> |
| <b>3. Results and Discussion</b>   | <b>21</b> |
| 3.1. Hydroxamic acid based ligands . . . . .   | 22        |
| 3.1.1. Coordination ability of benzohydroxamic acid with a sulfur donor atom in <i>ortho</i> -position - Transition metal complexes with <b>L3</b> . . . .   | 23        |
| 3.1.2. Coordination ability of benzohydroxamic acid with a nitrogen donor atom in <i>ortho</i> -position - Transition metal complexes with <b>L2</b> . . . . | 42        |
| 3.1.3. Coordination ability of benzohydroxamic acid with an oxygen donor atom in <i>ortho</i> -position - Transition metal complexes with <b>L1</b> . . . .  | 44        |
| 3.2. Metallacrown ligands with additional coordinating side arm in <i>ortho</i> -position  | 57        |
| 3.2.1. Setback with the side arm - Transition metal complexes with <b>L4</b> . .   | 58        |
| 3.3. Amidoximes - Turning point of this study!?  | 63        |
| 3.3.1. Coordination compounds with salicylamidoxime derivatives . . . . .  | 65        |
| <b>4. Summary and Outlook</b>  | <b>80</b> |
| <b>5. Experimental Part</b>  | <b>85</b> |
| 5.1. Ligand Synthesis . . . . .  | 87        |
| 5.1.1. 2-Mercaptobenzoic acid methyl ester ( <b>L3a</b> ) . . . . .  | 87        |
| 5.1.2. 2-Methylmercaptobenzoic acid methyl ester ( <b>L3b</b> ) . . . . .  | 88        |
| 5.1.3. 2-Methylmercaptobenzohydroxamic acid ( <b>L3</b> ) . . . . .  | 89        |
| 5.1.4. N-(2-Hydroxybenzyl)methylanthranilate ( <b>L5a</b> ) . . . . .  | 90        |
| 5.1.5. N-(2-Hydroxybenzyl)anthranilic hydroxamic acid ( <b>L5</b> ) . . . . .  | 92        |
| 5.1.6. N,2-Dihydroxybenzenecarbonimidoyl chloride ( <b>P1</b> ) . . . . .  | 93        |
| 5.1.7. N-Hydroxy-(2-pyridyl)carbonimidoyl chloride ( <b>P2</b> ) . . . . .   | 94        |
| 5.1.8. N-(Pyridin-2-ylmethyl)2-pyridylamidoxime ( <b>L6</b> ) . . . . .  | 95        |
| 5.1.9. N-(Pyridin-2-ylmethyl)salicylamidoxime ( <b>L7</b> ) . . . . .  | 96        |
| 5.1.10. N-(Pyridin-2-ylethyl)salicylamidoxime ( <b>L8</b> ) . . . . .  | 97        |
| 5.1.11. Di-(2-picolyl)amine ( <b>L9a</b> ) . . . . .   | 98        |

|   |            |
|---|------------|
| 5.1.12. N,N-Di-(2-picolyl)salicylamidoxime ( <b>L9</b> ) . . . . .  | 99         |
| 5.1.13. N-(2-Pyridylmethyl)-2-hydroxybenzylamine ( <b>L10a</b> ) . . . . .  | 100        |
| 5.1.14. N-(2-Hydroxybenzyl)-N-(pyridin-2-ylmethyl)salicylamidoxime ( <b>L10</b> )   | 101        |
| 5.1.15. 2,2'-Dihydroxydibenzylamine . . . . .   | 102        |
| 5.1.16. N,N-Diethylsalicylamidoxime ( <b>L11</b> ) . . . . .  | 103        |
| 5.2. Complex Synthesis . . . . .  | 104        |
| 5.2.1. $\text{Fe}^{\text{III}}(\text{L3H})_3$ ( <b>C1</b> ) . . . . .   | 104        |
| 5.2.2. $\{\text{Cu}^{\text{II}}\text{Cl}_2(\text{MeOH})[\mathbf{12} - \text{MC}_{\text{Cu}(\text{II})\text{N}(\text{L3})} - 4]\}_2 \cdot 4\text{MeOH}$ ( <b>C2</b> ) . .  | 104        |
| 5.2.3. $\text{Cu}_2^{\text{II}}\text{Cl}(\text{mmba})(\text{MeOH})_2(\text{H}_2\text{O})[\mathbf{12} - \text{MC}_{\text{Cu}(\text{II})\text{N}(\text{L3})} - 4]_2(\text{ClO}_4)_2$<br>( <b>C3</b> ) . . . . .                         | 105        |
| 5.2.4. $\text{Cu}^{\text{II}}(\mu_2 - \text{ClO}_4)(\text{MeOH})_2(\text{py})_4[\mathbf{12} - \text{MC}_{\text{Cu}(\text{II})\text{N}(\text{L3})} - 4]\text{ClO}_4$ ( <b>C4</b> )   | 105        |
| 5.2.5. $[\text{Co}_4^{\text{III/II}}(\text{L3})_4\text{piv}_2(\text{X})_2(\mathbf{12} - \text{MC}_{\text{Co}(\text{II})\text{Co}(\text{III})\text{N}(\text{L3})} - 4)]_2$ ( <b>X = NO</b><br>or <b>MeOH</b> ) ( <b>C5</b> ) . . . . . | 106        |
| 5.2.6. $[\text{Cd}_{14}^{\text{II}}(\text{L3})_{12}(\mu_6 - \text{O})(\text{DMF})_{10}](\text{ClO}_4)_2$ ( <b>C6</b> ) . . . . .  | 106        |
| 5.2.7. $\{\text{Cu}^{\text{II}}(\text{ClO}_4)(\text{MeOH})[\mathbf{12} - \text{MC}_{\text{Cu}(\text{II})\text{N}(\text{L2})} - 4]\}_2(\text{ClO}_4)_2 \cdot 2\text{MeOH}$<br>( <b>C7</b> ) . . . . .                                  | 107        |
| 5.2.8. $\{\text{Na}_2(\text{DMF})_3\text{Cu}^{\text{II}}\text{sal}_2[\text{Cu}^{\text{II}}(\mathbf{12} - \text{MC}_{\text{Cu}(\text{II})\text{N}(\text{L1})} - 4)]\}_n$ ( <b>C8</b> ) . .   | 107        |
| 5.2.9. $[\text{O}_{10}\text{py}_{10}(\mathbf{30} - \text{MC}_{\text{V}(\text{V})\text{N}(\text{L1})} - 10)]$ ( <b>C9</b> ) . . . . .  | 108        |
| 5.2.10. $[\text{Mn}(\text{II})(\text{HNEt}_3)_2[\mathbf{12} - \text{MC}_{\text{Mn}(\text{III})\text{N}(\text{L1})} - 4](\mu_4 - \text{CO}_3)_2]_2 \cdot (\text{H}_2\text{O})_8$<br>( <b>C10</b> ) . . . . .                           | 108        |
| 5.2.11. $\text{Mn}(\text{II})[\text{H}_2\text{NET}_2[\mathbf{12} - \text{MC}_{\text{Mn}(\text{III})\text{N}(\text{L1})} - 4](\text{MeO})_2]_2 \cdot (\text{MeOH})_2$ ( <b>C11</b> )   | 108        |
| 5.2.12. $\text{Co}_4^{\text{II}}(\text{L4a})_4(\mu_2\text{Piv})_2\text{Piv}_2$ ( <b>C12</b> ) . . . . .   | 109        |
| 5.2.13. $[\text{Cu}_6^{\text{II}}\text{Cl}_2(\text{L9})_2(\text{L9b})_2(\text{MeOH})_2](\text{ClO}_4)_2$ ( <b>C13</b> ) . . . . .   | 109        |
| 5.2.14. $[\text{Cu}_6^{\text{II}}(\text{L10b})_4(\text{ClO}_4)_2(\text{DMF})_6](\text{ClO}_4)_2$ ( <b>C14</b> ) . . . . .   | 110        |
| 5.2.15. $\text{Cu}_2^{\text{II}}(\text{L10cH})_2\text{Cl}_2$ ( <b>C15</b> ) . . . . .   | 110        |
| 5.2.16. $\text{Co}_2^{\text{II}}(\text{L10d})_2$ ( <b>C16</b> ) . . . . .   | 111        |
| 5.2.17. $[\text{Ni}_6^{\text{II}}(\text{L10})_2(\text{L10H})_2(\mu - \text{O}_2\text{COMe})_2(\text{MeOH})_6]$ ( <b>C17</b> ) . . . . .   | 111        |
| <b>6. Bibliography</b>  | <b>112</b> |
| <b>A. Additional Figures</b>  | <b>122</b> |
| <b>B. IR-Spectra</b>  | <b>129</b> |
| <b>C. NMR-Spectra</b>   | <b>139</b> |

|                             |            |
|-----------------------------|------------|
| <b>D. X-ray diffraction</b> | <b>154</b> |
| <b>E. Curriculum Vitae</b>  | <b>164</b> |



# List of Compounds

- L1:** Salicylhydroxamic acid  
**L2:** Anthranilhydroxamic acid  
**L3:** 2-Methylmercaptobenzohydroxamic acid  
**L4:** N-(Pyridin-2-ylmethyl)anthranilic hydroxamic acid  
**L5:** N-(2-Hydroxybenzyl)anthranilic hydroxamic acid  
**L6:** N-(Pyridin-2-ylmethyl)2-pyridylamidoxime  
**L7:** N-(Pyridin-2-ylmethyl)salicylamidoxime  
**L8:** N-(Pyridin-2-ylethyl)salicylamidoxime  
**L9:** N,N-Di-(2-picolyl)salicylamidoxime  
**L10:** N-(2-Pyridylmethyl)-2-hydroxybenzylamine  
**L11:** N,N-Diethylsalicylamidoxime  
**P1:** N,2-Dihydroxybenzenecarbonimidoyl chloride  
**P2:** N-Hydroxy-(2-pyridyl)carbonimidoyl chloride  
**C1:**  $\text{Fe}^{\text{III}}(\text{L3H})_3$   
**C2:**  $\{\text{Cu}^{\text{II}}\text{Cl}_2(\text{MeOH})[\text{12} - \text{MC}_{\text{Cu}(\text{II})\text{N}(\text{L3})} - 4]\}_2 \cdot 4\text{MeOH}$   
**C3:**  $\text{Cu}_2^{\text{II}}\text{Cl}(\text{mmba})(\text{MeOH})_2(\text{H}_2\text{O})[\text{12} - \text{MC}_{\text{Cu}(\text{II})\text{N}(\text{L3})} - 4]_2(\text{ClO}_4)_2$   
**C4:**  $\text{Cu}^{\text{II}}(\mu_2 - \text{ClO}_4)(\text{MeOH})_2(\text{py})_4[\text{12} - \text{MC}_{\text{Cu}(\text{II})\text{N}(\text{L3})} - 4]\text{ClO}_4$   
**C5:**  $[\text{Co}_4^{\text{III/II}}(\text{L3})_4\text{piv}_2(\text{X})_2(\text{12} - \text{MC}_{\text{Co}(\text{II})\text{Co}(\text{III})\text{N}(\text{L3})} - 4)]_2$  (X = NO or MeOH)  
**C6:**  $[\text{Cd}_{14}^{\text{II}}(\text{L3})_{12}(\mu_6 - \text{O})(\text{DMF})_{10}](\text{ClO}_4)_2$   
**C7:**  $\{\text{Cu}^{\text{II}}(\text{ClO}_4)(\text{MeOH})[\text{12} - \text{MC}_{\text{Cu}(\text{II})\text{N}(\text{L2})} - 4]\}_2(\text{ClO}_4)_2 \cdot 2\text{MeOH}$   
**C8:**  $\{\text{Na}_2(\text{DMF})_3\text{Cu}^{\text{II}}\text{sal}_2[\text{Cu}^{\text{II}}(\text{12} - \text{MC}_{\text{Cu}(\text{II})\text{N}(\text{L1})} - 4)]\}_n$   
**C9:**  $[\text{O}_{10}\text{py}_{10}(\text{30} - \text{MC}_{\text{V}(\text{V})\text{N}(\text{L1})} - 10)]$   
**C10:**  $[\text{Mn}(\text{II})(\text{HNEt}_3)_2[\text{12} - \text{MC}_{\text{Mn}(\text{III})\text{N}(\text{L1})} - 4](\mu_4 - \text{CO}_3)_2]_2 \cdot (\text{H}_2\text{O})_8$   
**C11:**  $\text{Mn}(\text{II})[\text{H}_2\text{NEt}_2[\text{12} - \text{MC}_{\text{Mn}(\text{III})\text{N}(\text{L1})} - 4](\text{MeO})_2]_2 \cdot (\text{MeOH})_2$   
**C12:**  $\text{Co}_4^{\text{II}}(\text{L4a})_4(\mu_2\text{Piv})_2\text{Piv}_2$   
**C13:**  $[\text{Cu}_6^{\text{II}}\text{Cl}_2(\text{L9})_2(\text{L9b})_2(\text{MeOH})_2](\text{ClO}_4)_2$   
**C14:**  $[\text{Cu}_6^{\text{II}}(\text{L10b})_4(\text{ClO}_4)_2(\text{DMF})_6](\text{ClO}_4)_2$   
**C15:**  $\text{Cu}_2^{\text{II}}(\text{L10cH})_2\text{Cl}_2$   
**C16:**  $\text{Co}_2^{\text{II}}(\text{L10d})_2$   
**C17:**  $[\text{Ni}_6^{\text{II}}(\text{L10})_2(\text{L10H})_2(\mu - \text{O}_2\text{COMe})_2(\text{MeOH})_6]$





# 1. Introduction

Quantum computing and spin based electronics are two of the most desired applications for molecular systems ever since the phenomenon of slow magnetic relaxation for discrete molecules has been discovered.<sup>[1-3]</sup> The alignment of magnetic momenta in an external magnetic field is known from macroscopic ferromagnets and has been used for decades in data storage devices. To maximize storage capacity the research goal is to decrease the size of magnetically controlled switches. Therefore, investigations concerning molecular magnetism are gaining more and more interest. The first breakthrough in molecular magnetism has been the characterization of a manganese acetate cluster ( $Mn_{12}O_{12}$ ) and with this the discovery of slow magnetic relaxation of magnetization and magnetic hysteresis below a certain threshold temperature on the molecular basis.<sup>[4]</sup>

Nowadays, molecules revealing these properties are known as *single molecule magnets* (SMMs). The composition of SMMs already reveals a broad variety. Transition metal, lanthanide and even actinide ions with a wide diversity of ligands have been explored in this research area.<sup>[5-8]</sup> In order to increase relaxation times of the spin reversal in single molecule magnets and therefore to reach a time region useful for data storage devices, research is aiming for a high energy barrier  $U_{eff}$ . This barrier is dependent on the spin ground state  $S$  and the anisotropy of the molecule represented with the axial zero-field splitting parameter  $D$ . The zero-field splitting causes a magnetic bistability of the spin ground state of a SMM by splitting it into  $2S + 1$   $M_S$  sublevels with  $-S \leq m_S \leq +S$ . If  $D$  becomes positive, the  $M_S = 0$  state is lowest in energy. Therefore, no magnetic bistability is present in the ground spin state of the molecular system. If  $D$  reaches negative values, it is called easy axis or Ising-type anisotropy leading the energy diagram of the  $M_S$  levels of the ground state to form a double well potential with  $M_S = 0$  highest in energy (see figure 1.1).<sup>[9]</sup> A SMM can be magnetized with an applied magnetic field. Magnetization of the molecule would lead to a loss of degeneracy of the sublevels and to a higher occupancy of the  $M_S$  lowest in energy (full occupancy in high magnetic fields). A change in the direction of magnetization or switching off the external field would reestablish the degeneracy of the sublevels with mainly one  $M_S$  level being occupied. This unfavored dispersion only reaches the equilibrium via relaxation processes. Four different processes are currently discussed in the literature. They can be described as predominantly temperature- or field-dependent relaxation. Orbach and Raman processes are temperature-dependent, obeying the Arrhenius

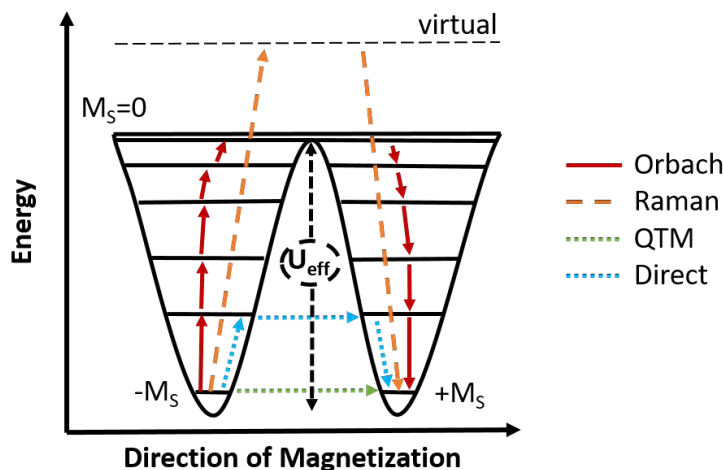


Figure 1.1.: Schematic representation of the degenerate  $M_S$  sublevels of the spin ground state  $S$  plotted in a double well potential dependent on the magnetization direction. The negative zero-field splitting parameter  $D$  yield  $2S + 1$   $M_S$  sublevels and an effective energy barrier  $U_{eff}$ . Arrows indicate possible relaxation processes.

law or higher dependencies, respectively. The Orbach process occurs via excitation of the electron to the next  $M_S$  state upon interaction with lattice phonons, overcoming the barrier and followed by a release of energy again through phonon interaction. The Raman process uses an excitation to virtual states instead. Field dependence is assigned to the quantum tunneling of magnetization (QTM) within the lowest lying  $M_S$  states and the Direct process, representing tunneling via excited states. Hence, Orbach, Raman and Direct process belong to the group of spin-lattice relaxation processes. A more detailed discussion of the possible relaxation paths is done in the results and discussion part of this work.

The energy barrier which has to be overcome to reach an equally distributed spin system is traditionally described as  $U_{eff} = |D|S^2$  for molecular systems with an integer spin ground state ( $U_{eff} = |D|(S^2 - 1/4)$  for half-integer spin systems). However, after two decades of research aiming for a molecule with a high spin ground state<sup>[10-13]</sup> the relevance and dependency of  $S$  on the effective energy barrier is less than previously expected. One explanation could be that an increasing spin ground state of molecules is accompanied by a higher nuclearity, which often leads to higher structural complexity and, as a consequence, to lower molecular anisotropy.<sup>[14]</sup> In other words, the magnetic anisotropy of molecules is the most important property of SMMs, which has been recently confirmed by theoretical

considerations.<sup>[15,16]</sup> Nevertheless, the spin ground state must be unequal to zero and ideally well separated from the lowest excited state to avoid QTM.

The aim to increase the molecular anisotropy in SMMs yielded another breakthrough in molecular magnetism, the discovery of slow magnetic relaxation of a single lanthanide ion complex in 2007 by Ishikawa.<sup>[17]</sup> Lanthanide (Ln) ions exhibit strong spin-orbit coupling (SOC) resulting in high single ion anisotropy, excluding an empty or half filled 4f shell in  $La^{3+}$  and  $Gd^{3+}$ , respectively. For these highly coupled systems, the spin ground state  $S$  cannot be considered anymore and the relevant good quantum number for describing the ground state terms of Ln ions is  $J$ . The intrinsic zero-field splitting leads to a bistable ground state due to a splitting of  $J$  into  $2J + 1$   $M_J$  sublevels. Additionally, as single ions are considered, it is particularly important to distinguish between ions with an odd electron count (Kramers ion) automatically yielding a bistable ground state or an ion with an even electron count (non-Kramers ion).<sup>[18]</sup> Non-Kramers ions, such as Co(II) or Tb(III) need to express axial anisotropy (negative  $D$  value) in a complex to yield a ground state term which is unequal to zero. A very important fact about Ln ions is that the splitting of the different  $M_J$  sublevels only occurs due to a ligand field. This lifting of the degeneracy is orders of magnitude smaller than the spin-orbit coupling effect but is still the crucial effect to observe blocking of the magnetization for these *single ion magnets* (SIMs). A detailed summary of lanthanide based SMMs is given in several reviews<sup>[5,7,8]</sup> and will not be further discussed in this work.

As for Ln based SIMs, it is possible to reach high magnetic anisotropy using 3d metal ions like Co(II) or high spin Fe(I,II) ions exhibiting unquenched orbital momentum in the ground state (strong SOC of the ground state, first-order) and thus contributing with high single ion anisotropy<sup>[18]</sup>. However, the incorporation of 3d metal ions offers additional tools to increase molecular anisotropy. It has been demonstrated that strong anisotropic exchange coupling leads to magnetic anisotropy.<sup>[19]</sup> Besides that, another promising approach is to make use of ligand field induced SOC present in tetragonally distorted Mn(III) complexes. The electronic ground state of the free Mn(III) ion is a  ${}^5D$  state further split into a  ${}^5E$  and  ${}^5T$  in an octahedral coordination environment ( $O_h$  symmetry). This ground state is not affected by first-order SOC, however, represents a Jahn-Teller system yielding to an additional splitting of the energy levels (see figure 1.2). These distorted  $d^4$  systems exhibit large axial magnetic anisotropy accompanied by a large zero-field splitting.<sup>[20]</sup> Responsible for this zfs is a second-order spin-orbit coupling effect.<sup>[21]</sup> The  ${}^5B_{1g}$  state lying lowest in energy mixes with the first and higher excited states. Even a mixing with the  ${}^3E_g$  state,

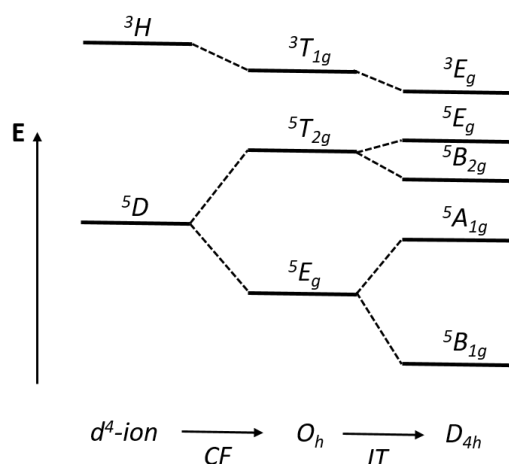


Figure 1.2.: Energy level diagram for  $d^4$  systems like Mn(III) as a free ion, in an octahedral ( $O_h$ ) crystal field (CF) and tetragonal distorted coordination environment ( $D_{4h}$ , elongated along  $z$  axis) due to a Jahn-Teller distortion (JT). The diagram is not scaled.

originating from the spin-flipped  $^3H$  excited state of the free ion, is highly involved to yield this large axial anisotropy.<sup>[21–23]</sup>

Manganese has been used for the very first investigated SMM ( $Mn_{12}O_{12}$  cluster) and is ever since well represented in the research field of molecular magnetism.<sup>[24]</sup> After an intense study of the  $Mn_{12}O_{12}$  molecular motif, manganese based molecules kept being in focus of the SMM research. The manganese acetate cluster investigated by Sessoli et al.<sup>[4]</sup> had the highest magnetic anisotropy barrier for 14 years and could only be replaced in 2007 by another manganese cluster, the oximate bridged Mn(III) hexamer published by Milios et al.<sup>[25]</sup> By that time, coordination chemists moved from investigating the carboxylate bridged Mn cluster to  $Mn_3$  subunits with an  $-\text{[Mn-N-O]}-$  repetition moiety.<sup>[26–29]</sup> Comparison of this planar trimers with Mn tetramers<sup>[30]</sup> and ferromagnetic coupled  $Mn_6$  structures<sup>[31,32]</sup> reveals that Mn(III) ions can contribute with high spin values ( $S = 2$  each) and with high single ion anisotropy in polynuclear cluster structures. The outstanding feature of Mn(III) ions, allowing to estimate overall magnetic anisotropy in cluster structures, is that their axial single ion anisotropy is oriented parallel to the JT axes of their coordination environment. A parallel alignment of all JT axes in the molecule lead to high molecular anisotropy.<sup>[33,34]</sup> However, in case of a misalignment or nearly perpendicular orientation of the elongated axes no slow magnetic relaxation of the magnetization can be observed.<sup>[31,32]</sup> SMM behavior can be probed via alternating current (ac) magnetic susceptibility mea-

surements. The sample is mounted in a SQUID magnetometer (superconducting quantum interference device) and a small (3 Oe) alternating magnetic field is applied. The frequency dependence is probed varying the ac field (1 Hz-1400 Hz). The measured response of the sample is separated into two parts, the real and the imaginary part of the ac magnetic susceptibility, commonly described as the *in-phase* and *out-of-phase* signal, respectively. An applied dc magnetic field is often used to suppress QTM. However, SMMs need to show a temperature-dependent *out-of-phase* signal without an additional magnetic dc field otherwise it must be denoted as SMM-like behavior. Further insights in measurement and evaluation techniques for the examination of SMM behavior will be given in the results and discussion part of this work.

Another advantage of the incorporation of 3d metal ions in SMMs compared to Ln ions is the possibility to adjust the molecular spin ground state. 3d metal ions are able to take part in strong exchange coupled clusters, as their d-orbitals overlap with orbitals of bridging ligand molecules. Therefore, 3d metal ions exhibit more covalency than 4f ions do, leading to stronger exchange between the magnetic orbitals. This strong exchange coupling can be used to achieve high spin ground states and to separate them from excited states in order to effectively suppress magnetic relaxation via close lying excited states.<sup>[35-37]</sup> Therefore, 3d metal ion clusters afford a direct manipulation of their magnetic anisotropy and spin ground states according to an elaborate ligand design.<sup>[38]</sup> With coordination chemistry it is possible to rationally influence the SMM character of compounds by varying the electronic structure of complexes. A well established synthetic strategy for this aim is the *bottom-up* approach.

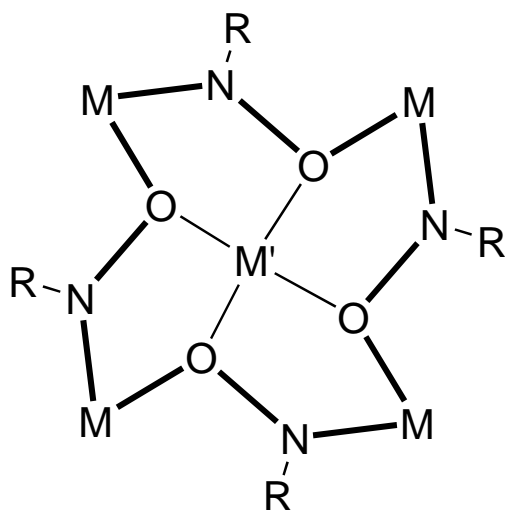


Figure 1.3.: Schematic representation of a 12-MC-4 structure, a metallacrown with four  $-[M-N-O]-$  repeating units and a coordinated metal guest ion  $M'$ .

According to this method, metallacrowns (MCs) expose themselves as an excellent compound class as their modular building blocks set the basis for a tremendous richness of variations. Metallacrowns consist of  $-[M-N-O]-$  repeating units of metal ion, nitrogen and oxygen atoms. They represent the inorganic counterpart of the well known organic crown ethers and mimic their ability of the coordination of a central guest ion according to their cavity size. The basic structure motif of a MC with four repeating units is shown in figure 1.3. Likewise to the organic crown ethers, MCs vary in their cavity size according to the nomenclature 12-MC-4 with 12 representing the number of atoms building the MC ring and 4 the number of oxygen atoms incorporated in the crown. The ring size varies from 9-MC-3 structures reaching MCs bigger than 30-MC-10. Their commonly used sum formula  $M'X[\text{ring size}-MC_{MZ(L)}\text{-ring oxygens}]Y$  is composed of the central guest ion  $M'$ , coordinating anions and solvent molecules  $X$ , the ring building metal ions  $M$ , the main ligand system  $L$  including the third heteroatom of the ring  $Z$  and non-coordinating counterions  $Y$ .  $Z$  is in most cases represented by a nitrogen donor atom, thus leading to the  $-[M-N-O]-$  repeating unit. The most established bridging units are oximes leading to commonly used ligands like salicylaldoxime and in particular important for the development of MCs salicylhydroxamic acid. The first reported metallacrown was a 12-MC-4 structure based on salicylhydroxamic acid with  $Mn(III)$  as ring building metal ions and a  $Mn(II)$  ion as central guest. The molecular structure of  $Mn^{II}(\text{acetate})_2[12-MC_{Mn^{III}N(\text{shi})}-4](DMF)_6$  synthesized by Lah and Pecoraro<sup>[39]</sup> is depicted in figure 1.4. All  $Mn(III)$  ions are embedded in octahedral coordi-

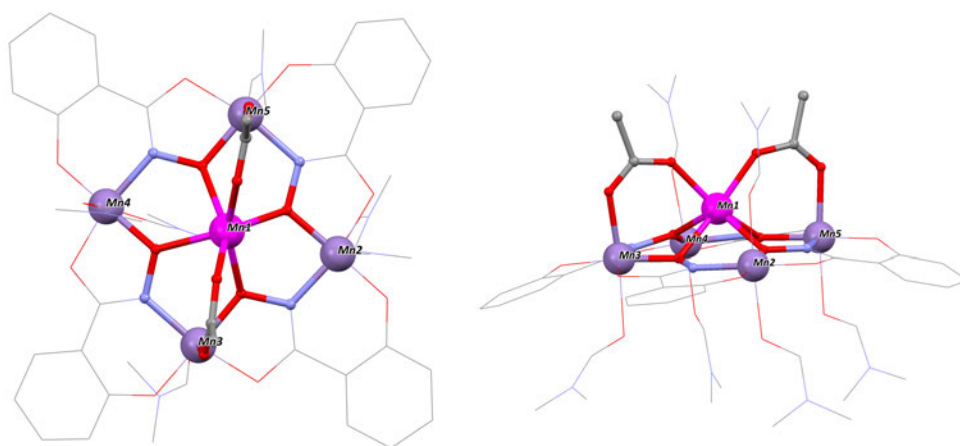


Figure 1.4.: Molecular structure of the first reported metallacrown<sup>[39]</sup>, a 12-MC-4 structure based on salicylhydroxamic acid and Mn(II/III) ions, from the top (left) and a side view (right) of the MC plane. Color code: Violet - Mn(III), magenta - Mn(II), red - oxygen, blue - nitrogen, gray - carbon. Hydrogen atoms and non-coordinating solvent molecules have been omitted for clarity.

nation environments whereas the guest ion is coordinated by the four hydroxamato oxygen atoms of the crown and additional two oxygen atoms of bridging acetate molecules building a trigonal prismatic environment. The apical coordination sites of each Mn(III) ion are occupied by carbonyl and hydroxamato oxygen atoms of one ligand and the oxime nitrogen and the hydroxy oxygen atoms of the next neighboring ligand. Hence, four of these ligands form a planar 12-membered ring. Salicylhydroxamic acid is often abbreviated with *shi* in the literature referring to its threefold deprotonated coordinating structure, salicylhydroximate (see figure 1.5 (top)). One key feature of MCs is their adjustable cavity size. Different main ligands lead to a different number of repetition units. Most relevant for the crown size is the binding angle between the two coordination pockets offered by each MC ligand (see figure 1.5 (bottom)). The combination of a six-membered ring and a juxtaposed five-membered ring embodied in salicylhydroxamic acid and its derivatives yield a  $90^\circ$  angle between the coordinated ring metal ions. For a closed cycle, four of these ligands must coordinate next to each other ending up with a 12-MC-4 structure. In comparison to that, a wider angle (ideally  $108^\circ$ ) stretched by ligands like picoline hydroxamic acid with two juxtaposed five-membered rings lead to the formation of a 15-MC-5. This feature allows for an optimized cavity design for the embedded central guest ion and highlights the extraordinary ability of a size dependent incorporation of for example both transition metal

and lanthanide ions. Distinct adjustable parameters from which the exceptional structural

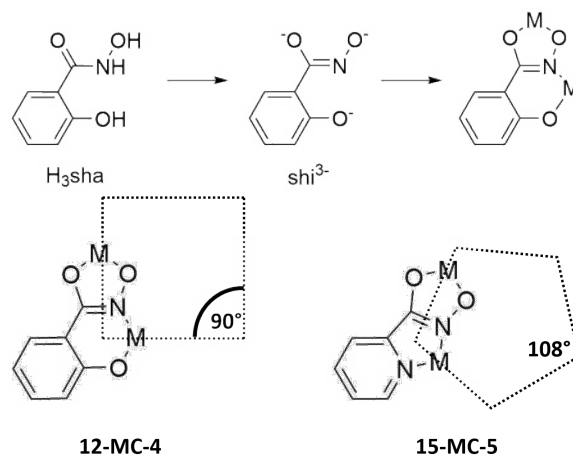


Figure 1.5.: Schematic representation of the bifunctionality of salicylhydroxamic acid ( $H_3sha$ ) its deprotonated form  $shi^{3-}$  and the coordination of metal ions M (top). Comparison of salicylhydroxamic acid and picoline hydroxamic acid leading to different binding angles between neighboring metal ions according to the ring sizes of both binding pockets (5/6-membered or 5/5-membered) and thus to a different count of  $-[M-N-O]-$  repetition units to form a closed crown structure (bottom).

versatility of metallacrowns arises are summarized in figure 1.6. Besides an optimization of the main ligand to reach selective cavity sizes of each MC, also the ring building metal ions can be varied. Thereby, examples for MCs with 3d metal ions, from vanadium(V) and manganese(III) over iron(III), cobalt(III) and nickel(II) up to copper(II) and even zinc(II) used as the ring forming metal ions, are known. However, the MC formation and its planarity is not only dependent on the main ligand. Solvent molecules can have a crucial impact on the MC structure.<sup>[40]</sup> Dendrinou-Samara et al.<sup>[41]</sup> demonstrated that different donor strength of the solvents can lead to inter-conversion of Mn(III) MCs. A more detailed view on this topic will be given in the results and discussion part of this work.

Further important influence on the MC structure is offered by the coordination of a broad variety of co-ligands. Monocarboxylates in combination with trivalent ring metal ions lead to the formation of single "half-sandwich" type 12-MC-4 complexes<sup>[42,43]</sup>. However, for divalent ring metal ions "sandwich" type double-decker MC complexes are formed, due to charge compensation.<sup>[44]</sup> Dicarboxylates instead or several other bifunctional co-ligands lead to a connection of MC molecules reaching even 3-dimensional networks.<sup>[45]</sup> A main advantage of



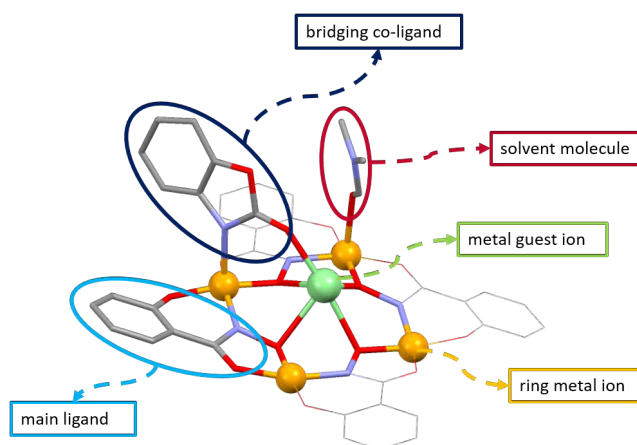


Figure 1.6.: Overview of adjustable structural features of the MC compound class in order to optimize the properties of the molecules.

MCs towards other coordination polymers or bigger cluster structures with similar features is their remarkable integrity in solution.<sup>[46]</sup> The self-assembled MCs exhibit a strong stability in solution whereas other compounds, although thermodynamically stable, often lack kinetic stability.<sup>[45]</sup> This uniqueness makes the MC compound class accessible for surface application techniques. Hence, the next step towards functional materials is already close to be fulfilled, as addressability of a single MC SMM is in principle reachable. Further, it enables MCs to be probed by surface-dependent measurement methods like *scanning tunneling microscopy* or *x-ray magnetic circular dichroism* studies.<sup>[47,48]</sup>

Another benefit of this structural versatility is a targeted manipulation of certain properties. Early studies of MCs were focused on their ability to act as molecular recognition agent.<sup>[49]</sup> Nowadays, research interest has shifted more towards building blocks for multidimensional solids, catalysis, bioactivity as well as luminescence and molecular magnetism.<sup>[46]</sup> Since years lanthanide ions are investigated with regards to their luminescent properties. However, Ln ion coordinating MCs are more recently gaining interest. The MC backbone ensures a spacial distance within the molecular structure of the emitting Ln ions and possible quenching vibrational modes (C-H, O-H, N-H). Especially zinc(II) is very useful to form the crown scaffold around a luminescent Ln(III) ion, as singly occupied orbitals or paramagnetic metal ions in the periphery of emitting centers cause a quenching of the emittance due to d-d transitions and should be avoided.<sup>[44,50]</sup> This makes zinc(II) the only d-block metal ion that has been effectively used in a MC scaffold of a luminescent compound. Main group elements did not show any improvement of the luminescence lifetime. For more insights in

luminescence properties of MCs the review article by Chow et al.<sup>[51]</sup> and the summarizing chapter by Athanasopoulou et al.<sup>[45]</sup> should be emphasized.

Short magnetic coupling pathways and the ability to undergo substitution of the coordinated guest metal ion<sup>[49]</sup> are key features of MCs, making them highly interesting for the application in magnetochemistry. In the following, an overview of MCs exhibiting SMM behavior with or without an applied dc field is given. This excerpt is focused on 12-MC-4 structures due to their relevance for this work. However, it should be mentioned that also 9-MC-3 and bigger crown structures are known to possess an energy barrier for the relaxation of the magnetization.<sup>[52]</sup> Among them the record holder in the field of 3d SMMs, a Mn(III) hexamer comprising two 9-MC-3 structures, published by Milios et al.<sup>[25]</sup>). By the time, first appearance of slow relaxation of the magnetization on a molecular scope was reported ( $Mn_{12}O_{12}$  cluster), Lah and Pecoraro<sup>[39]</sup> introduced the  $Mn^{II}(acetate)_2[12-MC_{Mn^{III}N(shi)}-4](DMF)_6$  complex to the research community. However, it lasted more than 20 years until this manganese metallacrown complex was magnetically characterized and found to exhibit SMM behavior.<sup>[53]</sup> Another five years later, in 2016, Boron et al.<sup>[54]</sup> reported the observation of SMM behavior for a mixed 3d-4f 12-MC-4. Both work groups expected blocking of magnetization based on a parallel alignment of the Jahn-Teller axes of the ring building Mn(III) ions due to a planar MC structure and thus leading to high molecular anisotropy. Indeed, both the Mn(II) and the dysprosium(III) centered manganese crown yield an effective energy barrier for the zero-field split ground state. However, Boron et al. intended to substitute the isotropic Mn(II) guest ion with a highly anisotropic Dy(III) ion in order to achieve an even higher anisotropy barrier. Zaleski et al. reported a value of  $14.7 \text{ cm}^{-1}$  while Boron et al. concluded only with the observation of an significant *out-of-phase* signal. In addition to that, several other Ln(III) centered manganese 12-MC-4 do not show any evidence of SMM behavior. Cao et al.<sup>[55]</sup> reported an Y(III) centered manganese 12-MC-4 also lacking the ability of blocking of the magnetization, which comes along with results obtained for other Mn(III) crown structures with diamagnetic guest ions.<sup>[53]</sup> However, the Mn(II) ion in the central cavity seems to have crucial influence on either the anisotropy or the spin ground state of the molecule. Any magnetic anisotropy effect can be neglected as Mn(II) ions exhibit a high spin  $d^5$  configuration leading to a fully isotropic electron distribution. Gd(III) compares well, as it also offers a half filled and isotropic valence electron shell, however, the corresponding Gd(III) centered Mn(III) 12-MC-4 molecule does not reveal any significant evidence for SMM behavior.<sup>[54]</sup> One positive outcome of the incorporation of a lanthanide ion in MC structures has been

reported by Li et al.<sup>[56]</sup>. The Yb(III) centered Zn(II) 12-MC-4 exhibits SMM-like behavior with an applied dc magnetic field of 600 Oe. As the diamagnetic ring metal ions do not contribute to the magnetic response of the molecule, the denotation SIM would be suitable for this compound. In the same year Rentschler and coworkers<sup>[57]</sup> published a series of three different Co(II) centered Co(III) 12-MC-4 complexes, two of them showing SMM behavior without any applied dc magnetic field. The authors demonstrated that the effective energy barrier for the spin reversal is highly dependent on the geometry of the coordination environment of the central Co(II) guest ion (figure 1.7). Leaving the octahedral coordination towards a more trigonal prismatic shape of the Co(II) environment led to an increase of the effective energy barrier from 14 K and 35 K of up to 79 K determined by ac susceptibility studies with an applied dc field of 1500 Oe. The diamagnetic ring building Co(III) metal ions do not affect the magnetic susceptibility of the molecule. Hence, the magnetic behavior of these molecules originates from a single ion (SIMs). And again transition metal-only MCs have shown to be a better choice for a rational SMM design compared to their lanthanide analogues. Whether the SIM behavior originates in a transition metal or a lanthanide ion in both cases the MC is only used to provide a suitable scaffold for the guest ion. Therefore, the possibility to adjust the magnetic properties even further by the contribution of ring metal ions is completely neglected.

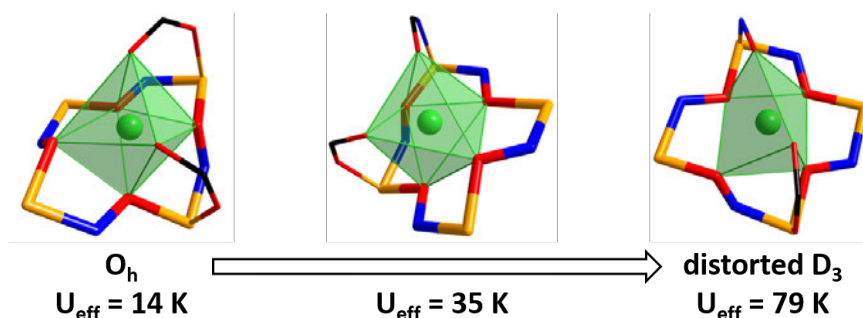


Figure 1.7.: Graphical representation of coordination polyhedra surrounding Co(II) ions in a series of three Co(III) 12-MC-4 structures reported by Rentschler and coworkers<sup>[57]</sup>. The change from an octahedral ( $O_h$ ) coordination environment towards a distorted trigonal prismatic ( $D_3$ ) leads to a tremendous increase of the effective energy barriers of these compounds, all showing SMM-like behavior. Color code: Green - Co(II), yellow - Co(III), blue - nitrogen, red - oxygen, black - carbon.

A different approach, aiming for a high spin ground state in 12-MC-4 structures, has been effectively followed and reported by Happ and Rentschler.<sup>[58]</sup> The authors used the 12-MC-4 scaffold to predict and systematically influence the strength of possible exchange coupling present in these MC molecules. The structure of a 12-MC-4 can be simplified with a fourfold rotational axis in the center to picture it as a star-like framework. Although the crystallographic symmetry of 12-MC-4 complexes often does not reveal a perfect fourfold axis, this is a suitable approach leading to the star-shaped coupling scheme in figure 1.8 to account for the two distinct exchange interaction paths. The radial coupling  $J_1$  between the central guest ion and the ring forming metal ions is promoted through the four hydroxamate oxygen atoms, whereas the tangential exchange coupling  $J_2$  uses the oximate N-O bridges as pathway. The star-like coupling scheme corresponds to the exchange Hamiltonian  $\hat{H}_{ex}(MC)$  (equation 1.1) and thus yields a linear dependence, as long as no anisotropy is considered, for the energy of different spin states regarding the ratio of both coupling constants  $J_1/J_2$ . Hence, this ratio determines the spin ground state of the molecule and for high values leads to a spin alignment of the peripheral metal ions, illustrated in figure 1.8.

$$\hat{H}_{ex}(MC) = -2J_1\hat{S}_5(\hat{S}_1 + \hat{S}_2 + \hat{S}_3 + \hat{S}_4) - 2J_2(\hat{S}_1\hat{S}_2 + \hat{S}_2\hat{S}_3 + \hat{S}_3\hat{S}_4 + \hat{S}_4\hat{S}_1) \quad (1.1)$$

Happ and Rentschler suggested the necessity of a magnetically directing central metal guest ion to afford a high spin ground state. For further understanding of the directing influence of the guest ion two copper centered MCs ( $(HNEt_3)_2Cu^{II}[12 - MC_{Cu(II)N(Shi)} - 4]$ ;  $Cu^{II}(DMF)_2Cl_2[12 - MC_{Fe(III)N(Shi)} - 4] - (DMF)_4 \cdot 2DMF$ ) were compared. Fitting of the magnetic susceptibility data for both compounds led to  $J_1/J_2$  ratios of 1.7 and 13 for the homometallic and the heterometallic MC, respectively. This tremendous increase is directly correlated to a change in the spin ground state of the molecules from  $S = \frac{1}{2}$  for the copper MC to a high spin state of  $S = \frac{11}{2}$  for the iron MC. Strong antiferromagnetic coupling between the copper(II) guest ion and the iron(III) ions suppresses the quenching of the total spin within the crown resulting in a MC with high spin ground state. The observed radial antiferromagnetic coupling between the central copper(II) ion and  $d^5$  high spin ions (Fe(III)) mainly originates from a strong overlap of both  $d_{x^2-y^2}$  orbitals and reaches a coupling constant of  $J_1 = -49 \text{ cm}^{-1}$ . A change towards  $d^4$  high spin ions in the crown should affect this exchange coupling tremendously. Depopulation of the  $d_{x^2-y^2}$  orbitals of the ring forming Mn(III) ions leaves the  $d_{xz}$ ,  $d_{yz}$ ,  $d_{xy}$  and  $d_{z^2}$  orbital to be the magnetic orbitals. Most importantly, they are orthogonal to the magnetic orbital of the central guest

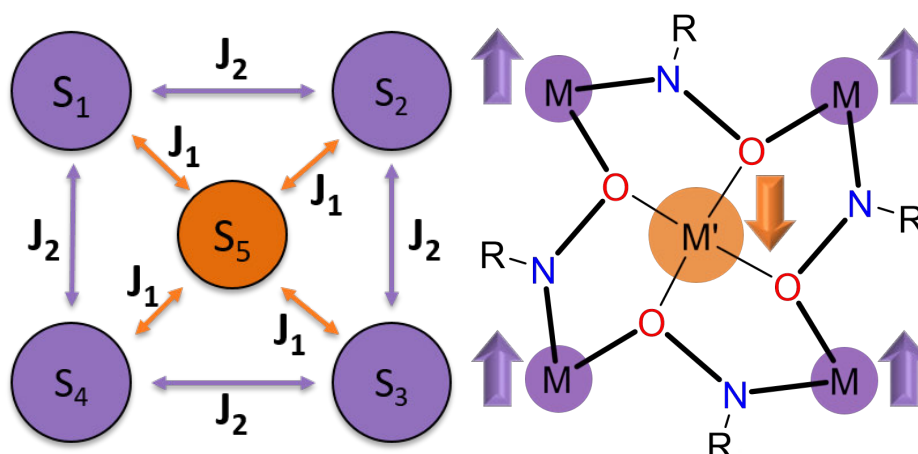


Figure 1.8.: Star-shaped coupling scheme for a 12-MC-4 (left) and a schematic representation of a 12-MC-4 structure with a spin alignment of the crown building metal ions due to a high ratio of both coupling constants (right).

ion ( $d_{x^2-y^2}$ ) and thus lead to strong ferromagnetic exchange coupling (figure 1.9 (left)).<sup>[59]</sup> Ohio et al.<sup>[59]</sup> reported a dinuclear Mn(III)-Cu(II) SMM with alkoxide bridged metal ions. The Mn-O-Cu bridging angle of  $102.1^\circ$ , present in their complex, lies within the range of hydroxamate oxygen bridging angles observed in MCs. Fitting of the magnetic susceptibility data led to a coupling constant of  $78 \text{ cm}^{-1}$ . Li et al. reported a weakening of the ferromagnetic interactions for a similar dinuclear complex upon coordination of an additional bridging carboxylate ion in axial position.<sup>[60]</sup> However, they still observed strong ferromagnetic exchange with a coupling constant of  $67.64 \text{ cm}^{-1}$ . For more variety of magnetically directing guest ions, the electron to hole equivalent of a  $d^9$  system, a  $d^1$  system, is a suitable choice. Hence, a change from the  $d^9$  Cu(II) ion for example to a  $d^1$  vanadyl ion  $VO^{2+}$  would cause a rotation of the magnetic orbital by  $45^\circ$ , as the unpaired electron occupies the  $d_{xy}$  orbital instead of the  $d_{x^2-y^2}$  orbital for V(IV) and Cu(II), respectively.<sup>[61,62]</sup> Regarding the Mn(III)  $d^4$  ion, most relevant for the radial exchange interactions is the singly occupied  $d_{xy}$  orbital, as  $d_{x^2-y^2}$  is unoccupied. It is not trivial to predict the exchange interaction for such a system, as many magnetic orbitals are involved. However, orthogonality is guaranteed for all magnetic orbitals which are not solely embedded in the xy-plane and herewith leading to ferromagnetic exchange. Hence, a more detailed study of the overlap of the remaining Mn(III) based  $d_{xy}$  orbital with the V(IV) based  $d_{xy}$  orbital is necessary for a better understanding. Without any supporting calculations, only a qualitative description of this overlap is possible. However, the overlap with a diamagnetic p orbital of the bridging

hydroxamato oxygen atom is not negligible and thus leading to antiferromagnetic exchange coupling. Only in the case of a Mn-O-V angle of  $90^\circ$  an "accidental orthogonality" leads to ferromagnetic exchange.<sup>[63]</sup>

Another advantage of Cu(II) as the magnetic director is its ionic radius of 73 pm. Hence, copper(II) ions fit well in the 12-MC-4 cavity ( $3.6 \text{ \AA} - 4 \text{ \AA}$ ) leading to a strong overlap of the singly occupied  $d_{x^2-y^2}$  orbital with the hydroxamato oxygen atoms. Larger guest ions are coordinated *out-of-plane* and thus participate only in minor exchange interactions. Al-

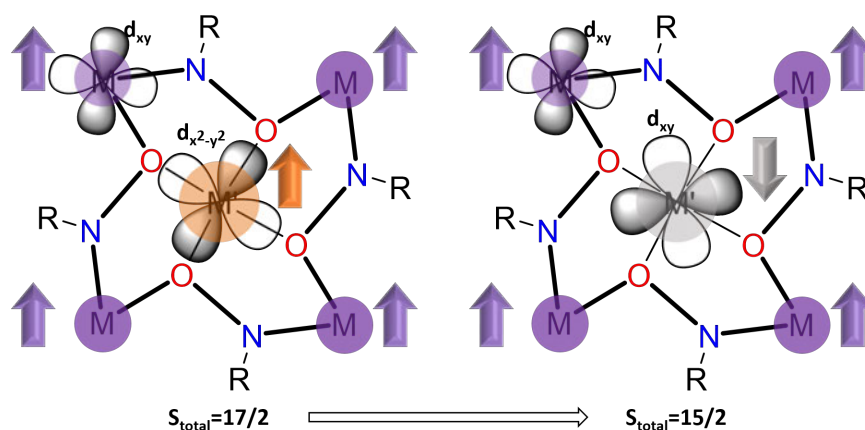


Figure 1.9.: Schematic representation of the influence of the orbital symmetry on the total spin ground state according to the spin alignment in a 12-MC-4 structure by changing the magnetic director position from a  $d^9$  (left) to a  $d^1$  ion (right). Values for the total spin of the ground state  $S_{total}$  correspond to either a Cu(II) or a V(IV) centered Mn(III) 12-MC-4.

though, the Cu(II) centered Fe(III) 12-MC-4 is not a SMM, the *magnetic director approach* represents the first step towards a targeted synthetic engineering of MC-based SMMs. However, the importance of high molecular anisotropy should be mentioned again, as Zaleski et al. reported SMM behavior for the Mn(II) centered Mn(III) 12-MC-4, although they obtained a spin ground state of only  $S = \frac{1}{2}$ . Additionally, excited spin states are separate from the ground state by only  $2 \text{ cm}^{-1}$  and  $6.6 \text{ cm}^{-1}$  for a  $S = \frac{3}{2}$  and another  $S = \frac{1}{2}$  state, respectively.<sup>[53]</sup>

A successful implementation of a directing guest ion into a metallacrown with magnetoanisotropy was reported by Cao et al.<sup>[55]</sup> A coordination of a tungsten(V) ion in the central void of a manganese 12-MC-4 structure led to a change of the ground spin state. The precursor MC, a Y(III) centered Mn(III) 12-MC-4, revealed the expected spin ground state of  $S = 0$ . Due to a diamagnetic guest ion, the star-like coupling scheme simplifies

to a square leaving just  $J_2$  to be determined, as  $J_1$  equals zero. Several examples have shown that the tangential coupling within the MC ring is of antiferromagnetic nature, as observed in the Y(III) centered Mn(III) MC with a fit result of  $-2.88 \text{ cm}^{-1}$  for  $J_2$ . The implementation of a paramagnetic metal ion (tungsten(V)) recovers the star-like exchange coupling. In the manganese 12-MC-4 reported by Cao et al., the central guest ion is bound to the crown via four additional cyanide bridges leading to an antiferromagnetic interaction of  $J_1 = -15.05 \text{ cm}^{-1}$ . Evaluation of the ac magnetic measurements at a zero applied dc field yielded an effective energy barrier for this SMM of  $U_{eff} = 17.8(1) \text{ K}$ . Fitting of the magnetic susceptibility data of the W(V) centered MC revealed a coupling constant ratio of  $J_1/J_2 = 12.66$  and a spin ground state of  $S = \frac{11}{2}$ . The first and second excited states are only  $1.1 \text{ cm}^{-1}$  and  $1.5 \text{ cm}^{-1}$  higher in energy than the ground spin state. For ratios of  $J_1/J_2 > 17$ , the highest possible spin state  $S = \frac{15}{2}$  is expected to be the ground spin state. Higher ratios would lead to a stronger separation of the ground spin state to the first excited states and thus to less QTM. Assuming an antiferromagnetic interaction of  $-1.19 \text{ cm}^{-1}$  for the tangential coupling  $J_2$  (fit result of Cao et al.),  $J_1$  must be of the magnitude of approximately  $-21 \text{ cm}^{-1}$  to yield a MC with its highest possible spin ground state. If the radial coupling occurs to be ferromagnetic instead, a value of  $+21 \text{ cm}^{-1}$  for  $J_2$  yields the ratio  $J_1/J_2 < -17$  and thus an even higher spin ground state of  $S = \frac{17}{2}$ . Regardless of the nature of the magnetic exchange, the necessary magnitude of  $J_2$  to reach the highest spin ground states should be easily reached implementing Cu(II) or V(IV) as the magnetic directors in a Mn(III) 12-MC-4. This overview on 12-MC-4 structures already underlines the outstanding property of MCs to combine magnetostructural concepts yielding a well performing SMM. However, further improvements are necessary to burst the barrier of applicability and reach materials with the targeted features.

## 2. Aim of this work

The *magnetic director approach* has shown to be valuable to effectively create 12-MC-4 structures carrying a high spin ground state.<sup>[58]</sup> However, high spin values alone do not lead to well performing SMMs as it was demonstrated by several studies from the early years of SMM research.<sup>[10–13]</sup> On the other hand, an alignment of the Jahn-Teller axes of structurally embedded manganese(III) ions in molecules is an established method in 3d SMM research to take the important step from single ion anisotropy to molecular magnetoanisotropy. The 12-MC-4 structure provides the necessary planar coordination scaffold to introduce an axial magnetic anisotropy in molecules as it was demonstrated by several groups.<sup>[53–55,64]</sup> However, not every Mn(III) based 12-MC-4 exhibits SMM behavior.<sup>[54]</sup> For all manganese MCs with a diamagnetic guest ion, a spin ground state of  $S = 0$  is reported, as the exchange interaction within the crown scaffold is antiferromagnetic, leading to an overall quenching of the net spin moment. The combination of both, high single ion anisotropy using Mn(III) ions in the periphery and a spin alignment due to a strongly coupled central guest ion is a unique approach towards a rational SMM design offered within the framework of 12-MC-4 compounds.

Hence, to examine a suitable magnetic director providing the necessary strong exchange coupling and its synthetic *in-plane* incorporation into a manganese(III) 12-MC-4 structure yielding a new heterometallic MC are the major goals of this work.

For a systematic synthesis of heterometallic molecules, selectivity of the different coordination pockets must be ensured. In order to keep the synthesis of the targeted 12-MC-4 structure to a reasonable level of complexity, the aim of this work is to engineer the crown forming ligand system, making it possible to coordinate a central metal guest ion, which is different to the ring metal ions, without any need of co-ligand coordination. Therefore, two different concepts, leading to distinct coordination ability of each chelating pocket of the crown building ligands were followed.

**1.)** In the first approach, based on the known salicylhydroxamic acid motif, one of the chelating functionalities was kept as it is while the other one was varied. Keeping the hydroxamato and carbonyl oxygen binding pocket, the influence of the ionization potential and electron affinity of the coordinating donor atom in *ortho*-position to the hydroxamic acid



moiety will be studied. Therefore, three different donor atoms were chosen, oxygen, nitrogen and sulfur (figure 2.1). The coordination environment of the central guest ion is not affected by this approach. The change of a donor atom in apical position of the ring forming metal ions leads to more flexibility for choosing a suitable metal ion for the targeted properties of the MC compound. Therefore, this approach is not only focused on magnetic features but also supports the studies of MCs showing luminescence. According to the *hard-soft acid-base* concept by Pearson,<sup>[65]</sup> the bigger and softer sulfur atom offers the possibility to coordinate softer metal ions. Hence, the coordination affinity to cadmium(II) ions could be examined for example. A MC with Cd(II) as the ring metal ion would be highly interesting for luminescence studies, as the filled 4d shell does not quench the luminescent transitions, often observed in cluster compounds with 3d metal ions exhibiting d-d transitions. Therefore, Pecoraro and coworkers are focused on lanthanide centered double-decker MCs with zinc(II) in the periphery.<sup>[44,50]</sup> This quenching can also be suppressed by the use of main group metal ions like gallium(III) or aluminum(III).<sup>[66]</sup> However, investigations of Ln(III) centered half-sandwich complexes with a Ga(III) 12-MC-4 scaffold so far have shown less luminescence efficiency. All in all, a  $d^{10}$  MC system with higher homologues of zinc(II) is of great interest for further luminescence studies and MC applications.

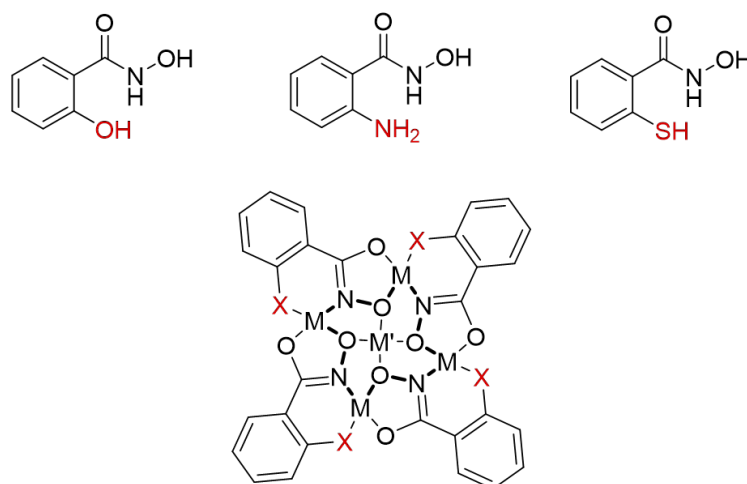


Figure 2.1.: Schematic representation of a 12-MC-4 structure showing that a change of the donor atom (X) in *ortho*-position to the hydroxamic acid moiety only affects the coordination environment of the ring building metal ions. Three possible ligands are shown, varying the donor atoms oxygen, nitrogen and sulfur.

2.) Optimizing the selectivity of the coordination pockets will be reached by attaching additional side arms providing further coordinating functionalities. Thus, the ligand's denticity increases from four (salicylhydroxamic acid) to five. The length of the side arms can

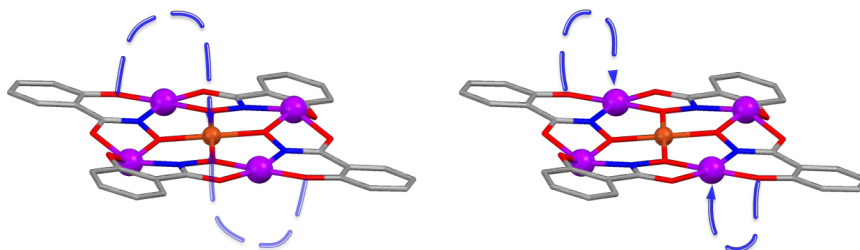


Figure 2.2.: Schematic representation of additional coordinating moieties (blue arrows) occupying axial coordination sites of the central guest ion (left) or optimizing the coordination polyhedra of the ring forming metal ions (right).

be adjusted according to whether the central guest ion should be coordinated in an octahedral environment or the ring forming metal ions should be embedded in a more selective vicinity (figure 2.2). Further functionalities were introduced via the primary amine group of athranilhydroxamic acid, as it is depicted in figure 2.3. A simple Schiff base reaction

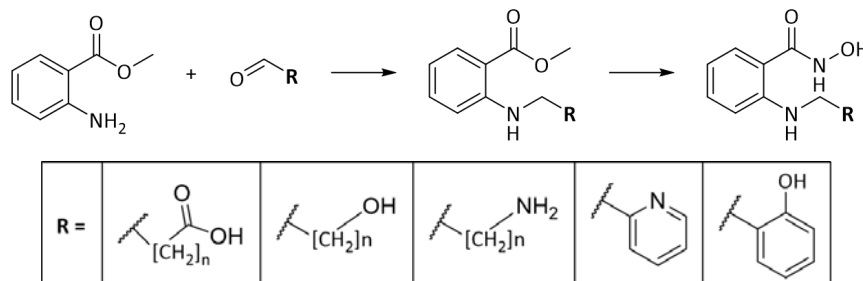


Figure 2.3.: Simplified reaction scheme for the introduction of a variety of coordinating functionalities into the crown forming ligand. Schiff base reaction with subsequent reduction and substitution with hydroxylamine to afford N-substituted derivatives of anthranilhydroxamic acid.

of methyl anthranilate followed by a substitution with hydroxylamine was used to attach a variation of side arms to the main ligand. The attached side arms diversify the crown forming ligand by introducing groups like carboxyl, alcohol, primary amine or even aromatic donors like pyridine or phenol. This method involves a change of the apical coordination sites compared to salicylhydroxamic acid yielding a  $N_2O_2$  donor set with a nitrogen donor pocket and an oxygen donor pocket (*cis* configuration).

The same donor set but with *trans* configuration is achieved using salicylamidoxime and its derivatives as the crown forming ligands. This class of ligands represents another opportunity of introducing additional functionalities into MC forming moieties (figure 2.4). The basic salicylamidoxime and alkyl substituted derivatives are known in the literature to form MC structures. Manganese(III) 9-MC-3, Ni(II) and Cu(II) 12-MC-4 and even a Cr(III) centered Ni(II) heterometallic 18-MC-6 using MC ligands with the amidoxime functionality were reported recently.<sup>[67–70]</sup> Based on a substitution reaction of N,2-dihydroxybenzene-

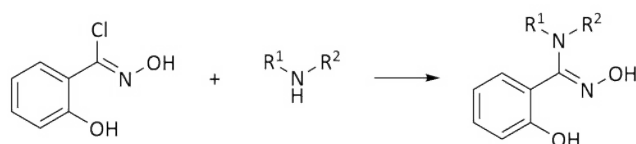


Figure 2.4.: Reaction scheme of the substitution reaction of N,2-dihydroxybenzenecarbonimidoyl chloride with primary and secondary amines to afford salicylamidoxime and its derivatives.  $R^1$  and  $R^2$  are organic side arms carrying additional coordinating functionalities.

carbonimidoyl chloride with primary or secondary amines, depicted in figure 2.4, a variety of additional functionalities can be introduced into the main MC ligand. Substitution with secondary amines can lead to even hexadentate ligands. Hence, all available coordination sites of an octahedral coordinated Mn(III) within the ring of a MC would be occupied using only one ligand system. Thus, any coordinating solvent molecules and co-ligands can be neglected and the JT axes are directly influenced by the main ligand leading to a systematic and targeted tuning of the molecular anisotropy.

Furthermore, amidoximes were chosen, because the provided  $N_2O_2$  donor set in equatorial position is already known to yield high zero-field splitting in Mn(III) SIMs both with nitrogen and oxygen donor atoms on axial coordination sites.<sup>[21,38,71]</sup> Hence, the coordinating functionality of the side arms can be adjusted to yield a targeted overall charge of the ligand (number of acidic protons). However, Duboc reported in 2016 that the largest values for the axial anisotropy parameter  $D$  in Mn(III) SIMs had been achieved by a solely oxygen donor set.

All in all, amidoximes represent a great opportunity to reach the ambitious goal of a heterometallic 12-MC-4 with Mn(III) ions in the crown scaffold. Four of these ligands are sufficient to form a 12-MC-4 structure with Mn(III) as the ring metal ion and Cu(II) as the guest ion with all necessary coordination sites occupied (figure 2.5). Additionally, fixed

side arms promote the formation of discrete MC complexes and avoid any coordination of neighboring MCs via the axial position. Therewith, a surface application of possible MC SMMs would be supported, as co-ligands, which can lead to a lack of integrity in solution, are avoided.<sup>[72]</sup>

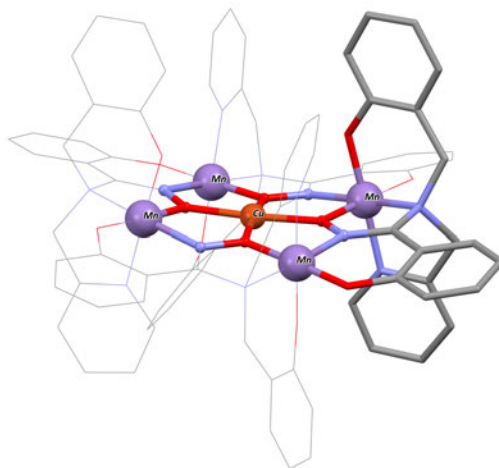
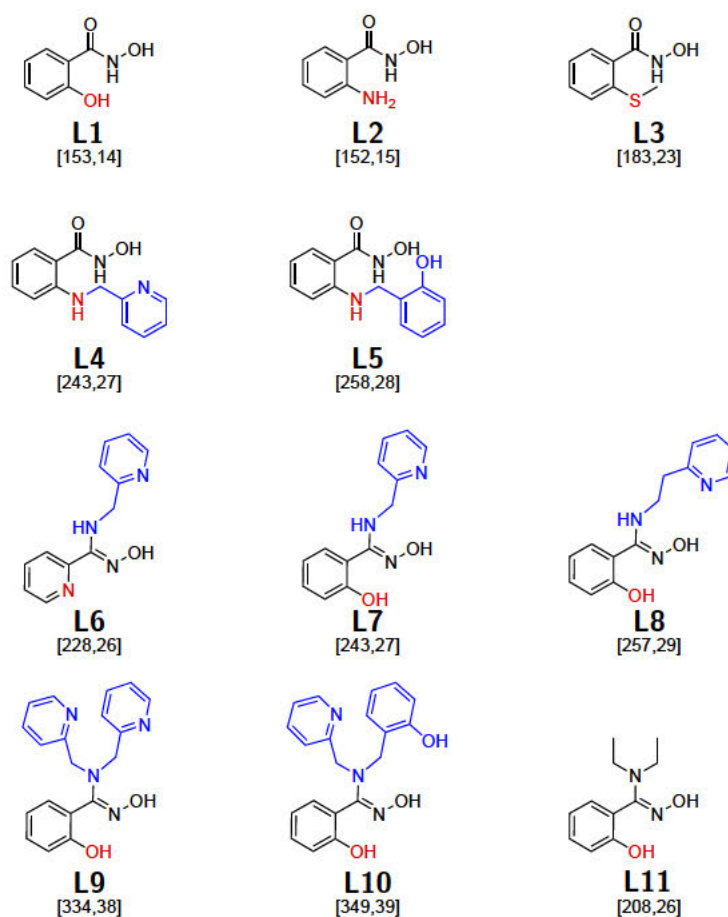


Figure 2.5.: Molecular structure of a fictive Cu(II) centered Mn(III) 12-MC-4 formed by the coordination of four amidoxime ligands. The presented ligand yield a crown scaffold with overall neutral charge and elongated octahedral coordination environments for each Mn(III) ion with a  $N_3O_3$  donor set. Color code: Violet - Mn(III), red - oxygen, blue - nitrogen, gray - carbon.

### 3. Results and Discussion

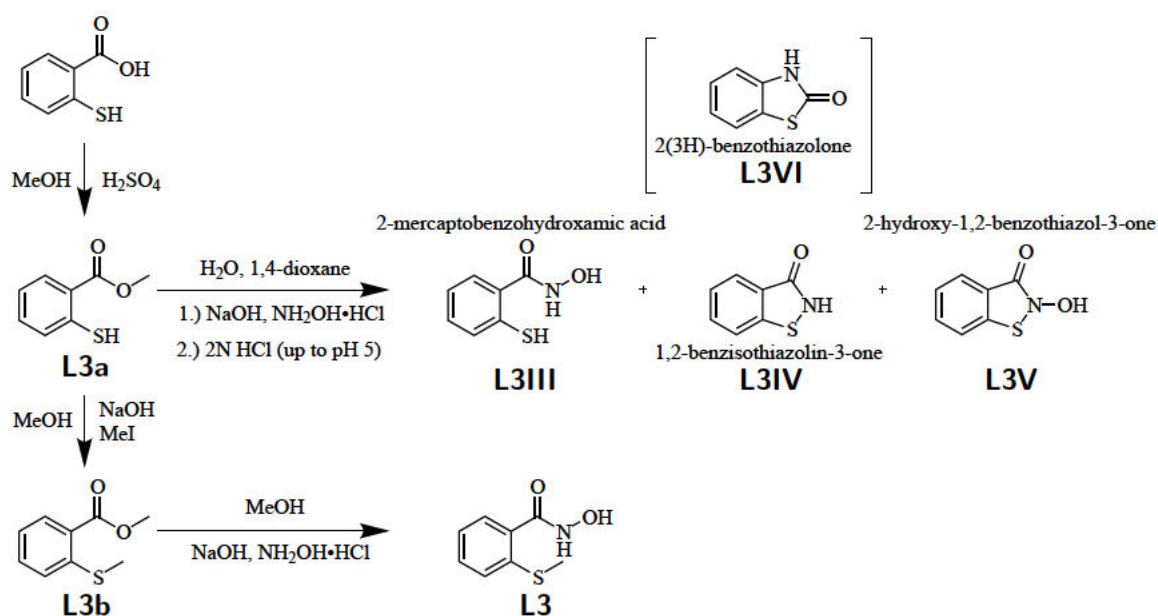
In the following chapter the synthesis of all ligands, shown in scheme 3.1, is elucidated in detail. Further, the broad variety of complexes obtained with these ligands, their molecular structure determined by X-ray diffraction on single crystals and magnetic properties are presented and discussed in respect of their use as building units for metal-lacrowns.



Scheme 3.1: Schematic representation of all ligands, which have been used for complex synthesis within the framework of this dissertation. Structural variations, which have been introduced to systematically fine tune the magnetic properties of the ring metal ions, such as the *ortho* donor groups and additional coordinating moieties are emphasized in red and blue, respectively.

### 3.1. Hydroxamic acid based ligands

Using salicylhydroxamic acid as a basic motif, the influence on coordination affinity of the main ligand has been studied by varying the heteroatom in *ortho*-position. The hydroxy, amine or methylmercapto group were compared, using salicylhydroxamic acid (**L1**), anthranilhydroxamic acid (**L2**) and 2-methylmercaptobenzohydroxamic acid (**L3**), respectively. While ligand **L1** has been purchased, ligand **L2** has been synthesized by Heike Pfaff (student internship) according to the literature<sup>[73]</sup>. The synthesis of 2-mercaptobenzohydroxamic acid revealed unforeseen difficulties. 2-Mercaptobenzohydroxamic acid easily undergoes cyclization accompanied by a dehydration reaction (scheme 3.2) under conditions which are commonly used for the synthesis of *ortho*-substituted benzohydroxamic acids.<sup>[74]</sup> **L3IV** could be identified as the main product of this reaction, whereas traces of the hydroxamic acid **L3III** and the side product **L3V** were also found via FD mass spectrometry. The <sup>1</sup>H-NMR spectrum (C.1) and the melting point of 150 °C of the main product indicate that no rearrangement has been involved in this reaction, which would lead to the structural isomer 2(3H)-benzothiazolone **L3VI**.<sup>[75,76]</sup> This is the reason, why the methylated derivative of 2-mercaptobenzohydroxamic acid, ligand **L3**, has been used, representing a ligand with a sulfur donor atom in *ortho*-position. The sulfur derivative **L3** has been synthesized following the three step procedure, shown in scheme 3.2. Starting with an esterification of 2-mercaptobenzoic acid resulted in the formation of 2-mercaptobenzoic acid methyl ester (**L3a**) in good yields. 2-Methylmercaptobenzoic acid methyl ester (**L3b**) was obtained in nearly quantitative yield from a methylation reaction of **L3a** with methyl iodide in methanol. The final product **L3** was then precipitated from the reaction of **L3b** with hydroxylamine hydrochloride under basic conditions.



Scheme 3.2: Synthesis plan for 2-mercaptobenzohydroxamic acid and the methylated derivate **L3**.

### 3.1.1. Coordination ability of benzohydroxamic acid with a sulfur donor atom in *ortho*-position - Transition metal complexes with **L3**

2-methylmercaptobenzohydroxamic acid (**L3**) can be deprotonated twice and realizes different coordination modes, known from complexes with salicylhydroxamic acid, as will be presented in the following chapter discussing the crystal structures. Beside the expected coordination of copper(II) in the complexes **C2**, **C3** and **C4**, **L3** also forms complexes with iron(III) (**C1**), cobalt(II,III) (**C5**) and cadmium(II) (**C6**). Except for the monomeric iron(III) compound **C1**, all obtained complexes show the 12-MC-4 structure motif.

The reaction of **L3** with iron(III) pivalate and pyridine in methanol yields well shaped red crystals of  $\text{Fe}^{\text{III}}(\text{L3H})_3$  (**C1**) after one day of slow evaporation or after layering with diethyl ether. **C1** crystallizes in the triclinic space group  $P\bar{1}$  with two molecules per unit cell. The iron(III) ion is embedded in a slightly distorted octahedral environment built from hydroxamato and carbonyl oxygen atoms of three ligand molecules (figure 3.1) each with a net charge of  $-1$ . The average length of the Fe-O bonds is 2.021 Å. The nitrogen atom of **L3** remains protonated yielding a neutral complex without further counter ion or co-ligands. Hydroxamato oxygen and nitrogen atoms are intermolecular connected by hy-

drogen bonds (see figure 3.2). Two of the ligands are oriented in the expected manner for a 12-MC-4 structure, generating a six-membered ring coordination pocket between the sulfur and nitrogen atom and a five-ring coordination pocket between hydroxamato and carbonyl oxygen atom. However, the third ligand is twisted around the C17-C18 bond, which is why this molecule does not exhibit any threefold rotational symmetry. Coordination of the sulfur atoms seems to be unfavored. However, it should be mentioned, that the formation of a 12-MC-4 structure with four Fe(III) ions would yield a highly charged molecule, which could also be an inhibiting factor for the MC formation.

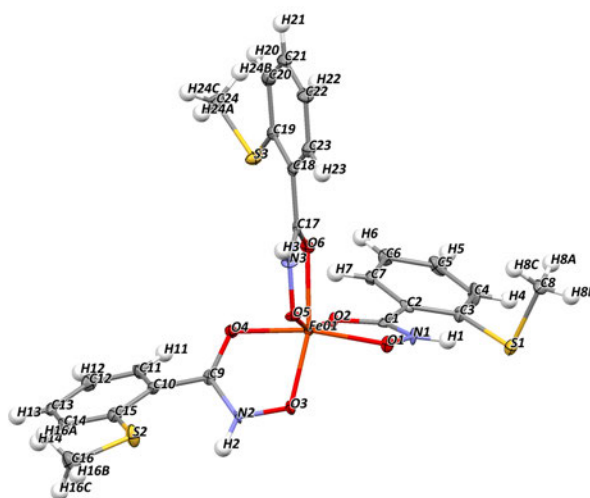


Figure 3.1.: Molecular structure of **C1**. Color code: Orange - Fe(III), red - oxygen, blue - nitrogen, yellow - sulfur, gray - carbon, white - hydrogen. ORTEP representation with atomic displacement parameters at 50% level of probability. Hydrogen atoms are drawn as fixed-size spheres with a radius of 0.22 Å.

Evaluation of the magnetic data of compound **C1** is in good agreement with the findings from the crystal structure. The Fe(III) monomer possesses a value for its  $\chi_M T$  product at 300 K of  $4.44 \text{ cm}^3 \text{Kmol}^{-1}$ , which is slightly higher than the theoretical value for a spin of  $S = \frac{5}{2}$  ( $4.375 \text{ cm}^3 \text{Kmol}^{-1}$ ) without orbital contribution.  $\chi_M T$  decreases linearly upon cooling with a very small slope. This feature can be explained with the presence of a temperature independent paramagnetism (TIP). At lower temperatures (10 K) the curve starts decreasing very rapidly, indicating either single ion anisotropy or present intermolecular exchange coupling. As the Fe(III) ion in an octahedral ligand field exhibits an isotropic electron distribution, exchange coupling was implemented by fitting the magnetic data with a mean field parameter  $zJ$  using the software PHI<sup>[77]</sup>. TIP, g-factor and  $zJ$  were fitted without bound-



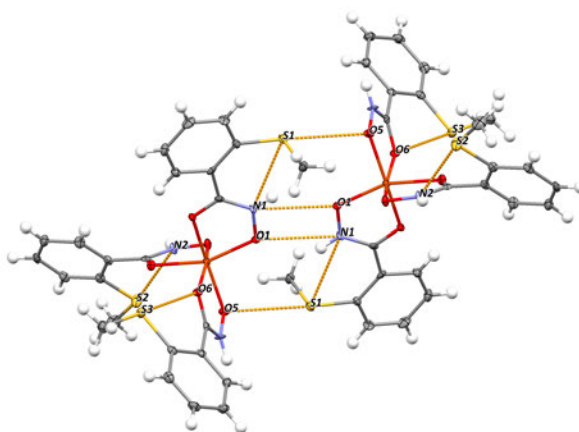


Figure 3.2.: Hydrogen bonds of **C1**. Color code: Orange - Fe(III), red - oxygen, blue - nitrogen, yellow - sulfur, gray - carbon, white - hydrogen. ORTEP representation with atomic displacement parameters at 50 % level of probability. Hydrogen atoms are drawn as fixed-size spheres with a radius of 0.22 Å.

aries yielding the *PHI fit* shown in figure 3.3 with the values  $294(117) \times 10^{-6} \text{ cm}^3 \text{ mol}^{-1}$ , 1.998(4) and  $-0.068(4) \text{ cm}^{-1}$ , respectively. Intermolecular interactions  $zJ$  and the TIP are implemented in *PHI* using equation 3.1. The error of the fit routine is calculated according to the sum of squares approach (see 3.2). Residual R for the best fitting reaches a value of  $2.76 \times 10^{-1}$   $2.7610^{-1}$ . The necessity of an intermolecular coupling parameter becomes clearly recognizable regarding the best fit result without  $zJ$ . Especially the low temperature region cannot be fitted properly anymore. In addition, intermolecular coupling is likely to be present in **C1** due to the hydrogen bond network (figure 3.2).

$$\chi_{zJ} = \frac{\chi_{TIP}}{1 - \left(\frac{zJ}{N_A \mu_B^2}\right) \chi_{TIP}} \text{ with } \chi_{TIP} = \chi_{calc} + TIP \quad (3.1)$$

$$Residual = \left[ \sum_{i=1}^{points} (A_{exp} - A_{calc})^2 \right] \left[ \sum_{i=1}^{points} (B_{exp} - B_{calc})^2 \right] A, B = \text{observables (e.g. } \chi) \quad (3.2)$$

Due to the thiomethyl group **L3** is of course expected to coordinate especially to softer metal ions. Hence, it is possible to synthesize different compounds by reacting **L3** with copper(II) salts. Three different 12-MC-4 structures (**C2**, **C3** and **C4**) were obtained by varying counter ions or bases.  $\{\text{Cu}^{\text{II}}\text{Cl}_2(\text{MeOH})[\text{12-MC}_{\text{Cu(II)N(L3)}-4}]\}_2 \cdot 4\text{MeOH}$  (**C2**) crystallizes after two days from a solution of **L3** and copper(II) chloride in methanol

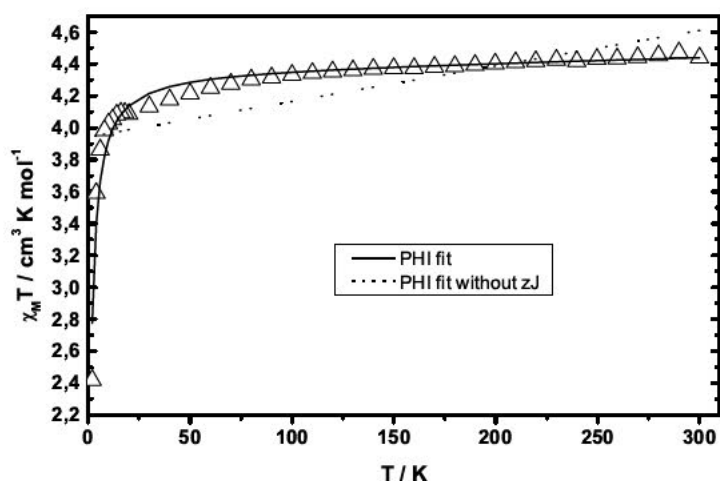


Figure 3.3.: Temperature-dependent magnetic behavior of C1. Best fit results considering TIP and either with (straight line) or without (dotted line) a mean field parameter  $zJ$ .

using triethylamine as base. C2 crystallizes in the triclinic space group  $P\bar{1}$ . All eight ligand molecules are fully deprotonated forming a double decker 12-MC-4 structure with ten copper(II) ions (see figure 3.4). Four additional chlorido ligands compensate the positive charge, yielding a neutral complex molecule. Additional four non-coordinating methanol molecules are present in the crystallographic unit cell. Each metallacrown unit consists of five copper(II) ions from which only the central guest ion (Cu1) is coordinated in a distorted octahedral environment whereas the ring building metal ions are fivefold coordinated in a square pyramidal environment. The axial coordination sites of Cu1 are occupied by one bridging chlorido ( $\mu_2$ -Cl1) and one hydroxamato oxygen atom (O5) from the second MC. The apical positions of the ring copper ions (Cu2-Cu5) vary from hydroxamato and carbonyl oxygen to nitrogen and sulfur atoms. The fifth coordination site varies from a methanol oxygen O9, the bridging chlorido Cl1, an additional hydroxamato oxygen atom O3 or a second chlorido Cl2 for Cu2, Cu3, Cu4 and Cu5, respectively (see figure 3.4). Distances for axial coordination of hydroxamato oxygen atoms of the neighboring MC are 2.661 Å (Cu1-O5') and 2.664 Å (Cu4-O3'). Both chlorido ligands are involved in hydrogen bonding to either the coordinating methanol (Cl1-O9) or the non-coordinating methanol molecules (Cl2-O10; Cl2-O11) (figure 3.5). It is noteworthy, that the torsion angles between the methyl groups and the benzyl planes of each ligand are close to 30° for C8, C24 and C32, for C16 about 101° though. This nearly perpendicular orientation is provoked by a non-classical hydrogen bond<sup>[78]</sup> between C16 and O10 (see figure 3.5). C8 and C24 also show non-classical

H-bonds with chloride ions (Cl2) from the neighboring molecules. This network of hydrogen bonds also hinders the methyl groups from free rotation. Hence, disorder in the molecular structure is not observed. Bond lengths between copper and sulfur vary from 2.256(1) Å to 2.336(1) Å. The bridging  $\mu_2$ -Cl1 causes a bending of Cu3 and coordinating ligands towards the central copper(II) ion. Therefore, the angle of the hydroxamate oxygen bridge between Cu1 and one of the ring building copper(II) ions deviates more than 12° (Cu1-O5-Cu3) from the others. This also affects the Cu-Cu distance to be shorter. Additionally, the Cu-N-O-Cu torsion angles vary a lot for this structure. Selected Cu-Cu distances, Cu-O-Cu bond angles and Cu-N-O-Cu torsion angles are given in table 3.1.

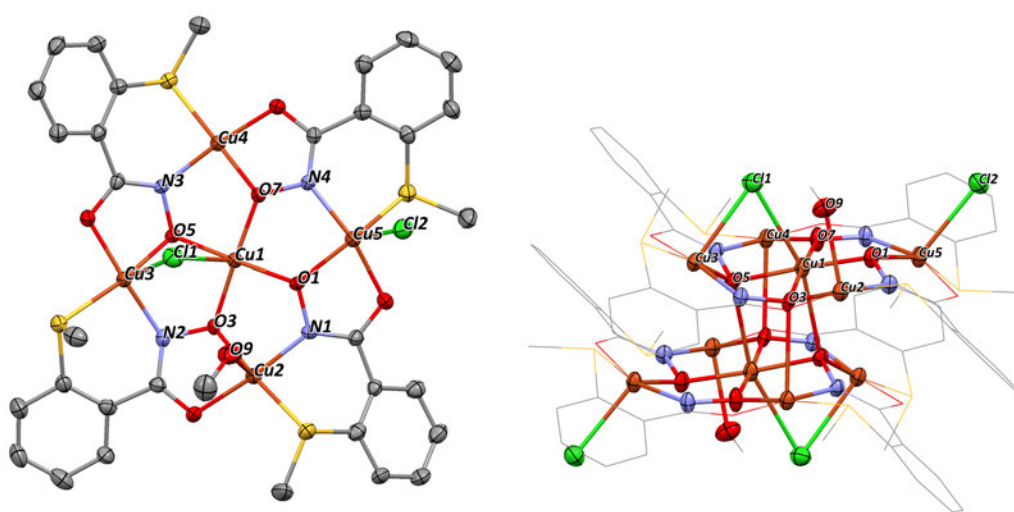


Figure 3.4.: Top view of a single 12-MC-4 motif (left) present in the molecular structure of **C2** (right). Color code: Orange - Cu(II), red - oxygen, blue - nitrogen, yellow - sulfur, gray - carbon, green - chlorine. ORTEP representation with atomic displacement parameters at 50% level of probability. Hydrogen atoms have been omitted for clarity.

Figure 3.6 shows the temperature dependence of the  $\chi_M T$  product of **C2**. Evaluation of the magnetic data has been performed for a single MC considering only five paramagnetic Cu(II) ions and using a mean field approximation to account for the coupling between both 12-MC-4 layers. In contrast to that, the full molecule with ten Cu(II) ions and a possible antiferromagnetic exchange coupling between both MC layers was evaluated to figure out the necessity of a precise determination of inter-MC exchange coupling. The fit results for both are presented in figure 3.6. Intramolecular exchange coupling was consid-

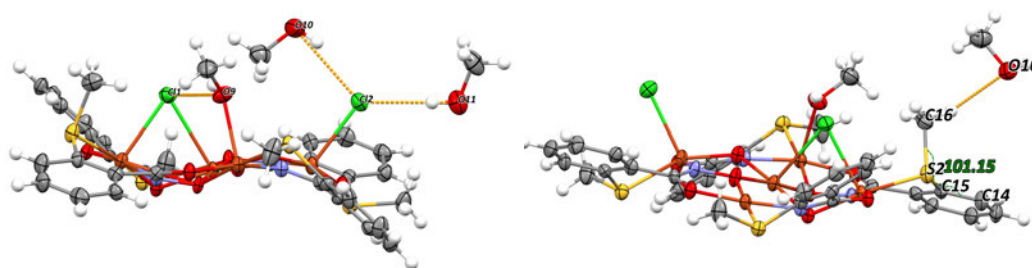


Figure 3.5.: Intra- and intermolecular hydrogen bonding present in compound **C2** (left). Torsion angle of  $101.15^\circ$  (C14-C15-S2-C16) indicating a nearly perpendicular orientation of the S2-C16 bond towards the benzyl plane of the ligand (right). H-bonds are illustrated as yellow dashed lines. Color code: Orange - Cu(II), red - oxygen, blue - nitrogen, yellow - sulfur, gray - carbon, green - chlorine. ORTEP representation with atomic displacement parameters at 50 % level of probability. Hydrogen atoms are drawn as fixed-size spheres with a radius of  $0.22 \text{ \AA}$ .

ered according to the star-like coupling scheme (figure 3.6) and the exchange Hamiltonian  $\hat{H}_{ex}(MC)$  (equation 1.1), even though bond distances and angles vary in each crown structure. The competing exchange coupling parameters are  $J_1$ , the radial superexchange via hydroxamato oxygen atoms and  $J_2$ , the tangential coupling bridged by the -NO- functionality. This notation will be used in the following evaluations of magnetic data of MC compounds. When taking into account only one single MC ring assuming thus half of the molecular weight ( $M(\mathbf{C2})/2 = 1209 \text{ g mol}^{-1}$ ), at 300 K **C2** reaches a value for  $\chi_{MT}$  of  $1.23 \text{ cm}^3 \text{ K mol}^{-1}$ . This is far below the theoretical value for five uncoupled Cu(II) ions

Table 3.1.: Selected atom distances and bond angles for the metallacrown structure **C2**.

| Ion  | Cu1-Cu distance ( $\text{\AA}$ ) | Cu1-O-Cu angle       | Cu-N-O-Cu torsion angle       |
|------|----------------------------------|----------------------|-------------------------------|
| Cu2  | 3.228                            | $113.03^\circ$ (O3)  | -N1-O1-Cu5 $174.180(4)^\circ$ |
| Cu3  | 3.058                            | $100.63^\circ$ (O5)  | -N2-O3-Cu2 $140.281(4)^\circ$ |
| Cu4  | 3.248                            | $117.74^\circ$ (O7)  | -N3-O5-Cu3 $149.967(4)^\circ$ |
| Cu5  | 3.290                            | $116.05^\circ$ (O1)  | -N4-O7-Cu4 $162.721(4)^\circ$ |
| Cu1' | 3.495                            | $96.35^\circ$ (O5)   |                               |
| Cu3' | 4.227                            | $130.46^\circ$ (O5') |                               |
| Cu4' | 3.854                            | $113.31^\circ$ (O3)  |                               |

with  $S = \frac{1}{2}$  ( $1.875 \text{ cm}^3\text{Kmol}^{-1}$ ). Upon cooling, the susceptibility decreases to a plateau about  $0.43 \text{ cm}^3\text{Kmol}^{-1}$  at 40 K. Below 10 K, the curve starts decreasing faster (see figure 3.6 inset). The overall shape and the low value at room temperature indicate, that strong antiferromagnetic exchange coupling is present in compound **C2**. The plateau reveals a spin ground state of  $S = \frac{1}{2}$ , expected for a  $Cu_5$ -MC unit.<sup>[58]</sup> The best fit could be obtained with  $J_1 = -88(1) \text{ cm}^{-1}$ ,  $J_2 = -64.7(3) \text{ cm}^{-1}$ ,  $g_{Cu} = 2.146(2)$  and  $zJ = -0.944(52) \text{ cm}^{-1}$ . These values are in very good agreement with the literature on  $Cu_5$ -MC compounds.<sup>[57,79-82]</sup> Further, the double decker molecule with full molecular mass ( $M(\mathbf{C2}) = 2419.2 \text{ g mol}^{-1}$ ) has been evaluated in order to avoid underestimation of exchange coupling between the MC units. The room temperature value of  $\chi_M T$  ( $2.34 \text{ cm}^3\text{Kmol}^{-1}$ ) is below the theoretical value for ten uncoupled spins of  $\frac{1}{2}$  ( $3.75 \text{ cm}^3\text{Kmol}^{-1}$ ). Strong intramolecular antiferromagnetic exchange is expected to be present. The plateau between 8 K and 30 K at around  $0.75 \text{ cm}^3\text{Kmol}^{-1}$  followed by a strong decrease of  $\chi_M T$  below 8 K is indicative for two spin centers with  $S = \frac{1}{2}$  undergoing weak antiferromagnetic coupling. This is why the third exchange coupling parameter  $J_3$  was introduced. Best fit results were obtained according to the exchange Hamiltonian  $\hat{H}_{ex}(10Cu)$  (equation 3.3) with  $J_1 = -88(1) \text{ cm}^{-1}$ ,  $J_2 = -65.9(4) \text{ cm}^{-1}$ ,  $J_3 = -8.2(5) \text{ cm}^{-1}$  and  $g_{Cu} = 2.070(3)$ . Both attempts to evaluate the magnetic data lead to same results for the intra-MC exchange coupling parameters and to reasonable g-values. Song et al.<sup>[81]</sup> already pointed out, that intermolecular magnetic exchange mediated via apical coordination sites and therefore using the occupied  $d_{z^2}$  orbital of a Cu(II) ion leads only to weak antiferromagnetic exchange. This was also observed for **C2** when introducing a third coupling parameter. Hence, the overall spin ground state of MC compounds effectively depends on the ratio of the intra-MC coupling parameters. It was shown, that they are independent from the evaluation model. Recently, it has been shown, that it is sufficient to determine the magnetic features of a single metallacrown, even though the compound consists of a MC network.<sup>[45]</sup> In addition, it is still possible to process the magnetic data considering ten individual spin centers, each contributing with  $S = \frac{1}{2}$ , but it reaches the limit of evaluability within the *PHI* program when bigger spin values are involved.

$$\hat{H}_{ex}(MC) = -2J_1\hat{S}_5(\hat{S}_1 + \hat{S}_2 + \hat{S}_3 + \hat{S}_4) - 2J_2(\hat{S}_1\hat{S}_2 + \hat{S}_2\hat{S}_3 + \hat{S}_3\hat{S}_4 + \hat{S}_4\hat{S}_1) - 2J_3\hat{S}_5\hat{S}_5' \quad (3.3)$$

Exchange of the counter ion from chloride to perchlorate also leads to the desired crown structure.  $\text{Cu}_2^{\text{II}}\text{Cl}(\text{mmba})(\text{MeOH})_2(\text{H}_2\text{O})[\mathbf{12} - \text{MC}_{\text{Cu(II)N(L3)}} - \mathbf{4}]_2(\text{ClO}_4)_2$  (**C3**) con-

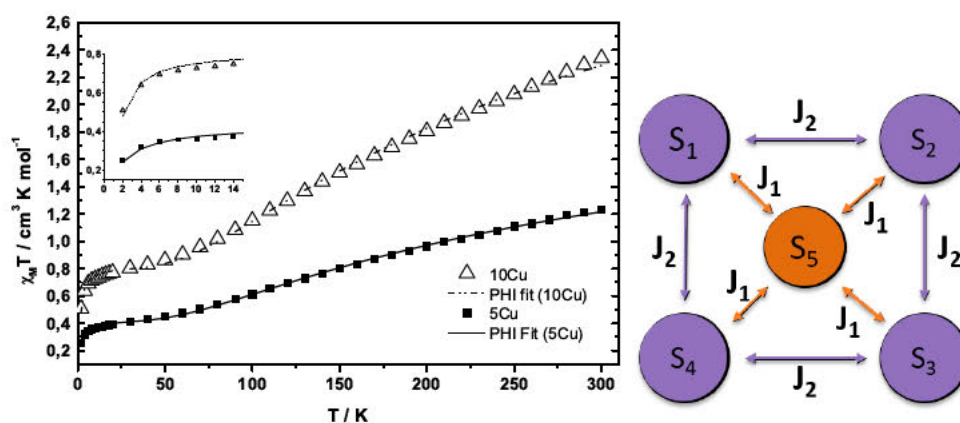


Figure 3.6.: Temperature-dependent magnetic behavior of C2 (left). Two evaluation methods have been used: Considering a single MC motif (5Cu) with a mean field parameter to account for intermolecular exchange coupling (black squares) and a full molecule method (10Cu) introducing a third exchange coupling parameter as inter-MC interaction (empty triangles). Coupling scheme for a 12-MC-4 structure (right) with five spin centers and the radial ( $J_1$ ) and tangential ( $J_2$ ) coupling.

sists of a very similar double decker core, which is charge balanced by different counter anions (figure 3.7). The charge of +4 is compensated by two non-coordinating perchlorate ions, one coordinating chlorido and one 2-methylmercaptobenzoic acid ligand (**mmba**). Both, chlorido and **mmba**, are formed in-situ and were not added to the reaction mixture. C3 crystallizes in the same space group as C2,  $P\bar{1}$ . Bond lengths between copper and sulfur vary from 2.264(5) Å to 2.307(5) Å. Due to an insufficient amount of C3 the temperature-dependent magnetic behavior was not studied yet. However, the temperature dependence is expected to be very similar to that of the previously discussed C2 since the counterions, whether coordinating or not, do not affect the intramolecular exchange coupling much.

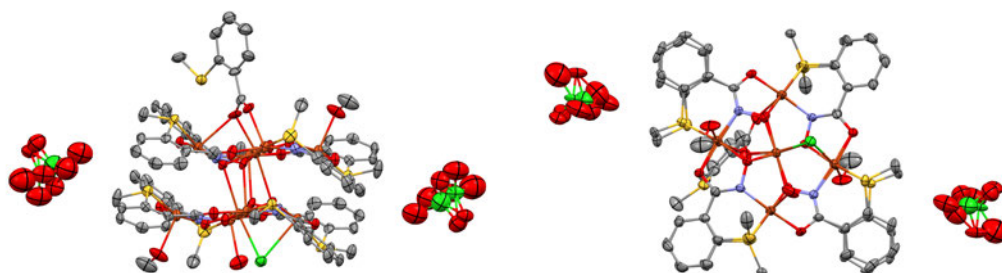


Figure 3.7.: Side (left) and top view (right) of the 12-MC-4 double-decker structure of **C3**. Color code: Orange - Cu(II), red - oxygen, blue - nitrogen, yellow - sulfur, gray - carbon, green - chlorine. ORTEP representation with atomic displacement parameters at 50 % level of probability. Hydrogen atoms have been omitted for clarity.

The reaction of **L3** with copper(II) perchlorate, pyridine and manganese(II) pivalate in methanol leads to the formation of another homometallic copper(II) metallacrown  $\text{Cu}^{\text{II}}(\mu_2 - \text{ClO}_4)(\text{MeOH})_2(\text{py})_4[\mathbf{12} - \text{MC}_{\text{Cu}(\text{II})\text{N}(\text{L3})} - 4]\text{ClO}_4$  (**C4**). Although there are neither manganese ions nor pivalate molecules in the crystal structure, it was not possible to reproduce compound **C4** in the absence of manganese(II) pivalate. The influence of manganese ions has been investigated by changing the copper salt to copper(II) pivalate or by replacing manganese pivalate with an equivalent amount of potassium pivalate. Neither these attempts nor an increased addition of base instead of using manganese pivalate led to a successful synthesis of **C4**. **C4** possesses high symmetry, as it crystallizes in the tetragonal space group  $I\bar{4}$ . The asymmetric unit consists of two copper(II) ions, which are symmetrically independent (figure 3.8).

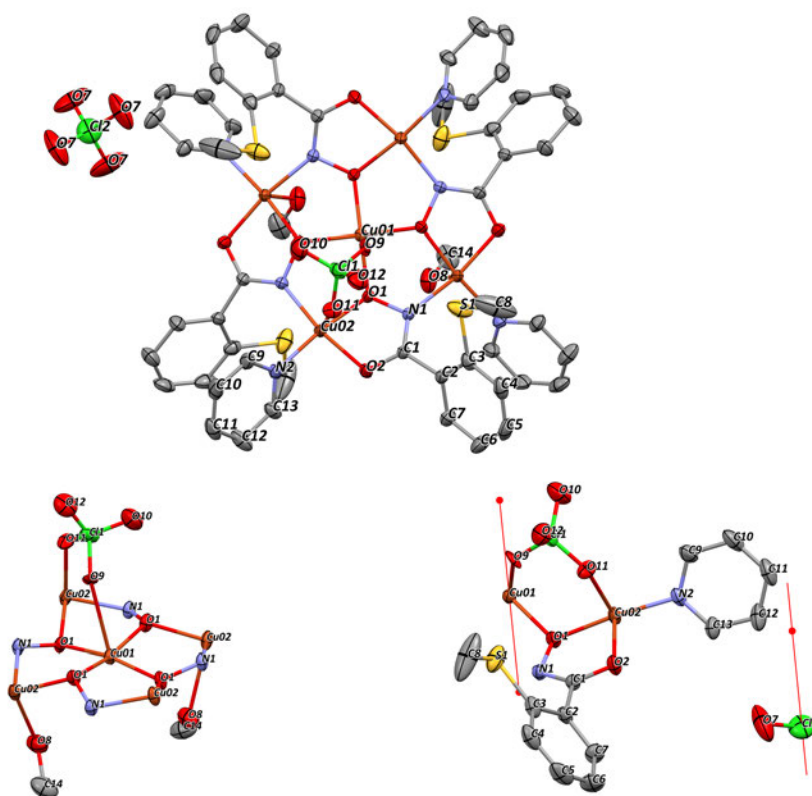


Figure 3.8.: Molecular structure of **C4** (top), the MC core with axial coordinating ligands (bottom left) and the asymmetric unit with displayed rotoinversion axis (bottom right). Color code: Orange - Cu(II), red - oxygen, blue - nitrogen, yellow - sulfur, gray - carbon, green - chlorine . ORTEP representation with atomic displacement parameters at 50% level of probability. Hydrogen atoms have been omitted for clarity.

Cu01 is located in a center of inversion of a fourfold rotoinversion axis and its square pyramidal coordination environment is formed by four hydroxamato and one perchlorate oxygen atom. The perchlorate ion bridges Cu01 and Cu02. A second non-coordinating perchlorate ion ensures neutral charge of the complex. Three Cu02 ions are also embedded in a square pyramidal environment formed by the bridging perchlorate and two coordinating methanol molecules. The fifth copper(II) ion exhibits a fourfold square planar coordination. The Cu01-Cu02 distance and the Cu01-O1-Cu02 bond angle are 3.257 Å and 116.20°, respectively. Magnetic properties of **C4** are presented in the form of a  $\chi_M T$  vs. T plot, shown in figure 3.9.



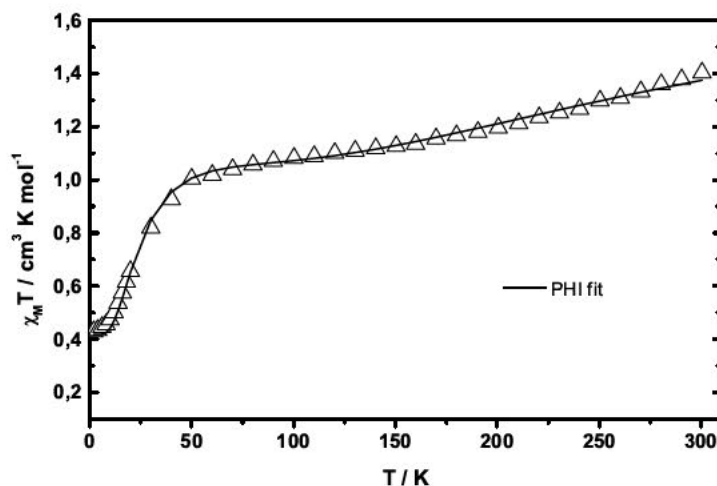


Figure 3.9.: Temperature-dependent magnetic behavior of C4.

The product of magnetic susceptibility and temperature decreases upon cooling from  $1.40 \text{ cm}^3 \text{K mol}^{-1}$  (at 300 K) to  $0.43 \text{ cm}^3 \text{K mol}^{-1}$  (at 2 K). The initial gentle slope becomes steeper below 50 K and flattens out at very low temperatures. The room temperature value is smaller than the expected value for five uncoupled  $S = \frac{1}{2}$  centers ( $1.875 \text{ cm}^3 \text{K mol}^{-1}$ ) indicating an overall antiferromagnetic exchange coupling. The behavior at low temperatures suggests an isolated  $S = \frac{1}{2}$  spin ground state. The magnetic data was fitted with *PHI* according to the star-like coupling scheme with two competing exchange coupling parameters and the exchange Hamiltonian  $\hat{H}_{ex}(MC)$  (equation 1.1). This simplified assumption is very well suitable for C4 as the molecule exhibits rotational symmetry towards a  $S_4$  rotoinversion axis located in the crowns center. The best fit is depicted in figure 3.9 yielding  $J_1 = -90.0(5) \text{ cm}^{-1}$ ,  $J_2 = -31.1(1) \text{ cm}^{-1}$  and  $g_{Cu} = 2.111(3)$ . The ratio  $J_1/J_2 = 2.9$  is much higher than observed for other  $Cu_5$ -MC compounds in the literature<sup>[58]</sup> and in this work (C2:  $J_1/J_2 = 1.3$ ). Compared to C2 the radial exchange value does not change, whereas the coupling between peripheral Cu(II) ions is less than half the size ( $J_2(\text{C2}) = -64.7(3) \text{ cm}^{-1}$ ). This decrease can be attributed to an increase of the Cu-N-O-Cu torsion angles inside the MC ring.<sup>[55]</sup> The observed angle in C4 ( $174.53^\circ$ ) is much higher than the averaged angle in C2 ( $156.78^\circ$ ). Simulating the zeeman effect (figure 3.10) based on the fit results revealed that the increased ratio leads to a lowering in energy of the first quartet state. While for C2 the first and second excited state are still doublets and only the third excited state is a quartet with an energy separation of  $\Delta E_3 \approx 170 \text{ cm}^{-1}$  towards the ground state doublet, the first excited state of C4 already represents a quartet ( $\Delta E_1 \approx 35 \text{ cm}^{-1}$ ). A higher coupling constant ratio is expected for C4, as the average of the bond angle between the central Cu(II) and

the peripheral Cu(II) ions is at  $116^\circ$  compared to  $111^\circ$  observed in **C2**, leading to stronger antiferromagnetic exchange coupling.

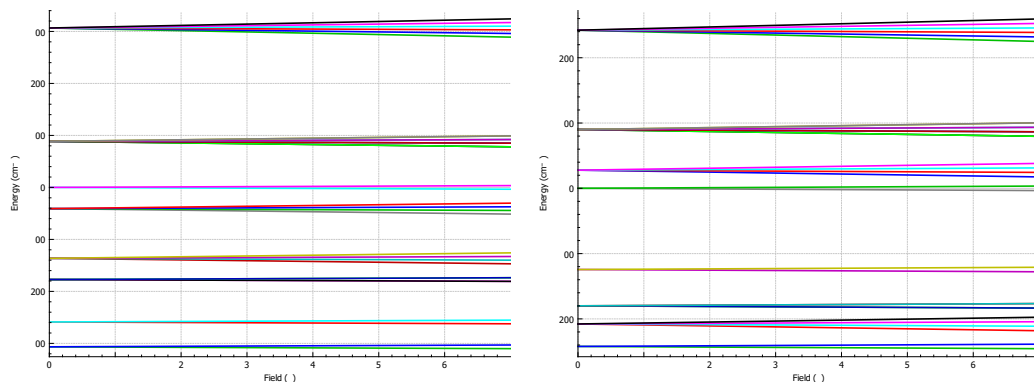


Figure 3.10.: Simulation results of the Zeeman effect for **C2** (left) and **C4** (right).

$[\text{Co}_4^{\text{III/II}}(\text{L3})_4\text{piv}_2(\text{X})_2(12 - \text{MC}_{\text{Co(II)Co(III)N(L3)} - 4})_2 (\text{X} = \text{NO} \text{ or } \text{MeOH})$  (**C5**) will just be structurally described, as it could not be reproduced during this work for further studies. Nevertheless, the reaction of cobalt pivalate with **L3** and pyridine in methanol underlines that this ligand is even able to form 12-MC-4 structures with cobalt ions, which is quite rare in the literature.<sup>[57]</sup> In figure 3.11 the crystal structure of **C5** is shown. Two cobalt octamers fill the unit cell of the triclinic crystal lattice. Each octamer consists of eight **L3** molecules and two coordinating  $\eta_2 : \mu_2$ -pivalate anions. However, they differ from each other in the coordination of either two methanol molecules or two nitrosyl ligands. One single octamer can be described as a 12-MC-4 structure with two Co(II) ions embedded out-of-plane in the central void. In addition, two capping cobalt ions are coordinated by the bridging  $\eta_2 : \mu_2$ -pivalate ligands. Determination of the charge of each cobalt ion emerged to be difficult. Eight **L3** molecules and two pivalate ions yield a total negative charge of  $-18$ . The bended nitrosyl coordination indicates that there is no or only very weak metal to ligand back bonding involved. The N-O stretching vibration for bended nitrosyl complexes is supposed to be present between  $1420 \text{ cm}^{-1}$  and  $1710 \text{ cm}^{-1}$  and is highly dependent on the M-N-O angle.<sup>[83]</sup> The N-O bond energy decreases with decreasing angle as the N-O- $\pi^*$  orbital has a better overlap with the filled metal d orbitals. This overlap leads to a weakening of the N-O bond resulting a shift in the IR absorption band to lower energy. The IR spectrum of compound **C5** (figure B.17) does not show any band between  $1579 \text{ cm}^{-1}$  and  $2817 \text{ cm}^{-1}$  which goes hand in hand with the observed bond angle of  $115^\circ$ . Therefore, the nitrosyl ligand can be assumed to contribute with a negative charge. The overall charge of  $-20$  has

to be balanced with eight cobalt ions, leading to four Co(III) and four Co(II) ions. Bond length and structural deviation from the perfect octahedral coordination environment are key indicators to assign the oxidation state to every cobalt ion. However, intense variations of the coordinating donor atoms make it difficult to compare the bond length. Regarding the nitrosyl containing octamer, it is clear that Co6 matches to a charge of +3 as the Co-O bond length varies between 1.869(4) Å and 1.923(4) Å. From literature<sup>[57]</sup> Co(III) is expected to occupy the MC ring positions. In compound **C5** the other two ring metal ions (Co7) show longer Co-O bonds (2.003(4) Å, 2.179(3) Å) indicating an oxidation state of +2. The capping cobalt ions (Co5) are most promising to assign them a positive charge of +3, as their Co-O bond length are also shorter than 2 Å. An overview of the cobalt to donor atom distances of compound **C5** is given in table 3.2. Regarding the other cobalt octamer of this structure it is less difficult to assign the oxidation states because a methanol molecule coordinates to each of the capping cobalt ions (Co1) instead of the bended nitrosyl ligand. Therefore, this octamer consists of six Co(II) ions and two Co(III) which are easy to identify as Co4 show the shortest Co-O bond length of 1.872(5) Å. Although compound **C5** was not investigated further, the structure is sufficient to demonstrate the ability of ligand **L3** to coordinate even Co(II) and Co(III) ions and to form 12-MC-4 structures with partly trivalent metal ions.

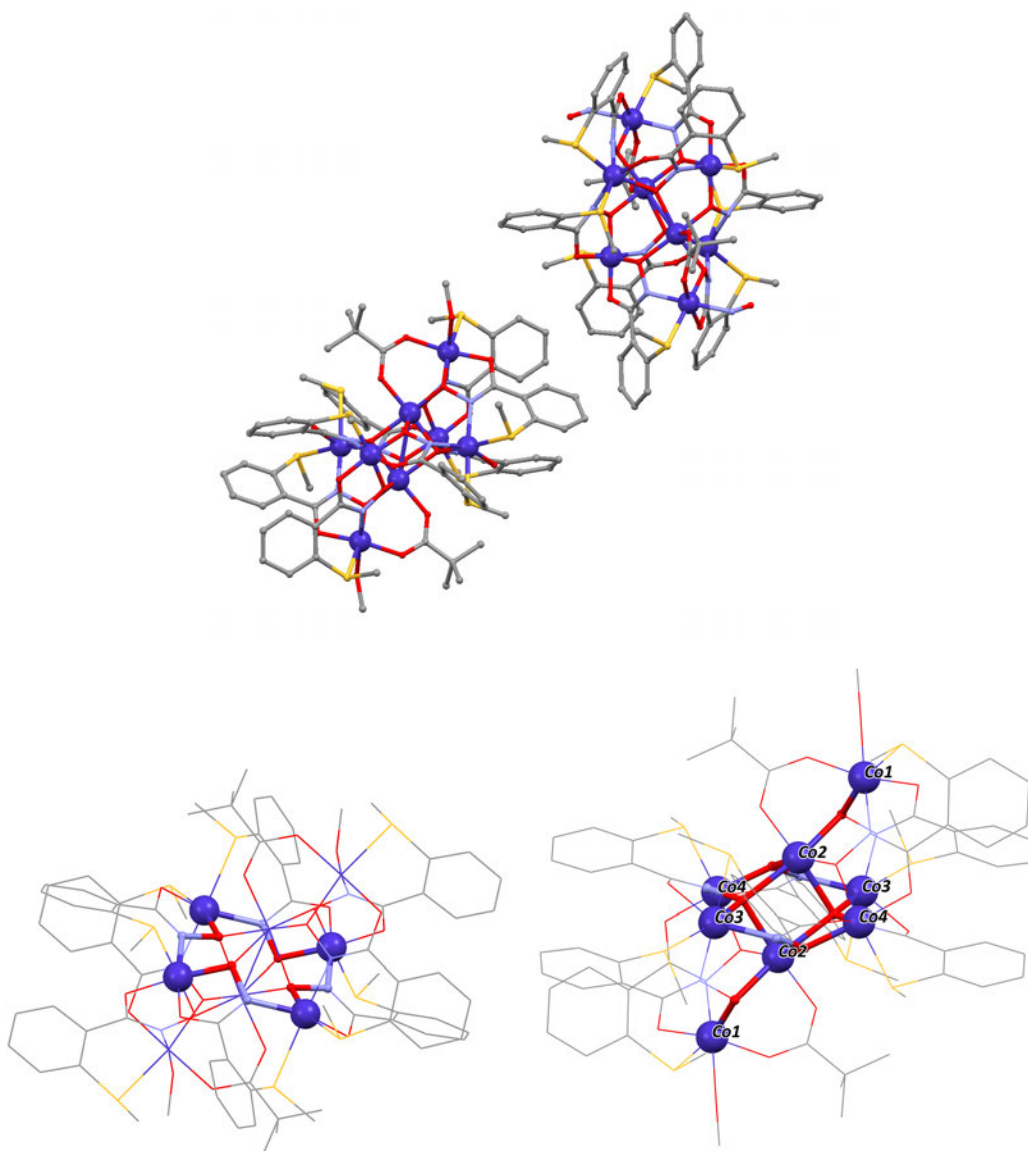


Figure 3.11.: Both cobalt octamers present in the crystal structure of **C5** (top). Representation of the MC unit of one of the octamers (bottom left) and molecular structure of the methanol coordinated octamer with highlighted guest and capping cobalt ions (bottom right). Color code: Dark blue - Co(II/III), red - oxygen, blue - nitrogen, yellow - sulfur, gray - carbon, green - chlorine . ORTEP representation with atomic displacement parameters at 50% level of probability. Hydrogen atoms have been omitted for clarity.

Table 3.2.: Selected bond lengths of each crystallographically independent cobalt ion of **C5**.

| Ion                   | Co1           | Co2           | Co3           | Co4            |
|-----------------------|---------------|---------------|---------------|----------------|
| Bond<br>length<br>(Å) | O4 1.9851(1)  | O5 2.0316(1)  | O6 1.9979(1)  | O9 1.8725(1)   |
|                       | O1 2.0200(1)  | O1 2.512(1)   | N3 2.0390(1)  | O10 1.8746(1)  |
|                       | O2 1.9961(1)  | O10 2.0758(1) | N1 2.0672(1)  | N4 1.8944(1)   |
|                       | N2 2.0332(1)  | O8 2.1005(1)  | O7 2.1567(1)  | O8 1.9139(1)   |
|                       | O3 2.1813(1)  | O7 2.1233(1)  | S4 2.4864(1)  | O11 1.9152(1)  |
|                       | S3 2.4483(2)  | O7' 2.1969(1) | S1 2.6403(1)  | S2 2.2489(1)   |
| Ion                   | Co5           | Co6           | Co7           | Co8            |
| Bond<br>length<br>(Å) | O16 1.9581(1) | O22 1.8696(1) | O20 2.0036(1) | O17 2.0300(1)  |
|                       | O15 1.9583(1) | O19 1.8760(1) | N9 2.0424(1)  | O15 2.0487(1)  |
|                       | O13 1.9857(1) | N7 1.8875(1)  | N8 2.0543(1)  | O22 2.0585(1)  |
|                       | N6 2.0256(1)  | O18 1.9147(1) | O21 2.1799(1) | O18 2.1139(1)  |
|                       | N5 2.0701(1)  | O23 1.9231(1) | S8 2.4858(1)  | O21 2.1174(1)  |
|                       | S7 2.3530(1)  | S6 2.2607(1)  | S5 2.7019(2)  | O21' 2.1715(1) |

The reaction of ligand **L3** with cadmium(II) perchlorate and triethylamine in dimethylformamide affords  $[\text{Cd}_{14}^{\text{II}}(\text{L3})_{12}(\mu_6 - \text{O})(\text{DMF})_{10}](\text{ClO}_4)_2$  (**C6**). This complex crystallizes in the monoclinic crystal system in the space group  $P2_1/c$ . The cluster structure involves 12 ligand molecules shown in figure 3.12. The core of **C6** is formed by a face-centered cube of 14 cadmium(II) ions. Put in another way, **L3** coordinates cadmium(II) ions to form 12-MC-4 structures in which the ring building metal ions are part of three different MCs and thereby represent the edges of a face-centered cube. The inner void of this cube is occupied by an oxo ( $\mu_6 - \text{O}^{2-}$ ) ligand coordinating the central metal ion of each MC. An overall neutral charge is achieved by two additional non-coordinating perchlorate anions. Furthermore, ten coordinating dimethylformamide molecules are involved in forming this cube structure.

Continuous Shape Measures (CShM) have been calculated for each of the cadmium centers and are summarized in table 3.3.<sup>[84]</sup> Beside different coordination numbers (5;6) and different structures of the cadmium coordination polyhedra, the coordinating atoms vary significantly in this complex. Slightly distorted octahedral environments with six coordinating oxygen atoms are present for Cd1, Cd3 and Cd5, whereas Cd2 is embedded in a trigonal prismatic

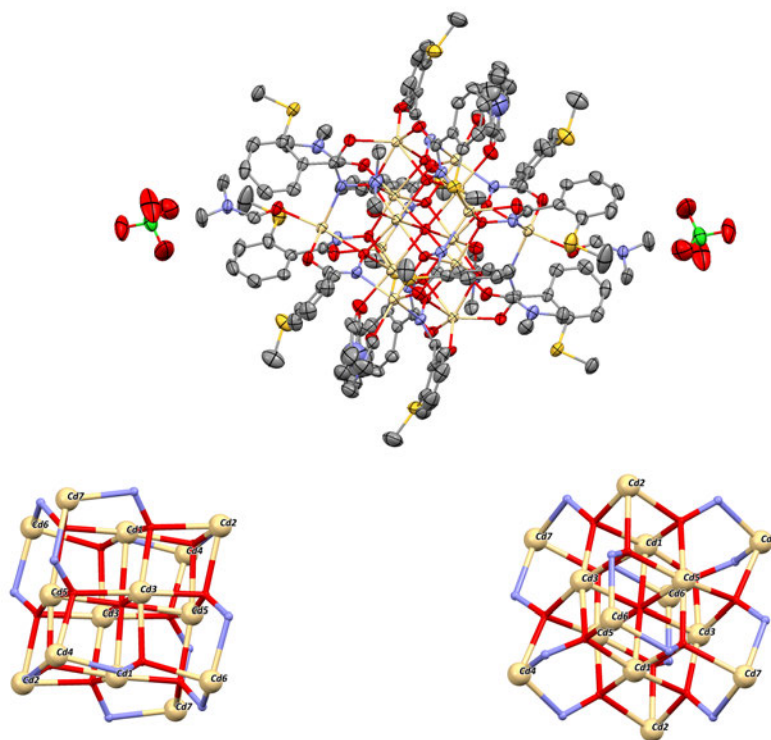


Figure 3.12.: Molecular structure of the full  $Cd_{14}$  cluster **C6** (top) and two different perspectives on the N-O bridged, face-centered Cd cube (bottom left and right). Color code: Pale yellow - Cd(II), red - oxygen, blue - nitrogen, yellow - sulfur, gray - carbon, green - chlorine. ORTEP representation with atomic displacement parameters at 50% level of probability. Hydrogen atoms have been omitted for clarity.

Table 3.3.: SHAPE 2.1 results of each of the seven crystallographically independent cadmium(II) ions of **C6**.

| Ion       | Cd1  | Cd2   | Cd3  | Cd4    | Cd5  | CD6    | Cd7    |
|-----------|------|-------|------|--------|------|--------|--------|
| Structure | OC-6 | TPR-6 | OC-6 | TBPY-5 | OC-6 | TBPY-5 | TBPY-5 |
| CShM      | 0.73 | 3.54  | 0.63 | 2.66   | 0.67 | 1.91   | 1.43   |

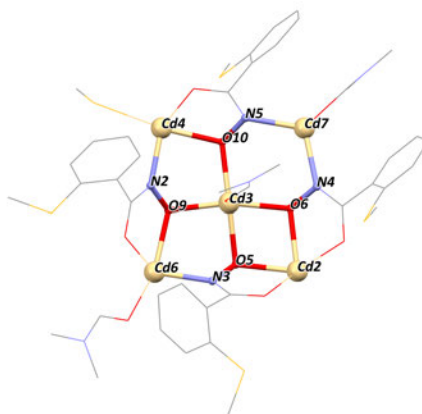


Figure 3.13.: Excerpt of the cube structure of **C6**. One single 12-MC-4 motif highlighting the irregular [M-N-O] repetition units. Color code: Pale yellow - Cd(II), red - oxygen, blue - nitrogen, yellow - sulfur, gray - carbon. ORTEP representation with atomic displacement parameters at 50 % level of probability. Hydrogen atoms have been omitted for clarity.

polyhedron. The ions Cd6 and Cd7 are surrounded by three oxygen and two nitrogen atoms forming a trigonal bipyramidal environment. The same coordination polyhedron is present for Cd4 but is generated by two nitrogen (N1;N2) and one oxygen atom (O11) in the horizontal plane and oxygen (O10) and sulfur atoms (S1) coordinating in axial position. CShM for the octahedral coordination show small values, which indicate polyhedra close to the ideal shape. The rather high value for the trigonal prismatic coordination of Cd2 represents the compression and herewith the distortion of the ideal polyhedron (figure A.1). One peculiarity of the single MC structure is shown in figure 3.13. The non-coordinating sulfur atoms in *ortho*-position lead to a lack of pre-orientation. Therefore, the metallacrown ring is not build up by four [M-N-O] repeating units, but it results in an irregular N-O arrangement instead (figure 3.13). One N-O bridge (Cd2-O6-N4-Cd7) is oriented opposite to the main direction.

This structure can also be described as a penetrated 18-MC-6 following the [M-N-O] units of Cd4, Cd6 and Cd7 (figure 3.14 and figure A.2). The MC's core is filled by two cubes sharing one corner. The cubes are built by Cd1, Cd2, Cd3, Cd5 and oxygen atoms. In which part of this combined structure each cadmium ion contributes, is directly correlated to their own coordination environment. All metallacrown ring building metal ions are embedded in a trigonal bipyramidal coordination (TBPY-5). The central building block of the cubes is a cadmium octahedron in which each Cd ion is coordinated by six oxygen atoms (OC-6). This octahedron of metal ions is capped by two Cd2 ions, the only cadmium showing a trigonal prismatic (TPR-6) coordination environment.

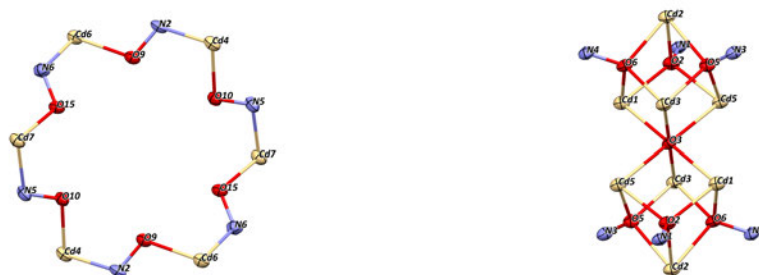


Figure 3.14.: Ring motif of a 18-MC-6 structure in **C6** (left). Penetrating cubes with eight Cd ions (right). Color code: Pale yellow - Cd(II), red - oxygen, blue - nitrogen, yellow - sulfur, gray - carbon. ORTEP representation with atomic displacement parameters at 50 % level of probability. Hydrogen atoms have been omitted for clarity.

This complex structure is very related to the face-centered cubes with Ni(II) and Co(II) ions, synthesized by Zhang et al.<sup>[85]</sup> This fact emphasizes, that the sulfur atoms are not involved or at least not crucial to form the MC structure, as the Ni(II) and Co(II) cubes are mainly formed from 4-bromo-benzohydroxamic acid, which lacks a coordinating donor atom in *ortho*-position.

A broad variety of manganese(II) salts (acetate/perchlorate/chloride/pivalate) have been tried to react with **L3** in several solvents (MeOH/MeCN/acetone/DCM/DMF) under basic conditions (pyridine/triethylamine). None of these attempts yielded any single crystal nor any precipitate, where the IR spectrum was indicative for a successful coordination of **L3** on manganese ions. As Mn(III) ions favor or even demand an elongated octahedral coordination environment, a monomeric complex structure as it was found for Fe(III) (**C1**) is not likely to



crystallize. A targeted 12-MC-4 structure from the divalent **L3** and any trivalent metal ion was only observed for Co(III) in **C5**. This is due to the fact, that the MC ring was formed from a combination of Co(III) and Co(II) ions. The Mn(II) ion tends to be coordinated in highly distorted octahedra or within polyhedra with higher coordination number, as it will be shown in manganese compounds with **L1**. Therefore, a planar ring formation with mixed Mn(III/II) ions would not be possible. While the charge consideration propose both nickel(II)<sup>[86]</sup> and zinc(II)<sup>[87]</sup> to act as proper candidates for a MC formation with **L3**, any attempt to crystallize these complexes remained unsuccessful. Zinc is rather less investigated in the research field of metallocrowns<sup>[50,87]</sup> and besides reactions of zinc(II) perchlorate, acetate or triflate with triethylamine in different solvents (MeOH/MeCN/acetone/DMF) no further attempts were performed. However, nickel(II) was investigated to a greater extent. Nickel(II) salts (perchlorate, chloride, acetate or pivalate), solvents (MeOH, MeCN, acetone, DCM, DMF) and the base (no base, piperidine, pyridine, triethylamine or morpholine) were varied to find the best crystallization parameters. Although the right coordination environment with a sulfur and nitrogen donor atom and two oxygen donor atoms in apical position of an octahedron is known from the literature<sup>[88]</sup>, N-O bridged multinuclear nickel(II) complexes are only present in the literature with additional oxygen or nitrogen  $\sigma$ -donors occupying apical coordination sites.<sup>[89]</sup> In summary, it was possible to crystallize complexes with **L3** and 3d (Fe,Co,Cu) or even 4d (Cd) metal ions. Solely trivalent ions do not form 12-MC-4 or any ring structure with **L3**, due to charge accumulation. Coordination of metal ions with the oxidation state +2 need to show flexibility with regards to their coordination polyhedra (HSAB concept - softer). Therefore, it is reasonable that for copper(II) a variety of MC molecules was obtained.

### 3.1.2. Coordination ability of benzohydroxamic acid with a nitrogen donor atom in *ortho*-position - Transition metal complexes with **L2**

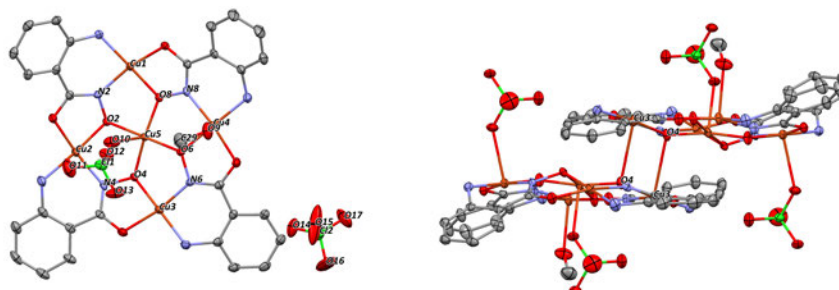


Figure 3.15.: Asymmetric unit (left) and molecular structure of **C7** (right). Yellow dots represent crystallographic centers of inversion. Color code: Orange - Cu(II), red - oxygen, blue - nitrogen, yellow - sulfur, gray - carbon, green - chlorine. ORTEP representation with atomic displacement parameters at 50 % level of probability. Hydrogen atoms have been omitted for clarity.

Anthranilhydroxamic acid and its methylated derivative are found in the literature in copper(II)<sup>[82,90–92]</sup> and nickel(II) MCs<sup>[93,94]</sup>. Here, **L2** was investigated to get insights in the coordination behavior and to find the right conditions to synthesize 12-MC-4 structures. The only compound, which was isolated as single crystals was obtained from the reaction of copper(II) perchlorate, **L2** and sodium hydroxide in methanol.

$\{\text{Cu}^{\text{II}}(\text{ClO}_4)(\text{MeOH})[\mathbf{12} - \text{MC}_{\text{Cu}(\text{II})\text{N}(\text{L2})} - 4]\}_2(\text{ClO}_4)_2 \cdot 2\text{MeOH}$  (**C7**) is very similar to the copper MC synthesized by McDonald et al.<sup>[82]</sup> Varying the stoichiometry of the starting materials and crystallizing at  $-18^\circ\text{C}$  led to the formation of compound **C7** instead of the single 12-MC-4 structure by McDonald et al. The crystal structure is shown in figure 3.15. **L2** together with copper(II) ions form a double decker metallacrown with shifted MC planes. Compared to **C2** the two MC units in **C7** are more shifted apart allowing just one hydroxamate oxygen atom (O4) to coordinate a copper ion (Cu3') of the neighboring MC in axial position (figure 3.15). This Cu3-O4-Cu3' bridge opens an angle of  $106.271(2)^\circ$  with the Cu3-Cu3' and Cu3-O4 distances of  $3.7888(1) \text{ \AA}$  and  $2.7847(1) \text{ \AA}$ , respectively. **C7** crystallizes in the triclinic space group  $P\bar{1}$ . The asymmetric unit (figure 3.15) consists of one MC with two perchlorate ions and two methanol molecules. One perchlorate ion (Cl1) and one methanol molecule (C29-O9) coordinate to copper ions. The non-coordinating perchlorate ion is surrounded by several MC units and is connected to one of them via hydrogen bonding

to an amine group of the ligand (figure A.3). The coordinating perchlorate ion functions as a bridging unit between neighboring double decker complexes by coordinating two different copper ions (Cu5-O10-Cl1-O12-Cu1'). The perchlorate bridged copper(II) ions (Cu1-Cu5') are separated by 6.9815(2) Å from each other.

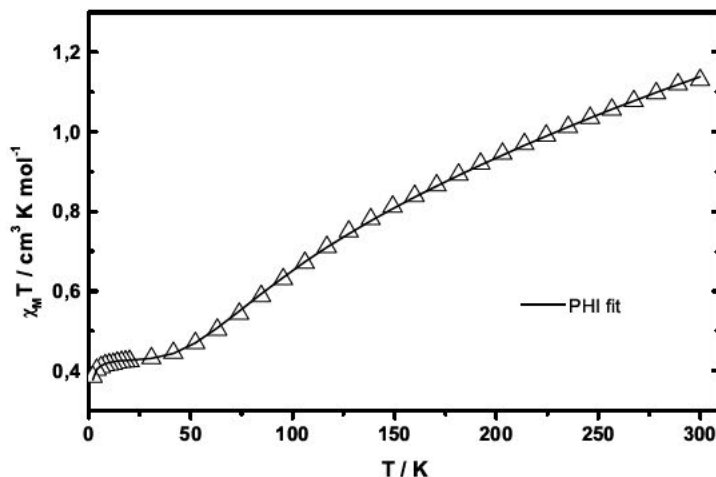


Figure 3.16.: Temperature-dependent magnetic behavior of **C7**.

The  $\chi_M T$  vs.  $T$  plot of **C7** is depicted in figure 3.16. The curve resembles the magnetic behavior of **C2** with a room temperature value of  $1.13 \text{ cm}^3 \text{ K mol}^{-1}$ , the steep slope from 300 K to 30 K reaching a quasi-plateau of around  $0.41 \text{ cm}^3 \text{ K mol}^{-1}$  and the drop at very low temperatures. The magnetic data was fitted according to the star-like coupling scheme using the exchange Hamiltonian  $\hat{H}_{ex}(MC)$  (equation 1.1) with two exchange coupling parameters ( $J_1, J_2$ ) and an additional mean field parameter ( $zJ$ ) to account for intermolecular interactions yielding  $J_1 = -122.0(5) \text{ cm}^{-1}$ ,  $J_2 = -70.0(1) \text{ cm}^{-1}$  and  $zJ = -0.17(1) \text{ cm}^{-1}$ . The  $g$ -factor was fixed to  $g_{Cu}(\text{fixed}) = 2.15$ , as it was done by McDonald et al.<sup>[82]</sup> for a very similar compound. However, fitting without a limited  $g$ -factor only leads to minor deviation ( $J_1 = -119.1(5) \text{ cm}^{-1}$ ,  $J_2 = -68.5(1) \text{ cm}^{-1}$ ,  $zJ = -0.14(1) \text{ cm}^{-1}$  and  $g_{Cu} = 2.138(1)$ ). The fit is in good agreement with other Cu-MC compounds from the literature and this work, revealing two competing antiferromagnetic exchange pathways resulting in an isolated spin ground state of  $S = \frac{1}{2}$ . In comparison to **C2**, the Cu-O-Cu bond angles between the central Cu and the ring building Cu ions ( $108.7^\circ$ - $121.1^\circ$ ) are generally wider in compound **C7**. This could lead to a stronger antiferromagnetic superexchange mediated by hydroxamate oxygen orbitals and is well reflected by the higher  $J_1$  value. The  $J_2$  value does not increase to the same extent, leading to the higher exchange coupling ratio  $J_1/J_2 = 1.74$ . The structural

shift of the MC double decker is also reflected by the fit parameters, as a lowering of the mean field parameter  $zJ$  is observed.

**L2** was not used for syntheses with metal ions which favor the oxidation state +3 due to the incomplete counterbalancing of the charge of a possible MC unit, as it was described before.

### 3.1.3. Coordination ability of benzohydroxamic acid with an oxygen donor atom in *ortho*-position - Transition metal complexes with **L1**

Examples for complexes with salicylhydroxamic acid coordinating one or more 3d transition metal ions range from vanadium<sup>[95]</sup>, manganese<sup>[39,41,53,96]</sup> and iron<sup>[97,98]</sup> over cobalt<sup>[57]</sup> and nickel<sup>[86,99]</sup> up to copper<sup>[58,100]</sup> and zinc<sup>[87]</sup>. However, often co-ligands are necessary to form the crown structure and planarity is often not retained, as bended 9-MC-3 or other structures are obtained. Additionally, the copper centered iron MC from Happ et al. is still the only published 3d heterometallic metallacrown.<sup>[58]</sup> Therefore, there is still more to discover in the field of salicylhydroxamic acid complexes, especially in the magnetic interplay of MCs and their guest ions.

In the following, new complexes of 3d metal ions with **L1** will be discussed. Besides a Cu MC network  $\{\text{Na}_2(\text{DMF})_3\text{Cu}^{\text{II}}\text{sal}_2[\text{Cu}^{\text{II}}(\mathbf{12} - \text{MC}_{\text{Cu}(\text{II})\text{N}(\text{L1})} - \mathbf{4})]\}_n$  (**C8**) and a vanadyl ring structure  $[\text{O}_{10}\text{py}_{10}(\mathbf{30} - \text{MC}_{\text{V}(\text{V})\text{N}(\text{L1})} - \mathbf{10})]$  (**C9**), two manganese double decker MC complexes  $[\text{Mn}(\text{II})(\text{HNEt}_3)_2[\mathbf{12} - \text{MC}_{\text{Mn}(\text{III})\text{N}(\text{L1})} - \mathbf{4}](\mu\mathbf{4} - \text{CO}_3)_2]_2 \cdot (\text{H}_2\text{O})_8$  (**C10**) and  $\text{Mn}(\text{II})[\text{H}_2\text{NEt}_2[\mathbf{12} - \text{MC}_{\text{Mn}(\text{III})\text{N}(\text{L1})} - \mathbf{4}](\text{MeO})_2]_2 \cdot (\text{MeOH})_2$  (**C11**) will be compared.

$\{\text{Na}_2(\text{DMF})_3\text{Cu}^{\text{II}}\text{sal}_2[\text{Cu}^{\text{II}}(\mathbf{12} - \text{MC}_{\text{Cu}(\text{II})\text{N}(\text{L1})} - \mathbf{4})]\}_n$  (**C8**) crystallizes in the triclinic space group  $P\bar{1}$  from the reaction of **L1** with copper chloride and sodium trichloroacetate in dimethylformamide. Five divalent copper(II) ions form a 12-MC-4 structure with four trivalent ligands yielding a net molecular charge of -2, which is compensated by two coordinated sodium ions. The alkali metal ions are five- and sixfold coordinated by oxygen atoms from DMF molecules, **L1** and bridging salicylate ligands (**sal**). Both, the single 12-MC-4 structure with attached sodium ions and the bridging copper(II) salicylate complex are shown in figure 3.17.

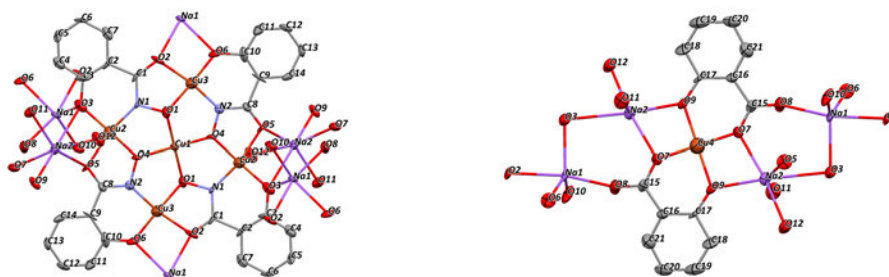


Figure 3.17.: MC unit with attached sodium ions (left) and the monomeric copper salicylate complex present in the crystal structure of **C8** (right). Color code: Orange - Cu(II), red - oxygen, blue - nitrogen, gray - carbon, purple - Na(I). ORTEP representation with atomic displacement parameters at 50 % level of probability. Hydrogen atoms have been omitted for clarity.

Coordination of Na1 and Na2 leads to a two-dimensional network of  $Cu_5$  MCs. The 2D layer structure has a stair-like construction with regards to the metallacrown building units. In figure 3.18, it is shown that each 12-MC-4 is connected to the four neighboring MCs, two via four sodium ions (Na1) along the crystallographic  $a$ -axis and two via the copper (Cu4) salicylate bridge along the diagonal of the unit cell. The ability of MCs to form extended networks has been summarized recently.<sup>[45]</sup> Alkali metal ions<sup>[101]</sup> or copper(II) monomers<sup>[102]</sup> are already known as linkers of metallacrowns. Solving the crystal structure revealed difficulties suggesting a twin or high disorder in the crystal lattice. The best result was obtained having a  $Cu_5$ -MC, which is not connected via copper monomer units but rotated by around  $22^\circ$  along the  $z$ -axis of the central copper ion and an occupancy of 0.17. It is worth noticing, that the presented two-dimensional network is the first multidimensional MC compound with salicylhydroxamic acid as the main ligand.

Aforementioned results of  $Cu_5$ -MC double decker structures (**C2** and **C7**) showed, that considering exchange coupling within one MC is sufficient to describe the magnetic behavior of compounds comprising a multidimensional MC network. Indeed, the temperature-dependent  $\chi_M T$  plot of **C8** depicted in figure 3.19 exhibits a similar shape of the curve to **C2** and **C7**. The room temperature value of  $1.41 \text{ cm}^3 \text{Kmol}^{-1}$  is lower than expected for a spin system with six uncoupled  $S = \frac{1}{2}$  centers ( $2.25 \text{ cm}^3 \text{Kmol}^{-1}$ ). In addition, the curve is decreasing upon cooling, reaching a plateau of  $0.71 \text{ cm}^3 \text{Kmol}^{-1}$  below 12 K indicating overall strong antiferromagnetic exchange coupling and a spin ground state of two uncoupled  $S = \frac{1}{2}$  states ( $0.75 \text{ cm}^3 \text{Kmol}^{-1}$ ). Fitting of the magnetic data was rather difficult due to

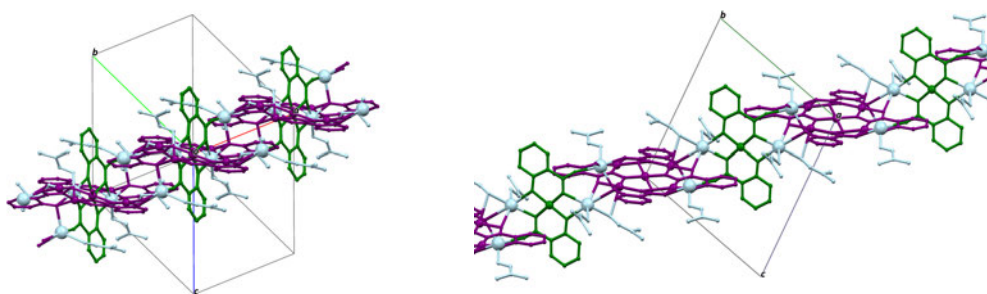


Figure 3.18.: Crystal structure of **C8**. Stair-like arrangement of MC units (purple) where all CuI ions are strung along the a-axis of the unit cell (left). Connected MC units via the Cu(II) salicylate bridge along the unit cell's diagonal (right). Cell axes of the crystal lattice is shown (O=origin). Color code: Purple - MC unit, green - Cu(II) salicylate bridge, pale blue - Na(I) with attached DMF molecules.

the described disorder of the crystal structure. To account for this disordered single MC a monomeric impurity parameter was implemented in the fitting procedure (see equation 3.4).

$$\chi = (1 - IMP)\chi_{calc} + (IMP)\chi_{IMP} \text{ with } IMP = \text{Fraction of magn. imp.} \quad (3.4)$$

The best fit result (with  $\hat{H}_{ex}(MC)$ , equation 1.1) is presented in figure 3.19 and yielded the values  $J_1 = -65(3) \text{ cm}^{-1}$ ,  $J_2 = -44.2(8) \text{ cm}^{-1}$  and  $g_{Cu} = 2.0463(9)$ . The impurity was included as a  $S = \frac{1}{2}$  center with 0.17 occupancy. As the implementation of an impurity is limited to monomeric spin centers it was not possible to calculate a 12-MC-4-like coupled spin system. Therefore, the resulting spin value of  $S = \frac{1}{2}$  is only true at low temperatures. This is why a better fitting of the lower temperature region was favored. However, the isotropic g factor is still lower than the expected for Cu(II) ions in a square planar coordination environment. Additionally, a paramagnetic impurity often leads to a kinked curve in the  $\chi_M$  vs. T plot leading to very high values for  $\chi_M$  at low temperatures, which is not observed in this measurement (figure A.4).

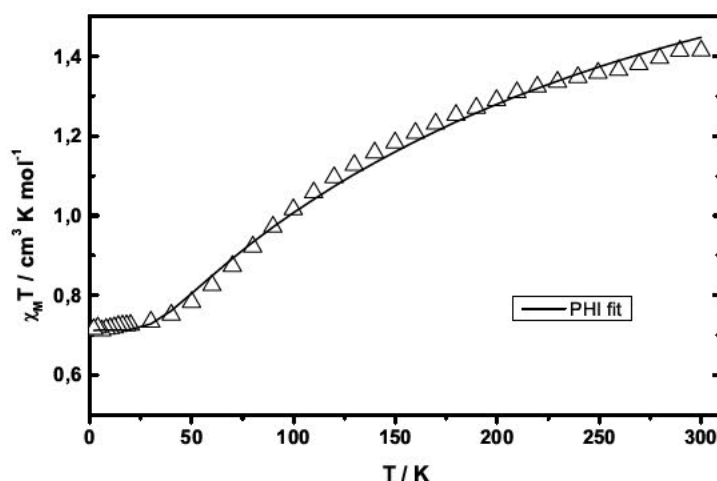


Figure 3.19.: Temperature-dependent magnetic behavior of C8.

As a result of the attempt to implement vanadium as a coupling guest ion, compound C9 was isolated.  $[(30 - \text{MC}_{\text{V}(\text{V})\text{N}(\text{L}1) - 10)]\text{O}_{10} \cdot 10\text{py}$  (C9) crystallizes in the triclinic space group  $\text{P}\bar{1}$  with two molecules per unit cell. Starting from trichlorotris(tetrahydrofuran)-vanadium(III), manganese(II) perchlorate with L1 and pyridine in acetone, dark blue crystals of this vanadyl ring structure were obtained. Figure 3.20 shows the 30-MC-10 ring with ten vanadyl units. A structurally disordered pyridine (py) molecule is located inside the void. The vanadium ions are all sixfold coordinated each in a distorted octahedron. The apical positions are occupied by one oxo ligand and three oxygen atoms from L1. Axial coordination sites are occupied by one pyridine nitrogen and an oxime nitrogen atom. All metal ions show propeller configuration but with alternate  $\Delta$  and  $\Lambda$  absolute stereochemical configuration. The present salicylhydroxamic acid zig-zag chain causes the oxo ligands to point out of the ring plane, alternating up and down. The resulting cavity is of the size of 4 to 5 Å. The oxo ligands form a pentagonal antiprism (figure A.5). The orientation of all ligands towards one side of the vanadyl ring and therefore an overall  $\Delta$  or  $\Lambda$  configuration seems only to be favorable for smaller ring sizes.<sup>[95]</sup> UV-Vis and magnetic susceptibility measurements revealed that vanadium is in the oxidation state 5+. Nevertheless, C9 represents the second example of a vanadyl MC albeit with a bigger ring size than the known 9-MC-3 structure<sup>[95]</sup>. This huge ring size is more known from aza-MCs.<sup>[103]</sup>

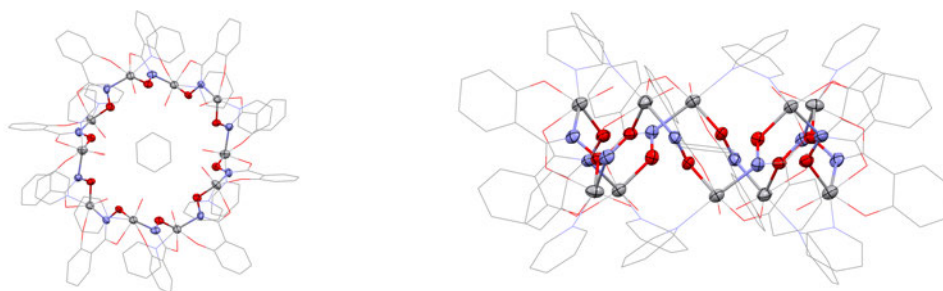


Figure 3.20.: Top (left) and side view (right) of the molecular structure of **C9**. Color code: Light gray - Vanadium(V), red - oxygen, blue - nitrogen, gray - carbon. ORTEP representation with atomic displacement parameters at 50% level of probability. Hydrogen atoms have been omitted for clarity.

Salicylhydroxamic acid is very well established for the coordination of manganese(III) ions and therefore the most frequently used ligand for the synthesis of manganese MCs.<sup>[39,53–55,96,104–106]</sup> The combination of **L1** with Mn ions leads to 12-MC-4 and 15-MC-5 structures, where the important criteria is the binding mode of the bidentate pockets, if overall planar or propeller configurations are present. The coordination mode can be varied by the right choice of co-ligands and solvents, which has been demonstrated by Dendrinou-Samara et al.<sup>[41]</sup> and Kessisoglou et al.<sup>[107]</sup> with the inter-conversion of a manganese 12-MC-4 structure into a 15-MC-5. This implies that the formation of manganese(III) metallacrowns is very sensitive to the reaction conditions and that they show a high structural flexibility. This observation can be confirmed by several synthetic approaches from the Rentschler group. Even the heterometallic approach of manganese and copper acetate with pyridine in acetonitrile led to crystals of the known 15-MC-5 compound<sup>[107]</sup> (figure A.8). In this structure, three manganese ions adopt a propeller configuration with  $\Delta, \Lambda, \Delta$  absolute stereochemistry and two planar coordinated manganese ions. The authors claim, the tendency of pyridine to coordinate in an apical position whereas weak oxygen donors like dimethylformamide or dimethylsulfoxide rather occupy the elongated Jahn-Teller axis, to be crucial for a planar or a propeller like coordination of manganese.

The reaction of manganese chloride with the non-coordinating base triethylamine and trichloroacetate in ethanol should lead, according to the previous mentioned assertion, to a fully planar coordination of the manganese metal ions. Indeed, the resulting complex forms a 12-MC-4 double decker structure with two stacked manganese(II) ions encapsulated as central guest ions.  $\{\text{Mn(II)(HNEt}_3)_2[\mathbf{12} - \text{MC}_{\text{Mn(III)N(L1)} - 4](\mu\mathbf{4} - \text{CO}_3)_2\}_2 \cdot (\text{H}_2\text{O})_8$ ,





Figure 3.21.: Side (left) and top view (right) of the molecular structure of **C10**. Color code: Violet - Mn(III), magenta - Mn(II), red - oxygen, blue - nitrogen, gray - carbon. Hydrogen atoms, non-coordinating solvent molecules and counterions have been omitted for clarity.

**C10**, has been described previously<sup>[108]</sup> and is structurally comparable to a calcium centered analog (see figure 3.21).<sup>[109]</sup>

Alaimo et al. synthesized the Ca(II) centered manganese metallacrown reacting manganese benzoate, calcium perchlorate, salicylhydroxamic acid and triethylamine in chloroform. What has not been mentioned before, the carbonate ions are generated in-situ by a reduction of elemental oxygen. The pure manganese double decker **C10** is available in even higher yields (31 %) than the calcium analog. Independently, both complexes show that the reaction needs to bind carbon dioxide and oxygen from the atmosphere. Magnetic data of **C10** was only measured to 10 K in previous work.<sup>[108]</sup> Therefore, the magnetic susceptibility was remeasured in the temperature region from 300 K to 2 K. The magnetization of **C10** was measured between 2 K and 10 K with applied magnetic fields of up to 7 T and the ac susceptibility was probed to investigate the spin reversal behavior at 2 K. The criteria of slow magnetic relaxation was neither observed at zero field nor with an applied magnetic dc field (200 Oe-600 Oe). Temperature-dependent susceptibility data and the magnetization plot are depicted in figure 3.22. The  $\chi_M T$  value decreases upon cooling from  $27.47 \text{ cm}^3 \text{ K mol}^{-1}$  (300 K) to  $2.38 \text{ cm}^3 \text{ K mol}^{-1}$  (2 K). The room temperature value is below the expected ( $32.75 \text{ cm}^3 \text{ K mol}^{-1}$ ) for a spin system of eight  $S = 2$  and two  $S = \frac{5}{2}$  centers. An overall antiferromagnetic exchange coupling is expected for a Mn(II) centered Mn(III) MC.<sup>[53]</sup> Zaleski et al.<sup>[53]</sup> showed that the  $S = \frac{1}{2}$  spin ground state is not well isolated and that anisotropy effects have to be considered. High molecular anisotropy is expected in **C10**, supported by the observation of strong deviations of the reduced magnetization curves at different temperatures (figure A.6), which is a significant feature of present

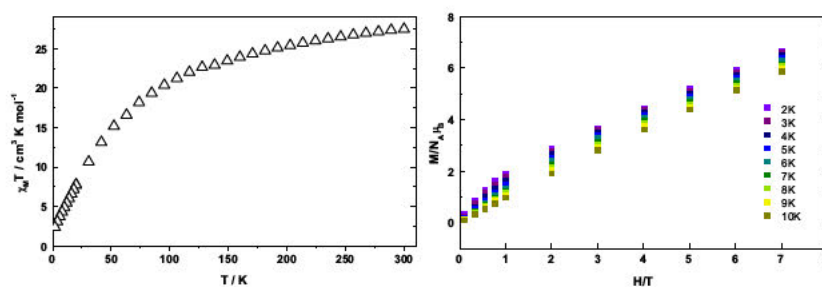


Figure 3.22.: Temperature (left) and field-dependent (right) magnetic behavior of **C10**.

magnetic anisotropy.<sup>[110]</sup> If in **C10** all Mn(III) ions couple antiferromagnetically their spin moments cancel each other out and only the resulting  $2 \cdot S = 2$  needs to be analyzed. An additional antiferromagnetic coupling between the carbonate bridged Mn(II) ions would yield a spin state of  $S = 0$ . This can neither be observed in the  $\chi_M T$  plot at 2 K nor is the magnetization plot indicative for an isolated spin ground state. In accordance with these observations and the absence of an *out-of-phase* signal at zero applied dc field, a giant spin approximation (GSA) to evaluate the data further was not used. Mixing of the ground state with low lying excited states seems to be apparent yielding possible QTM which would be neglected by a GSA.<sup>[111,112]</sup> Unfortunately, it was not possible to fit the magnetic data of **C10** in another way due to the matrix size.

A change towards the slightly better coordinating methanol instead of ethanol and using diethylamine as the base seems to suppress  $CO_3^{2-}$  uptake, as another manganese double decker Mn(II) $\{H_2NET_2(MeO)_2(MeOH)_2[12 - MC_{Mn(III)N(L1)} - 4]\}_2$  (**C11**) is the main product. **C11** crystallizes in the monoclinic space group  $C2/c$  with four molecules per unit cell. The first synthesis and the crystal structure refinement of **C11** were done by Dr. Peter Happ (former member of the Rentschler group). However, magnetic experiments and magneto-structural correlations were not carried out. The molecular structure of **C11** is depicted in figure 3.23. The two MC rings are connected via four methanolate molecules, bringing all hydroxamate oxygen atoms in close proximity to form a square antiprism, which coordinates the central manganese(II) ion. In order to reach an overall neutral charge, two diethylammonium cations are also present in the crystal structure. They connect each double decker molecule with the neighboring via hydrogen bonds (N5H-O3, N5H-O9, N5H-O13), see figure A.9. The average Mn(III)-Mn(III) distance ( $\mu_2 - O$  bridged) is 3.348 Å, whereas in **C10** the MC planes are more separate from each other (Mn(III)-Mn(III) distance of 6.238 Å) leaving more space for the second manganese(II) ion. Even the Mn-Mn separation within one crown (4.627 Å - 4.676 Å) is bigger than the distance between both

MC planes in **C11**. Both single 12-MC-4 rings are structurally identical, although their direction of rotation is opposite to each other, meaning their [Mn-N-O] repetition units are contra-rotating. Nevertheless, the crystallographically independent manganese(III) ions are embedded in different polyhedra. Table 3.4 summarizes the coordination environments of all Mn ions in the double decker MC complex **C11** by giving the SHAPE results and selected bond lengths of the coordination polyhedra. Mn1 and Mn3 are coordinated in an octahedral and a square pyramidal shape, respectively. All four apical positions are occupied by salicylhydroxamic acid donor atoms. This results in a planar coordination mode as expected for 12-MC-4 structures. However, the other two ring building metal ions, Mn2 and Mn4, can either be discussed as fivefold coordinated or as distorted octahedral. Describing the latter, additional hydroxamato oxygen atoms from the second 12-MC-4 layer, O1 and O7 for Mn2 and Mn4 respectively, are taken into account. Thus, O1-Mn2-O5 and O7-Mn4-O11 represent the elongated Jahn-Teller axes of the coordination polyhedra. Based on that, the absolute configuration of both coordination environments can be determined as  $\Lambda$ . The combination of half planar and half propeller coordination modes of Mn(III) ions has not been found in any other Mn MC complex so far.

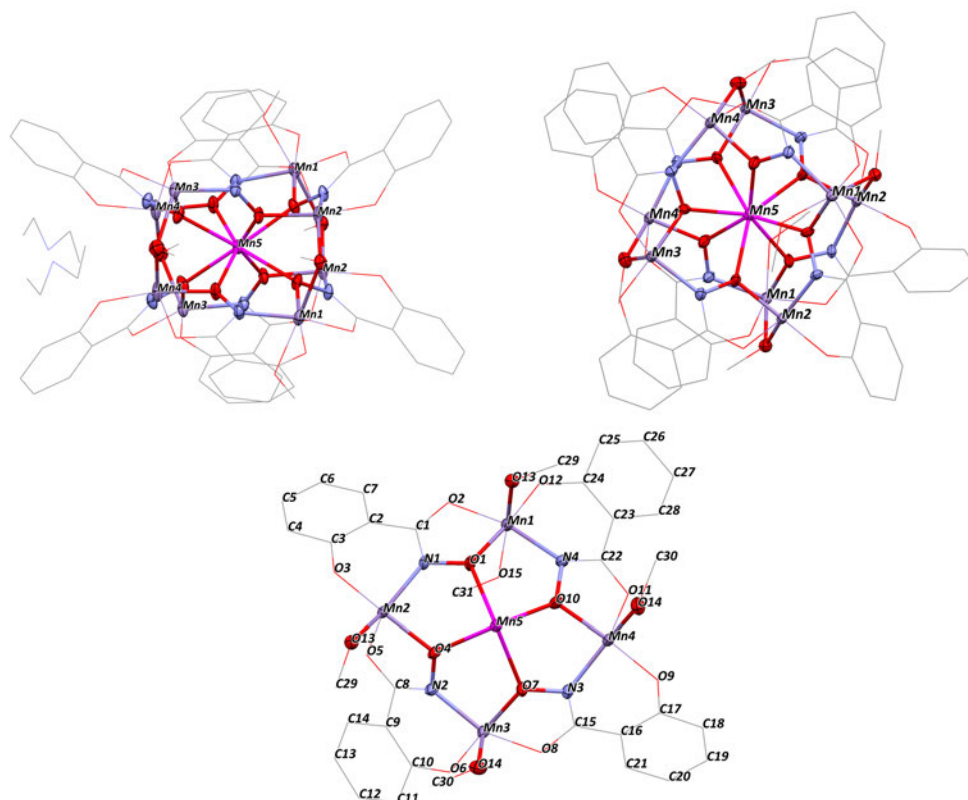


Figure 3.23.: Side (top left) and top view (top right) of the molecular structure of **C11** and top view (bottom) of only one of the two 12-MC-4 units in compound **C11** including the bridging methanolate oxygen atoms. Color code: Violet - Mn(III), magenta - Mn(II), red - oxygen, blue - nitrogen, gray - carbon. ORTEP representation with atomic displacement parameters at 50% level of probability. Hydrogen atoms have been omitted for clarity.

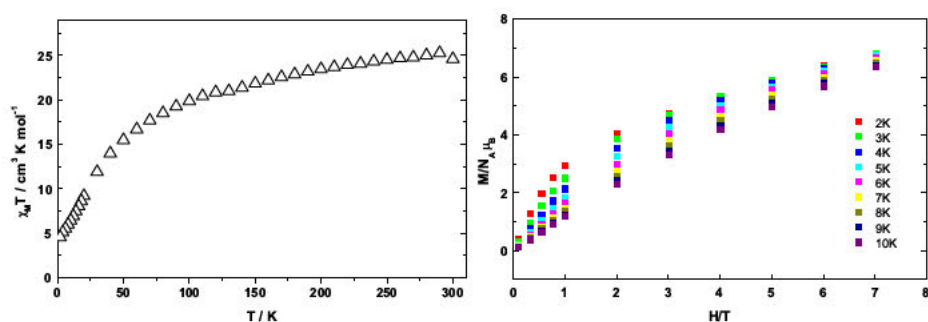


Figure 3.24.: Temperature and field-dependent magnetic behavior of C11.

Table 3.4.: SHAPE 2.1 results and selected bond lengths of each crystallographically independent manganese ion of C11. The number in brackets behind the ion label indicates how many neighboring atoms have been considered.

| Ion             | Mn1                 | Mn2(5)    | Mn2(6)   | Mn3                 | Mn4(5)    | Mn4(6)     | Mn5       |
|-----------------|---------------------|-----------|----------|---------------------|-----------|------------|-----------|
| Structure       | OC-6                | TBPY-5    | OC-6     | SPY-5               | TBPY-5    | TPR-6/OC-6 | SAPR-8    |
| CShM            | 1.31                | 1.82      | 5.95     | 1.17                | 2.34      | 5.81/7.15  | 0.06      |
| Bond length (Å) | N4 1.964            | N1 1.976  |          | N2 1.963            | N3 1.977  |            | O1 2.308  |
|                 | O1 1.917            | O3 1.877  |          | O6 1.834            | O9 1.886  |            | O4 2.244  |
|                 | O2 1.944            | O4 1.914  |          | O7 1.900            | O10 1.886 |            | O7 2.309  |
|                 | O12 1.843           | O5 2.079  |          | O8 1.952            | O11 2.053 |            | O10 2.283 |
|                 | O13 2.205           | O13 1.942 |          | O14 2.071           | O14 1.962 |            |           |
|                 | O15 2.411           |           | O1 2.672 |                     |           | O7 2.775   |           |
| Bond angles     | Mn1-O13-Mn2 107.98° |           |          | Mn3-O14-Mn4 111.65° |           |            |           |
|                 | Mn1-O1-Mn5 124.64°  |           |          | Mn2-O4-Mn5 114.58°  |           |            |           |
|                 | Mn3-O7-Mn5 123.98°  |           |          | Mn4-O10-Mn5 115.06° |           |            |           |

The temperature-dependent magnetic behavior of C11 is depicted in figure 3.24. The product of magnetic susceptibility and temperature decreases from  $24.6 \text{ cm}^3 \text{ K mol}^{-1}$  to  $4.6 \text{ cm}^3 \text{ K mol}^{-1}$  upon cooling from 300 K to 2 K. Fitting the data is impossible due to the dimension of the required matrix to be diagonalized. However, qualitative evaluation suggests overall antiferromagnetic exchange coupling as the  $\chi_M T$  plot does not reach the expected value for eight noninteracting Mn(III) ions and one Mn(II) ion ( $28.375 \text{ cm}^3 \text{ K mol}^{-1}$ ) at room temperature and a pronounced decrease of  $\chi_M T$  with decreasing temperature is observed. The 2 K value is close to  $4.375 \text{ cm}^3 \text{ K mol}^{-1}$ , the theoretical value of an isolated  $S = \frac{5}{2}$  center ( $g = 2$ ), leading to the suggestion that the spins of all Mn(III) ions align antiparallel to each other at low temperatures (due to inner MC afm coupling) leaving the spin moment of

a single Mn(II) ion as the magnetic ground state. Evaluation of the field-dependent magnetization plot, also depicted in figure 3.24, clearly demonstrates that saturation at high magnetic fields is not reached. Therefore, no well isolated spin ground state is present in **C11**. Nevertheless, expected high single ion anisotropy due to the incorporation of eight Mn(III) ions in combination with this frustrated antiferromagnetic system ( $S \neq 0$ ) led to the question whether **C11** behaves as a SMM. Frequency-dependent alternating current (ac) measurements were carried out with an applied ac magnetic field of 3 Oe in the frequency range from 1 Hz to 1400 Hz in the absence of a static magnetic field. The evaluated data at zero field is shown in figure A.10. However, in order to effectively suppress quantum tunneling of the magnetization and reach the highest resonance signal for  $\chi''$ , the *out-of-phase* susceptibility was probed in a static (dc) field-dependent experiment. Further discussed ac data of **C11** was measured with an applied dc field of 400 Oe. The uniaxial anisotropy of the system yields a frequency and temperature-dependent resonance of the imaginary part of the complex ac susceptibility ( $\chi''$ ), which is depicted in figure 3.26. This observation, due to the presence of slow relaxation of magnetization in **C11**, is also visualized in the Cole-Cole plot in figure 3.26 (bottom right). In order to quantify the relaxation time  $\tau$  and the effective energy barrier  $U_{eff}$  of this SMM a generalized Debye model<sup>[113]</sup> was used. Fitting of the Cole-Cole plot was carried out using the CC-FIT program by Chilton, which uses the Cole-Cole equation (3.5) to determine the isothermal susceptibility  $\chi_T$ , the adiabatic susceptibility  $\chi_S$ , the Cole-Cole parameter  $\alpha$  and the relaxation time  $\tau$  for each measured temperature. The relaxation rate ( $1/\tau$ ) follows the Arrhenius law according to equation 3.6. To fit the  $1/\tau$  vs.  $T^{-1}$  plot several relaxation processes were taken into consideration, the field-dependent QTM and direct process (tunneling process in excited states) and the temperature-dependent Orbach and Raman processes. However, the symmetrical shape of the semicircle in the Cole-Cole plot suggests one single relaxation process.<sup>[114]</sup> The decay of  $\chi''$  upon increasing temperatures (see figure 3.26  $\chi''$  vs. T plot) is indicative for a thermal activated relaxation process. As the Raman process exhibits a higher temperature dependency ( $T^n$ ), the Arrhenius plot in figure 3.25 would show a nonlinear curve leading to the assumption that the relaxation of the magnetization in **C11** is mainly governed by a thermal activated Orbach process. It should be reminded that these experiments were performed with an applied static field and that the QTM influence is diminished on purpose. However, fitting of the Arrhenius plot yielded a relaxation time of  $\tau_0 = 5.27 \times 10^{-9}$  s and an effective energy barrier for the reversal of magnetization  $|U_{eff}| = 25.64 \text{ cm}^{-1}$  for **C11**. The value of the estimated anisotropy barrier is slightly higher than it is known from other Mn(III)

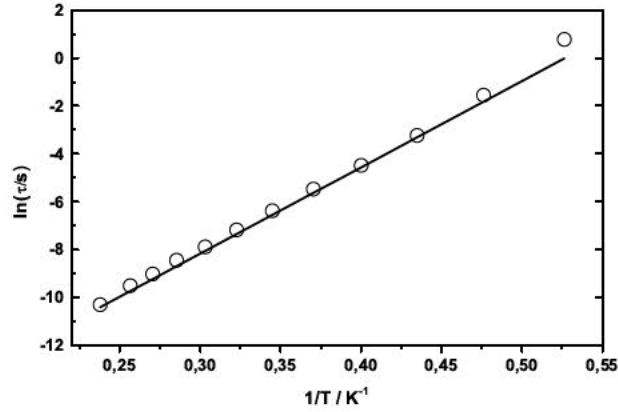


Figure 3.25.: Natural logarithm of the relaxation time  $\tau$  of the magnetization reversal of C11 plotted against the reciprocal temperature  $T^{-1}$ . The solid line represents the best fit with the Arrhenius equation 3.6 assuming a thermally activated Orbach relaxation process only.

12-MC-4 structures with a paramagnetic guest ion ( $|U_{eff}|(Y^{III}W^V Mn_4) = 12.37 \text{ cm}^{-1}$ <sup>[55]</sup>;  $|U_{eff}|(Mn^{II} Mn_4) = 14.7 \text{ cm}^{-1}$ <sup>[53]</sup>), whereas the relaxation time varies up to two orders of magnitude ( $\tau_0 = 2.68 \times 10^{-8} \text{ s}$ <sup>[55]</sup>;  $\tau_0 = 1.4 \times 10^{-7} \text{ s}$ <sup>[53]</sup>). It is worth mentioning that for very weak antiferromagnetically coupled paramagnetic guest ions ( $Gd^{(III)}Mn_4$ ) no *out-of-phase* signal is observed.<sup>[42]</sup> The introduction of a second 12-MC-4 layer could lead to very low lying excited states, which could be involved in a direct relaxation process and therefore yield short relaxation times. The increase in the energy barrier can be attributed to either higher molecular anisotropy by the addition of more Mn(III) ions with high single ion anisotropy or a change in the spin ground state compared to the single  $Mn^{II}Mn_4$  12-MC-4. However, a change of the spin ground state is unlikely as no increased  $J_1/J_2$  ratio was observed in any magnetic measurement of C11 (e.g. an increase of  $\chi_M T$  upon cooling).

$$\chi_{ac}(\omega) = \chi_S + \frac{\chi_T - \chi_S}{1 + (i\omega\tau)^{1-\alpha}} \quad (3.5)$$

$$\frac{1}{\tau} = \frac{1}{\tau_0} \cdot \exp\left(\frac{-U_{eff}}{kT}\right) \quad (3.6)$$

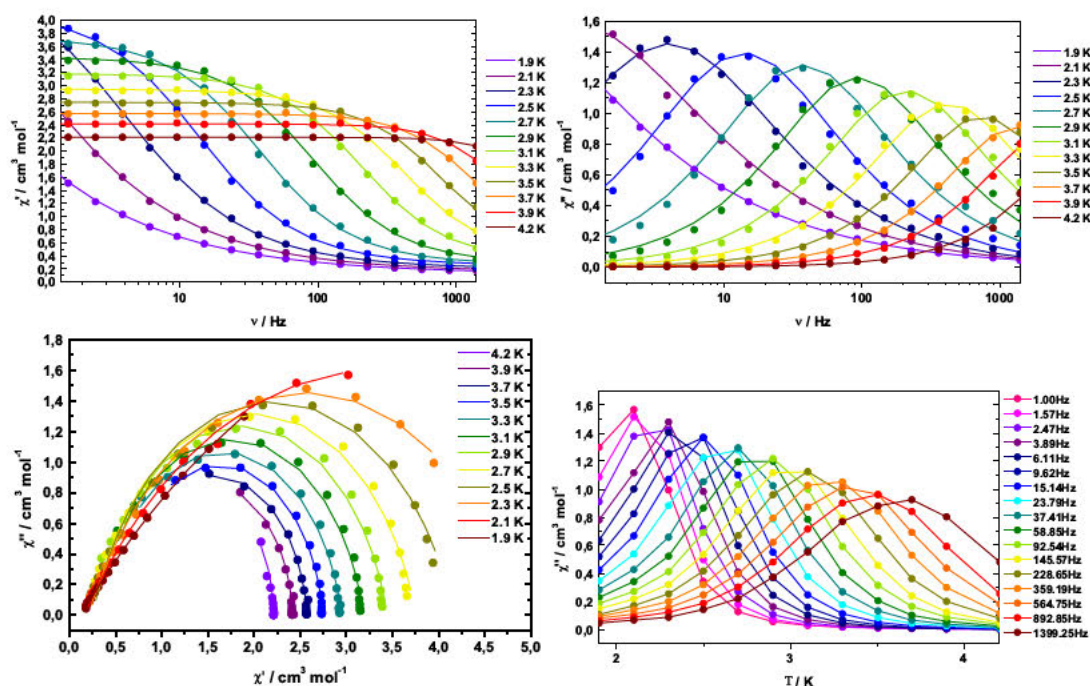


Figure 3.26.: AC susceptibility measurements of C11 with an applied static field of 400 Oe and best fitting results (solid lines). Top left: Frequency-dependent signal of the real part of the ac susceptibility  $\chi'$ . Top right: Frequency-dependent signal of the imaginary part of the ac susceptibility  $\chi''$ . Bottom left: Cole-Cole plot. Bottom right: Temperature-dependent signal of the imaginary part of the ac susceptibility  $\chi''$  (solid lines are only guidelines for the eyes)

The overview of obtained complexes in figure 3.27 summarizes how sensitive the coordination environment of the Mn ions reacts to changes of co-ligands or solvent molecules. The broad variety of MCs, which are accessible from the combination of manganese salts with L1 clearly demonstrates that there is high variability and flexibility in the system. Additionally, syntheses with manganese and a suitable magnetic director (Cu(II) or V(IV)) always led to homometallic complexes. This underlines the necessity of more selective coordination pockets within the MC ring. A strict planar orientation of the main ligand must be ensured, to guarantee the formation of a single 12-MC-4 structure with Mn(III) ions in the periphery. To fulfill this condition without the dependency on further co-ligands and several other parameters for the reaction procedure, which would increase the complicity and introduce additional uncertainties, the attachment of distinct coordinating side arms was striven for and will be further discussed in the next chapter.



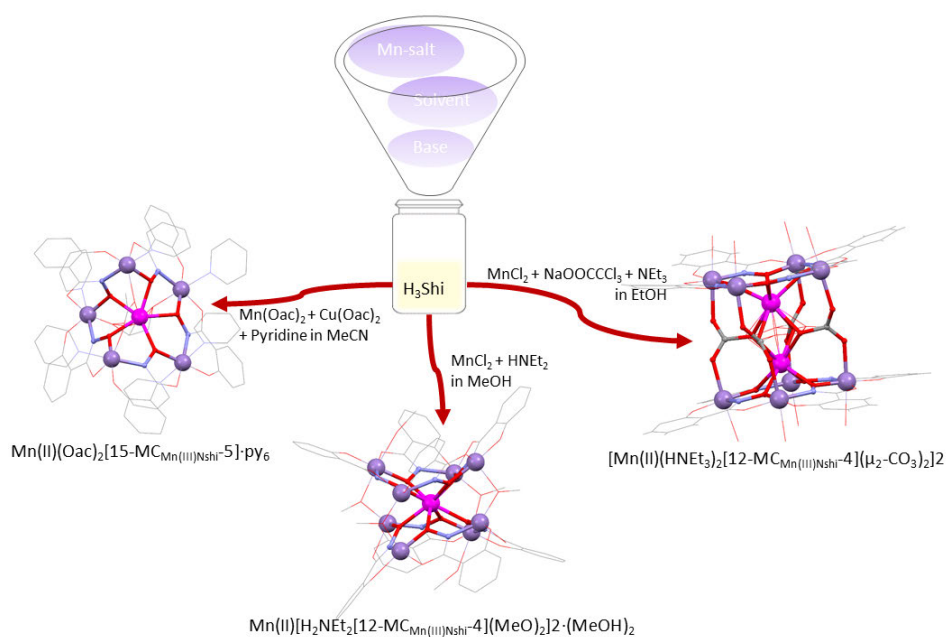
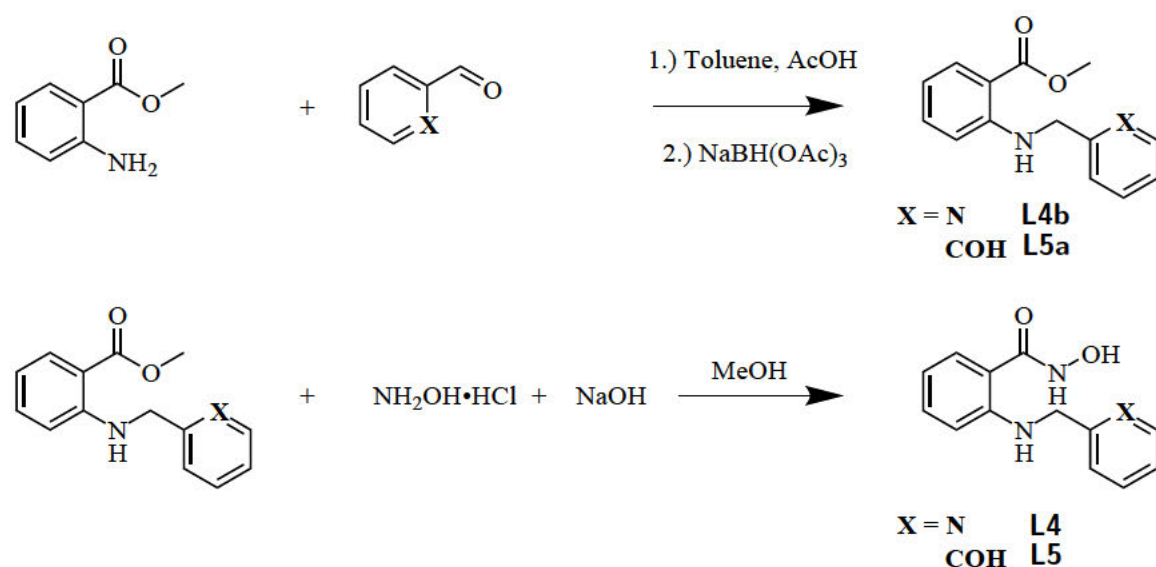


Figure 3.27.: Schematic overview of crystallized products from the reaction of manganese salts with **L1**.

### 3.2. Metallacrown ligands with additional coordinating side arm in *ortho*-position

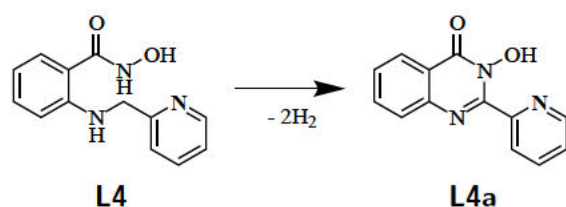
One synthetic way to introduce coordinating side arms into known hydroxamic acid molecules is the reaction of an amine group with an aldehyde function, yielding the Schiff base conjugate. This reaction was carried out using the amine group of anthranilhydroxamic acid (**L2**). In scheme 3.3 the general multi-step reaction to synthesize ligands like **L4** and **L5** is presented. Starting from methyl anthranilate several side arms can be attached. It should be mentioned that other attempts like a substitution reaction with alkyl halogenides and ligand **L4** have been developed and carried out in a previous study.<sup>[108]</sup> For the synthesis of ligand **L5** the methyl ester of anthranilic acid has been reacted with salicylaldehyde in toluene under acidic conditions. After heating the reaction mixture for 2.5 hours, a reduction of the Schiff base conjugate has been provoked by adding the mild reduction agent sodium triacetoxyborohydride. The isolated intermediates **L4b** and **L5a** were then reacted with hydroxylamine hydrochloride in methanol under basic conditions to form **L4** and **L5** respectively.



Scheme 3.3: Multi-step reaction scheme to form hydroxamic acid ligands with additional coordinating side arms based on anthranilhydroxamic acid.

### 3.2.1. Setback with the side arm - Transition metal complexes with L4

The reaction of cobalt(II) pivalate with **L4** in DMF led to complex  $\text{Co}_4^{\text{II}}(\text{L4a})_4(\mu_2\text{Piv})_2\text{Piv}_2$  (**C12**). The molecular structure in figure 3.28 reveals, that the main ligand underwent an oxidative cyclization reaction. This reaction has to be accompanied by either the release of two equivalents hydrogen as shown in scheme 3.4 or a Co(II) catalyzed oxidation most probably with atmospheric oxygen. Co(II) catalyzed cyclization reactions were investigated by Zhang et al.<sup>[115]</sup> and Sivakumar et al.<sup>[116]</sup> supporting this mechanism to be involved in forming **L4a**.



Scheme 3.4: Schematic representation of a possible in-situ side reaction yielding the cyclization product of **L4**.

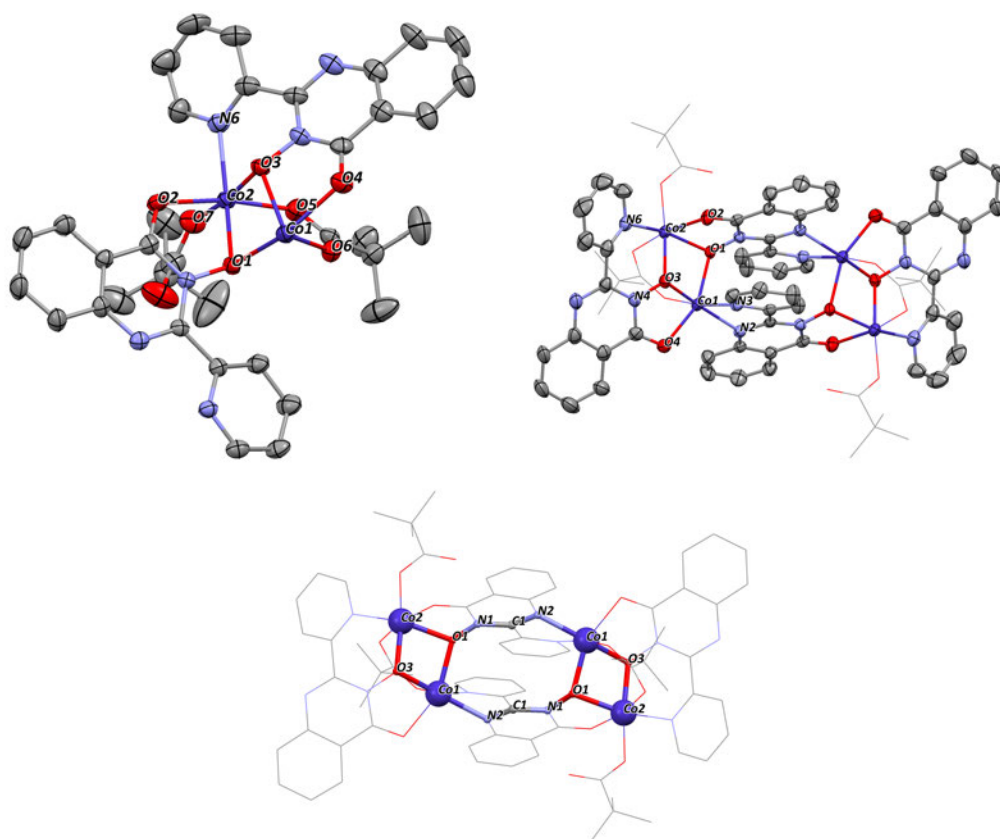


Figure 3.28.: Asymmetric unit (top left) and molecular structure (top right) of **C12**. Possible coupling pathways highlighted within the the cobalt(II) tetramer (bottom). Color code: Dark blue - Co(II), red - oxygen, blue - nitrogen, gray - carbon. ORTEP representation with atomic displacement parameters at 50 % level of probability. Hydrogen atoms have been omitted for clarity.

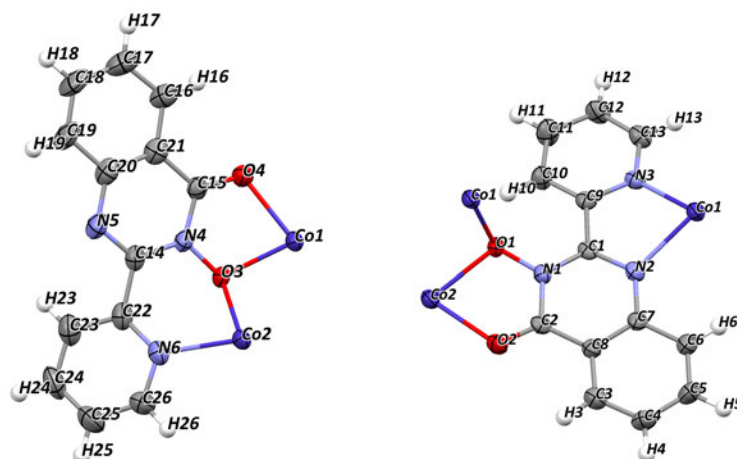


Figure 3.29.: Coordination modes of ligand **L4a**, capping (left) and bridging (right). Color code: Dark blue - Co(II), red - oxygen, blue - nitrogen, gray - carbon. ORTEP representation with atomic displacement parameters at 50 % level of probability. Hydrogen atoms are drawn as fixed-size spheres with a radius of 0.22 Å.

Four of these in-situ generated ligands **L4a** form the cobalt tetramer (**C12**) together with four coordinating pivalate anions (Piv). Two of the pivalate ions are end-on attached to Co2 and Co2', whereas the other two bridge Co1 and Co2. **L4a** coordinates in two distinct modes, both shown in figure 3.29. The ligand in capping mode coordinates via both oxygen atoms O3, O4 and with the pyridine nitrogen N6. O3 bridges between both cobalt ions spanning an Co1-O3-Co2 angle of 95.2°. The ligand **L4a** in bridging mode coordinates via two pockets, where Co1 is embedded in a five membered ring between N1 and N2 while Co2 is chelated by O1 and O2. Likewise O3 from the capping ligand, O1 also bridges both cobalt ions, resulting in a Co1-O1-Co2 angle of 93.5°. Two of these bridging ligands connect both cobalt dimers with each other, yielding a Co1-Co2 distance of 7.062 Å. The distance between Co1 and Co2 within one dimer amounts 3.091 Å.

The  $\chi_M T$  vs. T plot of **C12**, depicted in figure 3.30, shows a plateau at 12.8(1) cm<sup>3</sup>Kmol<sup>-1</sup> in the temperature range from 300 K to  $\approx$  80 cm<sup>3</sup>Kmol<sup>-1</sup>. Below 80 K the curve starts decreasing, followed by a step drop below 10 K reaching a  $\chi_M T$  value of 1.57 cm<sup>3</sup>Kmol<sup>-1</sup> at 2 K. This behavior indicates overall antiferromagnetic exchange coupling within the cobalt tetramer. The room temperature value (12.87 cm<sup>3</sup>Kmol<sup>-1</sup>) is far above the expected spin-only value (7.5 cm<sup>3</sup>Kmol<sup>-1</sup>) for an uncoupled spin system with four  $S = \frac{3}{2}$  spin centers.

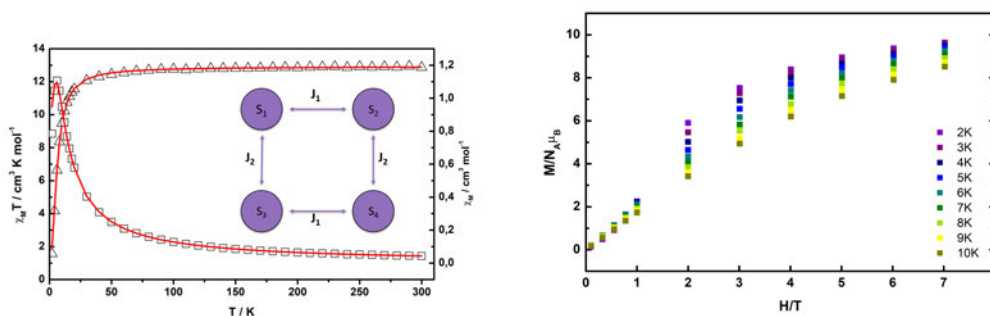


Figure 3.30.: Temperature and field-dependent magnetic behavior of **C12**.  $\chi_M$  (open squares) and  $\chi_M T$  (open triangles) vs.  $T$  plots and the best fit (solid red line) using a 2J model according to the shown coupling scheme (left). Low temperature magnetization plot of **C12** (right).

This fact can be attributed to the neglected orbital moment of Co(II) ions commonly found in cobalt complexes exhibiting distorted octahedral coordination of the metal ions.<sup>[117,118]</sup> Very similar Co(II) dimer subunits have been investigated by Samulewski et al.<sup>[118]</sup> and they concluded that the evaluation of magnetic data for Co(II) complexes is very difficult due to their orbital angular momentum, spin-orbit coupling and magnetic anisotropy. Fitting the magnetization and susceptibility data of the tetranuclear compound **C12** is even more complex. An inclusion of parameters to account for the orbital momentum and spin-orbit coupling is necessary to precisely discuss the molecular magnetism of **C12**. However, it would by far exceed the limit of the fitting routines within *PHI*. Therefore, the magnetic data was fitted using a simple Hamiltonian (equation 3.7) accounting for one coupling constant  $J$  and the Zeeman splitting, neglecting a possible second coupling across the cobalt dimers.

$$\hat{H} = -2J(\hat{S}_1\hat{S}_2 + \hat{S}_3\hat{S}_4) + \mu_B \sum_{i=1}^N \vec{S}_i \cdot \vec{g}_i \cdot \vec{B} \quad (3.7)$$

The resulting fit yields  $J = -0.84(2) \text{ cm}^{-1}$  and  $g_{Co} = 2.650(6)$  ( $R = 2.63$ ). The high  $g$ -factor is a result of the disregarded orbital momentum, but from the  $\chi_M$  vs.  $T$  plot (figure A.11) it is obvious that the fit deviates from the susceptibility data at low temperatures. To cover the low temperature region, another exchange constant was implemented in the Hamiltonian (equation 3.8) according to the coupling scheme shown in figure 3.30.

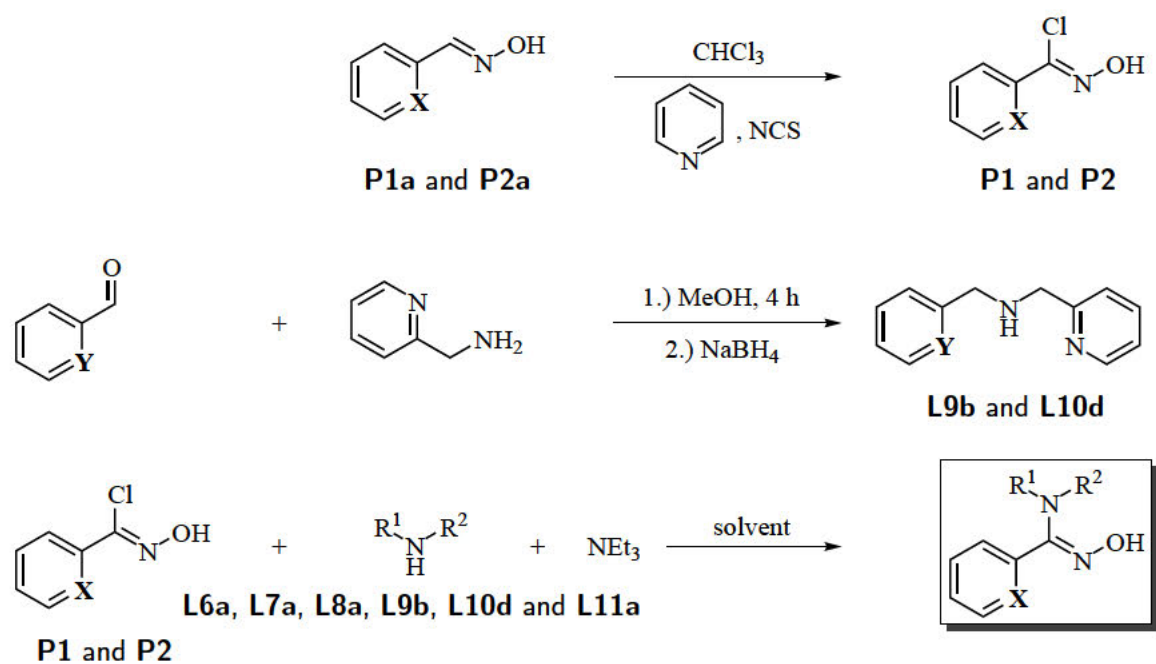
$$\hat{H} = -2J_1(\hat{S}_1\hat{S}_2 + \hat{S}_3\hat{S}_4) - 2J_2(\hat{S}_1\hat{S}_3 + \hat{S}_2\hat{S}_4) + \mu_B \sum_{i=1}^N \vec{S}_i \cdot \vec{g}_i \cdot \vec{B} \quad (3.8)$$

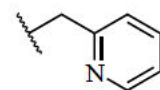
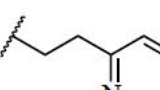
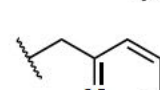
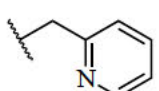
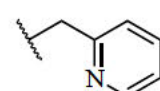
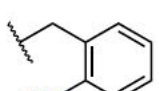
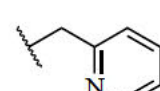
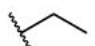

Fitting with this 2J model yielded  $J_1 = -1.004(6) \text{ cm}^{-1}$ ,  $J_2 = 0.69(2) \text{ cm}^{-1}$  and  $g_{Co} = 2.626(1)$  ( $R = 1.85 * 10^{-1}$ ). The antiferromagnetic exchange within the cobalt dimers is in good agreement with several findings in the literature.<sup>[118-123]</sup> However, the ferromagnetic coupling constant is not reasonable and the decrease and the low temperature magnetic behavior of **C12** is more likely caused by zero-field splitting and anisotropy effects of the cobalt(II) ions. This assumption is supported by the observation that the magnetization data of **C12** could not be fitted with the set of given parameters. The magnetization vs. field plot (figure 3.30) nearly reaches saturation with a maximum value of  $9.63N_{\alpha}\mu_B$  at 2 K and 7 T, significantly lower than the expected  $3N_{\alpha}\mu_B$  ( $g = 2$ ) per Co(II) ion.<sup>[124]</sup> This is due to the fact that for Co(II) ions in an octahedral coordination environment at low temperatures an effective spin  $S_{eff} = \frac{1}{2}$  must be considered<sup>[125]</sup> and is further supporting the presence of an antiferromagnetic coupling.<sup>[121]</sup> The fanned out signal in the reduced magnetization plot (figure A.12) is indicative for a significant molecular anisotropy. Therefore, **C12** was probed for the presence of slow relaxation of magnetization. The ac susceptibility measurement was carried out applying a 3 Oe alternating magnetic field at frequencies between 1 Hz and 1400 Hz. Neither at zero field nor with an applied dc field of 200 Oe any *out-of-phase* signal was detected.

The change from picolyl to a 2-hydroxybenzyl side arm yields a trivalent ligand (**L5**) instead. This enables the coordination of Mn(III) ions without increasing the charge of a possible 12-MC-4 structure too much. However, the inorganic synthesis was stopped after a few attempts, knowing about the instability or reactivity of the attached side arms. If the cyclization mechanism depends on the C-H acidity of the methylene bridge, the attached pyridine ring promotes the reaction even more than the electron rich 2-hydroxyphenyl ring does. Due to this fact and knowledge about the coordination affinity of a nitrogen donor atom in *ortho*-position to manganese(III), ligand **L5** was not further investigated. In earlier studies<sup>[108]</sup> it was shown that the introduction of a side arm using the hydroxy group for synthesizing the corresponding ether did not yield a ligand suitable for MC structures. Hence, it is necessary to maintain the hydroxy group and attach the coordinating arm to any other functionality of the ligand. Amidoximes offer these possibilities and will be described in detail in the following chapter.

### 3.3. Amidoximes - Turning point of this study!?

A second way to introduce coordinating side arms to MC ligands is described in this section. As a result from previous work the new aim is to create ligands that provide the appropriate geometrical prerequisites based on a coordinating functionality like a hydroxamic acid with an aromatic backbone and a hydroxy group in *ortho*-position. Crucial requirements for the ligand to form a 12-MC-4 structure have been described in the introductory part of this thesis. Maintaining the hydroxy functionality, another way to introduce additional coordinating moieties in the ligand system is to change the main NO-group carrying motif from hydroxamic acids to amidoximes. Ligands **L7**, **L8**, **L9**, **L10** and **L11** represent salicylamidoxime derivatives, whereas ligand **L6** is based on a pyridine backbone. Their generalized synthesis is presented in scheme 3.5. All amidoximes were synthesized via a two or three step reaction procedure starting with the corresponding oxime precursors **P1a** and **P2a**. They react within a chlorination reaction with N-chlorosuccinimide (NCS) and pyridine in chloroform to form **P1** and **P2**, respectively. These precursors were then used in a substitution reaction with primary (**L6a**, **L7a** and **L8a**) and secondary (**L9a**, **L10a** and **L11a**) amines under basic conditions (triethylamine) in either DMF or THF. The synthesis of **L10** was carried out in both solvents with similar yields. Due to the toxicity of DMF and difficulties in working up reactions with DMF, THF should be chosen as solvent for further syntheses of amidoximes. Furthermore, the generated triethylammonium chloride precipitates in THF and could easily be separated from the reaction mixture. The selected secondary amines were synthesized reacting 2-picolylamine with 2-pyridinecarboxaldehyde or salicylaldehyde in a Schiff base reaction and subsequent reduction with sodium borohydride to yield **L9a** or **L10a**, respectively. The symmetrically substituted 2,2'-dihydroxydibenzylamine was also synthesized with good yields (see figure 5.1.15). However, the final amidoxime synthesis with this amine was not successful. The introduction of nucleophilic hydroxy groups increases the amount of side reactions, as it was described recently by Bittner.<sup>[126]</sup> Protection of the hydroxy groups was tried with a benzyl protection group, but the reaction with benzylbromide left one hydroxy group unprotected while the secondary amine was benzylated. Therefore, no further effort has been made to isolate the final amidoxime ligand. To show the broad variety of possible amines, which could be introduced in the ligand system, **L11** was synthesized according to the literature.<sup>[70]</sup>



| Ligand     | X   | Y   | R <sup>1</sup>  | R <sup>2</sup>   |
|------------|-----|-----|---|--|
| <b>L7</b>  | COH | /   | H   |  |
| <b>L8</b>  | COH | /   | H   |  |
| <b>L6</b>  | N   | /   | H   |  |
| <b>L9</b>  | COH | N   |  |  |
| <b>L10</b> | COH | COH |  |  |
| <b>L11</b> | COH | /   |  |  |

Scheme 3.5: Generalized synthesis of amidoximes from precursors **P1a** and **P2a** yielding **L6**, **L7**, **L8**, **L9**, **L10** and **L11**.



### 3.3.1. Coordination compounds with salicylamidoxime derivatives

As previously summarized in the introductory part of this thesis, amidoximes are known in the research field of MCs. **L11**, salicylamidoxime and the methylated derivative are able to form 9-MC-3 structures with Mn(III) ions.<sup>[70,127–129]</sup> However, **L7**, **L8**, **L9** and **L10** have never been published before. Although **L9** and **L11** represent divalent ligands, it is worth exploring them, in order to gain insights into their coordination behavior. The reaction of **L7** and **L11** with transition metal salts did not afford any coordination compound within the scope of this dissertation. Therefore, binding modes and structural peculiarities of 3d transition metal ion complexes with **L9** and **L10** will be elucidated in this section.

First knowledge about geometrical orientation of the ligand was collected by crystallizing and solving the crystal structure of **L9** itself. Single crystal X-ray diffraction data were solved in the orthorhombic space group  $P2_12_12_1$  with four molecules per unit cell. The molecular structure of **L9** is presented in figure 3.31. The protonated ligand is twisted with

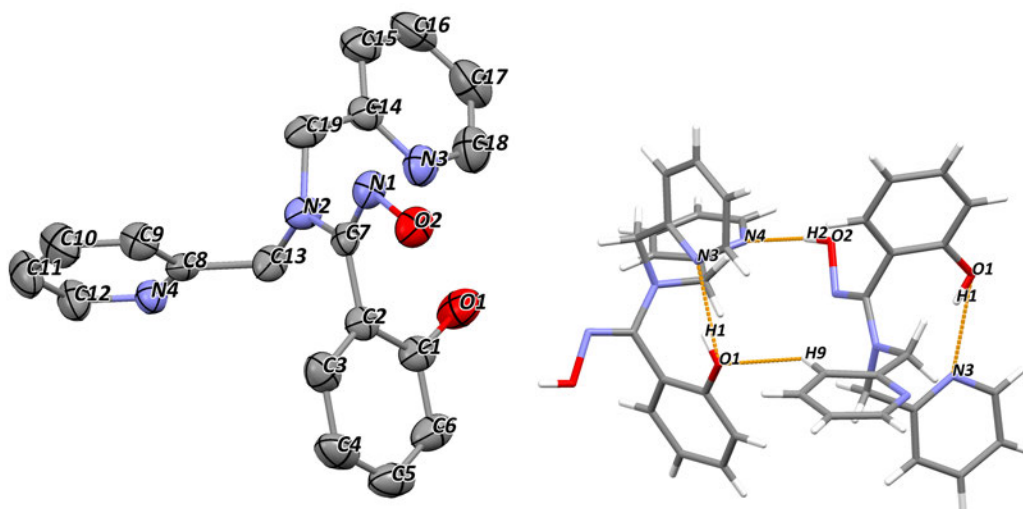


Figure 3.31.: Molecular structure of **L9** (left) and possible inter- and intramolecular hydrogen bonding (right). Color code: Red - oxygen, blue - nitrogen, gray - carbon. ORTEP representation with atomic displacement parameters at 50% level of probability (left).

regards to the necessary orientation to form a 12-MC-4 structure. This is due to inter- and intramolecular hydrogen bonds (figure 3.31 right) as well as steric and electronic repulsion

of the respective groups. The hydroxamato oxygen atom O2 is in trans conformation with respect to N2, building the O2H2-N4 bond to a pyridine nitrogen atom of the neighboring molecule. The intramolecular H-bond O1H1-N3 causes the phenoxy ring to rotate along the C2-C7 bond. Therefore, the hydroxy oxygen atom in *ortho*-position is hindered to form a planar six-membered ring with N2, which would be obligatory for a MC formation. The pyridine side arms are also hindered to occupy the axial positions of a fictive octahedron. However, a parallel orientation of both pyridine rings with the nitrogen atoms pointing towards each other, would have been very unlikely due to Coulomb repulsion of the lone pairs. Further discussion of this crystal structure in terms of complex geometries would exceed the amount of information, which can be gathered, as the fully or at least partially deprotonated ligand will be involved in the complex synthesis.

The reaction of manganese(II) chloride and copper(II) perchlorate with triethylamine in methanol led to dark brown crystals of  $[\text{Cu}_6^{\text{II}}\text{Cl}_2(\text{L9})_2(\text{L9b})_2(\text{MeOH})_2](\text{ClO}_4)_2$  (**C13**). **C13** crystallizes in the monoclinic space group  $P2_1/a$  with two molecules per unit cell. The molecular structure is shown in figure 3.32. Each molecule represents a copper(II) hexamer formed by two structurally similar trinuclear subunits. The three crystallographically distinct metal ions are embedded in square pyramidal (Cu1, Cu3) and an elongated octahedral (Cu2) coordination environments. An overall neutral charge is ensured by two coordinating chloride ions, two non-coordinating perchlorate ions and four ligands with a charge of -2 each (2**L9**, 2**L9b**).

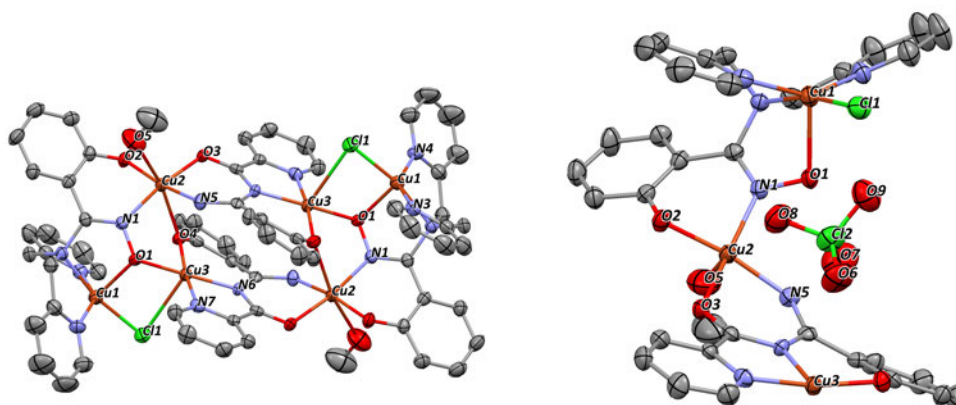


Figure 3.32.: Molecular structure of **C13** (left) and asymmetric unit of the Cu(II) hexamer (right). Color code: Orange - Cu(II), red - oxygen, blue - nitrogen, gray - carbon. ORTEP representation with atomic displacement parameters at 50% level of probability. Hydrogen atoms have been omitted for clarity.

**L9b** is generated in-situ. Purity of **L9** has been tested by ESI-MS and NMR prior to complex syntheses and did not indicate the presence of **L9b**. The molecular rearrangement of **L9** is shown in scheme 3.6. The oxidation reaction on one of the methylene bridges is accompanied by a reduction of the oxime nitrogen. The mechanism of this side reaction has not been solved yet. Nevertheless, if this is an intramolecular reaction and no additional reagent like atmospheric oxygen is involved, the second side product must be  $\alpha$ -picoline. N-benzoyl-salicylamidine (**L9b**) is stabilized via tautomerism as it is known from similar functional groups.<sup>[130]</sup> However, the doubly deprotonated ligand functions as bridging unit between both copper trimers in **C13**. **L9b** represents a pentadentate ligand offering two coordination pockets, as it is shown in figure 3.33. Not only that this ligand connects both subunits with each other, but it also forms a phenoxo bridge between Cu2 and Cu3 within one trinuclear unit. The Cu2-O4-Cu3 angle amounts  $97.23(13)^\circ$  and causes a bending of the main ligand, hindering a perpendicular orientation of the salicyl ring plane towards the pyridine ring planes (figure 3.33 right).

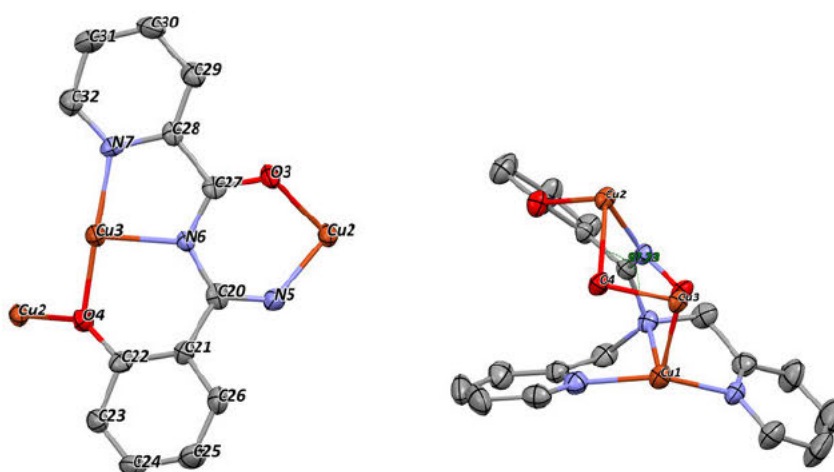
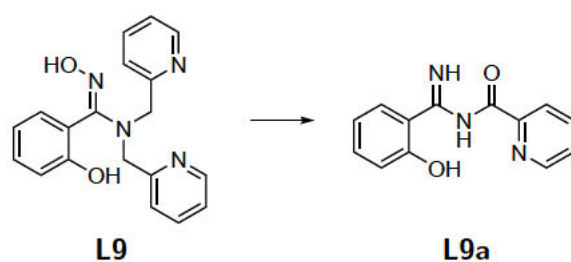


Figure 3.33.: Coordination of the bridging pentadentate amidine **L9b** (left) and the main amidoxime ligand **L9** (right). Color code: Orange - Cu(II), red - oxygen, blue - nitrogen, gray - carbon. ORTEP representation with atomic displacement parameters at 50 % level of probability. Hydrogen atoms have been omitted for clarity.



Scheme 3.6: Schematic representation of the in-situ side reaction of **L9** yielding the bridging ligand **L9b**.

Although the conformation of **L9** in **C13** promises, that the synthesized amidoximes could in principle form 12-MC-4 structures, this approach also shows, that most probably due to the higher charge to be equalized, Mn(III) ions are not involved in the crystal structure. Therefore, further coordination chemistry was focused on **L10**.

The reaction of **L10** with copper(II) perchlorate, tetrabutylammonium perchlorate (TBAP) and triethylamine in DMF yields another copper hexamer  $[\text{Cu}_6^{\text{II}}(\text{L10b})_4(\text{ClO}_4)_2(\text{DMF})_6](\text{ClO}_4)_2$  (**C14**). Remarkably, this molecular structure does not contain any **L10**, but four of the already introduced N-benzoyl-salicylamidine ligands (**L9b**) instead. To avoid confusion,

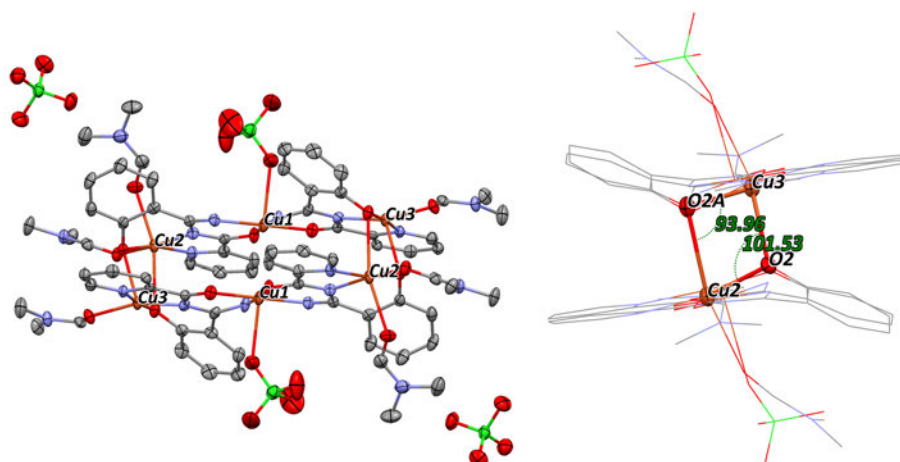


Figure 3.34.: Molecular structure of **C14** (left) and the side view of the hexamer (right). Color code: Orange - Cu(II), red - oxygen, blue - nitrogen, gray - carbon. ORTEP representation with atomic displacement parameters at 50 % level of probability. Hydrogen atoms have been omitted for clarity.

ligand **L9b** will be called **L10b** as it originates from **L10**. Compound **C14** crystallizes in the triclinic space group  $P\bar{1}$  with one complex per unit cell. In comparison to **C13**, two non-coordinating perchlorate anions are still present in the crystal lattice, whereas the chloride ions are substituted by two end-on coordinating perchlorate ions (figure 3.34). Six additional DMF molecules occupy coordination sites, which again yields two square pyramidal (Cu1, Cu3) and one elongated octahedral (Cu2) coordination environment. The trinuclear subunits form a linear chain and there are no bridging ligands between Cu2 and Cu3 (within one subunit), as it was observed for **C13**. However, the trimers are coordinately bonded to each other via phenoxo bridges. Cu-O-Cu bond angles are  $93.69^\circ$  (Cu2-O2A-Cu3') and  $101.56(14)^\circ$  (Cu2-O2-Cu3'). The Cu-Cu distance within one subunit amounts  $5.255 \text{ \AA}$  and  $5.241 \text{ \AA}$  for Cu1-Cu3 and Cu1-Cu2, respectively. The stack distance of these trimers is significantly shorter, measuring a Cu1-Cu1' displacement of  $3.275 \text{ \AA}$  and  $3.251 \text{ \AA}$  for Cu2-Cu3'. The imine groups of each ligand occupy apical coordination sites of the central Cu1 coordination polyhedron in cis position. This orientation of the ligand is favored by hydrogen bonding to one DMF molecule (N3H3N-O1S and N3AH3NA-O1S, see figure A.13).

The  $\chi_M T$  value of **C14** is steadily decreasing from  $2.41 \text{ cm}^3 \text{Kmol}^{-1}$  to  $1.08 \text{ cm}^3 \text{Kmol}^{-1}$  with a very small slope in the temperature region between 300 K and 30 K. Below 30 K the curve drops faster. This behavior suggests the presence of antiferromagnetic coupling. If overall

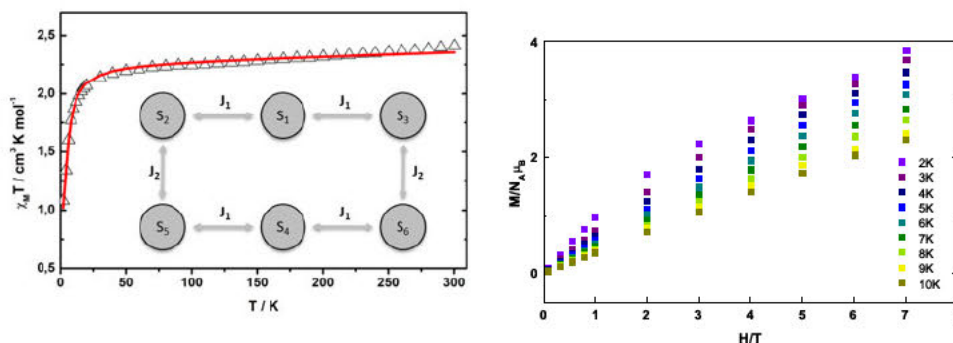


Figure 3.35.: Temperature (left) and field-dependent (right) magnetic behavior of C14. Coupling scheme for a 2J model (inset) yielding the best fit for the susceptibility data (red line).

afm coupling is dominating in a cluster with an even number of spin centers the expected spin ground state would be  $S = 0$ . However, the  $\chi_M T$  value at 2 K fits well to a spin only value for  $S = 1$  ( $1 \text{ cm}^3 \text{ K mol}^{-1}$ ). Unfortunately, this observation cannot be supported by evaluating the magnetization vs. field plot. Even at fields of 7 T saturation is not reached, as it is shown in figure 3.35. The small and steady slope up to high temperatures in the  $\chi_M T$  plot is indicative for a temperature-independent paramagnetism. TIP is included with a fixed value of  $60 \times 10^{-6} \text{ cm}^3 \text{ K mol}^{-1}$  per Cu(II) ion as it is done for copper MC structures in the literature.<sup>[81,123]</sup> Fitting of the magnetic data of C14 was done using a 2J model, covering the exchange coupling between the central Cu1 ion and the outer Cu2 and Cu3 ions ( $J_1$ ) and an additional exchange between both trimeric units  $J_2$  (Cu2-Cu3) according to the exchange Hamiltonian in equation 3.9 and the coupling scheme in figure 3.35.

$$\hat{H}_{ex} = -2J_1(\hat{S}_1\hat{S}_2 + \hat{S}_1\hat{S}_3 + \hat{S}_4\hat{S}_5 + \hat{S}_4\hat{S}_6) - 2J_2(\hat{S}_2\hat{S}_5 + \hat{S}_3\hat{S}_6) \quad (3.9)$$

The first fitting attempt yielded the values  $J_1 = -2.19(4) \text{ cm}^{-1}$ ,  $J_2 = 1.54(14) \text{ cm}^{-1}$  and  $g_{Cu} = 2.003(2)$ . The exchange coupling parameters are unaffected by the addition of a paramagnetic impurity to the fit routine, whereas the g-factor is only physically reasonable if an impurity of ten percent ( $S = \frac{1}{2}$ ) is included in the fitting procedure. Including this impurity, the best fit yielded  $J_1 = -2.22(4) \text{ cm}^{-1}$ ,  $J_2 = 1.45(15) \text{ cm}^{-1}$  and  $g_{Cu} = 2.098(2)$  ( $R = 2.01 \times 10^{-2}$ ) and is represented as the solid line in the  $\chi_M T$  plot (figure 3.35). Fitting of the magnetization and susceptibility data simultaneously did not change the values. Ruiz et al.<sup>[131]</sup> investigated hydroxo- and alkoxo-bridged copper dimers and concluded that ferromagnetic exchange between two bridged Cu(II) centers is expected for

Cu-O-Cu bond angles smaller than  $98^\circ$ . This observation is well represented by the fit results for **C14** ( $J_2$ ). However, what has to be considered is that the bridging oxygen atom coordinates on Cu2 in apical position whereas on Cu3 it occupies the axial coordination site of the square pyramidal environment. Therefore, the magnetic orbital  $d_{x^2-y^2}$  of Cu3 is barely involved in this interaction leading to only weak exchange coupling regardless of its nature.<sup>[123]</sup>

Looking at the results of both approaches, which led to Cu(II) hexamers with ligand **L9b/L10b** regardless of the use of  $\text{MnCl}_2$  as a reagent, it is obvious, that manganese(II) ions do not affect the side reaction. Moreover, the C-H acidity of the methylene unit seems to be the crucial parameter of the reaction mechanism. As pyridine is an electron-poor ring system, while phenol represents an electron-rich aromatic compound, the picolyl side arm is oxidized. This suggests a direct influence of the used base. A more detailed insight into the mechanism needs further investigation, which is not the purpose of this thesis. However, a change of the solvent often leads to tremendous difference concerning the outcome of a reaction.

Dissolving **L10**, Mn(II) perchlorate and Cu(II) chloride under the same basic conditions (triethylamine) in acetonitrile instead of DMF or methanol leads to a copper dimer, which does not contain N-benzoyl-salicylamidine (**L9b**).  $\text{Cu}_2^{\text{II}}(\text{L10cH})_2\text{Cl}_2$  (**C15**) crystallizes in the monoclinic space group C2/c with two dimers per unit cell. The reaction was carried out at  $87^\circ\text{C}$ . Another in-situ rearrangement of the main ligand **L10** yielding **L10c** is observed. Neither the reduction of the oxime nitrogen nor a full oxidation of the methylene bridge occurs to form **L10c**. The two electron oxidation reaction of the picolyl methylene group yields the cyclization product shown in scheme 3.7. In addition, a rearrangement takes place, transferring the phenolic side arm from the tertiary amine nitrogen to the oxime nitrogen atom. A pericyclic reaction like a thermally activated [1,3] sigmatropic shift<sup>[132]</sup> would possibly explain this rearrangement. However, a detailed examination of the reaction mechanism is not of further interest to this work. The molecular structure of this Cu(II) dimer is shown in figure 3.36. The asymmetric unit of this complex consists of one copper ion, one chloride ion and one ligand. The intramolecular Cu-Cu distance amounts  $3.622 \text{ \AA}$  with a Cu1-Cl1-Cu1' binding angle of  $93.19(3)^\circ$ . It should be mentioned, that although three equivalents of triethylamine were used in this reaction, **L10c** remains partially protonated, enabling to form hydrogen bonding (O2H2-O1), shown in figure 3.36.

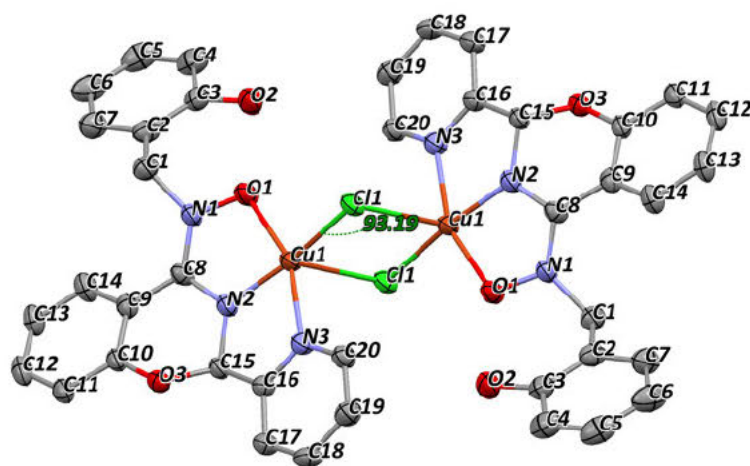
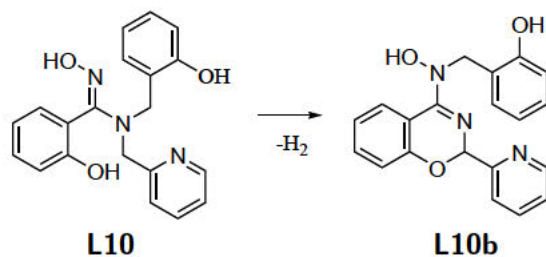


Figure 3.36.: Molecular structure of C15. Color code: Orange - Cu(II), red - oxygen, blue - nitrogen, gray - carbon. ORTEP representation with atomic displacement parameters at 50% level of probability. Hydrogen atoms have been omitted for clarity.



Scheme 3.7: Schematic representation of the in-situ side reaction of L10 yielding the ligand L10c.

Another change in the solvent and the use of a different transition metal ion lead to reaction conditions which are suitable to maintain the phenolic side arm. The reaction of cobalt(II) perchlorate, TBAP with L10 in the presence of triethylamine in acetone yields the formation of  $\text{Co}_2^{\text{II}}(\text{L10d})_2$  (C16). C16 crystallizes in the triclinic space group  $P\bar{1}$  with two dimers per unit cell. Both dimers are crystallographically independent, whereas the cobalt ions of one dimer are indistinguishable due to a center of inversion (see figure 3.37). Both metal ions are embedded in a nearly perfect trigonal bipyramidal coordination environ-



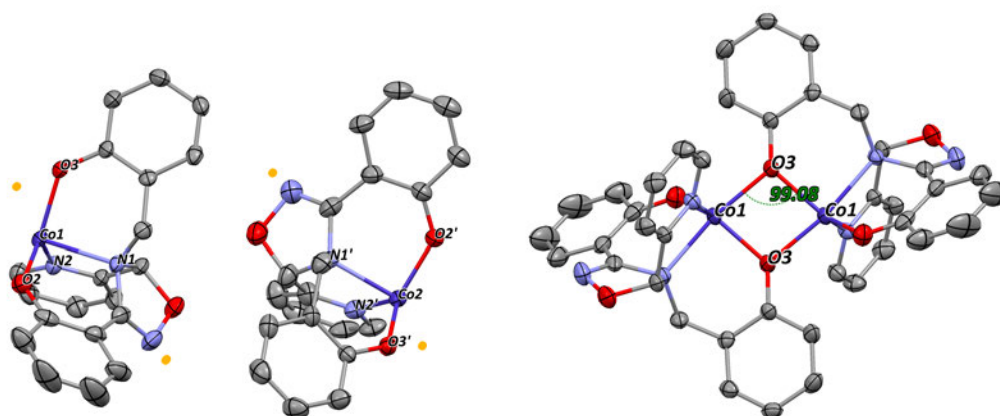


Figure 3.37.: Asymmetric unit of the crystal structure of **C16** (left) and molecular structure of one dimer (right). Color code: Dark blue - Co(II), red - oxygen, blue - nitrogen, gray - carbon, orange - center of inversion. ORTEP representation with atomic displacement parameters at 50 % level of probability. Hydrogen atoms have been omitted for clarity.

ment ( $\text{CShM}(\text{Co1})=0.81994$  and  $\text{CShM}(\text{Co2})=0.79740$ ). Ligand **L10d** offers a tetradentate pocket with the oxygen atom of the phenolic side arm (O3, O3') bridging between Co1 or Co2. The dimer metal distances and the Co-O-Co bond angles are 3.074 Å or 3.084 Å and 99.07(10)° or 98.84(10)° for Co1 or Co2, respectively. The crystallographic center of inversion between the cobalt ions of one dimer forces the ligands to exhibit a staggered conformation (see figure A.14). The side reaction which has taken place to form **L10d** is again an oxidation of the methylene unit of the picolyl side arm. Unlike the reaction yielding **L10b**, it is an intramolecular oxidation, as the former hydroxy group of the oxime moiety reacts with the methylene bridge to form the cyclization product (see figure 3.8). The carbon atom of the picolyl methylene unit represents a diastereotopic center resulting in a new stereocenter of the product. However, as the crystal structure is symmetrical towards an inversion both diastereoisomers are present. Very similar cobalt(II) dimers have been described by Mukherjee et al.<sup>[133]</sup>

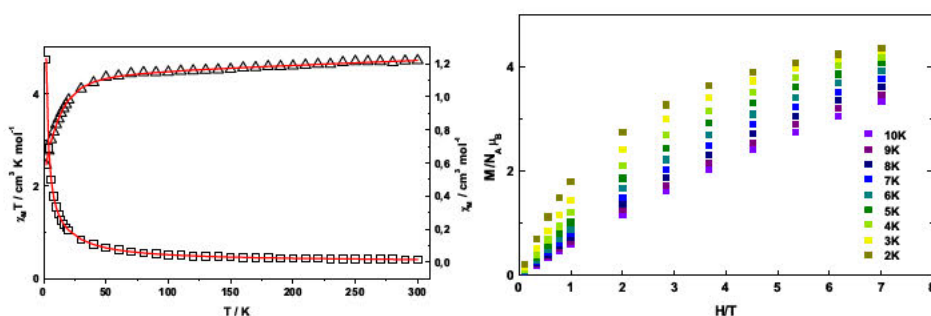
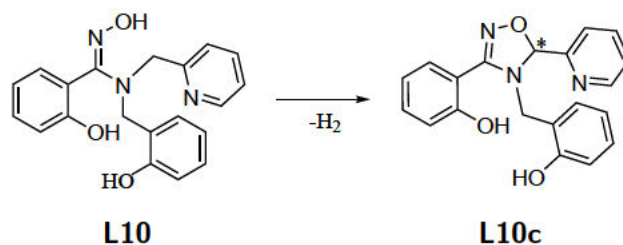


Figure 3.38.: Temperature and field-dependent magnetic behavior of **C16**.  $\chi_M$  (open squares) and  $\chi_M T$  (open triangles) vs.  $T$  plots and the best fit (solid red line) (left). Low temperature magnetization plot of **C16** (right).



Scheme 3.8: Schematic representation of the in-situ side reaction of **L10** yielding the ligand **L10d**. The resulting new stereocenter is marked with \*.

The  $\chi_M T$  product of compound **C16** is plotted against the temperature in figure 3.38 showing steadily decreasing values from  $4.71 \text{ cm}^3 \text{ K mol}^{-1}$  at 300 K to  $4.35 \text{ cm}^3 \text{ K mol}^{-1}$  at 50 K followed by a steeper drop reaching a value of  $2.45 \text{ cm}^3 \text{ K mol}^{-1}$  at 2 K. This behavior suggests a rather weak intramolecular antiferromagnetic exchange coupling and the presence of a TIP. Due to the structural accordance of **C16** with the Co(II) dimers published by Mukherjee et al.<sup>[133]</sup> a similar spin Hamiltonian (equation 3.10) was used accounting for  $g_{Co}$ , the coupling constant  $J$  and the zero-field splitting parameter  $D$ . To avoid over-parameterization the isotropic  $g$ -factor and the  $D$  parameter were estimated to be identical for all metal ions. Although the dimers in compound **C16** slightly deviate in bond angles and distances, this was neglected to simplify the calculations.

$$\hat{H} = -2J\hat{S}_1\hat{S}_2 + D(\hat{S}_{z1}^2 + \hat{S}_{z2}^2) + \mu_B \sum_{i=1}^2 \vec{\hat{S}}_i \cdot \vec{g}_i \cdot \vec{B} \quad (3.10)$$

The resulting fit values  $J = -0.081(3) \text{ cm}^{-1}$ ,  $D = 15.8(1) \text{ cm}^{-1}$  and  $g_{Co} = 2.168$  with  $TIP = 1034(22) \text{ cm}^3 \text{ mol}^{-1}$  and  $R = 1.64 * 10^{-2}$  are in very good agreement with the findings of Mukherjee et al.<sup>[133]</sup> The high TIP value is a result of intense spin-orbit coupling

(present in **C16**) compared to the weak exchange coupling.<sup>[134]</sup> It should be mentioned, that quite similar fit results can be obtained with a negative zero-field splitting parameter  $D = -16.6(1) \text{ cm}^{-1}$  (with  $J = -0.042(1) \text{ cm}^{-1}$ ,  $g_{Co} = 2.164$ ,  $TIP = 1086(21) \text{ cm}^3 \text{ mol}^{-1}$  and  $R = 1.10 \times 10^{-2}$ ). Electron paramagnetic resonance studies could be used to identify the right sign of  $D$ . However, as no *out-of-phase* signal of the ac susceptibility could be observed, a positive sign of  $D$  is likely. Another tool, that has been used for a better comparison of Co(II)<sup>[133]</sup> and Cu(II)<sup>[135]</sup> dimers exhibiting fivefold coordination environments, is the distortion parameter  $\tau$ .  $\tau$  equals zero for an ideal square-pyramidal coordination of the metal ion and reaches the value 1 for ideal trigonal-bipyramidal geometry. The cobalt(II) dimers in **C16** reach a value of  $\tau = 0.79 - 0.80$ , which leads to a higher overlap of the  $d_{z^2}$  orbital of the metal ions with the ligand orbitals involved in bridging of the Co(II) centers. Mukherjee et al.<sup>[133]</sup> suggest that  $\tau$  correlates with the exchange coupling in a manner that an increasing  $\tau$  value leads to lowering of the afm exchange coupling. Exactly this behavior is supported by the observations of **C16** compared to their compounds ( $\tau = 0.76$ ,  $J = -1.84(1) \text{ cm}^{-1}$  and  $\tau = 0.63/0.49$ ,  $J = -5.70(3) \text{ cm}^{-1}$ ). A spin ground state of  $S = 0$  with low lying excited states, which would result from such a small exchange coupling, is supported by the field dependency of the magnetization of **C16**, depicted in figure 3.38. The M vs H plot shows that saturation is not reached and that anisotropy must be present, most probably upon mixing of the ground state with higher excited states.

In-situ side reactions of **L10** were observed for copper(II) trials in acetonitrile or DMF and cobalt(II) attempts in acetone. However, the combination of nickel(II) perchlorate, TBAP and **L10** in methanol under the same basic conditions (three equivalents of triethylamine) leads to the formation of a nickel hexamer, in which **L10** proves full constitutional integrity.  $[\text{Ni}_6^{\text{II}}(\text{L10})_2(\text{L10H})_2(\mu - \text{O}_2\text{COMe})_2(\text{MeOH})_6]$  (**C17**) crystallizes in the monoclinic space group P 21/c with two hexamers per unit cell. The asymmetric unit contains three nickel ions, one fully deprotonated **L10**, one **L10** molecule with protonated oxime moiety, one in-situ generated monomethyl carbonate ion and three coordinating methanol molecules. The hexamer can be divided in two trinuclear subunits, which are phenoxo bridged (N1-O1-N1' angle =  $96.93(12)^\circ$ ). The fully deprotonated **L10** is a hexadentate ligand, forming a tetradentate pocket around Ni3, in which both side arms coordinate *cis* to each other. Besides the mentioned connection between both trimers, all nickel ions are bridged to another, as it is shown in figure 3.39. While Ni2 and Ni3 are only bridged via the  $\mu_2 - O$  hydroxamato oxygen atom (Ni2-O2-Ni3 angle =  $132.57(15)^\circ$ ), Ni2 is connected to Ni1 along a phenoxo bridge (Ni2-O4-Ni1 angle =  $110.75(13)^\circ$ ), the oxime (Ni1-N1O2-

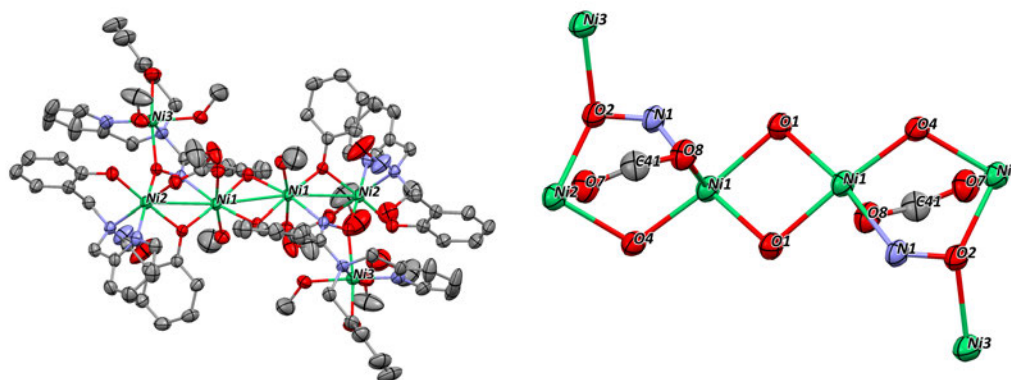


Figure 3.39.: Molecular structure of **C17** (left) and hexanuclear core with all bridging atoms (right). Color code: Green - Ni(II), red - oxygen, blue - nitrogen, gray - carbon. ORTEP representation with atomic displacement parameters at 50 % level of probability. Hydrogen atoms have been omitted for clarity.

Ni2) unit and the carboxylate ion (Ni1-O8C41O7-Ni2). One peculiarity of this structure is the protonated main ligand. Three equivalents of triethylamine must partially react in a side reaction. One explanation for that could be the  $CO_2$  fixation reaction. According to the literature, deprotonated methoxo ligands react in a nucleophilic attack with carbon dioxide to form monomethyl carbonate.<sup>[136]</sup> However, it is still unclear and unexpected why the hydroxamato oxygen remains protonated while the other two hydroxy moieties are deprotonated, as the oxime group represents the most acidic functionality of this molecule.  $CO_2$  fixation is known for transition metal complexes, especially binuclear compounds were studied.<sup>[136–139]</sup> A bridged precursor complex is often presented as a crucial step of the reaction mechanism, which is followed by a  $CO_2$  insertion reaction.<sup>[140]</sup> **L10** seems to build a suitable coordination environment around two neighboring nickel ions, allowing the carbonates to form.

The  $\chi_M T$  vs. T plot of **C17** is depicted in figure 3.40 and reveals overall antiferromagnetic exchange coupling between the nickel centers. The room temperature value of  $6.17 \text{ cm}^3 \text{ K mol}^{-1}$  is slightly higher than the spin only value for six spin centers with  $S = 1$  ( $6 \text{ cm}^3 \text{ K mol}^{-1}$ ) but fits perfectly to the expected value for a  $Ni_6$  cluster with  $g_{Ni} > g_e = 2.00$ . All nickel(II) ions are expected to contribute with a spin moment of  $S = 1$  according to their octahedral coordination environments. Upon cooling the  $\chi_M T$  product steadily decreases to  $0.14 \text{ cm}^3 \text{ K mol}^{-1}$  at 2 K indicating a  $S = 0$  spin ground state

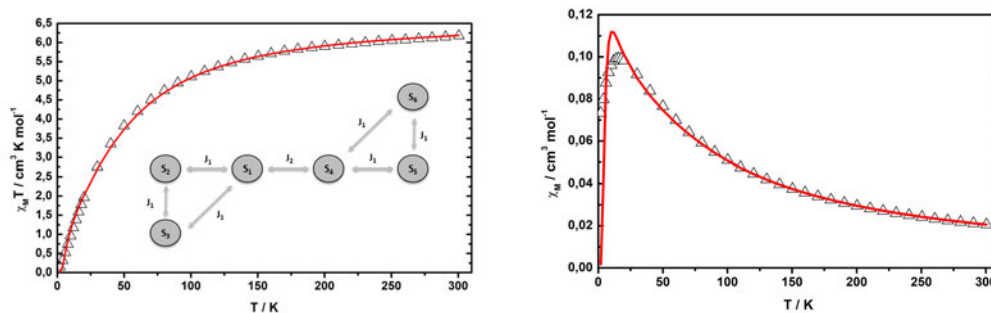


Figure 3.40.: Temperature-dependent magnetic behavior of **C17** in the form of a  $\chi_M T$  vs.  $T$  plot (left) and a  $\chi_M$  vs.  $T$  plot (right). A possible coupling scheme including two different  $J$  parameters to estimate the exchange coupling of **C17** is proposed (inset). Solid red lines represent the best fit with  $J_1 = -8.98(10) \text{ cm}^{-1}$ ,  $J_2 = 24(1) \text{ cm}^{-1}$ ,  $g_{Ni} = 2.106(3)$  and  $R = 1.93 * 10^{-1}$ .

of the system. Fitting of the magnetic susceptibility of **C17** was done taking into account different coupling paths within the nickel hexamer. A  $2J$  (figure 3.40) and a  $3J$  model (figure 3.41) were compared to yield the best fit. To avoid over-parametrization a model with two different coupling constants was chosen first. Using the Hamiltonian  $\hat{H}(2J)$  presented in equation 3.11 yielded the values  $J_1 = 24(1) \text{ cm}^{-1}$ ,  $J_2 = -8.98(10) \text{ cm}^{-1}$ ,  $g_{Ni} = 2.106(3)$  and  $R = 1.93 * 10^{-1}$ . These results correspond very well to findings of Pavlishchuk et al.<sup>[89]</sup> on magnetic properties of oximate-bridged Ni(II) tetramers. Similar Ni-O-Ni bond angles ( $\approx 97^\circ$ ) are observed in their nickel clusters resulting in small ferromagnetic exchange coupling. Nanda et al.<sup>[141]</sup> concluded that the cross-over angle for phenoxy-bridged dinuclear nickel(II) complexes indicating the point where the Ni-Ni exchange can be neglected ( $J = 0$ ) is at  $97^\circ$ . However, the  $\chi_M$  vs  $T$  plot (figure 3.40) reveals rather low agreement of the  $2J$  fit with the magnetic data of **C17** at low temperatures. Therefore, an additional coupling was taken into account. The coupling scheme for a  $3J$  model and the best fit are depicted in figure 3.41. The three exchange parameters were implemented according to the exchange coupling Hamiltonian  $\hat{H}_{ex}(3J)$  in equation 3.12 yielding  $J_1 = -4.28(76) \text{ cm}^{-1}$ ,  $J_2 = -8.23(17) \text{ cm}^{-1}$ ,  $J_3 = -7.05(29) \text{ cm}^{-1}$ ,  $g_{Ni} = 2.155(4)$  and  $R = 2.86 * 10^{-1}$ . Not only, that the fit ends with an improbable set of three antiferromagnetic exchange coupling

parameters but it also does not reach a higher agreement with the data, in particular at the low temperature region (see figure 3.41).

$$\hat{H}(2J) = -2J_1(\hat{S}_1\hat{S}_4) - 2J_2(\hat{S}_1\hat{S}_2 + \hat{S}_1\hat{S}_3 + \hat{S}_2\hat{S}_3 + \hat{S}_4\hat{S}_5 + \hat{S}_4\hat{S}_6 + \hat{S}_5\hat{S}_6) + \mu_B \sum_{i=1}^N \vec{S}_i \cdot \vec{g}_i \cdot \vec{B} \quad (3.11)$$

$$\hat{H}_{ex}(3J) = -2J_1(\hat{S}_1\hat{S}_4) - 2J_2(\hat{S}_1\hat{S}_2 + \hat{S}_2\hat{S}_3 + \hat{S}_4\hat{S}_5 + \hat{S}_5\hat{S}_6) - 2J_3(\hat{S}_1\hat{S}_3 + \hat{S}_4\hat{S}_6) \quad (3.12)$$

$$\hat{H}_{ex}(4J) = -2J_1(\hat{S}_3\hat{S}_4) - 2J_2(\hat{S}_3\hat{S}_2 + \hat{S}_5\hat{S}_6) - 2J_3(\hat{S}_1\hat{S}_2 + \hat{S}_4\hat{S}_5) - 2J_4(\hat{S}_1\hat{S}_3 + \hat{S}_4\hat{S}_6) \quad (3.13)$$

Regarding each Ni-Ni exchange coupling separately leads to a  $4J$  model using the exchange Hamiltonian  $\hat{H}_{ex}(4J)$  (equation 3.13) and the fit values  $J_1 = -4.74(7) \text{ cm}^{-1}$ ,  $J_2 = -10.69(7) \text{ cm}^{-1}$ ,  $J_3 = -6.04(10) \text{ cm}^{-1}$ ,  $J_4 = -1.80(12) \text{ cm}^{-1}$ ,  $g_{Ni} = 2.123(1)$  and  $R = 1.83 * 10^{-2}$  presented in figure 3.41. Only with four different exchange coupling parameters a sufficient modeling of the low temperature region is possible. However, fitting of just one data set with too many free variables lacks the ability of a significant physical interpretation. Additionally, only low temperature data occurred to be fitted difficultly, the  $2J$  model already was sufficient for the higher temperature data. Instead of fitting more possible coupling paths, the introduction of a crystal field potential in order to estimate the zero-field splitting parameter could be successful. This approach acquires the support of more magnetic data, in particular the magnetization vs. field plot of C17, which has not been measured yet.

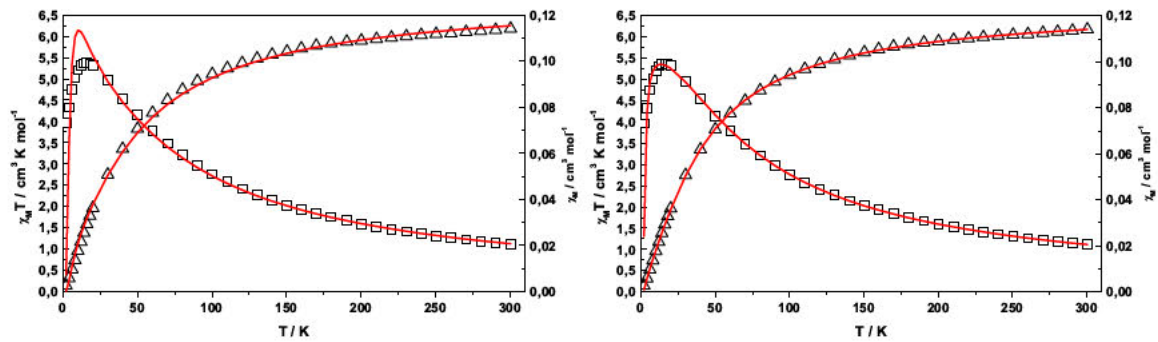


Figure 3.41.: Temperature-dependent magnetic behavior of C17 in the form of a  $\chi_M T$  vs. T plot and  $\chi$  vs. T plot. Solid red line represents the best fitting for a 3J (left) and a 4J exchange coupling model (right).

Reacting **L9** or **L10** with cobalt(II), copper(II) or nickel(II) ions yielded five different coordination compounds, which have been elucidated in this section. Four of these crystal structures revealed major difficulties to form a 12-MC-4 structure from these ligands, as different products from in-situ side reactions were identified. The methylene unit of the picolyl side arm seems to be very reactive, leading to a lack of constitutional integrity in the ligand system. However, crystallization of a nickel(II) hexamer (**C17**) demonstrated, that ligand **L10** can maintain its chemical constitution in complex molecules. The coordination ability of these ligands towards trivalent transition metal ions is still under investigation. First attempts with manganese salts did not lead to any crystalline product yet.

## 4. Summary and Outlook

Two new approaches to engineer a heterometallic 12-MC-4 forming ligand system were presented in this work. Systematic synthesis of heterometallic molecules requires varying selectivity of the coordination pockets of a ligand. This strategy has been followed using the compound class of metallacrowns. The combination of the *magnetic director approach* with the alignment of high single ion anisotropy is suitable to reach a well performing *single molecule magnet* with high spin ground state and high magnetoanisotropy.

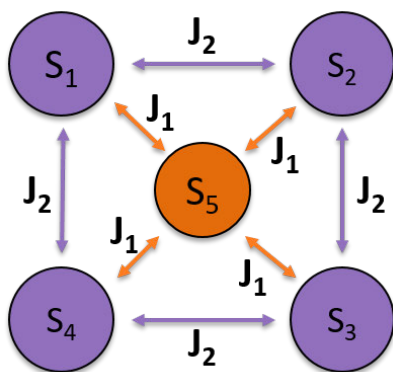


Figure 4.1.: Star-like coupling scheme for a 12-MC-4.

The variation of the *ortho* hydroxy group in salicylhydroxamic acid (**L1**) allowed to synthesize anthranilhydroxamic acid (**L2**) and a new sulfur derivative, 2-methylmercaptobenzo-hydroxamic acid (**L3**). All three ligands were studied with regards to their binding affinity towards various ring forming metal ions. **L2** yielded the Cu(II) 12-MC-4 double decker complex  $\{\text{Cu}^{\text{II}}(\text{ClO}_4)(\text{MeOH})[\mathbf{12} - \text{MC}_{\text{Cu}(\text{II})\text{N}(\text{L2})} - 4]\}_2(\text{ClO}_4)_2 \cdot 2\text{MeOH}$  (**C7**) with the two MC planes shifted in relation to each other. Only one ring forming Cu(II) ion is coordinated in axial position by a hydroxamato oxygen atom of the second MC plane. Magnetic characterization of **C7** led to the expected spin ground state for  $\text{Cu}_5$  MCs of  $S = \frac{1}{2}$ . The ratio of the radial exchange coupling constant  $J_1$  to the tangential  $J_2$  according to a star-like coupling scheme (figure 4.1) is the crucial criterion to reach a well isolated high spin ground states in 12-MC-4 complexes. For **C7** it was determined to be  $J_1/J_2 = 1.74$ . The sulfur derivative **L3** was investigated to selectively bind softer transition metal ions in the MC ring, such as copper(II) or cadmium(II) ions. Indeed, three distinct Cu(II) MC complexes,



**C2**, **C3** and **C4**, were isolated.  $\{\text{Cu}^{\text{II}}\text{Cl}_2(\text{MeOH})[\mathbf{12} - \text{MC}_{\text{Cu(II)N(L3)} - 4}]_2 \cdot 4\text{MeOH}$  (**C2**) and  $\text{Cu}_2^{\text{II}}\text{Cl}(\text{mmba})(\text{MeOH})_2(\text{H}_2\text{O})[\mathbf{12} - \text{MC}_{\text{Cu(II)N(L3)} - 4}]_2(\text{ClO}_4)_2$  (**C3**) represent Cu(II) 12-MC-4 double decker structures with different co-ligands in axial position. However, the MC planes are less shifted towards each other compared to **C7** thus leading to an axial coordination of even the central Cu(II) by a hydroxamate oxygen atom of the second MC plane. Evaluation of the magnetic data of **C2** revealed smaller values for both exchange coupling constants and even a smaller ratio of  $J_1/J_2 = 1.3$  compared to **C7**. However, it was shown that the magnetic behavior of MC double decker complexes can be sufficiently described focusing on the intramolecular exchange interaction and taking intermolecular interactions only into account by a mean field approximation.

The third synthesized Cu(II) MC with **L3** structurally differs from **C2**, **C3** and **C7**.  $\text{Cu}^{\text{II}}(\mu_2 - \text{ClO}_4)(\text{MeOH})_2(\text{py})_4[\mathbf{12} - \text{MC}_{\text{Cu(II)N(L3)} - 4}]\text{ClO}_4$  (**C4**) crystallized as a single 12-MC-4 structure. The isolation of **C4** revealed an important influence of the used base. Triethylamine yielding **C2** and **C3** and sodium hydroxide yielding **C7** were substituted by pyridine to synthesize **C4**. The coordination ability of pyridine leads to a substitution of the sulfur donor atoms in apical position. A peculiarity of the synthesis of **C4** was the necessity of manganese ions. Reproduction of **C4** was only successful in the presence of manganese pivalate although neither manganese ions nor pivalate ions are present in the crystal structure. Fitting of the magnetic susceptibility data of **C4** revealed the expected spin ground state of  $S = \frac{1}{2}$ . However, a simulation of the Zeeman effect on **C2** and **C4** illustrated that the first excited quartet state is lowered in energy for **C4**, which is directly related to the increased coupling constant ratio of  $J_1/J_2 = 2.9$ .

Metallacrowns are not only studied for their magnetic properties, luminescence is another highly desired feature and thus subject to current investigations. The implementation of a softer donor atom into one of the binding pockets of a MC forming ligand in **L3** led to the successful isolation of the first Cd(II) MC structure,  $[\text{Cd}_{14}^{\text{II}}(\mathbf{L3})_{12}(\mu_6 - \text{O})(\text{DMF})_{10}](\text{ClO}_4)_2$  (**C6**). **C6** consists of 14 Cd(II) ions and 12 **L3** molecules forming a face-centered cube with a  $\mu_6 - \text{O}^{2-}$  ligand occupying the cube's inner cavity. Each face of the cube represents a 12-MC-4 structure. A second way to describe this structure is as a penetrated 18-MC-6 having the MC's core filled by two corner-sharing cubes of Cd(II) ions and oxygen atoms. The necessary next step is the coordination of a 4f metal ion as the central guest ion to provoke luminescence. A mixed 4d-4f MC complex would be the first of its kind and is an interesting compound class not only for luminescence properties but also in a magneto-chemistry respect.

Beside forming copper(II) and cadmium(II) complexes, **L3** reacts with iron(III) and cobalt(II/III) ions forming an iron monomer  $\text{Fe}^{\text{III}}(\text{L3H})_3$  (**C1**) and a cobalt octamer with 12-MC-4 structure  $[\text{Co}_4^{\text{III/II}}(\text{L3})_4\text{piv}_2(\text{X})_2(\mathbf{12} - \text{MC}_{\text{Co(II)Co(III)N(L3)} - 4})_2$  ( $\text{X} = \text{NO}$  or  $\text{MeOH}$ ) (**C5**). **C1** suggests that most likely due to charge accumulation the 12-MC-4 formation of trivalent metal ions with **L3** is hindered.

In addition to complexes with **L2** and **L3**, the variety of salicylhydroxamic acid based MCs has been increased by a rare vanadyl ring structure  $[\text{O}_{10}\text{py}_{10}(\mathbf{30} - \text{MC}_{\text{V(V)N(L1)} - 10})]$  (**C9**), a 2D Cu(II) MC network  $\{\text{Na}_2(\text{DMF})_3\text{Cu}^{\text{II}}\text{sal}_2[\text{Cu}^{\text{II}}(\mathbf{12} - \text{MC}_{\text{Cu(II)N(L1)} - 4})]\}_n$  (**C8**) and two Mn(II) centered Mn(III) double decker MC complexes  $\{\text{Mn}(\text{II})(\text{HNEt}_3)_2[\mathbf{12} - \text{MC}_{\text{Mn(III)N(L1)} - 4}](\mu_4 - \text{CO}_3)_2\}_2 \cdot (\text{H}_2\text{O})_8$  (**C10**) and  $\text{Mn}(\text{II})\{\text{H}_2\text{NEt}_2(\text{MeO})_2(\text{MeOH})_2[\mathbf{12} - \text{MC}_{\text{Mn(III)N(L1)} - 4}]\}_2$  (**C11**). **C11** reaches the highest effective energy barrier for the relaxation of magnetization observed so far in Mn(III) 12-MC-4 complexes. While **C10** consists of two Mn(II) centered Mn(III) 12-MC-4 units with both guest ions being bridged by four carbonate ions, **C11** comprises only one Mn(II) guest ion between two Mn(III) 12-MC-4 planes with an inter-MC Mn(III)-Mn(III) bridging via methanolate ions. Fitting of the dc magnetic data of both compounds was not possible due to the dimension of the required matrix to be diagonalized. However, qualitative evaluation of the magnetic behavior led to the suggestion of a spin ground state of  $S = 0$  and  $S = \frac{5}{2}$  for **C10** and **C11**, respectively. Hence, an *out-of-phase* signal indicating the presence of slow relaxation of the magnetization was only observed for **C11**. The effective energy barrier was evaluated as  $|U_{eff}| = 25.64 \text{ cm}^{-1}$  following an Orbach type relaxation. Low lying excited states accompanied by QTM are expected to be present, making **C11** a good candidate to further investigate the influence of the QTM.<sup>[55]</sup> A precise evaluation of the spin ground states of both manganese complexes (**C10** and **C11**) should be possible by examining the temperature-dependent ac magnetic susceptibility data. Regardless of the absence of an *out-of-phase* signal, the *in-phase* signal may show temperature dependence leading to a possibility to determine the spin ground state of systems with high nuclearity.<sup>[109]</sup> These double decker molecules could be more effectively used as SMMs with a suitable magnetic director encapsulated between the MC planes. Thus, an *out-of-plane* coordinating and strongly coupled guest ion could not only increase the effective energy barrier of a possible SMM but also yield a well separated ground state with less QTM. A tungsten(V) ion as used in the Mn(III) MC reported by Cao et al. would be a good choice. However, bridging co-ligands should be avoided to make use of the strong exchange coupling mediated via the hydroxamto oxygen atoms. Due to their ionic size, 4d or 5d transition metal ions should be used to

provoke the *out-of-phase* coordination make a square antiprismatic environment with a coordination number of 8 possible. Additionally, Pedersen et al. already demonstrated that a substitution of a 3d metal ion with a 5d metal ion can lead to anisotropic exchange coupling and therewith to an increased molecular magnetic anisotropy.<sup>[19]</sup>

The second approach, which has been followed in this work, is the introduction of additional functionalities in basic MC forming ligand systems. Therefore, the apical donor set of the ring forming metal ions was changed from  $NO_3$  in salicylhydroxamic acid based MCs to *cis* and *trans*  $N_2O_2$  donor sets for anthranilhydroxamic acid and salicylamidoxime derivatives, respectively. Introduction of a picolyl or a 2-hydroxybenzyl side arm via the primary amine group of anthranilhydroxamic acid led to the isolation of **L4** and **L5**. Crystallization of a cobalt(II) tetramer  $Co_4^{II}(L4a)_4(\mu_2Piv)_2Piv_2$  (**C12**) revealed major issues of the ligand's structural integrity during the inorganic synthesis. An oxidative cyclization reaction most probably involving Co(II) and atmospheric oxygen yielded the side product **L4a**. In order to keep the established  $NO_3$  donor set O-substituted salicylhydroxamic acid derivatives could be further investigated. O-(3-hydroxypropyl)salicylhydroxamic acid, did not show any crown forming ability in previous studies.<sup>[108]</sup> However, the introduction of an 2-hydroxybenzyl side arm yields a  $NO_4$  donor set and could affect the coordination affinity to Mn(III) greatly.

Derivatives of salicylamidoxime were synthesized and their coordination behavior to several 3d transition metal ions has been tested. A substitution reaction of hydroxyiminoyl chloride precursors **P1** and **P2** with primary and secondary amines has been effectively used to introduce a variety of coordinating side arms. Reaction with 2-picolylamine or 2-aminoethylpyridine led to the divalent ligands **L7** and **L8** with a  $N_3O_2$  donor set. The secondary amines di-(2-picolyl)amine (**L9a**) and N-(2-pyridylmethyl)-2-hydroxybenzylamine (**L10a**) were used to synthesize the hexadentate amidoximes **L9** and **L10** providing a  $N_4O_2$  and  $N_3O_3$  donor set, respectively. Hence, this compound class offers the formation of a Mn(III) 12-MC-4 with all coordination sites occupied without any use of co-ligands or solvent dependency. Reaction of **L9** with copper(II) and manganese(II) salts led to the copper(II) hexamer **C13**. The coordination mode of the **L9** in **C13** demonstrated its potential to form MC structures. However, an in-situ side reaction of the ligand to **L9b** suggested an instability of the side arm. This side reaction should be avoidable by alkylation of the bridging  $CH_2$  units or by extending the alkyl unit of the side arm to decrease the proton donor strength of the reacting methylene bridge. The divalent ligand **L9** could be used in further studies to incorporate Fe(II) ions in the 12-MC-4 ring structure. The  $N_4O_2$  donor

set in octahedral coordination environments of Fe(II) ions has been intensively studied regarding their spin crossover behavior.<sup>[142]</sup> Ideally, the combination of a magnetic director and these four spin crossover centers could yield a SMM showing light induced spin transition and thus allow to manipulate the SMM behavior. Anthranilamidoxime derivatives ( $N_5O$  donor set) are also suitable ligand systems for this purpose.

Reaction of **L10** with copper(II) perchlorate led to another copper(II) hexamer  $[\text{Cu}_6^{\text{II}}(\text{L10b})_4(\text{ClO}_4)_2(\text{DMF})_6](\text{ClO}_4)_2$  (**C14**), revealing the same side product, observed in **C13** already. The magnetic behavior of **C14** was probed. The low temperature value of  $\chi_M T$  suggests a spin ground state of  $S = 1$ . However, magnetization data did not support this assumption. Further reactions of **L10** with transition metal ions yielded a copper(II) dimer  $\text{Cu}_2^{\text{II}}(\text{L10cH})_2\text{Cl}_2$  (**C15**), a cobalt(II) dimer  $\text{Co}_2^{\text{II}}(\text{L10d})_2$  (**C16**) and a nickel(II) hexamer  $[\text{Ni}_6^{\text{II}}(\text{L10})_2(\text{L10H})_2(\mu - \text{O}_2\text{COMe})_2(\text{MeOH})_6]$  (**C17**). Both dimers form due to different in-situ side reaction of **L10**. A cyclization reaction accompanied with a rearrangement leads to **L10c**, whereas the oxadiazol side product **L10d** forms via an intramolecular cyclization. Ac magnetic susceptibility studies of **C16** showed the absence of an *out-of-phase* signal. This is most probably due to a positive  $D$  value in combination with small antiferromagnetic exchange interactions. The nickel hexamer **C17** is formed by four **L10** molecules without the observation of any side reaction. However, a  $\text{CO}_2$  fixation via monomethyl carbonate suppresses the formation of a MC structure.

Further functionalization of these amidoxime ligands could be used to bind MC structures on surfaces. Co-ligands often show less integrity than a chelating ligand occupying all coordination sites. The axial binding side arms of **L9** and **L10** could be substituted by aromatic systems with two binding moieties, like a pyrazine ring and thus making it possible to axially coordinate the ring metal ion of a MC and deposit the molecule on surface.

All in all, introduction of additional coordinating side arms is a promising tool to reach the aim of a heterometallic MC with Mn(III) as the ring forming metal ion. The ligand class of amidoximes offer a wide variety of accessible side arms and thus allow for rational design and selective coordination environments. First reactions with transition metal ions showed possible side reactions. Further investigations, how to avoid them and make the ligands to coordinate like intended, are necessary. Therewith, amidoximes are promising to be established as suitable ligands for the formation of discrete metallacrowns with desired properties.

## 5. Experimental Part

### General Information

All used chemicals were commercially available and have been used without further purification. Anthranilhydroxamic acid has been synthesized by Heike Pfaff supervised by Dr. Marcel Diehl. Pivalate salts of different metal ions were synthesized by dissolving the corresponding carbonate salts in pivalic acid and heating up the reaction mixture. Cooling down to room temperature yielded the crystallized pivalate salts.

### Instrumental Details

#### X-Ray Structure Analysis

X-ray crystallographic data was collected at different institutions. Regine Jung Pothmann and Dr. Dieter Schollmeyer measured the crystalline samples of **L9**, **C2**, **C3**, **C4**, **C5**, **C6**, **C7**, **C9**, **C10**, **C11**, **C12**, **C13** and **C15** at the Johannes Gutenberg-University. Samples **C14** and **C16** were measured in Moscow (Russia) by Dr. Konstantin Lyssenko and samples **C1**, **C8** and **C17** were measured on test devices at Bruker (Karlsruhe) or STOE (Darmstadt). Any further details on collection temperature, type of applied radiation or device type are provided in the corresponding XRD tables in the following chapter. Solving of the crystal structures and refinement was done using SHELXS/T/D<sup>[143]</sup> and SHELXL<sup>[144]</sup> in combination with Olex2<sup>[145]</sup>. Data of **C14** and **C16** was evaluated by Dr. Lyssenko.

#### Infrared Spectroscopy

Infrared spectra have been recorded on a Nicolet 5700 FT-IR-Spectrometer with an attached Smart Orbit ATR (Diamond) probe head from Thermo Electron Cooperation. The background has been measured prior to the samples and is subtracted from the spectra. The measurement range was from 400 – 4000  $cm^{-1}$ . The spectra were averaged over 32

measurements and baseline corrected using the software Omnic<sup>®</sup> (7.3) from Thermo Electron Cooperation. The IR spectrum of **L5a** was recorded on a JASCO FT/IR-4200 as a potassium bromide pellet.

### Nuclear Magnetic Resonance Spectroscopy

<sup>1</sup>H and <sup>13</sup>C-NMR spectra were obtained on a Bruker DRX-400 at room temperature. All compounds were measured in deuterated dimethyl sulfoxide unless otherwise noted. Chemical shifts were reported in parts per million with the residual solvent peak used as an internal standard (DMSO-d<sup>6</sup> = 2.50 ppm for <sup>1</sup>H and 39.52 ppm for <sup>13</sup>C). For the analysis of the spectra MestreNova 10.0 was used.

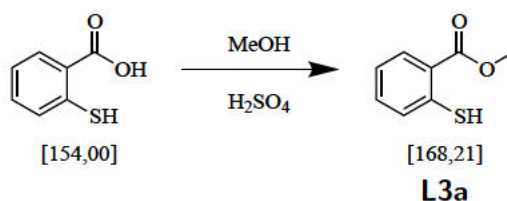
### Magnetic Susceptibility Measurements

Magnetic susceptibility studies were obtained on a Quantum Design MPMS-XL SQUID magnetometer in a temperature range from 2 to 300 K. Crystalline samples were filled in a gelatin capsule which was mounted in a plastic straw. 24 data points have been measured over a length of 4 cm. The volume magnetization derived from the measured response function was corrected by the magnetic contribution of holder and capsule using the julX 1.4.1 program by Bill.<sup>[146]</sup> Including the molar mass of the sample, the molar magnetic susceptibility could be calculated. The diamagnetic contribution of the sample  $\chi_D$  was taken into account by formula 5.1, which results in values very close to those deriving from Pascal's constants.<sup>[147]</sup>

$$\chi_D \approx -\frac{MW}{2} 10^{-6} emu mol^{-1} \quad (5.1)$$

## 5.1. Ligand Synthesis

### 5.1.1. 2-Mercaptobenzoic acid methyl ester (L3a)



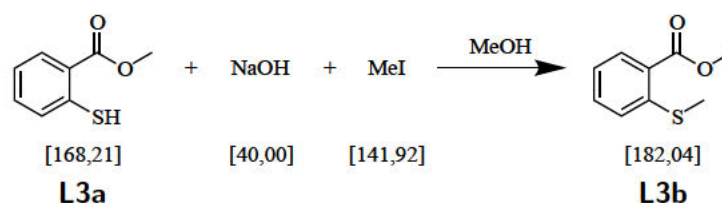
#### Procedure

REN-CG-006-04

2-Mercaptobenzoic acid (20 g, 0.130 mol) was suspended in 300 ml methanol and the mixture was cooled to 5 °C under  $N_2$  atmosphere. 21 ml sulfuric acid were added dropwise within 5 min. Then the mixture was heated to reflux and stirred over night. The benzoic acid dissolved under elevated temperatures and the solution became clear and yellow. After 16 h of heating the solution was cooled to room temperature and concentrated under reduced pressure. The reaction mixture was diluted with 200 ml dichloromethane and 200 ml water. The organic layer was separated and successively washed with 100 ml saturated sodium hydrogen carbonate solution and 200 ml brine. After drying over sodium sulfate the solvent was removed under reduced pressure. The resulting residue was purified via fractional distillation. **L3a** was collected at 10 mbar and 120 °C as a light yellow liquid (14.28 g, 84.9 mmol, 65 % of theory).

$^1\text{H-NMR}$  (DMSO- $d_6$ , 400 MHz,  $\delta$  (ppm)): 7.90 (dd, 1H, Ar-CH), 7.55 (dd, 1H, Ar-CH), 7.40 (td, 1H, Ar-CH), 7.20 (td, 1H, Ar-CH), 5.29 (s, 1H, SH), 3.83 (s, 3H,  $\text{OCH}_3$ ). (Figure C.2)  $^{13}\text{C-NMR}$  (DMSO- $d_6$ , 101 MHz,  $\delta$  (ppm)): 166.55 (OCO), 138.56 (Ar-C-S), 133.19 (Ar-C-H), 131.55 (Ar-C-H), 131.44 (Ar-C-H), 126.03 (Ar-C-COO), 125.13 (Ar-C-H), 52.57 ( $\text{OCH}_3$ ). (Figure C.3)

## 5.1.2. 2-Methylmercaptobenzoic acid methyl ester (L3b)

Procedure<sup>[148]</sup>

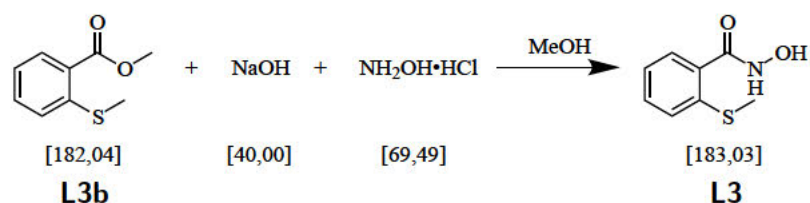
REN-CG-006-13

Sodium hydroxide (0.95 g, 23.75 mmol, 1.06 eq) was suspended in 20 ml methanol. The mixture was stirred while L3a (3.75 g, 22.30 mmol, 1 eq) was added. At 40 °C methyl iodide (3.25 g, 22.90 mmol, 1.02 eq) was added dropwise and the mixture became pale pink. The reaction mixture was heated to reflux for 2 h, then concentrated to one third of the total volume via distillation. 40 ml hot water were added to the residue provoking precipitation of a lightly pinkish solid. L3b could be isolated by filtration (3.983 g, 21.8 mmol, 98 % of theory).

<sup>1</sup>H-NMR (DMSO-d<sup>6</sup>, 400 MHz,  $\delta$  (ppm)): 7.90 (dd,  $J = 7.9, 1.6$  Hz, 1H, Ar-CH), 7.57 (td,  $J = 7.9, 1.6$  Hz, 1H, Ar-CH), 7.38 (d,  $J = 8.1$  Hz, 1H, Ar-CH), 7.28 – 7.17 (m, 1H, Ar-CH), 3.82 (s, 3H, OCH<sub>3</sub>), 2.42 (s, 3H, SCH<sub>3</sub>). (Figure C.4) <sup>13</sup>C-NMR (DMSO-d<sup>6</sup>, 101 MHz,  $\delta$  (ppm)): 166.03 (OCO), 142.47 (Ar-C-S), 132.91 (Ar-C-H), 130.78 (Ar-C-H), 126.33 (Ar-C-COO), 124.87 (Ar-C-H), 123.71 (Ar-C-H), 52.06 (OCH<sub>3</sub>), 14.79 (SCH<sub>3</sub>). (Figure C.5) IR (ATR,  $\tilde{\nu}$  (cm<sup>-1</sup>)): 2951 (vw), 2920 (vw), 1704 (w), 1584 (w), 1560 (w), 1461 (w), 1432 (w), 1304 (vw), 1285 (w), 1267 (w), 1245 (m), 1187 (w), 1144 (w), 1119 (vw), 1101 (w), 1059 (w), 1044 (w), 954 (w), 866 (vw), 825 (w), 798 (vw), 744 (m), 704 (w), 690 (w), 653 (w), 513 (w), 490 (w), 450 (w), 426 (vw), 409 (vw). (Figure B.1)



### 5.1.3. 2-Methylmercaptobenzohydroxamic acid (**L3**)



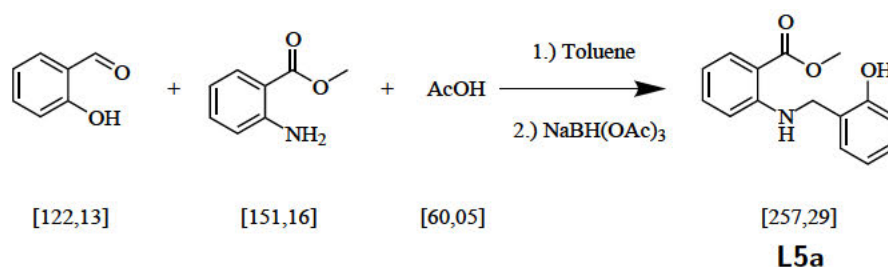
#### Procedure

REN-CG-006-20

Hydroxylamine hydrochloride (11.670 g, 168 mmol, 4 eq) was dissolved in 250 ml water. Then sodium hydroxide (13.440 g, 336 mmol, 8 eq) was added. **L3b** (7.654 g, 42 mmol, 1 eq) suspended in 110 ml 1,4-dioxane was added dropwise to the clear solution. A colorless precipitate occurred. After 2 h of stirring the mixture became a clear solution again. Stirring was continued for 72 h. The clear light yellow solution was concentrated to one third of its volume, then acidified with 2 N hydrochloric acid to pH=7. The solution was extracted five times with 25 ml ethyl acetate and washed with brine. The resulting colorless precipitate was filtered yielding **L3** (1.792 g, 9.8 mmol). The organic layer was dried over magnesium sulfate and the solvent was removed to isolate further product **L3** (1.913 g, 10.5 mmol). (Combined isolated colorless solid **L3** (3.705 g, 20.2 mmol, 48 % of theory))

<sup>1</sup>H-NMR (DMSO-d<sup>6</sup>, 400 MHz, δ (ppm)): 10.90 (s, 1H, OH), 9.11 (s, 1H, NH), 7.53 – 7.39 (m, 1H, Ar-CH), 7.35 (d, J = 8.2 Hz, 1H, Ar-CH), 7.32 – 7.24 (m, 1H, Ar-CH), 7.17 (t, J = 7.4 Hz, 1H, Ar-CH), 2.40 (s, 3H, S-CH<sub>3</sub>). (Figure C.6) <sup>13</sup>C-NMR (DMSO-d<sup>6</sup>, 101 MHz, δ (ppm)): 164.91 (OCN), 138.01 (Ar-C-S), 133.17 (Ar-C-CON), 130.39 (Ar-C-H), 127.71 (Ar-C-H), 125.78 (Ar-C-H), 124.22 (Ar-C-H), 15.25 (SCH<sub>3</sub>). (Figure C.7) IR (ATR,  $\tilde{\nu}$  (cm<sup>-1</sup>)): 3257 (vw), 3135 (vw), 2918 (w), 1743 (vw), 1677 (vw), 1608 (w), 1583 (w), 1561 (w), 1529 (w), 1461 (w), 1433 (w), 1414 (w), 1311 (w), 1286 (vw), 1271 (vw), 1253 (w), 1233 (w), 1165 (w), 1131 (vw), 1076 (vw), 1063 (vw), 1043 (vw), 1026 (w), 974 (vw), 958 (vw), 898 (w), 742 (w), 708 (w), 697 (vw), 652 (w), 586 (w), 546 (w), 490 (w), 467 (w), 455 (vw). (Figure B.2)

## 5.1.4. N-(2-Hydroxybenzyl)methylantranilate (L5a)



## Procedure

REN-CG-010-01

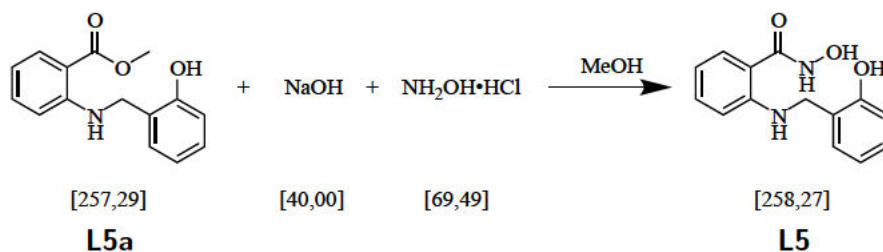
Methylantranilate (2.27 g, 15 mmol, 1 eq) was mixed with 50 ml toluene and 1 ml acetic acid. Salicylaldehyde (3.05 g, 25 mmol, 1.66 eq) was dissolved in 40 ml toluene and added dropwise. The yellow solution was stirred over night. The reaction mixture was heated to reflux and stirred for further 2.5 h. After cooling down to room temperature, sodium triacetoxyborohydride (3.03 g, 15 mmol, 1 eq) was added to the solution. The mixture was stirred over night. After 40 min of stirring at 50 °C, no further gas exposure was observed. The solvent was removed under reduced pressure. 10.5 g of a yellow solid could be isolated. This residue was treated with 80 ml ethyl acetate, filtered and extracted with saturated sodium hydrogen carbonate solution (3\*15 ml) and brine (3\*15 ml). The organic layer was dried over magnesium sulfate and the solvent was removed. The crude product was dissolved in a cyclohexane/EtOAc mixture to isolate the product **L5a** via column chromatography (SiO<sub>2</sub>; EtOAc/Cyclohexane, 1:4, *R<sub>f</sub>* = 0.28) as a yellow powder (1.781 g, 6.9 mmol, 46 % of theory).

<sup>1</sup>H-NMR (DMSO-d<sup>6</sup>, 400 MHz, δ (ppm)): 9.65 (s, 1H, OH), 8.03 (t, J = 5.8 Hz, 1H, NH), 7.79 (dd, J = 8.0, 1.7 Hz, 1H), 7.34 (td, J = 8.7, 7.0, 1.8 Hz, 1H), 7.17 (dd, J = 7.5, 1.7 Hz, 1H), 7.08 (td, J = 7.7, 1.8 Hz, 1H), 6.84 (dd, J = 8.0, 1.1 Hz, 1H), 6.79 – 6.69 (m, 2H), 6.60 – 6.52 (m, 1H), 4.36 (d, J = 5.8 Hz, 2H, NH-CH<sub>2</sub>), 3.79 (s, 3H, O-CH<sub>3</sub>). (Figure C.8) <sup>13</sup>C-NMR (DMSO-d<sup>6</sup>, 101 MHz, δ (ppm)): 168.10 (OCO), 155.21, 150.57, 134.71, 131.10, 128.55, 128.08, 124.69, 118.87, 115.07, 114.35, 111.70, 109.21, 51.50 (O-CH<sub>3</sub>), 41.27 (CH<sub>2</sub>). (Figure C.9) IR (KBr pellet,  $\tilde{\nu}$  (cm<sup>-1</sup>)): 3343 (m), 3045 (m), 2955 (s), 2884 (m), 2685 (m), 2628 (m), 2524 (w), 1921 (vw), 1712 (vs), 1676 (vs,  $\nu_{CO}$ ), 1606 (s), 1579 (vs), 1518 (vs), 1480 (s), 1460 (s), 1434 (vs), 1415 (s), 1334 (vs), 1317 (s), 1264 (vs), 1246 (vs), 1220 (vs), 1168 (s), 1152 (s), 1111 (vs), 1073 (s), 1049 (m), 964 (w), 927 (m), 846 (m), 812

(w), 793 (w), 749 (vs), 701 (m), 682 (m), 666 (w), 613 (w), 527 (m), 499 (m), 430 (w).  
(Figure B.9)

## 5.1.5. N-(2-Hydroxybenzyl)anthranilic hydroxamic acid

(L5)



## Procedure

REN-CG-010-02

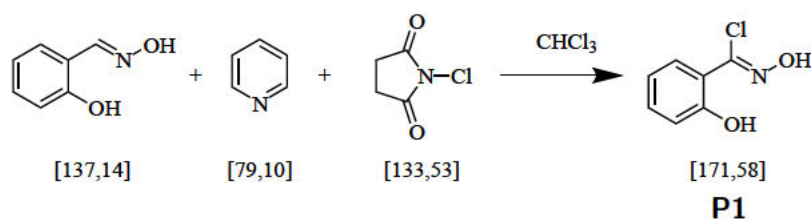
Sodium hydroxide (381 mg, 9.52 mmol, 3.5 eq) was dissolved in 10 ml water and added to a solution of hydroxylamine hydrochloride (284 mg, 4.08 mmol, 1.5 eq) in 5 ml water. L5a (700 mg, 2.72 mmol, 1 eq) was dissolved in 5 ml 1,4-dioxane and added dropwise to the mixture. The solution became nontransparent and was stirred over night. The mixture was concentrated to one half under reduced pressure and acidified with 2N hydrochloric acid to a pH value of 7. L5 (190 mg, 0.74 mmol, 27 % of theory) could be obtained as a colorless precipitate.

<sup>1</sup>H-NMR (DMSO-d<sup>6</sup>, 400 MHz,  $\delta$  (ppm)): 9.44 (s, 0H), 7.72 (s, 1H, NH), 7.38 (d, J = 7.7 Hz, 1H), 7.30 – 7.10 (m, 2H), 7.06 (t, J = 7.7 Hz, 1H), 6.85 (d, J = 8.1 Hz, 1H), 6.73 (t, J = 7.5 Hz, 1H), 6.64 (d, J = 8.4 Hz, 1H), 6.51 (t, J = 7.4 Hz, 1H), 4.25 (s, 3H, NH-CH<sub>2</sub>).

<sup>13</sup>C-NMR (DMSO-d<sup>6</sup>, 101 MHz,  $\delta$  (ppm)): 166.92 (OCO), 155.25, 148.67, 131.99, 128.43, 127.90, 127.76, 125.07, 118.79, 115.07, 114.29, 113.95, 111.10, 41.27 (CH<sub>2</sub>). (Figure C.11)

IR (ATR,  $\tilde{\nu}$  (cm<sup>-1</sup>)): 3451 (vw), 3359 (w), 2981 (w), 2889 (vw), 1666 (m), 1612 (w,  $\nu_{CO}$ ), 1574 (w), 1518 (w), 1453 (w), 1441 (w), 1414 (vw), 1376 (vw), 1342 (w), 1322 (vw), 1276 (w), 1249 (m), 1227 (m), 1172 (w), 1151 (m), 1089 (w), 1046 (w), 938 (vw), 914 (w), 837 (w), 828 (w), 755 (m), 746 (m), 713 (w), 694 (w), 661 (w), 632 (w), 596 (w), 578 (w), 560 (w), 544 (w), 535 (w), 518 (w), 446 (vw), 427 (w). (Figure B.10)

## 5.1.6. N,2-Dihydroxybenzenecarbonimidoyl chloride (P1)

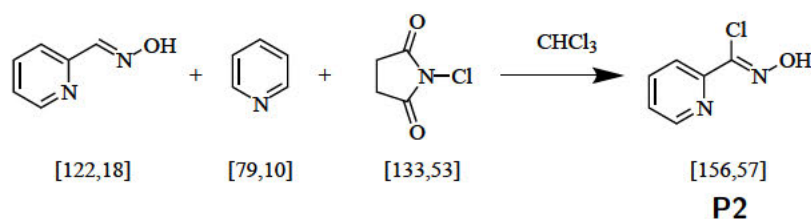
Procedure<sup>[149]</sup>

REN-CG-012-04

Pyridine (0.243 g, 3.1 mmol, 0.1 eq) was added to a solution of salicylaldehyde (4.23 g, 30.8 mmol, 1 eq) in 29 ml chloroform. The mixture was heated to 40 °C and N-chlorosuccinimide (4.53 g, 33.9 mmol, 1.1 eq) was added. Stirring was continued at this temperature for 3.5 h before the orange solution was diluted by 200 ml dichloromethane. The organic layer was washed with water (100 ml) and with brine (30 ml). Then it was dried over sodium sulfate and the solvent was removed under reduced pressure to yield **P1** as a bright yellow powder (4.956 g, 28.9 mmol, 94 % of theory).

<sup>1</sup>H-NMR (DMSO-d<sub>6</sub>, 400 MHz,  $\delta$  (ppm)): 12.38 (s, 1H, N-OH), 10.16 (s, 1H, C-OH), 7.47 (dd, J = 7.8, 1.6 Hz, 1H), 7.32 (td, J = 7.8, 1.7 Hz, 1H), 6.92 (dd, J = 17.1, 8.2 Hz, 2H). (Figure C.12) <sup>13</sup>C-NMR (DMSO-d<sub>6</sub>, 101 MHz,  $\delta$  (ppm)): 155.70, 135.39, 131.55, 129.62, 119.20, 118.92, 116.46. (Figure C.13) IR (ATR,  $\tilde{\nu}$  (cm<sup>-1</sup>)): 3289 (m), 1775 (w), 1699 (m), 1605 (m), 1586 (m), 1498 (w), 1471 (m), 1428 (w), 1411 (m), 1303 (w), 1268 (m), 1244 (m), 1212 (m), 1181 (m), 1156 (m), 1117 (w), 1027 (m), 940 (m), 850 (w), 817 (m), 754 (m), 700 (m), 670 (m), 646 (m), 557 (m), 526 (w), 502 (w), 442 (w). (Figure B.3)

## 5.1.7. N-Hydroxy-(2-pyridyl)carbonimidoyl chloride (P2)



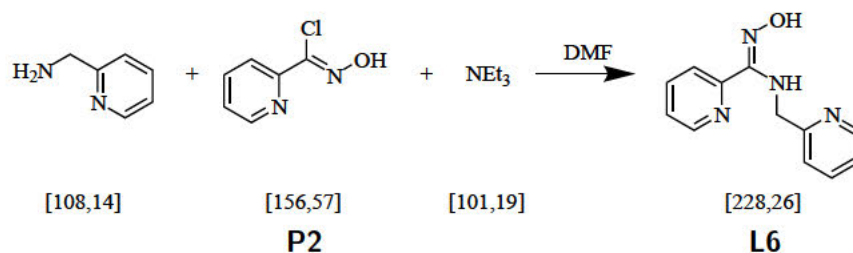
## Procedure

REN-CG-024-03

2-Picolylaldehyde oxime (1.34 g, 11 mmol, 1 eq) was dissolved in 40 ml chloroform and pyridine (80  $\mu\text{l}$ , 1 mmol, 0.09 eq) was added. After heating up to 45 °C N-chlorosuccinimide (1.76 g, 13.2 mmol, 1.2 eq) was added in portions. After the finished addition, the pale yellow solution was stirred for 3 h at 45 °C. The mixture became orange and was added to 50 ml ice water. The solution was extracted with diethyl ether (4 \* 30 ml). The combined organic layer was dried over sodium sulfate and the solvent was removed under reduced pressure to afford P2 (1.76 g, 11.2 mmol, 102% of theory) as a yellow powder.

$^1\text{H-NMR}$  (DMSO- $d_6$ , 400 MHz,  $\delta$  (ppm)): 12.68 (s, 1H, OH), 8.66 (d,  $J = 4.8$  Hz, 1H, N-CH), 7.89 (dd,  $J = 6.4, 1.8$  Hz, 2H), 7.50 (ddd,  $J = 6.7, 4.8, 2.3$  Hz, 1H), 2.56 (s, 1H). (Figure C.14) IR (ATR,  $\tilde{\nu}$  ( $\text{cm}^{-1}$ )): 3141 (w), 3082 (w), 3007 (w), 2792 (w), 1772 (w), 1692 (m), 1588 (w), 1567 (w), 1484 (w), 1430 (w), 1402 (w), 1371 (w), 1294 (w), 1268 (w), 1254 (w), 1238 (w), 1185 (m), 1158 (w), 1098 (w), 1018 (m), 995 (m), 954 (m), 819 (m), 776 (m), 741 (m), 690 (m), 641 (m), 620 (m), 578 (m), 556 (w), 510 (w), 501 (w), 496 (w), 465 (w), 420 (m), 403 (m). (Figure B.11)

## 5.1.8. N-(Pyridin-2-ylmethyl)2-pyridylamidoxime (L6)



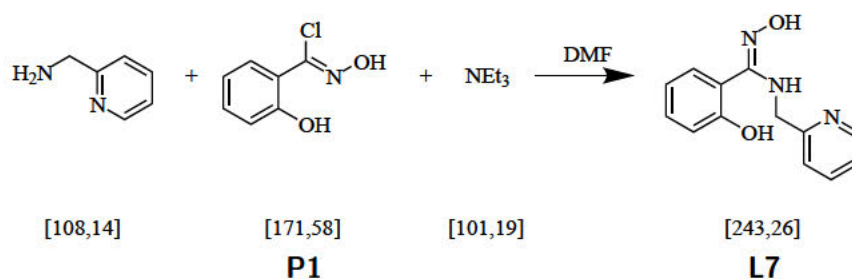
## Procedure

REN-CG-025-02

2-Picolylamine (757 mg, 7 mmol, 1 eq) and triethylamine (1.062 g, 10.5 mmol, 1.5 eq) were dissolved in 12 ml dimethylformamide. **P2** (1.201 g, 7.7 mmol, 1.1 eq) was dissolved in 8 ml dimethylformamide and added dropwise to the solution. After stirring 2 h at room temperature, the mixture was quenched with 40 ml water and extracted with ethyl acetate (4 \* 20 ml). The organic layer was dried over magnesium sulfate and concentrated yielding **L6** (700 mg, 3.1 mmol, 44 % of theory) as a brown solid.

<sup>1</sup>H-NMR (DMSO-d<sup>6</sup>, 400 MHz, δ (ppm)): 9.95 (s, 1H, OH), 8.57 (d, J = 4.8 Hz, 1H), 8.49 – 8.38 (m, 1H), 7.78 (td, J = 7.7, 1.8 Hz, 1H), 7.72 (td, J = 7.6, 1.8 Hz, 1H), 7.65 (d, J = 7.9 Hz, 1H), 7.39 (ddd, J = 7.6, 4.8, 1.3 Hz, 1H), 7.28 (d, J = 7.9 Hz, 1H), 7.24 – 7.14 (m, 1H), 6.80 (t, J = 6.4 Hz, 1H, NH), 4.68 (d, J = 6.3 Hz, 2H, CH<sub>2</sub>). (Figure C.15) IR (ATR,  $\tilde{\nu}$  (cm<sup>-1</sup>)): 3313 (vw), 2731 (vw), 1627 (w), 1598 (vw), 1582 (w), 1574 (vw), 1562 (vw), 1508 (w), 1472 (w), 1447 (w), 1435 (vw), 1380 (w), 1339 (vw), 1319 (vw), 1287 (vw), 1215 (vw), 1146 (w), 1096 (vw), 1047 (vw), 1012 (w), 994 (vw), 959 (w), 927 (w), 901 (w), 879 (w), 842 (vw), 795 (w), 768 (m), 752 (w), 727 (w), 687 (w), 667 (vw), 640 (w), 622 (vw), 607 (w), 520 (w), 507 (w), 411 (w). (Figure B.12)

## 5.1.9. N-(Pyridin-2-ylmethyl)salicylamidoxime (L7)



## Procedure

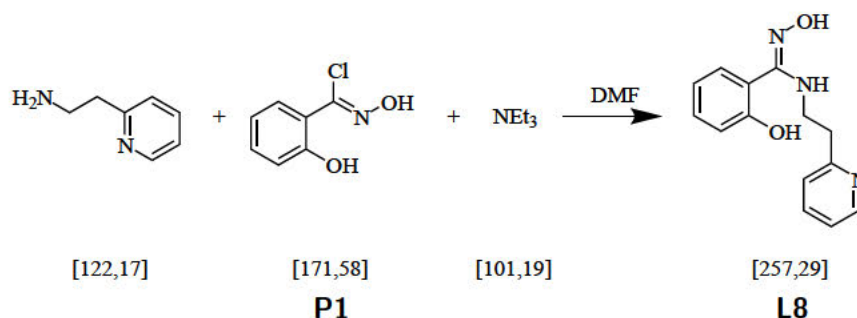
REN-CG-019-04

**P1** (1.539 g, 9 mmol, 1 eq) was dissolved in 20 ml dimethylformamide. 2-Picolylamine (1.18 g, 10.9 mmol, 1.2 eq) dissolved in 10 ml dimethylformamide was added dropwise. Then 3 ml pure dimethylformamide were added. Triethylamine (2.760 g, 27 mmol, 3 eq) was dissolved in 7 ml dimethylformamide and added dropwise to the dark orange reaction solution. After 5 h of stirring, the orange suspension was quenched with 70 ml water and the organic layer was extracted with ethyl acetate (7\*20 ml), washed with brine, dried over sodium sulfate and concentrated under reduced pressure. **L7** (1.969 g, 8 mmol, 90% of theory) could be isolated as a brown solid.

<sup>1</sup>H-NMR (DMSO-d<sup>6</sup>, 400 MHz,  $\delta$  (ppm)): 10.10 (s, 1H, N-OH), 9.63 (s, 1H, C-OH), 8.43 (d, J = 5.1 Hz, 1H, py-N-CH), 7.73 (t, J = 7.7 Hz, 1H), 7.27 (d, J = 7.9 Hz, 1H), 7.20 (q, J = 8.3, 7.4 Hz, 2H), 7.13 (d, J = 7.6 Hz, 1H), 6.85 (d, J = 8.1 Hz, 1H), 6.74 (t, J = 7.4 Hz, 1H), 6.56 (t, J = 6.4 Hz, 1H, NH), 4.25 (d, J = 6.3 Hz, 2H, CH<sub>2</sub>). (Figure C.16) <sup>13</sup>C-NMR (DMSO-d<sup>6</sup>, 101 MHz,  $\delta$  (ppm)): 162.33, 159.47, 155.90, 152.89, 148.55, 136.64, 130.27, 130.18, 121.93, 120.86, 118.62, 118.58, 115.82, 47.84 (CH<sub>2</sub>). (Figure C.17) IR (ATR,  $\tilde{\nu}$  (cm<sup>-1</sup>)): 3394 (vw), 2922 (vw), 1646 (w), 1604 (vw), 1595 (vw), 1572 (vw), 1491 (vw), 1474 (w), 1456 (w), 1438 (w), 1419 (vw), 1369 (w), 1343 (w), 1297 (w), 1275 (w), 1254 (vw), 1226 (vw), 1213 (w), 1170 (vw), 1120 (vw), 1086 (vw), 1053 (vw), 1008 (vw), 978 (vw), 957 (vw), 915 (w), 889 (vw), 863 (vw), 845 (w), 806 (vw), 787 (vw), 757 (w), 725 (w), 660 (vw), 632 (vw), 605 (w), 553 (w), 523 (w), 476 (w), 456 (vw). (Figure B.8)



## 5.1.10. N-(Pyridin-2-ylethyl)salicylamidoxime (L8)



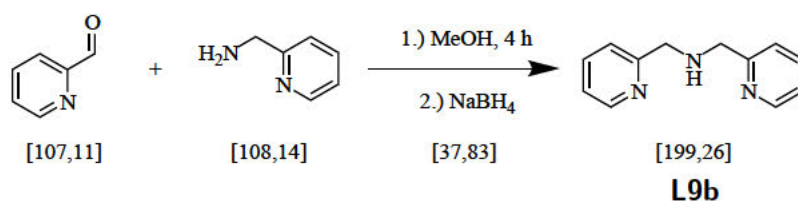
## Procedure

REN-CG-023-01

P1 (305 mg, 9 mmol, 1 eq) was dissolved in 5 ml dimethylformamide. 2-Aminoethylpyridine (260 mg, 2.1 mmol, 1.2 eq) and triethylamine (539 mg, 5.3 mmol, 2.9 eq) were dissolved in 5 ml dimethylformamide each and added slowly. The orange solution was stirred over night. The mixture was quenched with 30 ml water and the aqueous phase was extracted with ethyl acetate (5 \* 10 ml), washed with brine, dried over sodium sulfate and concentrated under reduced pressure. The resulting brown oil was dissolved in toluene and the solvent was removed again under reduced pressure yielding 851 mg of a brown solid. DMF was not entirely removed resulting the high amount of crude product.

<sup>1</sup>H-NMR (DMSO-d<sup>6</sup>, 400 MHz, δ (ppm)): 9.98 (s, 1H, N-OH), 9.45 (s, 1H, C-OH), 8.43 (d, J = 4.9 Hz, 1H, py-N-CH), 7.66 (td, J = 7.7, 2.0 Hz, 1H), 7.28 – 7.02 (m, 4H), 6.91 – 6.69 (m, 2H), 5.95 (t, J = 6.3 Hz, 1H, NH), 3.30 – 3.19 (m, 2H, NCH<sub>2</sub>C), 2.83 (t, J = 7.1 Hz, 2H, CCH<sub>2</sub>C). (Figure C.18)

## 5.1.11. Di-(2-picolyl)amine (L9a)



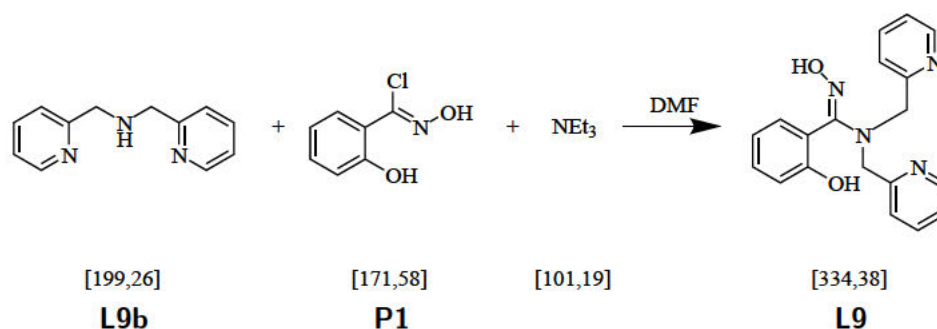
## Procedure

REN-CG-020-06

2-Picolylamine (3.39 g, 31 mmol, 1 eq) was dissolved in 30 ml methanol. 2-Pyridinecarboxaldehyde (3.36 g, 31 mmol, 1 eq) was added dropwise. The mixture was stirred at 40 °C for 2 h. The yellow brown solution was cooled to 0 °C and sodium borohydride (3.0 g, 79 mmol, 2.5 eq) was added in small portions. Gas exposure was observable. The mixture was stirred at room temperature over night. The yellow solution was quenched with 40 ml water and concentrated under reduced pressure until the mixture became nontransparent. The organic layer was extracted with dichloromethane (3 \* 15 ml), washed with brine and dried over sodium sulfate. Removing the solvent yielded **L9a** (4.668 g, 23.5 mmol, 76 % of theory) as a yellow oil.

<sup>1</sup>H-NMR (DMSO-d<sup>6</sup>, 400 MHz,  $\delta$  (ppm)): 8.56 – 8.42 (m, 2H, N-CH), 7.74 (td, J = 7.6, 1.8 Hz, 2H), 7.46 (d, J = 7.8 Hz, 2H, C-CH-C), 7.23 (td, J = 7.5, 2H), 3.83 (s, 4H, CH<sub>2</sub>). (Figure C.19)

## 5.1.12. N,N-Di-(2-picolyl)salicylamidoxime (L9)



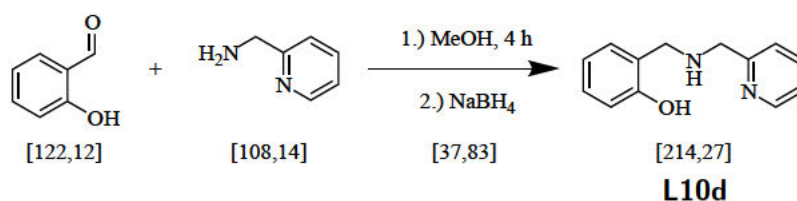
## Procedure

REN-CG-020-01

P1 (343 mg, 2 mmol, 1 eq) was dissolved in 10 ml dimethylformamide. Under ice cooling was added dropwise L9a (478 mg, 2.4 mmol, 1.2 eq) dissolved in 5 ml dimethylformamide then triethylamine (607 mg, 6 mmol, 3 eq) dissolved in 5 ml dimethylformamide. Stirring was continued under ice cooling for 2 h then at room temperature over night. The orange suspension was quenched with 40 ml water. The mixture became a bright orange solution and heated up. The combined organic layer from extracting with ethyl acetate (4\*30 ml) was washed with brine, dried over magnesium sulfate and concentrated under reduced pressure yielding 631 mg of a brown oil. Layering with acetone provoked crystallization of the product L9 (135 mg, 0.40 mmol, 20 % of theory).

<sup>1</sup>H-NMR (DMSO-d<sup>6</sup>, 400 MHz,  $\delta$  (ppm)): 10.43 (s, 1H, N-OH), 9.05 (s, 1H, C-OH), 8.53 – 8.37 (m, 2H, py-N-CH), 7.84 – 7.69 (m, 2H), 7.43 (d, J = 7.9 Hz, 2H), 7.33 – 7.13 (m, 3H), 7.12 – 7.02 (m, 1H), 6.89 (d, J = 8.2 Hz, 1H), 6.78 (t, J = 7.2 Hz, 1H), 4.42 (s, 4H, CH<sub>2</sub>). (Figure C.20) <sup>13</sup>C-NMR (DMSO-d<sup>6</sup>, 101 MHz,  $\delta$  (ppm)): 158.20, 154.79, 154.34, 148.64, 136.89, 130.24, 130.07, 122.12, 121.55, 118.68, 118.55, 116.17, 53.41 (CH<sub>2</sub>). (Figure C.21) IR (ATR,  $\tilde{\nu}$  (cm<sup>-1</sup>)): 3060 (w), 2981 (w), 2919 (w), 2358 (vw), 1773 (vw), 1667 (w), 1624 (w), 1608 (w), 1593 (w), 1569 (w), 1473 (w), 1435 (w), 1417 (w), 1403 (w), 1363 (w), 1300 (vw), 1284 (vw), 1242 (w), 1146 (w), 1093 (vw), 1049 (vw), 1003 (w), 966 (w), 947 (w), 747 (w), 619 (w), 597 (w), 581 (w), 549 (vw), 532 (vw), 506 (vw), 473 (vw), 458 (vw). (Figure B.7) X-ray diffraction: Table D.1

## 5.1.13. N-(2-Pyridylmethyl)-2-hydroxybenzylamine (L10a)



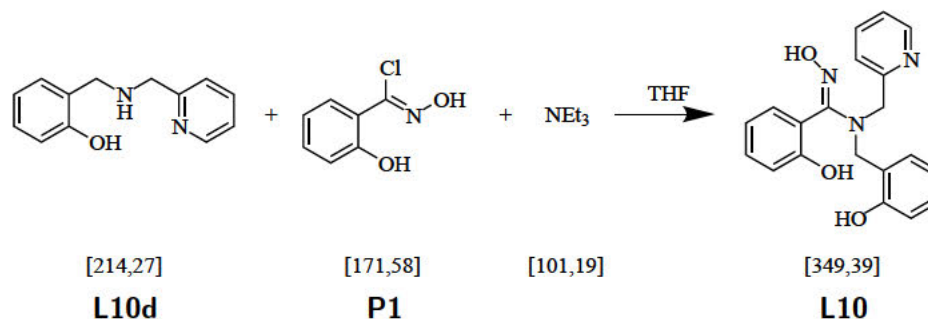
## Procedure

REN-CG-021-12

Salicylaldehyde (9.77 g, 8.5 ml, 80 mmol, 1 eq) was added dropwise to a solution of 2-picolylamine (8.65 g, 8.25 ml, 80 mmol, 1 eq) in 75 ml methanol. The mixture was stirred for 4 h at room temperature. Then sodium borohydride (7.57 g, 200 mmol, 2.5 eq) was added gradually to the ice-cooled mixture. After strong gas development, the mixture was stirred at room temperature over night. Then 100 ml water were added and stirring was maintained for 4 hour. Part of the solvent was removed under reduced pressure and the residue was extracted with dichloromethane (1 \* 100 ml + 3 \* 50 ml). The combined organic layer was washed with water (1 \* 50 ml) and dried over sodium sulfate. Concentrating under reduced pressure afforded **L10a** (16.38 g, 76 mmol, 96 % of theory) as a colorless oil. After cooling the oil for one week in the fridge it crystallized by taking it out.

$^1\text{H-NMR}$  (DMSO- $d_6$ , 400 MHz,  $\delta$  (ppm)): 8.61 – 8.40 (m, 1H, py-N-CH), 7.75 (dt,  $J = 7.6, 4.6$  Hz, 1H), 7.41 (d,  $J = 7.8$  Hz, 1H), 7.31 – 7.17 (m, 1H), 7.09 (dd,  $J = 13.1, 7.2$  Hz, 2H), 6.74 (dd,  $J = 10.7, 7.6$  Hz, 2H), 3.82 (s, 4H,  $\text{CH}_2$ ). (Figure C.22)  $^{13}\text{C-NMR}$  (DMSO- $d_6$ , 101 MHz,  $\delta$  (ppm)): 159.20, 156.99, 148.88, 136.60, 128.80, 127.89, 124.52, 122.10, 122.05, 118.57, 115.34, 53.30, 49.62. (Figure C.23) **IR** (ATR,  $\tilde{\nu}$  ( $\text{cm}^{-1}$ )): 3046 (w), 3010 (w), 2848 (w), 2719 (w), 2361 (w), 1588 (m), 1570 (m), 1489 (m), 1473 (m), 1455 (m), 1432 (m), 1362 (w), 1254 (m), 1184 (w), 1150 (w), 1091 (w), 1048 (w), 1036 (w), 994 (w), 932 (w), 843 (w), 751 (m), 621 (w), 465 (w). (Figure B.4)

### 5.1.14. N-(2-Hydroxybenzyl)-N-(pyridin-2-ylmethyl)salicylamidoxime (L10)



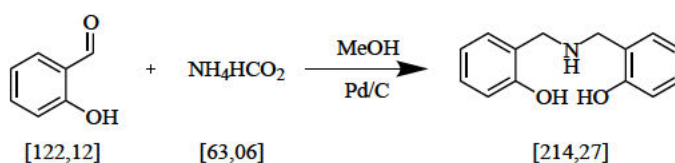
#### Procedure

REN-CG-021-14

**L10a** (428 mg, 2 mmol, 1 eq) dissolved in 5 ml tetrahydrofuran was added to a solution of **P1** (343 mg, 2 mmol, 1 eq) in 5 ml tetrahydrofuran. Then triethylamine (202 mg, 2 mmol, 1 eq) dissolved in 5 ml tetrahydrofuran was added dropwise. Precipitation occurred in the orange solution. The suspension was stirred over night, filtered and the solvent was removed yielding a yellow solid (612 mg). The crude product was dissolved in acetone and adsorbed on silica to isolate the product **L10** (268 mg, 0.76 mmol, 39 % of theory) as a colorless solid via column chromatography (SiO<sub>2</sub>; EtOAc/Cyclohexane, 2:3,  $R_f = 0.22$ )

<sup>1</sup>H-NMR (DMSO-d<sub>6</sub>, 400 MHz,  $\delta$  (ppm)): 10.12 (s, 1H, N-OH), 9.62 (s, 1H, N-methyl-phenyl-OH), 8.98 (s, 1H, C-OH), 8.45 (d,  $J = 5.0$  Hz, 1H, py-N-CH), 7.77 (td,  $J = 7.8, 2.0$  Hz, 1H), 7.44 (d,  $J = 7.9$  Hz, 1H), 7.35 – 7.12 (m, 3H), 7.13 – 6.96 (m, 2H), 6.87 (d,  $J = 8.2$  Hz, 1H), 6.82 – 6.59 (m, 3H), 4.41 (s, 2H), 4.20 (s, 2H). (Figure C.24) <sup>13</sup>C-NMR (DMSO-d<sub>6</sub>, 101 MHz,  $\delta$  (ppm)): 158.21, 155.81, 155.15, 154.31, 148.47, 136.93, 130.16, 130.00, 128.53, 127.79, 124.38, 122.07, 121.59, 118.91, 118.83, 118.59, 115.97, 115.17, 52.26, 46.85. (Figure C.25) IR (ATR,  $\tilde{\nu}$  (cm<sup>-1</sup>)): 3370 (vw), 1620 (w), 1598 (w), 1589 (w), 1484 (w), 1442 (w), 1390 (w), 1359 (w), 1346 (w), 1323 (vw), 1282 (vw), 1269 (w), 1258 (w), 1213 (w), 1186 (w), 1163 (vw), 1147 (w), 1093 (vw), 1054 (vw), 1035 (vw), 1014 (w), 973 (w), 960 (w), 940 (w), 932 (w), 918 (w), 803 (vw), 769 (vw), 752 (m), 727 (w), 684 (vw), 659 (vw), 634 (w), 601 (vw), 585 (vw), 531 (vw), 512 (vw), 492 (w), 462 (vw), 414 (vw). (Figure B.5)

## 5.1.15. 2,2'-Dihydroxydibenzylamine



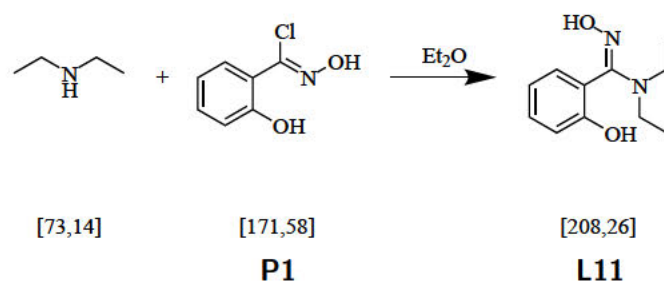
## Procedure

REN-CG-028-06

Salicylaldehyde (3.68 g, 26.9 mmol, 1 eq) was dissolved in 40 ml methanol. Ammonium formate (8.47 g, 134.5 mmol) and Pd/C 10 (1.035 g) were added. The black mixture was stirred over night. 150 ml EtOAc were added to the suspension before it was filtered through celite and washed with 150 ml methanol. The solvent was removed under reduced pressure yielding a colorless solid (3.687 g, 16.1 mmol, 76 % of theory).

$^1\text{H-NMR}$  ( $\text{DMSO-d}_6$ , 400 MHz,  $\delta$  (ppm)): 8.38 (s, 1H), 7.14 – 7.00 (m, 4H), 6.82 – 6.66 (m, 4H), 3.77 (s, 4H). (Figure C.26)

## 5.1.16. N,N-Diethylsalicylamidoxime (L11)



## Procedure

REN-CG-029-01

Diethylamine (731 mg, 10 mmol, 2 eq) dissolved in 10 ml diethyl ether was added to a solution of **P1** (783 mg, 5 mmol, 1 eq) in 5 ml diethyl ether. After stirring for 3 h, the orange suspension was filtered and the solvent was removed under reduced pressure. **L11** (400 mg, 1.9 mmol, 38 % of theory) was isolated as a yellow solid from the oily residue via column chromatography (SiO<sub>2</sub>; EtOAc/Cyclohexane, 1:2,  $R_f = 0.51$ ).

<sup>1</sup>H-NMR (DMSO-d<sub>6</sub>, 400 MHz,  $\delta$  (ppm)): 9.11 (s, 1H, N-OH), 8.83 (s, 1H, C-OH), 7.17 (t,  $J = 7.8$  Hz, 1H), 6.97 (d,  $J = 7.4$  Hz, 1H), 6.89 – 6.71 (m, 2H), 3.02 (q,  $J = 7.0$  Hz, 4H, CH<sub>2</sub>), 0.98 (t,  $J = 7.1$  Hz, 6H, CH<sub>3</sub>). (Figure C.27) IR (ATR,  $\tilde{\nu}$  (cm<sup>-1</sup>)): 3201 (w), 2971 (w), 2928 (w), 2870 (w), 1758 (m), 1639 (m), 1615 (m), 1582 (m), 1546 (w), 1482 (m), 1457 (m), 1402 (w), 1359 (m), 1315 (w), 1295 (m), 1269 (w), 1247 (m), 1214 (m), 1155 (w), 1125 (w), 1088 (w), 1075 (w), 1035 (w), 1006 (w), 957 (w), 941 (w), 913 (m), 863 (w), 851 (w), 832 (w), 782 (w), 750 (m), 697 (m), 609 (w), 582 (w), 534 (w), 504 (w), 477 (w). (Figure B.6)

## 5.2. Complex Synthesis

### 5.2.1. Fe<sup>III</sup>(L3H)<sub>3</sub> (C1)

#### Procedure

REN-CG-640-05

Iron pivalate (214 mg, 0.68 mmol (Fe(III)), 2,3 eq) and **L3** (54 mg, 0.3 mmol, 1 eq) were mixed in 16 ml methanol. Pyridine (145  $\mu$ L, 1.8 mmol, 6 eq) was added and the solution was stirred for 2 h. After filtration 5 mL of the red solution were covered with 10 mL diethyl ether, the rest was left for slow evaporation (glass vial with two holes in the cap). Red crystals appeared after one day in both solutions. The iron monomer **C1** (10.8 mg, 0.02 mmol, 18 % of theory (ligand)) was isolated by filtration.

**X-ray diffraction:** Table D.1 **IR** (ATR,  $\tilde{\nu}$  (cm<sup>-1</sup>)): 3199 (vw), 3069 (vw), 2914 (vw), 1588 (w), 1575 (w), 1515 (w), 1486 (w), 1449 (w), 1430 (w), 1340 (w), 1318 (w), 1285 (vw), 1255 (vw), 1151 (w), 1120 (vw), 1074 (w), 1042 (w), 1024 (w), 968 (vw), 956 (vw), 908 (w), 837 (vw), 774 (w), 746 (vw), 729 (w), 709 (w), 693 (w), 652 (w), 555 (w), 530 (vw), 508 (w), 497 (w), 475 (w), 452 (w). (Figure B.13)

### 5.2.2. {Cu<sup>II</sup>Cl<sub>2</sub>(MeOH)[12 – MC<sub>Cu(II)N(L3) – 4]}<sub>2</sub> · 4MeOH (C2)</sub>

#### Procedure

REN-CG-611-01k

**L3** (111 mg, 0.61 mmol, 1 eq) was dissolved in 36 ml methanol. CuCl<sub>2</sub> (120 mg, 0.9 mmol, 1,5 eq) was added and the green solution was stirred over night. Triethylamine (498  $\mu$ L, 3.6 mmol, 6 eq) was added and stirring was continued for 2 h. After filtration the reaction mixture was left for slow evaporation (8 ml were used for layering experiments). Green crystals of **C2** (20.1 mg, 0.04 mmol, 10 % of theory (Cu)) could be isolated by filtration after one week.

**X-ray diffraction:** Table D.2 **IR** (ATR,  $\tilde{\nu}$  (cm<sup>-1</sup>)): 3384 (vw), 1630 (vw), 1573 (w), 1522 (w), 1471 (w), 1421 (w), 1369 (m), 1282 (w), 1261 (vw), 1154 (w), 1120 (vw), 1064 (w), 1043 (vw), 1012 (w), 976 (w), 946 (w), 929 (w), 913 (w), 769 (w), 734 (w), 693 (vw), 675 (w), 646 (w), 622 (w), 505 (w), 477 (w), 435 (w), 418 (w), 414 (w), 401 (vw). (Figure B.14)



**5.2.3.  $\text{Cu}_2^{\text{II}}\text{Cl}(\text{mmba})(\text{MeOH})_2(\text{H}_2\text{O})[\mathbf{12} - \text{MC}_{\text{Cu}(\text{II})\text{N}(\text{L3})} - \mathbf{4}]_2(\text{ClO}_4)_2$   
(C3)**

**Procedure**

**REN-CG-612-02**

**L3** (37 mg, 0.2 mmol, 1 eq) was dissolved in 12 ml methanol.  $\text{Cu}(\text{ClO}_4)_2 \cdot 6\text{H}_2\text{O}$  (111 mg, 0.3 mmol, 1.5 eq) was added and the green solution was stirred over night. Triethylamine (166  $\mu\text{L}$ , 1.2 mmol, 6 eq) was added and stirring was continued for 2 h. After filtration the reaction mixture was left for slow evaporation. Green crystals of **C2** suitable for X-ray diffraction could be isolated by filtration after one week.

**X-ray diffraction:** Table D.2 **IR** (ATR,  $\tilde{\nu}$  ( $\text{cm}^{-1}$ )): 3475 (w), 1574 (m), 1531 (m), 1515 (m), 1472 (w), 1421 (w), 1368 (m), 1285 (w), 1156 (w), 1091 (m), 1062 (m), 999 (w), 977 (w), 931 (w), 915 (m), 770 (w), 731 (m), 677 (w), 642 (w), 621 (m), 529 (w), 521 (w), 511 (m), 506 (w), 478 (w), 441 (w), 415 (vw). (Figure B.15)

**5.2.4.  $\text{Cu}^{\text{II}}(\mu_2 - \text{ClO}_4)(\text{MeOH})_2(\text{py})_4[\mathbf{12} - \text{MC}_{\text{Cu}(\text{II})\text{N}(\text{L3})} - \mathbf{4}]\text{ClO}_4$   
(C4)**

**Procedure**

**REN-CG-620-02-2**

Manganese pivalate (111 mg, 0.4 mmol, 2 eq) and **L3** (73 mg, 0.4 mmol, 2 eq) were stirred in 12 ml methanol. After adding pyridine (33  $\mu\text{L}$ , 0.4 mmol, 2 eq)  $\text{Cu}(\text{ClO}_4)_2 \cdot 6\text{H}_2\text{O}$  (74 mg, 0.2 mmol, 1 eq) was added and the mixture was stirred for 3.5 h, filtered and left for slow evaporation. Filtration was repeated within the first week to keep a clear green solution. Green crystals of **C4** (9.2 mg, 0.006 mmol, 14 % of theory (Cu)) were isolated by filtration after one week.

**X-ray diffraction:** Table D.3 **IR** (ATR,  $\tilde{\nu}$  ( $\text{cm}^{-1}$ )): 3495 (vw), 2926 (vw), 2833 (vw), 1606 (w), 1590 (vw), 1567 (w), 1541 (w), 1486 (w), 1474 (w), 1446 (w), 1380 (w), 1326 (vw), 1282 (vw), 1261 (w), 1239 (vw), 1215 (vw), 1153 (vw), 1095 (m), 1070 (m), 1045 (w), 1017 (w), 968 (w), 926 (m), 770 (w), 758 (w), 740 (w), 696 (m), 666 (w), 643 (w), 622 (m), 580 (w), 495 (w), 476 (w), 443 (vw), 431 (vw), 419 (w), 407 (vw). (Figure B.16)  
 **$^1\text{H-NMR}$**  ( $\text{DMSO-d}_6$ , 400 MHz,  $\delta$  (ppm)): 14.28 (s, 3H), 9.38 (s, 3H), 7.67 (d,  $J = 95.6$  Hz, 3H), 4.60 (s, 2H), 4.11 (s, 1H), 3.16 (s, 3H). (Figure C.28)

**5.2.5. [Co<sub>4</sub><sup>III/II</sup>(L3)<sub>4</sub>piv<sub>2</sub>(X)<sub>2</sub>(12 - MC<sub>Co(II)Co(III)N(L3) - 4)]<sub>2</sub> (X = NO or MeOH) (C5)</sub>****Procedure****REN-CG-600-02**

Cobalt pivalate (142 mg, 0.3 mmol, 1.5 eq) and **L3** (37 mg, 0.2 mmol, 1 eq) were dissolved in 12 ml methanol and stirred over night. Pyridine (93  $\mu$ L, 1.2 mmol, 6 eq) was added and stirring was continued for 3 h. The dark brown solution was filtered and left for slow evaporation. Dark brown crystals suitable for X-ray diffraction were isolated after two weeks.

**X-ray diffraction:** Table D.3 **IR** (ATR,  $\tilde{\nu}$  (cm<sup>-1</sup>)): 3361 (vw), 2955 (vw), 2924 (vw), 2817 (vw), 1579 (m), 1538 (m), 1480 (w), 1409 (w), 1354 (w), 1317 (w), 1222 (w), 1161 (vw), 1148 (vw), 1119 (vw), 1067 (vw), 1028 (w), 975 (w), 910 (w), 822 (vw), 769 (w), 737 (w), 711 (vw), 703 (vw), 667 (w), 653 (w), 639 (w), 608 (w), 576 (w), 562 (w), 511 (w), 505 (w), 493 (w), 485 (vw), 465 (w), 442 (w). (Figure B.17)

**5.2.6. [Cd<sub>14</sub><sup>II</sup>(L3)<sub>12</sub>( $\mu_6$  - O)(DMF)<sub>10</sub>](ClO<sub>4</sub>)<sub>2</sub> (C6)****Procedure****REN-CG-662-01b**

Cadmium perchlorate (94 mg, 0.3 mmol, 1 eq) and ligand **L3** (37 mg, 0.3 mmol, 1 eq) were dissolved in 12 ml dimethylformamide. Triethylamine (75  $\mu$ L, 0.6 mmol, 2 eq) was added to the colorless solution. After stirring for 3 h the solution was filtered. 5 ml of the filtrate were layered with 10 ml diethyl ether. After two weeks colorless crystals could be collected and identified as **1** (11 mg, 0.03 mmol, 24 % of theory (Cd)).

**X-ray diffraction:** Table D.4 **IR** (ATR,  $\tilde{\nu}$  (cm<sup>-1</sup>)): 3440 (vw), 2923 (w), 1668 (m), 1642 (s), 1583 (m), 1568 (m), 1532 (m), 1495 (m), 1466 (w), 1432 (m), 1415 (m), 1386 (m), 1370 (m), 1348 (m), 1255 (w), 1151 (vw), 1085 (m), 1064 (m), 1039 (w), 974 (w), 906 (m), 872 (w), 772 (w), 745 (m), 728 (w), 705 (w), 678 (w), 655 (m), 622 (m), 574 (w), 500 (w), 481 (w), 449 (w), 415 (vw). (Figure B.18)

**5.2.7.**  $\{\text{Cu}^{\text{II}}(\text{ClO}_4)(\text{MeOH})[\mathbf{12} - \text{MC}_{\text{Cu}(\text{II})\text{N}(\text{L2})} - \mathbf{4}]\}_2(\text{ClO}_4)_2 \cdot 2\text{MeOH}$   
**(C7)**

**Procedure****REN-CG-912-01a**

**L2** (46 mg, 0.3 mmol, 1 eq) and sodium hydroxide (12 mg, 0.3 mmol, 1 eq) were dissolved in 9 ml methanol.  $\text{Cu}(\text{ClO}_4)_2 \cdot 6\text{H}_2\text{O}$  (139 mg, 0.375 mmol, 1.25 eq) was dissolved in 9 ml methanol and added to the ligand solution. Stirring was continued over night. Then dark green mixture was filtered and divided into two parts. One half was sealed and stored in the freezer, the other half was left for slow evaporation. In both solutions occurred green crystals after two weeks. Bigger green crystals of **C7** (19.48 mg, 0.016 mmol, 44 % of theory (Cu)) were collected from the solution, which was stored in the freezer.

**X-ray diffraction:** Table D.4 **IR** (ATR,  $\tilde{\nu}$  ( $\text{cm}^{-1}$ )): 3585 (vw), 3264 (vw), 3215 (w), 1595 (w), 1556 (w), 1538 (w), 1531 (w), 1496 (w), 1446 (vw), 1378 (w), 1309 (w), 1289 (w), 1154 (w), 1124 (w), 1092 (m), 1065 (m), 1036 (m), 959 (w), 937 (w), 876 (w), 827 (vw), 774 (w), 744 (w), 702 (w), 679 (w), 656 (w), 619 (w), 573 (w), 526 (vw), 492 (vw), 471 (w), 449 (w), 415 (w). (Figure B.19)  **$^1\text{H-NMR}$**  ( $\text{DMSO-d}_6$ , 400 MHz,  $\delta$  (ppm)): 15.52 (s, 1H), 8.84 (s, 1H), 2.89 (s, 1H), -0.28 (s, 1H). (Figure C.29)

**5.2.8.**  $\{\text{Na}_2(\text{DMF})_3\text{Cu}^{\text{II}}\text{sal}_2[\text{Cu}^{\text{II}}(\mathbf{12} - \text{MC}_{\text{Cu}(\text{II})\text{N}(\text{L1})} - \mathbf{4})]\}_n$   
**(C8)**

**Procedure****REN-CG-211-07-2**

**L11** (115 mg, 0.75 mmol, 1 eq) and  $\text{NaOCCCl}_3$  (278 mg, 1.5 mmol, 2 eq) were dissolved in 7.5 ml DMF.  $\text{CuCl}_2$  (101 mg, 0.75 mmol, 1 eq) was dissolved in 7.5 ml DMF and added to the ligand solution, stirred and filtered. The dark green reaction mixture was separated in four crystallization approaches: Two times 5 ml layered with 10 ml  $\text{Et}_2\text{O}$  and two times 2.5 ml layered with a mixture of 5 ml  $\text{Et}_2\text{O}$  and 5 ml n-hexane. Green crystals of **C8** (31.32 mg, 0.018 mmol, 15 % of theory (Cu)) were collected from all solutions after one week.

**X-ray diffraction:** Table D.5 **IR** (ATR,  $\tilde{\nu}$  ( $\text{cm}^{-1}$ )): 1656 (w), 1601 (w), 1565 (w), 1523 (w), 1469 (w), 1454 (vw), 1434 (w), 1410 (vw), 1386 (w), 1377 (w), 1361 (w), 1310 (w), 1251 (w), 1143 (vw), 1094 (w), 1063 (vw), 1038 (vw), 1021 (vw), 941 (w), 893 (vw), 855 (vw), 836 (vw), 774 (vw), 759 (w), 703 (vw), 689 (w), 661 (w), 582 (w), 544 (vw), 478 (w), 428 (w), 419 (w), 403 (w). (Figure B.20)

**5.2.9. [O<sub>10</sub>py<sub>10</sub>(30 – MC<sub>V(V)N(L1)</sub> – 10)] (C9)****Procedure****REN-CG-222-05**

Trichlorotris(tetrahydrofuran)vanadium(III) (75 mg, 0.2 mmol, 1 eq) and **L1** (61 mg, 0.4 mmol, 2 eq) were dissolved in 15 ml acetone. Mn(ClO<sub>4</sub>)<sub>2</sub> · 6H<sub>2</sub>O (145 mg, 0.4 mmol, 2 eq) was added to the red solution. Pyridine (93 µl, 1.15 mmol, 6 eq) was added and the mixture was stirred over night. The blue solution was filtered and left for slow evaporation. Very dark crystals of **C9** (8.57 mg, 0.0029 mmol, 15 % of theory (V)) were isolated after two weeks.

**X-ray diffraction:** Table D.5 **IR** (ATR,  $\tilde{\nu}$  (cm<sup>-1</sup>)): 1703 (vw), 1597 (w), 1567 (w), 1500 (w), 1487 (w), 1465 (w), 1444 (w), 1409 (vw), 1341 (w), 1318 (w), 1245 (w), 1216 (w), 1153 (vw), 1097 (w), 1068 (w), 1039 (w), 956 (w), 925 (w), 865 (w), 752 (w), 691 (w), 674 (w), 637 (w), 621 (w), 576 (w), 533 (vw), 506 (vw), 496 (w), 476 (vw). (Figure B.21)

**5.2.10. [Mn(II)(HNEt<sub>3</sub>)<sub>2</sub>][12 – MC<sub>Mn(III)N(L1)</sub> – 4]( $\mu$ 4 – CO<sub>3</sub>)<sub>2</sub>]<sub>2</sub> · (H<sub>2</sub>O)<sub>8</sub>  
(C10)****Procedure****REN-CG-201-15**

MnCl<sub>2</sub> (126 mg, 1 mmol, 1 eq) and a mixture of NaOCCCl<sub>3</sub> (185 mg, 2 mmol, 2 eq) with **L1** (153 mg, 1 mmol, 1 eq) were dissolved in 6 ml ethanol each. NaOCN was suspended in 3 ml ethanol. Then all solutions were combined. Triethylamine (18 drops) was added dropwise. After stirring over night, the dark brown solution was filtered and left for slow evaporation. Brown needles of **C10** (82 mg, 0.031 mmol, 31 % of theory (Mn)) occurred after ten days and were collected after 19 days.

**X-ray diffraction:** Table D.6 **IR** (ATR,  $\tilde{\nu}$  (cm<sup>-1</sup>)): 1597 (w), 1567 (w), 1508 (w), 1471 (w), 1431 (w), 1387 (w), 1313 (w), 1255 (w), 1243 (w), 1155 (vw), 1098 (w), 1032 (w), 934 (w), 862 (w), 835 (vw), 750 (w), 679 (w), 649 (w), 614 (w), 586 (w), 534 (w), 482 (w), 407 (w). (Figure B.22)

**5.2.11. Mn(II)[H<sub>2</sub>NEt<sub>2</sub>[12 – MC<sub>Mn(III)N(L1) – 4](MeO)<sub>2</sub>]<sub>2</sub> · (MeOH)<sub>2</sub> (C11)</sub>**

**Procedure**

**REN-CG-221-15**

To MnCl<sub>2</sub> (126 mg, 1 mmol, 1 eq) and **L1** (153 mg, 1 mmol, 1 eq) was added a solution of diethylamine (311 µl, 3 mmol, 3 eq) in 10 ml methanol. Then 20 ml methanol were added and the brown solution was stirred over night, filtered, divided into two parts and left for slow evaporation. To one vial CuCl<sub>2</sub> was added. From the other vial dark brown crystals of **C11** (26.8 mg, 0.013 mmol, 24 % of theory (Mn)) could be isolated after four days.

**X-ray diffraction:** Table D.6 **IR** (ATR,  $\tilde{\nu}$  (cm<sup>-1</sup>)): 1595 (w), 1567 (w), 1495 (w), 1431 (w), 1383 (w), 1304 (w), 1257 (w), 1239 (w), 1155 (w), 1145 (w), 1099 (w), 1020 (w), 923 (w), 855 (w), 782 (w), 772 (w), 756 (w), 692 (w), 676 (w), 646 (w), 587 (w), 530 (w), 470 (w), 444 (w), 408 (vw). (Figure B.23)

**5.2.12. Co<sup>II</sup>(L4a)<sub>4</sub>(μ<sub>2</sub>Piv)<sub>2</sub>Piv<sub>2</sub> (C12)**

**Procedure**

**REN-CG-801-05-2**

Cobalt pivalate (178 mg, 0.2 mmol, 1 eq) and **L4** (73 mg, 0.3 mmol, 1,5 eq) were dissolved in 5 ml DMF each, mixed and stirred for 2 h. The solution was filtered, 5 ml of the reaction mixture were layered with 10 ml Et<sub>2</sub>O, 2 ml were used for slow diffusion experiments in 5 ml Et<sub>2</sub>O and the rest was left for slow evaporation. Red crystals of **C12** (5 mg, 0.003 mmol, 5 % of theory (Co)) were collected from all solutions.

**X-ray diffraction:** Table D.7 **IR** (ATR,  $\tilde{\nu}$  (cm<sup>-1</sup>)): 3122 (vw), 3069 (vw), 2951 (vw), 2919 (vw), 2860 (vw), 1681 (w), 1634 (w), 1607 (w), 1548 (w), 1475 (w), 1438 (vw), 1416 (w), 1392 (w), 1338 (w), 1229 (w), 1216 (w), 1192 (w), 1177 (w), 1149 (w), 1114 (w), 1088 (w), 1057 (w), 1026 (vw), 1003 (w), 964 (vw), 919 (w), 881 (vw), 773 (w), 745 (w), 722 (vw), 693 (w), 674 (w), 660 (w), 642 (w), 600 (w), 559 (vw), 533 (w), 480 (vw), 465 (w), 454 (w). (Figure B.24)

**5.2.13. [Cu<sup>II</sup>Cl<sub>2</sub>(L9)<sub>2</sub>(L9b)<sub>2</sub>(MeOH)<sub>2</sub>](ClO<sub>4</sub>)<sub>2</sub> (C13)**

**Procedure**

**REN-CG-2024-01**

**L9** (67 mg, 0.2 mmol, 2 eq) and MnCl<sub>2</sub> (25 mg, 0.2 mmol, 2 eq) were dissolved in 8 ml

methanol. The solution became dark brown upon addition of triethylamine (12 drops). Then  $\text{Cu}(\text{ClO}_4)_2 \cdot 6\text{H}_2\text{O}$  (37 mg, 0.1 mmol, 1 eq) was dissolved in 2 ml methanol and added to the reaction mixture. After stirring for 3 h, the solution was filtered and left for slow evaporation. Suitable crystals for X-ray diffraction of **C13** were collected after six days.

**X-ray diffraction:** Table D.7

#### 5.2.14. $[\text{Cu}_6^{\text{II}}(\text{L10b})_4(\text{ClO}_4)_2(\text{DMF})_6](\text{ClO}_4)_2$ (**C14**)

##### Procedure

REN-CG-2112-02b

**L10** (105 mg, 0.3 mmol, 1,5 eq) and  $\text{Cu}(\text{ClO}_4)_2 \cdot 6\text{H}_2\text{O}$  (139 mg, 0.375 mmol, 1,875 eq) were dissolved in 12 ml DMF. The green solution became dark brown after the addition of triethylamine (120  $\mu\text{l}$ , 0.9 mmol, 4,5 eq). Then tetrabutylammonium perchlorate (68 mg, 0.2 mmol, 1 eq) was added and the brown suspension was stirred over night. After filtration, 5 ml of the reaction mixture was layered with 10 ml  $\text{Et}_2\text{O}$ . Green crystals of **C14** (13.4 mg, 0.0058 mmol, 22 % of theory (Cu)) were collected after seven days.

**X-ray diffraction:** Table D.8 **IR** (ATR,  $\tilde{\nu}$  ( $\text{cm}^{-1}$ )): 3265 (vw), 3233 (vw), 2930 (vw), 1645 (w), 1611 (w), 1586 (w), 1538 (w), 1497 (vw), 1463 (w), 1436 (w), 1419 (w), 1370 (w), 1327 (w), 1302 (w), 1267 (w), 1254 (w), 1155 (vw), 1074 (w), 1045 (w), 1026 (w), 889 (vw), 863 (w), 760 (w), 713 (w), 701 (w), 685 (vw), 660 (w), 620 (w), 587 (vw), 571 (w), 522 (vw), 511 (w), 418 (vw). (Figure B.25)

#### 5.2.15. $\text{Cu}_2^{\text{II}}(\text{L10cH})_2\text{Cl}_2$ (**C15**)

##### Procedure

REN-CG-2122-06c

$\text{Mn}(\text{ClO}_4)_2 \cdot 6\text{H}_2\text{O}$  (109 mg, 0.3 mmol, 1,5 eq),  $\text{CuCl}_2$  (26 mg, 0.2 mmol, 1 eq), **L10** (105 mg, 0.3 mmol, 1,5 eq) and triethylamine (125  $\mu\text{l}$ , 0.9 mmol, 4,5 eq) were mixed in 15 ml acetonitrile, heated at 87 °C for 30 min and let to cool down again. The dark brown solution with dark brown precipitate was filtered. 4 ml of the reaction solution was layered with a mixture of 5 ml  $\text{Et}_2\text{O}$  and 5 ml n-hexane. Green crystals of **C15** suitable for X-ray diffraction were collected after 19 days.

**X-ray diffraction:** Table D.8 **IR** (ATR,  $\tilde{\nu}$  ( $\text{cm}^{-1}$ )): 1611 (vw), 1593 (w), 1558 (vw), 1518 (vw), 1480 (vw), 1465 (vw), 1444 (vw), 1421 (vw), 1347 (vw), 1322 (vw), 1293 (vw), 1273 (vw), 1254 (vw), 1228 (vw), 1208 (vw), 1180 (vw), 1151 (vw), 1110 (vw), 1093 (vw), 1047

(vw), 1023 (vw), 987 (vw), 964 (vw), 945 (vw), 888 (vw), 860 (vw), 779 (vw), 764 (vw), 747 (w), 702 (vw), 662 (vw), 633 (vw), 612 (vw), 594 (vw), 542 (vw), 523 (vw), 481 (vw), 464 (vw), 419 (vw). (Figure B.26)

### 5.2.16. $\text{Co}_2^{\text{II}}(\text{L10d})_2$ (**C16**)

#### Procedure

REN-CG-2102-03-2b

$\text{Co}(\text{ClO}_4)_2 \cdot 6\text{H}_2\text{O}$  (137 mg, 0.375 mmol, 1,875 eq) and **L10** (105 mg, 0.3 mmol, 1,5 eq) were dissolved in 15 ml acetone. Then triethylamine (120  $\mu\text{l}$ , 0.9 mmol, 4,5 eq) and tetrabutylammonium perchlorate (68 mg, 0.2 mmol, 1 eq) were added. The mixture was stirred for 2 h and filtered. 4 ml of the reaction solution was layered with 10 ml  $\text{Et}_2\text{O}$  (three times). Pink needles of **C16** (5 mg, 0.0062 mmol, 5% of theory (ligand)) were collected after three days. **X-ray diffraction:** Table D.9 **IR** (ATR,  $\tilde{\nu}$  ( $\text{cm}^{-1}$ )): 1713 (vw), 1595 (w), 1569 (w), 1544 (vw), 1484 (w), 1455 (w), 1441 (w), 1364 (vw), 1329 (w), 1298 (w), 1265 (w), 1221 (w), 1152 (w), 1117 (w), 1093 (w), 1046 (w), 1027 (w), 1005 (vw), 982 (w), 943 (w), 908 (vw), 871 (w), 825 (w), 793 (vw), 778 (vw), 751 (w), 726 (w), 653 (w), 627 (vw), 609 (w), 574 (w), 558 (w), 497 (w), 477 (w), 446 (vw), 417 (w). (Figure B.27)

### 5.2.17. $[\text{Ni}_6^{\text{II}}(\text{L10})_2(\text{L10H})_2(\mu - \text{O}_2\text{COMe})_2(\text{MeOH})_6]$ (**C17**)

#### Procedure

REN-CG-2132-06b

$\text{Ni}(\text{ClO}_4)_2 \cdot 6\text{H}_2\text{O}$  (137 mg, 0.375 mmol, 1,875 eq) and **L10** (105 mg, 0.3 mmol, 1,5 eq) were dissolved in 15 ml methanol. Then triethylamine (120  $\mu\text{l}$ , 0.9 mmol, 4,5 eq) and tetrabutylammonium perchlorate (68 mg, 0.2 mmol, 1 eq) were added. The mixture was stirred for 2 h, filtered and left for slow evaporation. **C17** (5.5 mg, 0.0024 mmol, 4% of theory (ligand)) was isolated as green crystalline precipitate after 18 days.

**X-ray diffraction:** Table D.9 **IR** (ATR,  $\tilde{\nu}$  ( $\text{cm}^{-1}$ )): 1592 (w), 1572 (vw), 1557 (vw), 1474 (w), 1454 (w), 1437 (w), 1295 (w), 1260 (vw), 1232 (vw), 1092 (w), 1055 (w), 1040 (w), 975 (w), 939 (vw), 898 (vw), 756 (w), 734 (vw), 685 (vw), 643 (vw), 621 (vw), 524 (vw), 500 (vw), 470 (vw), 452 (vw), 427 (vw). (Figure B.28)

## 6. Bibliography

- [1] J. M. Clemente-Juan, E. Coronado, A. Gaita-Ariño, *Chemical Society Reviews* **2012**, *41*, 7464–7478.
- [2] J. Camarero, E. Coronado, *Journal of Materials Chemistry* **2009**, *19*, 1678–1684.
- [3] S. Sanvito, *Chemical Society Reviews* **2011**, *40*, 3336–3355.
- [4] R. Sessoli, D. Gatteschi, A. Caneschi, M. A. Novak, *Nature* **1993**, *365*, 141–143.
- [5] H. L. C. Feltham, S. Brooker, *Coordination Chemistry Reviews* **2014**, *276*, 1–33.
- [6] K. R. Dunbar, *Inorganic Chemistry* **2012**, *51*, 12055–12058.
- [7] D. N. Woodruff, R. E. P. Winpenny, R. A. Layfield, *Chemical Reviews* **2013**, *113*, 5110–5148.
- [8] R. Sessoli, A. K. Powell, *Coordination Chemistry Reviews* **2009**, *253*, 2328–2341.
- [9] G. Christou, D. Gatteschi, D. N. Hendrickson, R. Sessoli, *MRS Bulletin* **2000**, *25*, 66–71.
- [10] D. Gatteschi, R. Sessoli, *Angewandte Chemie International Edition* **2003**, *42*, 268–297.
- [11] A. K. Powell, S. L. Heath, D. Gatteschi, L. Pardi, R. Sessoli, G. Spina, F. Del Giallo, F. Pieralli, *Journal of the American Chemical Society* **1995**, *117*, 2491–2502.
- [12] M. Murugesu, M. Habrych, W. Wernsdorfer, K. A. Abboud, G. Christou, *Journal of the American Chemical Society* **2004**, *126*, 4766–4767.
- [13] A. M. Ako, I. J. Hewitt, V. Mereacre, R. Clérac, W. Wernsdorfer, C. E. Anson, A. K. Powell, *Angewandte Chemie* **2006**, *118*, 5048–5051.
- [14] S. Hill, S. Datta, J. Liu, R. Inglis, C. J. Milios, P. L. Feng, J. J. Henderson, E. d. Barco, E. K. Brechin, D. N. Hendrickson, *Dalton Transactions* **2010**, *39*, 4693–4707.
- [15] F. Neese, D. A. Pantazis, *Faraday Discussions* **2010**, *148*, 229–238.
- [16] O. Waldmann, *Inorganic Chemistry* **2007**, *46*, 10035–10037.
- [17] N. Ishikawa, *Polyhedron* **2007**, *26*, 2147–2153.
- [18] J. M. Frost, K. L. M. Harriman, M. Murugesu, *Chem. Sci.* **2016**, *7*, 2470–2491.
- [19] *Chemistry – A European Journal* **2010**, *16*, 13458–13464.



- 
- [20] D. V. Azamat, A. G. Badalyan, A. Dejneka, V. A. Trepakov, L. Jastrabik, Z. Frait, *Journal of Physics and Chemistry of Solids* **2012**, *73*, 822–826.
- [21] J. Vallejo, A. Pascual-Álvarez, J. Cano, I. Castro, M. Julve, F. Lloret, J. Krzystek, G. De Munno, D. Armentano, W. Wernsdorfer, R. Ruiz-García, E. Pardo, *Angewandte Chemie International Edition* **2013**, *52*, 14075–14079.
- [22] R. Boča, *Coordination Chemistry Reviews* **2004**, *248*, 757–815.
- [23] C. Duboc, *Chemical Society Reviews* **2016**, *45*, 5834–5847.
- [24] R. Clérac, *Angewandte Chemie International Edition* **2012**, *51*, 7079–7080.
- [25] C. J. Milios, A. Vinslava, W. Wernsdorfer, S. Moggach, S. Parsons, S. P. Perlepes, G. Christou, E. K. Brechin, *Journal of the American Chemical Society* **2007**, *129*, 2754–2755.
- [26] T. C. Stamatatos, S. Dionyssopoulou, G. Efthymiou, P. Kyritsis, C. P. Raptopoulou, A. Terzis, R. Vicente, A. Escuer, S. P. Perlepes, *Inorganic Chemistry* **2005**, *44*, 3374–3376.
- [27] R. Inglis, L. F. Jones, C. J. Milios, S. Datta, A. Collins, S. Parsons, W. Wernsdorfer, S. Hill, S. P. Perlepes, S. Piligkos, E. K. Brechin, *Dalton Transactions* **2009**, 3403–3412.
- [28] R. Inglis, L. F. Jones, K. Mason, A. Collins, S. A. Moggach, S. Parsons, S. P. Perlepes, W. Wernsdorfer, E. K. Brechin, *Chemistry – A European Journal* **2008**, *14*, 9117–9121.
- [29] T. C. Stamatatos, D. Foguet-Albiol, S.-C. Lee, C. C. Stoumpos, C. P. Raptopoulou, A. Terzis, W. Wernsdorfer, S. O. Hill, S. P. Perlepes, G. Christou, *Journal of the American Chemical Society* **2007**, *129*, 9484–9499.
- [30] M. W. Wemple, D. M. Adams, K. S. Hagen, K. Folting, D. N. Hendrickson, G. Christou, *Journal of the Chemical Society Chemical Communications* **1995**, 1591–1593.
- [31] G. Aromí, J.-P. Claude, M. J. Knapp, J. C. Huffman, D. N. Hendrickson, G. Christou, *Journal of the American Chemical Society* **1998**, *120*, 2977–2978.
- [32] G. L. Abbati, A. Cornia, A. C. Fabretti, A. Caneschi, D. Gatteschi, *Inorganic Chemistry* **1998**, *37*, 1430–1431.
-

- [33] D. Gatteschi, R. Sessoli, J. Villain, *Molecular Nanomagnets*, Oxford University Press, **2006**.
- [34] P. L. Feng, C. Koo, J. J. Henderson, M. Nakano, S. Hill, E. del Barco, D. N. Hendrickson, *Inorganic Chemistry* **2008**, *47*, 8610–8612.
- [35] T. Gupta, G. Rajaraman, *Chemical Communications* **2016**, DOI 10.1039/C6CC01251E.
- [36] L. Ungur, M. Thewissen, J.-P. Costes, W. Wernsdorfer, L. F. Chibotaru, *Inorganic Chemistry* **2013**, *52*, 6328–6337.
- [37] S. K. Langley, D. P. Wielechowski, V. Vieru, N. F. Chilton, B. Moubaraki, B. F. Abrahams, L. F. Chibotaru, K. S. Murray, *Angewandte Chemie International Edition* **2013**, *52*, 12014–12019.
- [38] R. Ishikawa, R. Miyamoto, H. Nojiri, B. K. Breedlove, M. Yamashita, *Inorganic Chemistry* **2013**, *52*, 8300–8302.
- [39] M. S. Lah, V. L. Pecoraro, *Journal of the American Chemical Society* **1989**, *111*, 7258–7259.
- [40] J. Jankolovits, J. W. Kampf, V. L. Pecoraro, *Inorganic Chemistry* **2014**, *53*, 7534–7546.
- [41] C. Dendrinou-Samara, A. N. Papadopoulos, D. A. Malamataris, A. Tarushi, C. P. Raptopoulou, A. Terzis, E. Samaras, D. P. Kessissoglou, *Journal of Inorganic Biochemistry* **2005**, *99*, 864–875.
- [42] A. Athanasopoulou, L. Carrella, E. Rentschler, A. A. Athanasopoulou, L. M. Carrella, E. Rentschler, *Inorganics* **2018**, *6*, 66.
- [43] Y. Qin, Q. Gao, Y. Chen, W. Liu, F. Lin, X. Zhang, Y. Dong, Y. Li, *Journal of Cluster Science* **2017**, *28*, 891–903.
- [44] J. Jankolovits, C. M. Andolina, J. W. Kampf, K. N. Raymond, V. L. Pecoraro, *Angewandte Chemie International Edition* **2011**, *50*, 9660–9664.
- [45] A. A. Athanasopoulou, C. Gamer, L. Völker, E. Rentschler in *Novel Magnetic Nanostructures*, (Eds.: N. Domracheva, M. Caporali, E. Rentschler), Elsevier, **2018**, pp. 51–96.
- [46] G. Mezei, C. M. Zaleski, V. L. Pecoraro, *Chemical Reviews* **2007**, *107*, 4933–5003.

- [47] A. Alhassanat, C. Gamer, A. Rauguth, A. A. Athanasopoulou, J. Sutter, C. Luo, H. Ryll, F. Radu, A. A. Sapozhnik, T. Mashoff, E. Rentschler, H. J. Elmers, *Physical Review B* **2018**, *98*, 064428.
- [48] P. Happ, A. Sapozhnik, J. Klanke, P. Czaja, A. Chernenkaya, K. Medjanik, S. Schuppler, P. Nagel, M. Merz, E. Rentschler, H. J. Elmers, *Physical Review B* **2016**, *93*, DOI 10.1103/PhysRevB.93.174404.
- [49] V. L. Pecoraro, A. J. Stemmler, B. R. Gibney, J. J. Bodwin, H. Wang, J. W. Kampf, A. Barwinski in *Progress in Inorganic Chemistry*, Wiley-Blackwell, **2007**, pp. 83–177.
- [50] E. R. Trivedi, S. V. Eliseeva, J. Jankolovits, M. M. Olmstead, S. Petoud, V. L. Pecoraro, *Journal of the American Chemical Society* **2014**, *136*, 1526–1534.
- [51] C. Y. Chow, E. R. Trivedi, V. Pecoraro, C. M. Zaleski, *Comments on Inorganic Chemistry* **2015**, *35*, 214–253.
- [52] J. C. Lutter, C. M. Zaleski, V. L. Pecoraro in *Advances in Inorganic Chemistry*, Vol. 71, (Eds.: R. van Eldik, R. Puchta), Academic Press, **2018**, pp. 177–246.
- [53] C. M. Zaleski, S. Tricard, E. C. Depperman, W. Wernsdorfer, T. Mallah, M. L. Kirk, V. L. Pecoraro, *Inorganic Chemistry* **2011**, *50*, 11348–11352.
- [54] T. T. Boron, J. C. Lutter, C. I. Daly, C. Y. Chow, A. H. Davis, A. Nimthong-Roldán, M. Zeller, J. W. Kampf, C. M. Zaleski, V. L. Pecoraro, *Inorganic Chemistry* **2016**, *55*, 10597–10607.
- [55] F. Cao, R.-M. Wei, J. Li, L. Yang, Y. Han, Y. Song, J.-M. Dou, *Inorganic Chemistry* **2016**, DOI 10.1021/acs.inorgchem.6b00255.
- [56] Q.-W. Li, J.-L. Liu, J.-H. Jia, Y.-C. Chen, J. Liu, L.-F. Wang, M.-L. Tong, *Chemical Communications* **2015**, *51*, 10291–10294.
- [57] P. Happ, C. Plenk, E. Rentschler, *Coordination Chemistry Reviews* **2015**, *289*, 238–260.
- [58] P. Happ, E. Rentschler, *Dalton transactions (Cambridge England : 2003)* **2014**, *43*, 15308–15312.
- [59] H. Oshio, M. Nihei, A. Yoshida, H. Nojiri, M. Nakano, A. Yamaguchi, Y. Karaki, H. Ishimoto, *Chemistry – A European Journal* **2005**, *11*, 843–848.

- [60] Z.-W. Li, P.-P. Yang, L.-C. Li, D.-Z. Liao, *Inorganica Chimica Acta* **2009**, *362*, 3381–3384.
- [61] O. Kahn, P. Tola, J. Galy, H. Coudanne, *Journal of the American Chemical Society* **1978**, *100*, 3931–3933.
- [62] O. Kahn, J. Galy, Y. Journaux, J. Jaud, I. Morgenstern-Badarau, *Journal of the American Chemical Society* **1982**, *104*, 2165–2176.
- [63] O. Kahn, *VCH Publishers Inc.(USA) 1993* **1993**, 393.
- [64] T. T. Boron, J. W. Kampf, V. L. Pecoraro, *Inorganic Chemistry* **2010**, *49*, 9104–9106.
- [65] R. G. Pearson, *Journal of the American Chemical Society* **1963**, *85*, 3533–3539.
- [66] C. Y. Chow, S. V. Eliseeva, E. R. Trivedi, T. N. Nguyen, J. W. Kampf, S. Petoud, V. L. Pecoraro, *Journal of the American Chemical Society* **2016**, *138*, 5100–5109.
- [67] G.-Y. An, C.-M. Ji, A.-L. Cui, H.-Z. Kou, *Inorganic Chemistry* **2011**, *50*, 1079–1083.
- [68] B. Gole, R. Chakrabarty, S. Mukherjee, Y. Song, P. S. Mukherjee, *Dalton Transactions* **2010**, *39*, 9766–9778.
- [69] F. E. Kakaroni, A. Collet, E. Sakellari, D. I. Tzimopoulos, M. Siczek, T. Lis, M. Murrie, C. J. Milios, *Dalton Transactions* **2017**, *47*, 58–61.
- [70] J. Martínez-Lillo, L.-M. Chamoreau, A. Proust, M. Verdaguer, P. Gouzerh, *Comptes Rendus Chimie* **2012**, *15*, 889–894.
- [71] G. A. Craig, M. Murrie, *Chem. Soc. Rev.* **2015**, *44*, 2135–2147.
- [72] A. Alhassanat, L. Völker, C. Gamer, A. Rauguth, A. Kredel, C. Luo, F. Radu, A. A. Sapozhnik, T. Mashoff, E. Rentschler, H. J. Elmers, **2018**, in preparation.
- [73] D. Griffith, K. Krot, J. Comiskey, K. B. Nolan, C. J. Marmion, *Dalton Transactions* **2007**, 137–147.
- [74] D. M. Griffith, A. Haughey, S. Chahal, H. Müller-Bunz, C. J. Marmion, *Inorganica Chimica Acta* **2010**, *363*, 2333–2337.
- [75] F. Wang, C. Chen, G. Deng, C. Xi, *The Journal of Organic Chemistry* **2012**, *77*, 4148–4151.
- [76] K. E. Ryu, B. R. Kim, G. H. Sung, H. J. Yoon, Y.-J. Yoon, *Synlett* **2015**, *26*, 1985–1990.

- [77] N. F. Chilton, R. P. Anderson, L. D. Turner, A. Soncini, K. S. Murray, *Journal of Computational Chemistry* **2013**, *34*, 1164–1175.
- [78] D. J. Sutor, *Journal of the Chemical Society (Resumed)* **1963**, 1105–1110.
- [79] A. V. Pavlishchuk, S. V. Kolotilov, M. Zeller, O. V. Shvets, I. O. Fritsky, S. E. Lofland, A. W. Addison, A. D. Hunter, *European Journal of Inorganic Chemistry* **2011**, *2011*, 4826–4836.
- [80] A. V. Pavlishchuk, S. V. Kolotilov, M. Zeller, L. K. Thompson, I. O. Fritsky, A. W. Addison, A. D. Hunter, *European Journal of Inorganic Chemistry* **2010**, *2010*, 4851–4858.
- [81] Y. Song, J.-C. Liu, Y.-J. Liu, D.-R. Zhu, J.-Z. Zhuang, X.-Z. You, *Inorganica Chimica Acta* **2000**, *305*, 135–142.
- [82] C. McDonald, T. Whyte, S. M. Taylor, S. Sanz, E. K. Brechin, D. Gaynor, L. F. Jones, *CrystEngComm* **2013**, *15*, 6672–6681.
- [83] C. Janiak, H.-J. Meyer, D. Gudat, R. Alsfasser, H.-J. Meyer, *Riedel Moderne Anorganische Chemie*, De Gruyter, Berlin, Boston, **2012**.
- [84] J. Cirera, E. Ruiz, S. Alvarez, *Organometallics* **2005**, *24*, 1556–1562.
- [85] Y. Zhang, R. Lv, J. Wang, L. Yang, S. Liao, J. Tian, W. Gu, X. Liu, *Dalton Transactions* **2016**, *45*, 3247–3250.
- [86] G. Psomas, A. J. Stemmler, C. Dendrinou-Samara, J. J. Bodwin, M. Schneider, M. Alexiou, J. W. Kampf, D. P. Kessissoglou, V. L. Pecoraro, *Inorganic Chemistry* **2001**, *40*, 1562–1570.
- [87] M. Alexiou, C. Dendrinou-Samara, C. P. Raptopoulou, A. Terzis, D. P. Kessissoglou, *Inorganic Chemistry* **2002**, *41*, 4732–4738.
- [88] P. E. Kruger, V. McKee, *Chemical Communications* **1997**, 1341–1342.
- [89] V. V. Pavlishchuk, S. V. Kolotilov, A. W. Addison, M. J. Prushan, D. Schollmeyer, L. K. Thompson, T. Weyhermüller, E. A. Goreshnik, *Dalton Transactions* **2003**, 1587–1595.
- [90] D. Gaynor, Z. A. Starikova, W. Haase, K. B. Nolan, *Journal of the Chemical Society Dalton Transactions* **2001**, 1578–1581.
- [91] C. McDonald, D. W. Williams, P. Comar, S. J. Coles, T. D. Keene, M. B. Pitak, E. K. Brechin, L. F. Jones, *Dalton Transactions* **2015**, *44*, 13359–13368.

- [92] B. R. Gibney, D. P. Kessissoglou, J. W. Kampf, V. L. Pecoraro, *Inorganic Chemistry* **1994**, *33*, 4840–4849.
- [93] D. Gaynor, Z. A. Starikova, S. Ostrovsky, W. Haase, K. B. Nolan, *Chemical Communications* **2002**, 506–507.
- [94] C. McDonald, S. Sanz, E. K. Brechin, M. K. Singh, G. Rajaraman, D. Gaynor, L. F. Jones, *RSC Advances* **2014**, *4*, 38182–38191.
- [95] T. K. Si, S. Chakraborty, A. K. Mukherjee, M. G. B. Drew, R. Bhattacharyya, *Polyhedron* **2008**, *27*, 2233–2242.
- [96] C. Atzeri, V. Marzaroli, M. Quaretti, J. R. Travis, L. Di Bari, C. M. Zaleski, M. Tegoni, *Inorganic Chemistry* **2017**, *56*, 8257–8269.
- [97] C. Y. Chow, R. Guillot, E. Rivière, J. W. Kampf, T. Mallah, V. L. Pecoraro, *Inorganic Chemistry* **2016**, *55*, 10238–10247.
- [98] M. S. Lah, M. L. Kirk, W. Hatfield, V. L. Pecoraro, *Journal of the Chemical Society Chemical Communications* **1989**, 1606–1608.
- [99] G. Psomas, C. Dendrinou-Samara, M. Alexiou, A. Tsohos, C. P. Raptopoulou, A. Terzis, D. P. Kessissoglou, *Inorganic Chemistry* **1998**, *37*, 6556–6557.
- [100] J. Herring, M. Zeller, C. M. Zaleski, *Acta Crystallographica Section E: Structure Reports Online* **2011**, *67*, m419–m420.
- [101] A. B. Lago, J. Pasán, L. Cañadillas-Delgado, O. Fabelo, F. J. M. Casado, M. Julve, F. Lloret, C. Ruiz-Pérez, *New Journal of Chemistry* **2011**, *35*, 1817–1822.
- [102] E. Gumienna-Kontecka, I. A. Golenya, N. M. Dudarenko, A. Dobosz, M. Haukka, I. O. Fritsky, J. Swiatek-Kozłowska, *New Journal of Chemistry* **2007**, *31*, 1798–1805.
- [103] S.-X. Liu, S. Lin, B.-Z. Lin, C.-C. Lin, J.-Q. Huang, *Angewandte Chemie International Edition* **2001**, *40*, 1084–1087.
- [104] M. R. Azar, T. T. Boron, J. C. Lutter, C. I. Daly, K. A. Zegalia, R. Nimthong, G. M. Ferrence, M. Zeller, J. W. Kampf, V. L. Pecoraro, C. M. Zaleski, *Inorganic Chemistry* **2014**, *53*, 1729–1742.
- [105] B. R. Gibney, H. Wang, J. W. Kampf, V. L. Pecoraro, *Inorganic Chemistry* **1996**, *35*, 6184–6193.
- [106] D. P. Kessissoglou, J. J. Bodwin, J. Kampf, C. Dendrinou-Samara, V. L. Pecoraro, *Inorganica Chimica Acta* **2002**, *331*, 73–80.

- [107] D. P. Kessiosoglou, J. Kampf, V. L. Pecoraro, *Polyhedron* **1994**, *13*, 1379–1391.
- [108] C. Gamer, Derivate der Salicylhydroxamsäure als Komplexliganden in Metallakronen mit hoher magnetischer Anisotropie, Diplomarbeit, Johannes Gutenberg-Universität, Mainz, **2015**.
- [109] A. A. Alaimo, E. S. Koumoussi, L. Cunha-Silva, L. J. McCormick, S. J. Teat, V. Psycharis, C. P. Raptopoulou, S. Mukherjee, C. Li, S. D. Gupta, A. Escuer, G. Christou, T. C. Stamatatos, *Inorganic Chemistry* **2017**, *56*, 10760–10774.
- [110] S. Accorsi, A.-L. Barra, A. Caneschi, G. Chastanet, A. Cornia, A. C. Fabretti, D. Gatteschi, C. Mortalò, E. Olivieri, F. Parenti, P. Rosa, R. Sessoli, L. Sorace, W. Wernsdorfer, L. Zobbi, *Journal of the American Chemical Society* **2006**, *128*, 4742–4755.
- [111] A. Wilson, J. Lawrence, E.-C. Yang, M. Nakano, D. N. Hendrickson, S. Hill, *Physical Review B* **2006**, *74*, 140403.
- [112] A. Wilson, E.-C. Yang, D. N. Hendrickson, S. Hill, *Polyhedron* **2007**, *26*, 2065–2068.
- [113] K. S. Cole, R. H. Cole, *The Journal of Chemical Physics* **1941**, *9*, 341–351.
- [114] Y.-N. Guo, G.-F. Xu, Y. Guo, J. Tang, *Dalton Transactions* **2011**, *40*, 9953–9963.
- [115] J. Zhang, H. Chen, C. Lin, Z. Liu, C. Wang, Y. Zhang, *Journal of the American Chemical Society* **2015**, *137*, 12990–12996.
- [116] G. Sivakumar, A. Vijeta, M. Jeganmohan, *Chemistry – A European Journal* **2016**, *22*, 5899–5903.
- [117] J. Tong, S. Demeshko, M. John, S. Dechert, F. Meyer, *Inorganic Chemistry* **2016**, *55*, 4362–4372.
- [118] R. B. Samulewski, J. C. da Rocha, O. Fuganti, R. Stieler, E. S. Lang, M. d. G. Fialho Vaz, F. S. Nunes, *Journal of Molecular Structure* **2010**, *984*, 354–358.
- [119] D. A. Brown, W. Errington, W. K. Glass, W. Haase, T. J. Kemp, H. Nimir, S. M. Ostrovsky, R. Werner, *Inorganic Chemistry* **2001**, *40*, 5962–5971.
- [120] D. Black, A. J. Blake, K. P. Dancey, A. Harrison, M. McPartlin, S. Parsons, P. A. Tasker, G. Whittaker, M. Schröder, *Journal of the Chemical Society Dalton Transactions* **1998**, 3953–3960.
- [121] M. J. Murphy, P. M. Usov, F. J. Rizzuto, C. J. Kepert, D. M. D’Alessandro, *New Journal of Chemistry* **2014**, *38*, 5856–5860.

- [122] A. Mukherjee, F. Lloret, R. Mukherjee, *Inorganic Chemistry* **2008**, *47*, 4471–4480.
- [123] L. Rodríguez, E. Labisbal, A. Sousa-Pedrares, J. A. García-Vázquez, J. Romero, M. L. Durán, J. A. Real, A. Sousa, *Inorganic Chemistry* **2006**, *45*, 7903–7914.
- [124] M. Fondo, A. M. García-Deibe, N. Ocampo, J. Sanmartín, M. R. Bermejo, A. L. Llamas-Saiz, *Dalton Transactions* **2006**, 4260–4270.
- [125] W. K. Robinson, S. A. Friedberg, *Physical Review* **1960**, *117*, 402–408.
- [126] D. Bittner, PhD thesis, Johannes Gutenberg - Universität, Mainz, **2018**.
- [127] J. Martínez-Lillo, A.-R. Tomsa, Y. Li, L.-M. Chamoreau, E. Cremades, E. Ruiz, A.-L. Barra, A. Proust, M. Verdaguer, P. Gouzerh, *Dalton Transactions* **2012**, *41*, 13668–13681.
- [128] J. Martínez-Lillo, J. Cano, W. Wernsdorfer, E. K. Brechin, *Chemistry – A European Journal* **2015**, *21*, 8790–8798.
- [129] A.-R. Tomsa, J. Martínez-Lillo, Y. Li, L.-M. Chamoreau, K. Boubekeur, F. Farias, M. A. Novak, E. Cremades, E. Ruiz, A. Proust, M. Verdaguer, P. Gouzerh, *Chemical Communications* **2010**, *46*, 5106–5108.
- [130] C. L. Bell, C. N. V. Nambury, L. Bauer, *The Journal of Organic Chemistry* **1964**, *29*, 2873–2877.
- [131] E. Ruiz, P. Alemany, S. Alvarez, J. Cano, *Journal of the American Chemical Society* **1997**, *119*, 1297–1303.
- [132] R. B. Woodward, R. Hoffmann, *The Conservation of Orbital Symmetry*, Google-Books-ID: tTsXBQAAQBAJ, Elsevier, **2013**.
- [133] A. Mukherjee, F. Lloret, R. Mukherjee, *European Journal of Inorganic Chemistry*, *2010*, 1032–1042.
- [134] S. M. Ostrovsky, K. Falk, J. Pelikan, D. A. Brown, Z. Tomkowicz, W. Haase, *Inorganic Chemistry* **2006**, *45*, 688–694.
- [135] A. W. Addison, T. Nageswara Rao, J. Reedijk, J. v. Rijn, G. C. Verschoor, *Journal of the Chemical Society Dalton Transactions* **1984**, 1349–1356.
- [136] Y. Dussart, C. Harding, P. Dalgaard, C. McKenzie, R. Kadirvelraj, V. McKee, J. Nelson, *Journal of the Chemical Society Dalton Transactions* **2002**, 1704–1713.
- [137] D. A. Palmer, R. Van Eldik, *Chemical Reviews* **1983**, *83*, 651–731.
- [138] M. Kato, T. Ito, *Inorganic Chemistry* **1985**, *24*, 504–508.



- [139] N. Kitajima, S. Hikichi, M. Tanaka, Y. Morooka, *Journal of the American Chemical Society* **1993**, *115*, 5496–5508.
- [140] B. Kersting, *Angewandte Chemie International Edition* **2001**, *40*, 3987–3990.
- [141] K. K. Nanda, L. K. Thompson, J. N. Bridson, K. Nag, *Journal of the Chemical Society Chemical Communications* **1994**, 1337–1338.
- [142] A. Arroyave, A. Lennartson, A. Dragulescu-Andrasi, K. S. Pedersen, S. Piligkos, S. A. Stoian, S. M. Greer, C. Pak, O. Hietsoi, H. Phan, S. Hill, C. J. McKenzie, M. Shatruk, *Inorganic Chemistry* **2016**, *55*, 5904–5913.
- [143] G. M. Sheldrick, *Acta Crystallographica Section A* **2015**, *71*, 3–8.
- [144] G. M. Sheldrick, *Acta Crystallographica Section C* **2015**, *71*, 3–8.
- [145] O. V. Dolomanov, L. J. Bourhis, R. J. Gildea, J. A. K. Howard, H. Puschmann, *Journal of Applied Crystallography* **2009**, *42*, 339–341.
- [146] E. Bill, julX - Simulation of molecular magnetic data, **2008**.
- [147] G. A. Bain, J. F. Berry, *Journal of Chemical Education* **2008**, *85*, 532.
- [148] T. L. Fletcher, M. J. Namkung, H.-L. Pan, C. A. Cole, *Journal of Medicinal Chemistry* **1971**, *14*, 1113–1115.
- [149] J. W. Bode, Y. Hachisu, T. Matsuura, K. Suzuki, *Organic Letters* **2003**, *5*, 391–394.

## A. Additional Figures

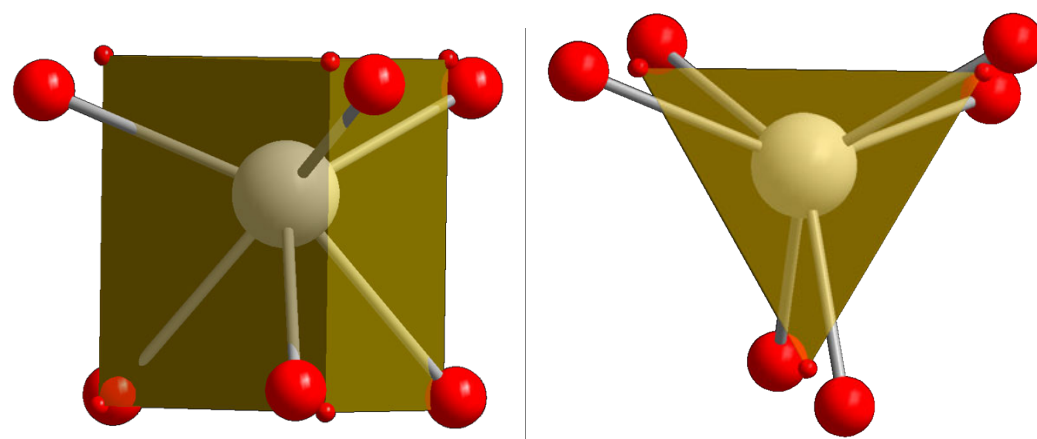


Figure A.1.: Presentation of the coordination environment of Cd2 in **C6** and the comparison with the ideal trigonal prismatic polyhedron. Color code: Gray = Cadmium, Red = Oxygen. Red dots represent the edges of the ideal polyhedron.

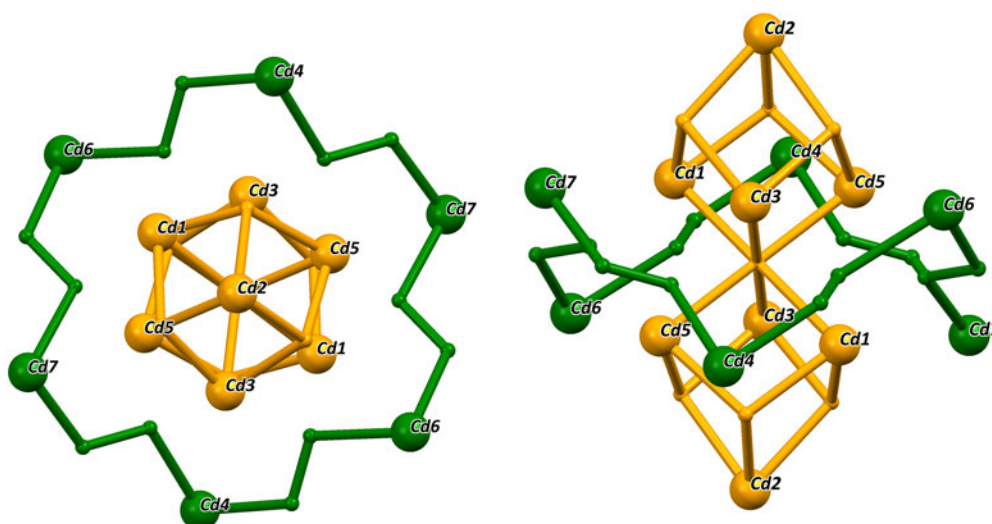


Figure A.2.: 18-MC-6 representation of Cd compound **C6**. Cubic core colored in yellow, the MC ring is colored in green.

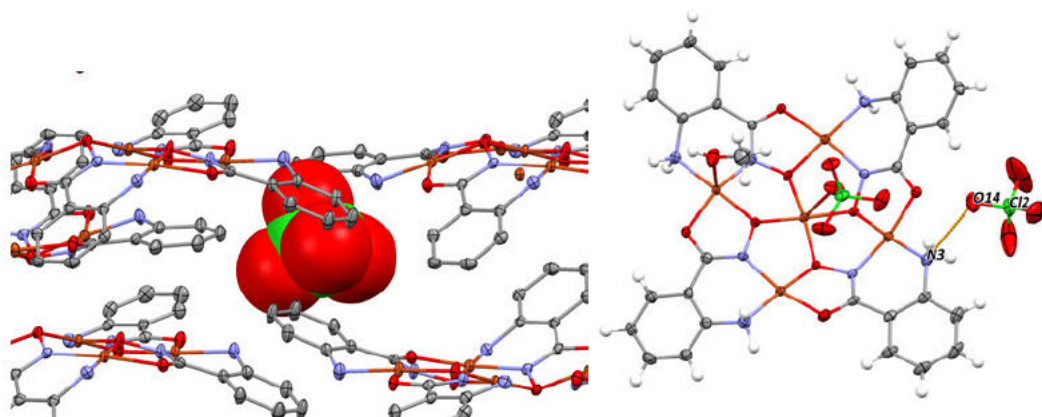


Figure A.3.: Non-coordinating perchlorate counter ion of C7 represented as spacefill (left) and its hydrogen bonding to the amine group of the MC plane (right). ORTEP representation with atomic displacement parameters at 50% level of probability. Hydrogen atoms are drawn as fixed-size spheres with a radius of 0.22 Å.

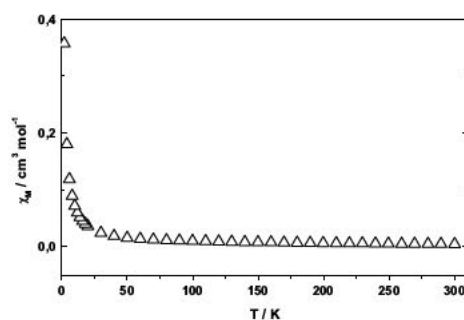


Figure A.4.: Temperature dependence of the magnetic susceptibility of C8.

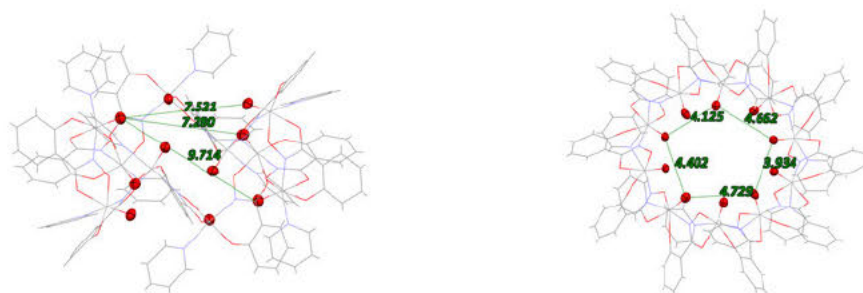


Figure A.5.: Pentagonal antiprismatic structure and distances of oxo ligands in C9

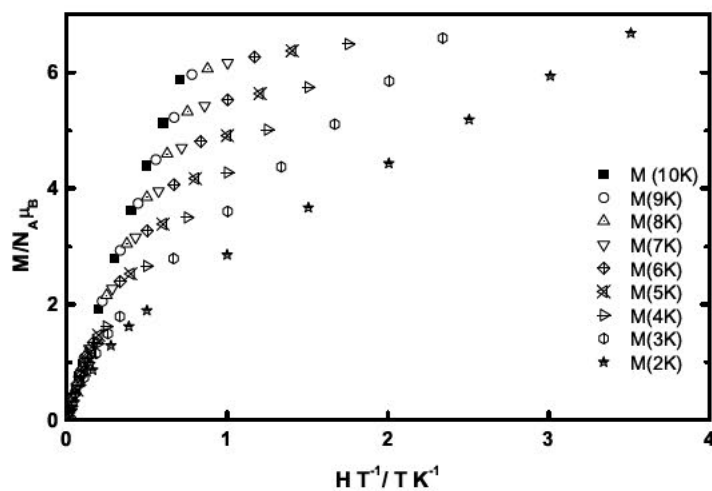


Figure A.6.: Reduced magnetization plot of C10.

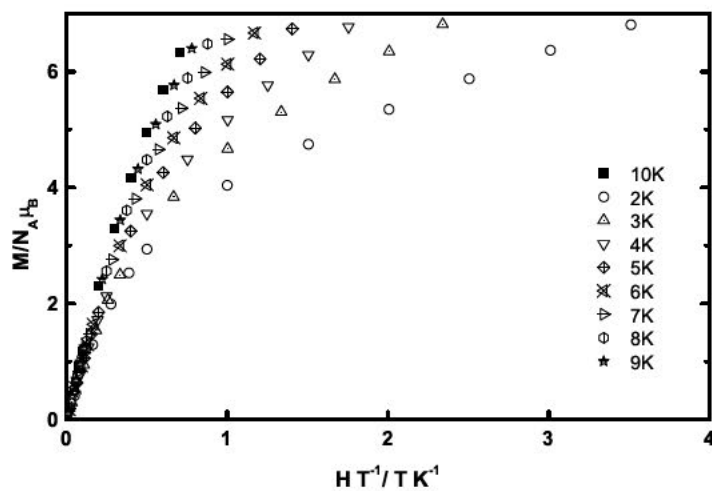


Figure A.7.: Reduced magnetization plot of C11.

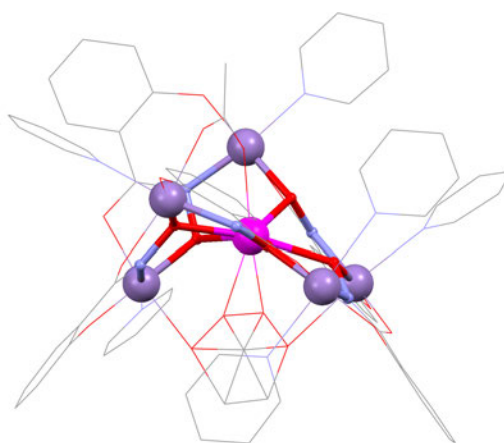


Figure A.8.: Molecular structure of Mn 15-MC-5. Color code: Violet - Mn(III), magenta - Mn(II), red - oxygen, blue - nitrogen, gray - carbon.

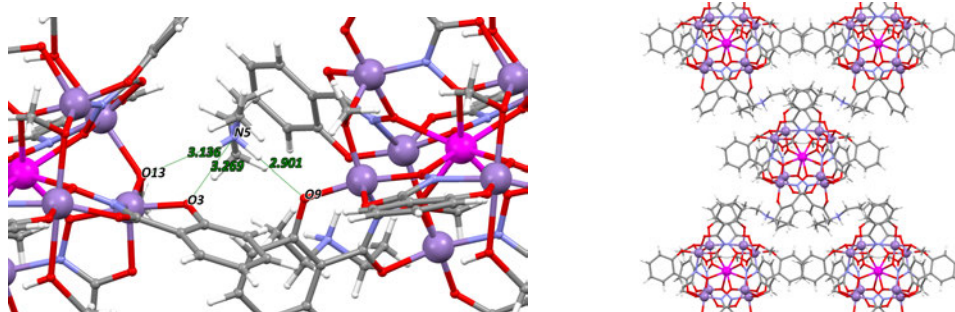


Figure A.9.: Hydrogen bonding (left) and packing of the Mn9 clusters (right) in the crystal structure of **C11**. Color code: Violet - Mn(III), magenta - Mn(II), red - oxygen, blue - nitrogen, gray - carbon.

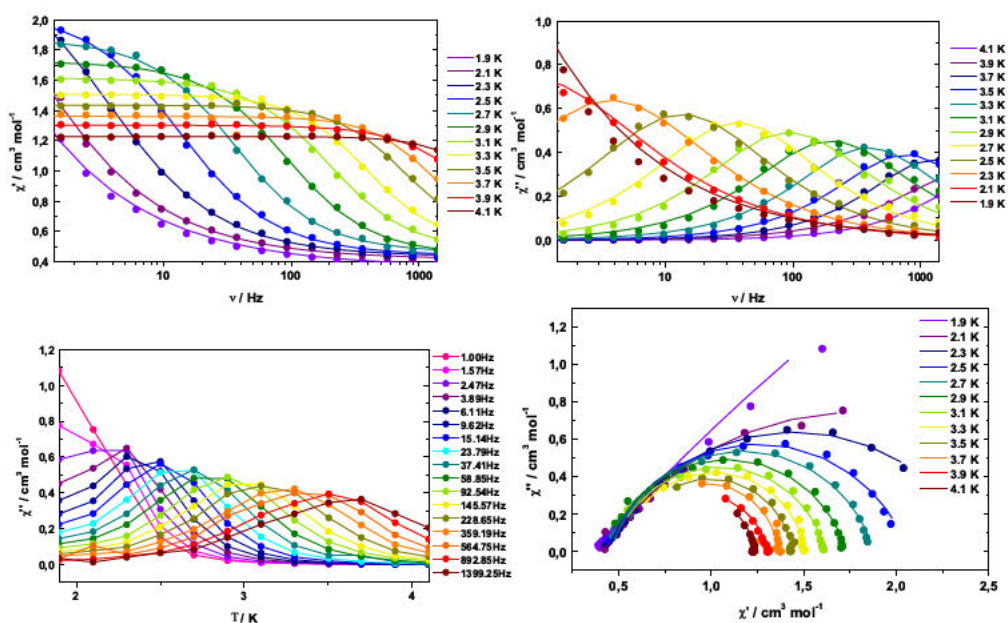


Figure A.10.: Results of ac susceptibility measurements of C11 without applied static field.

Top left: Frequency-dependent signal of the real part of the ac susceptibility  $\chi'$ . Top right: Frequency-dependent signal of the imaginary part of the ac susceptibility  $\chi''$ . Bottom left: Temperature-dependent signal of the imaginary part of the ac susceptibility  $\chi''$ . Bottom right: Cole-Cole plot

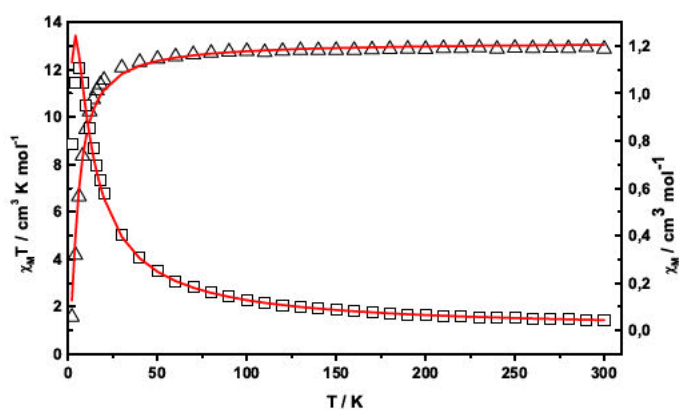


Figure A.11.: Temperature-dependent magnetic behavior of C12.  $\chi_M$  (open squares) and  $\chi_M T$  (open triangles) vs. T plots and the best fit (solid red line) using a 1J model.

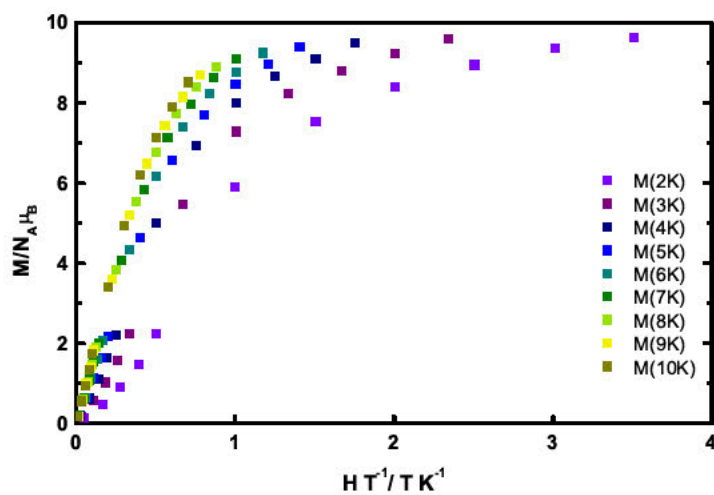


Figure A.12.: Reduced magnetization plot of C12.

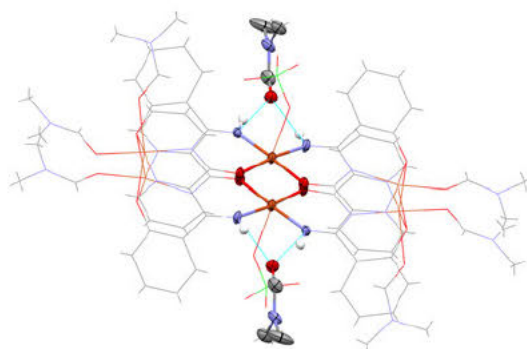


Figure A.13.: Hydrogen bonding between two solvent molecules and the copper(II) hexamer present in the crystal structure of C14.

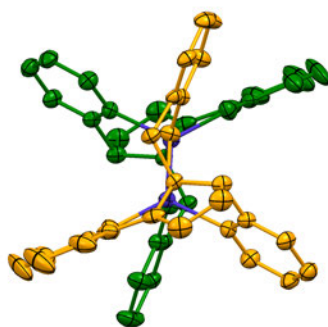


Figure A.14.: Staggered conformation of **L10d** in **C16**. The two ligands are colored green and orange for a better representation.

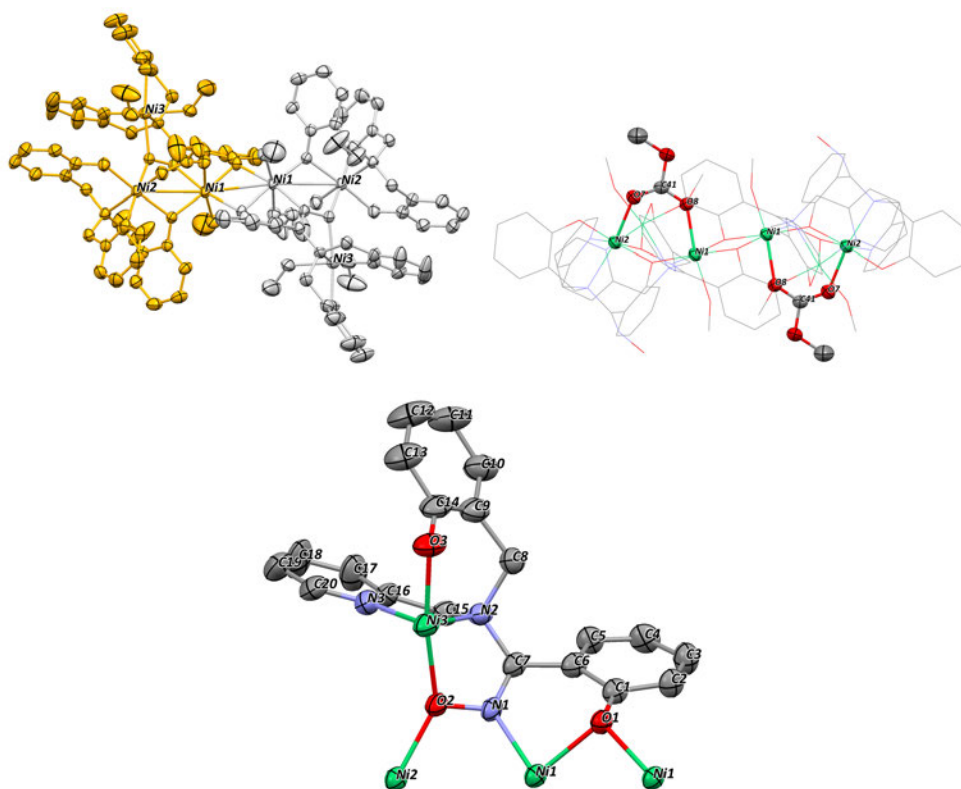
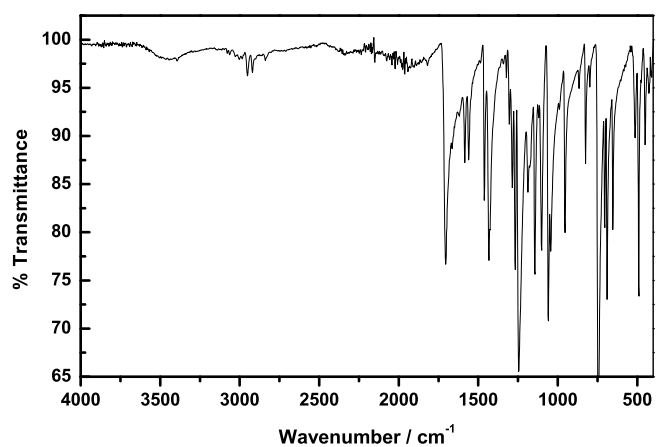
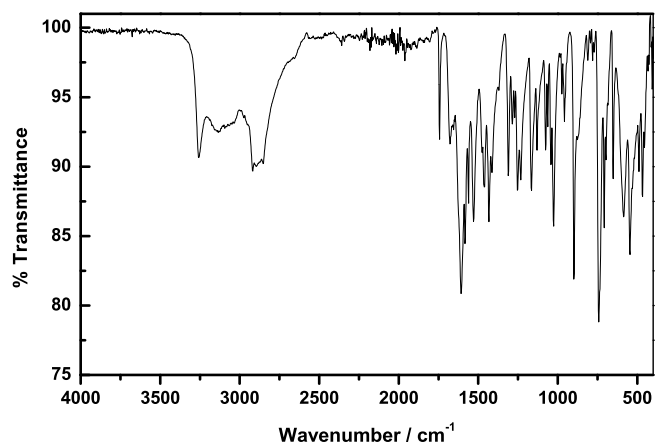


Figure A.15.: Molecular structure of **C17** colored by symmetry operation (left) and carbonate bridges of the in situ generated monomethyl carbonate anions (right). Coordination of **L10** (bottom). Color code: Green - Ni(II), red - oxygen, blue - nitrogen, gray - carbon, yellow dots - crystallographic centers of inversion. ORTEP representation with atomic displacement parameters at 50% level of probability. Hydrogen atoms have been omitted for clarity.



## B. IR-Spectra

Figure B.1.: IR spectrum of **L3b**Figure B.2.: IR spectrum of **L3**

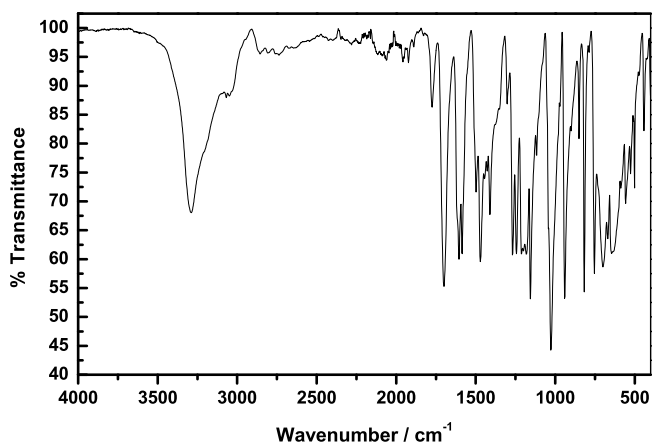


Figure B.3.: IR spectrum of **P1**

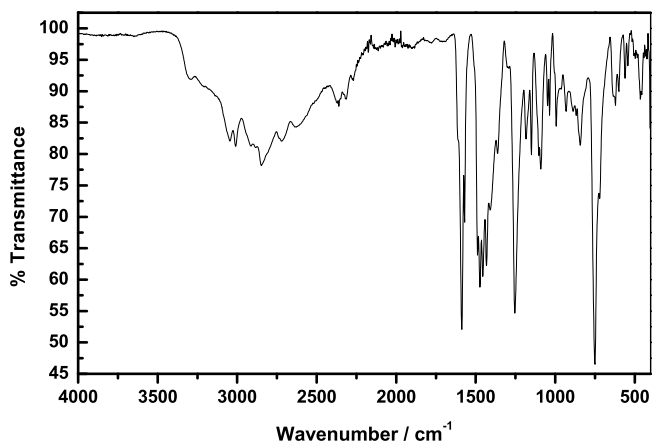


Figure B.4.: IR spectrum of **L10a**

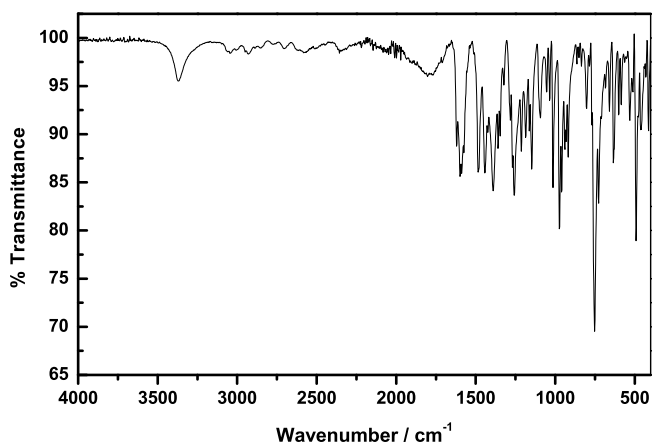


Figure B.5.: IR spectrum of **L10**

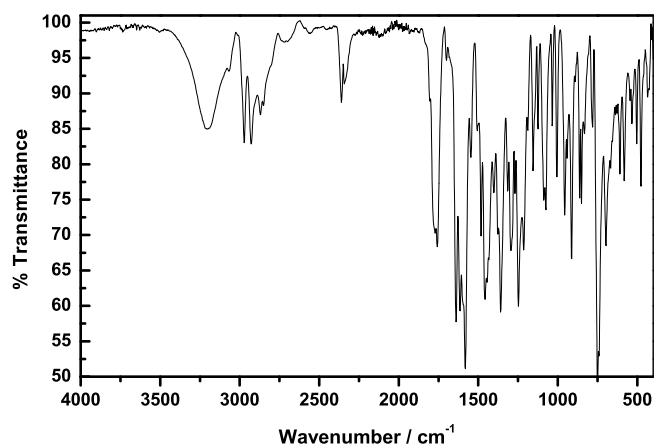


Figure B.6.: IR spectrum of **L11**

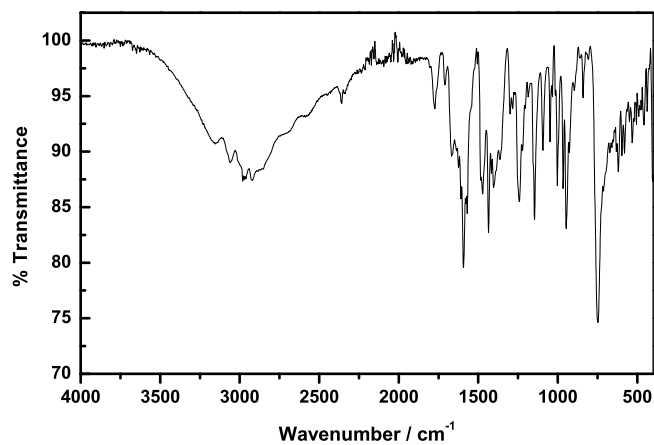


Figure B.7.: IR spectrum of **L9**

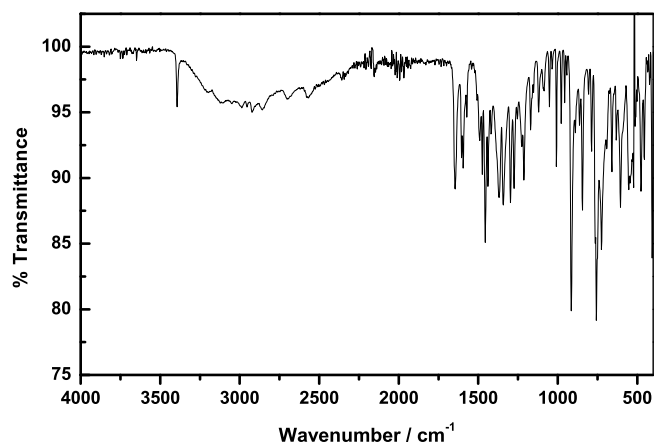


Figure B.8.: IR spectrum of **L7**

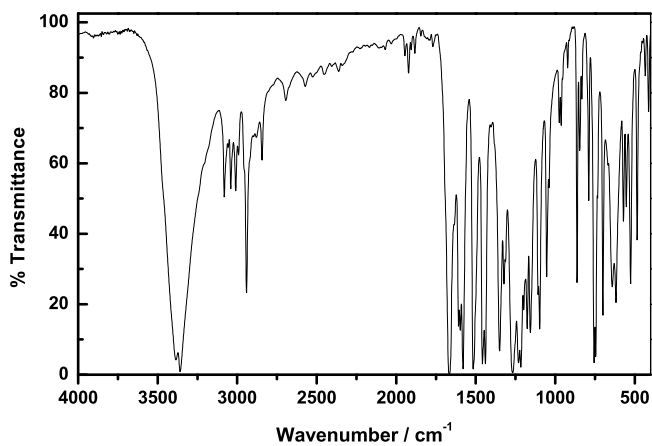


Figure B.9.: IR spectrum of **L5a**

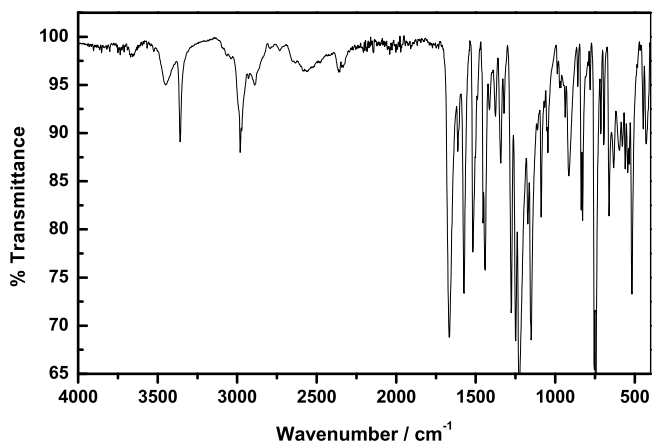


Figure B.10.: IR spectrum of **L5**

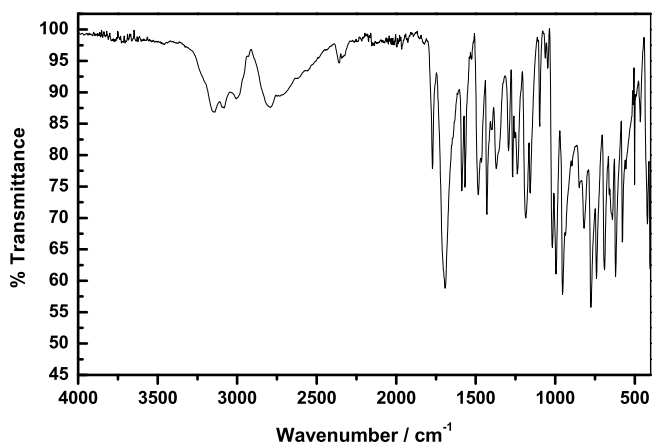
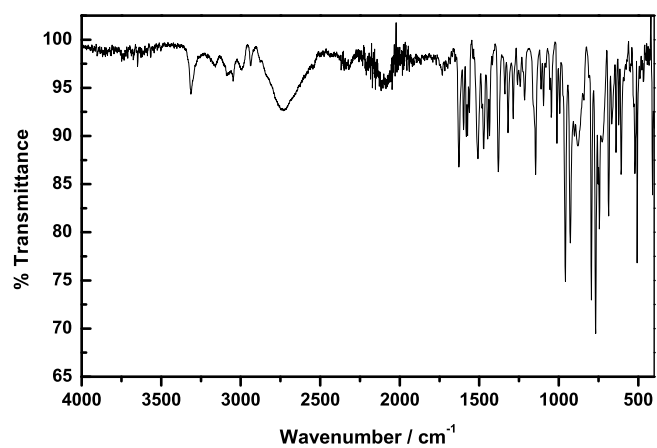
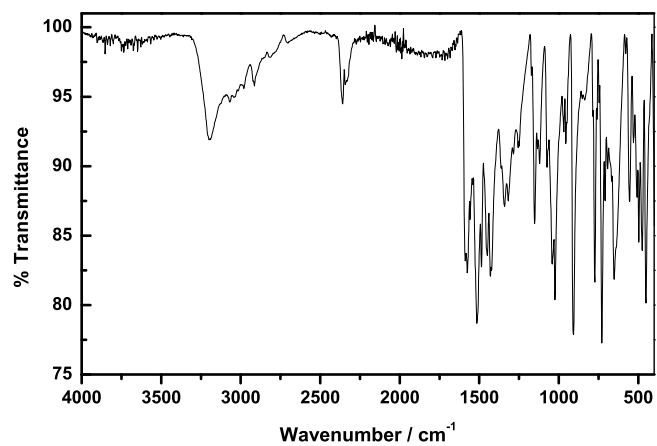
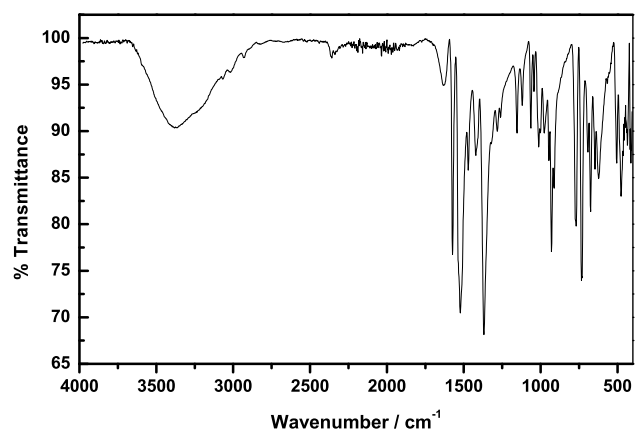


Figure B.11.: IR spectrum of **P2**

Figure B.12.: IR spectrum of **L6**Figure B.13.: IR spectrum of **C1**Figure B.14.: IR spectrum of **C2**

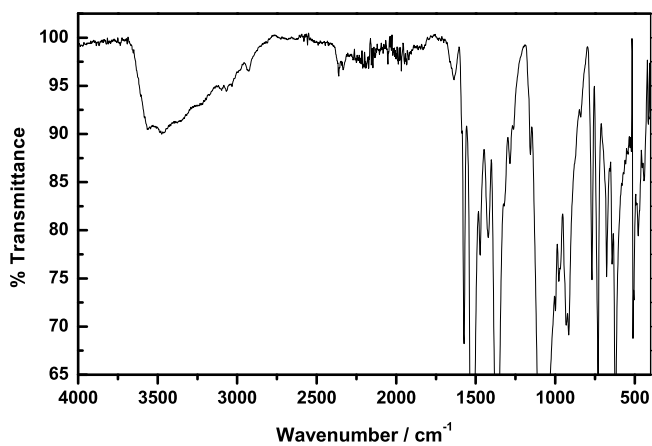


Figure B.15.: IR spectrum of **C3**

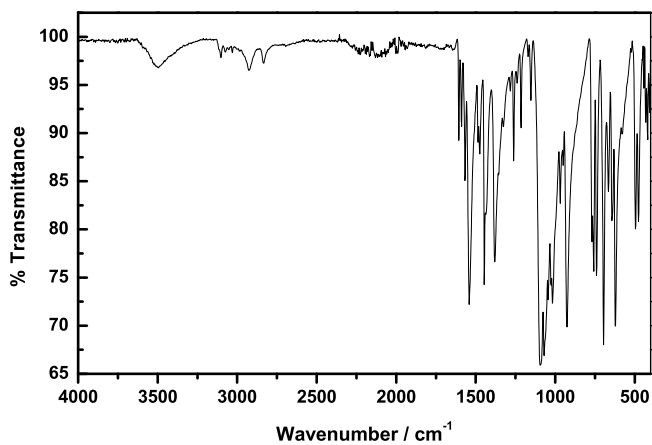


Figure B.16.: IR spectrum of **C4**

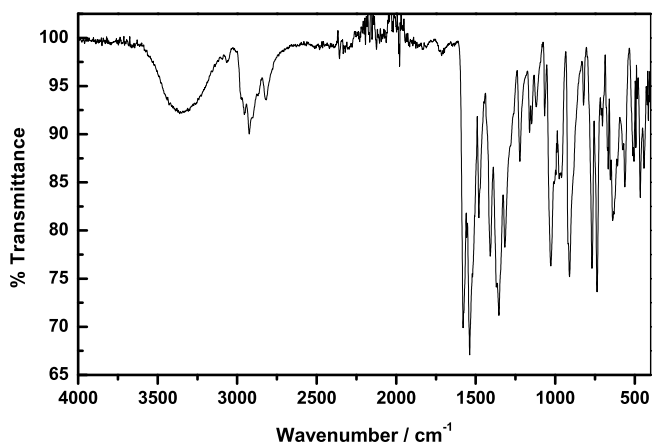
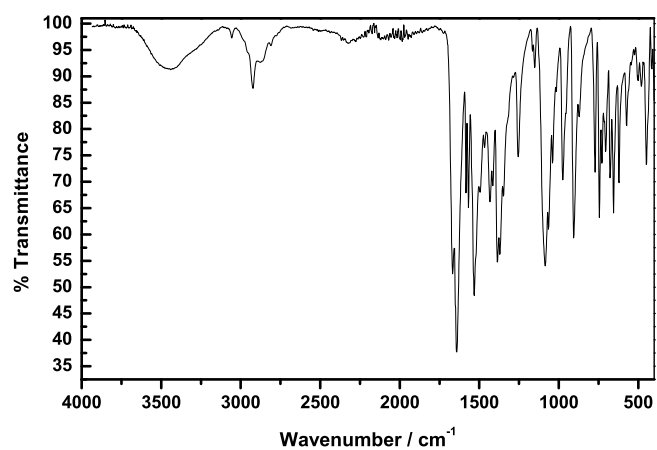
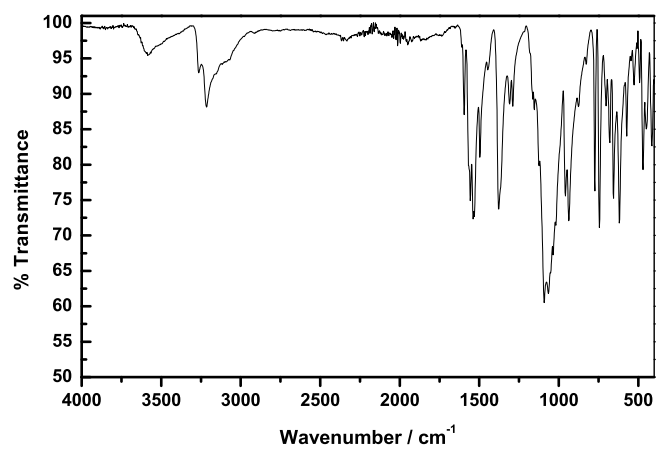
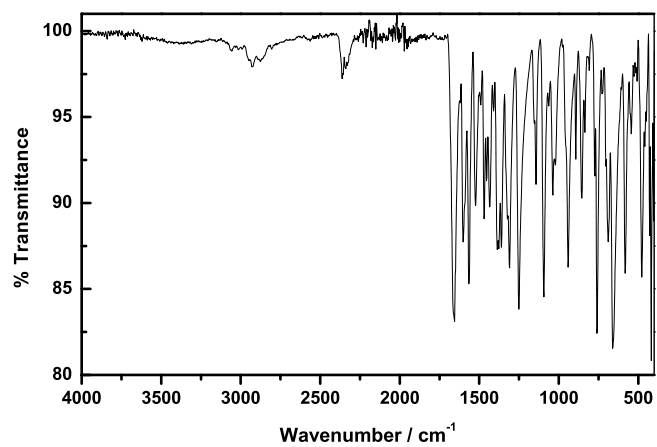


Figure B.17.: IR spectrum of **C5**

Figure B.18.: IR spectrum of **C6**Figure B.19.: IR spectrum of **C7**Figure B.20.: IR spectrum of **C8**

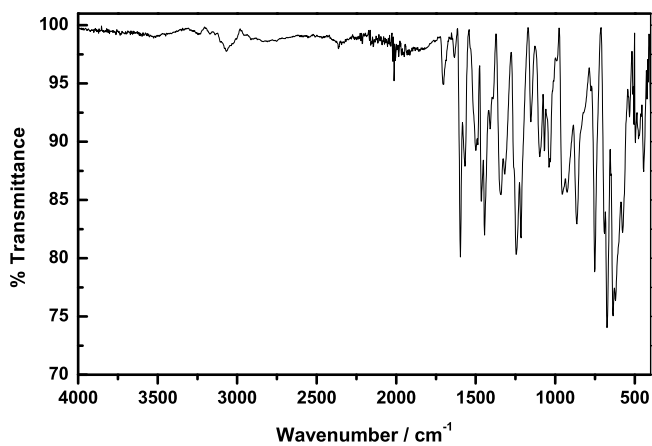


Figure B.21.: IR spectrum of **C9**

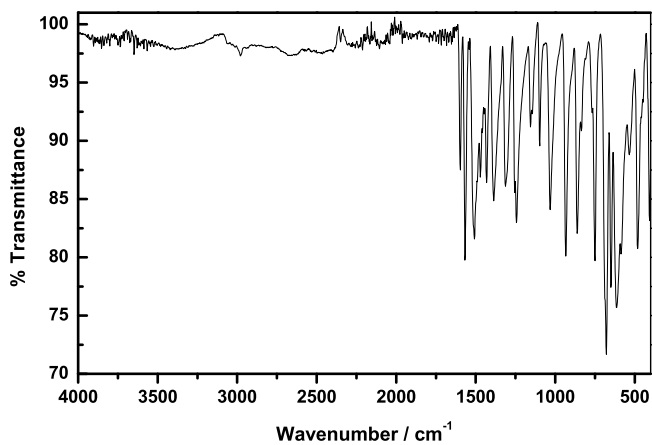


Figure B.22.: IR spectrum of **C10**

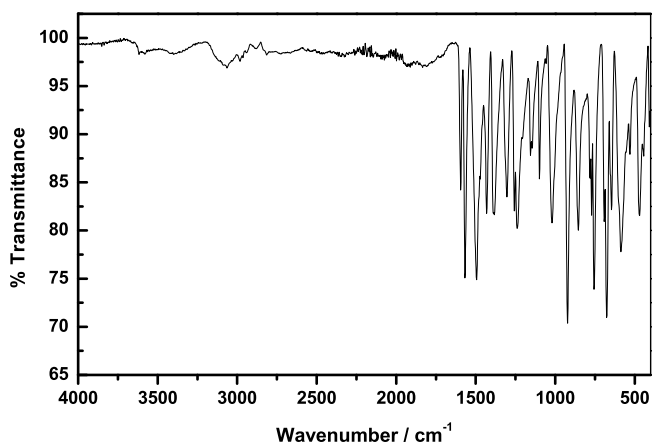
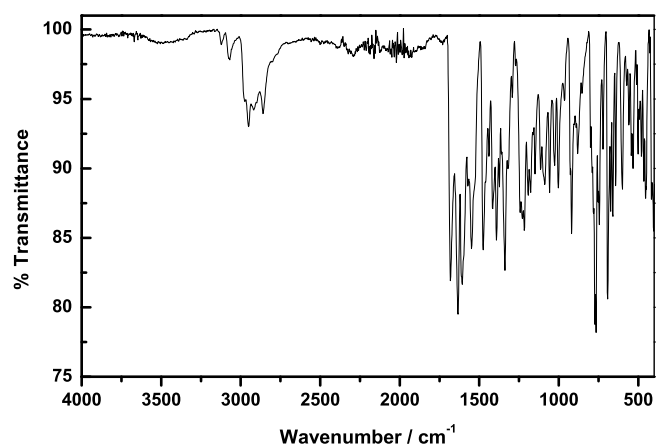
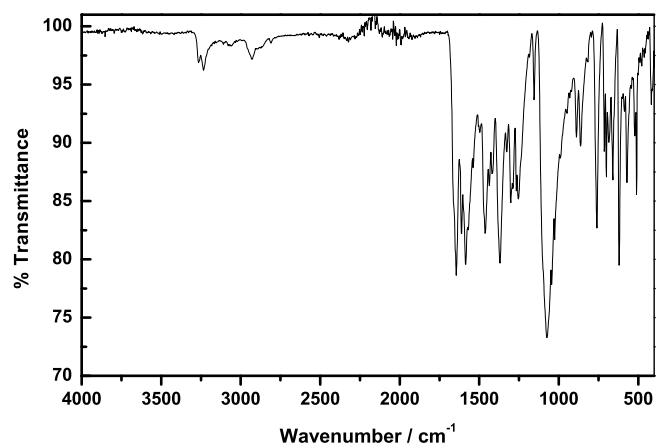
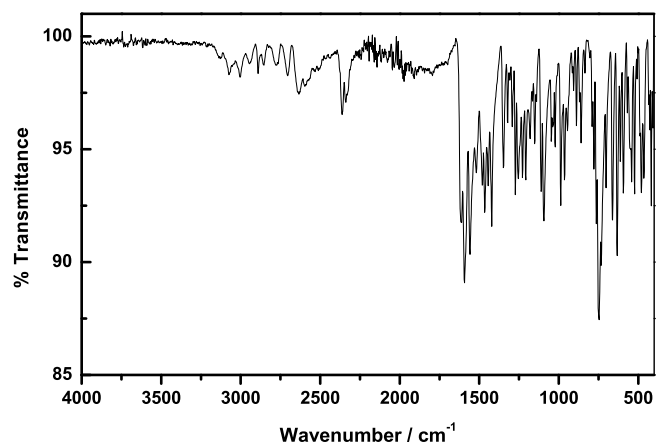


Figure B.23.: IR spectrum of **C11**



Figure B.24.: IR spectrum of **C12**Figure B.25.: IR spectrum of **C14**Figure B.26.: IR spectrum of **C15**

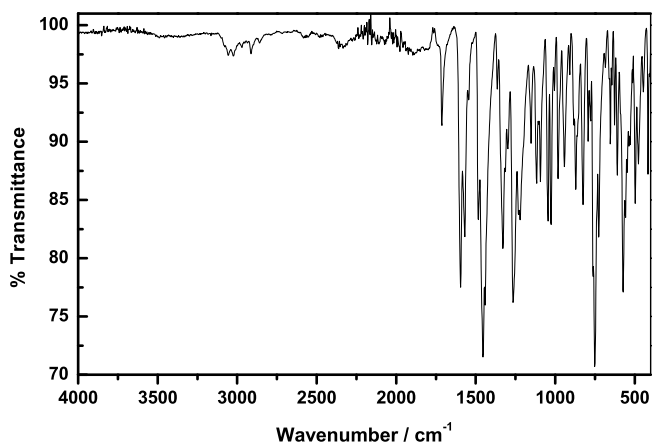


Figure B.27.: IR spectrum of **C16**

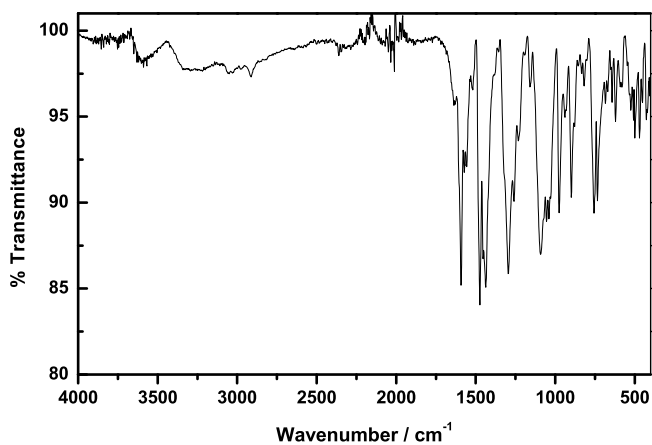
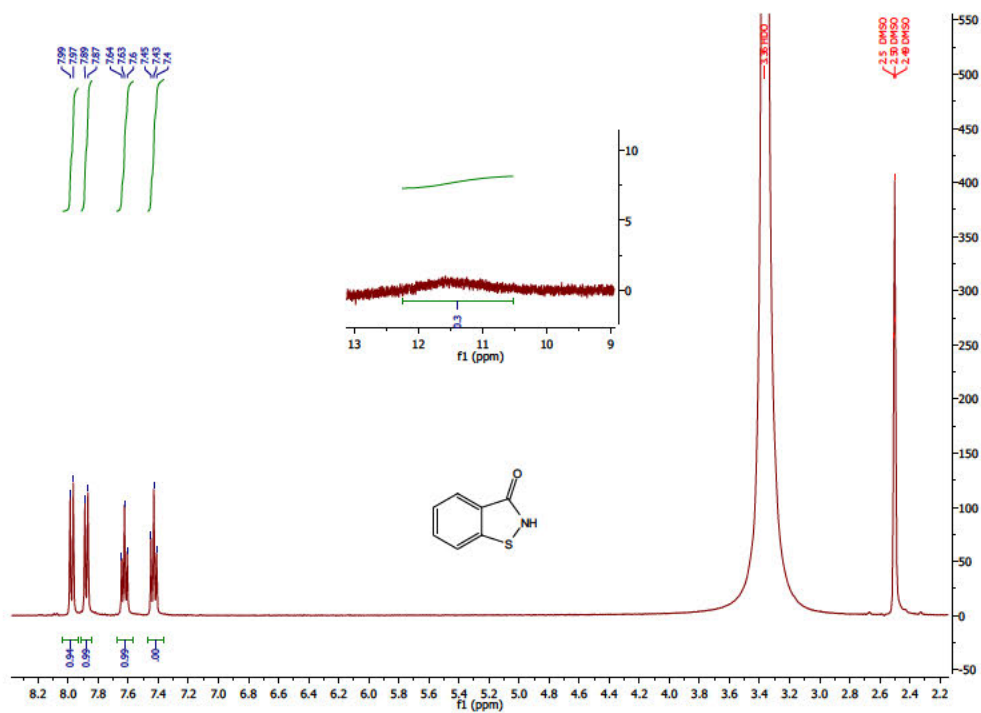


Figure B.28.: IR spectrum of **C17**

## C. NMR-Spectra

Figure C.1.:  $^1\text{H-NMR}$  of 1,2-benzisothiazolin-3-one

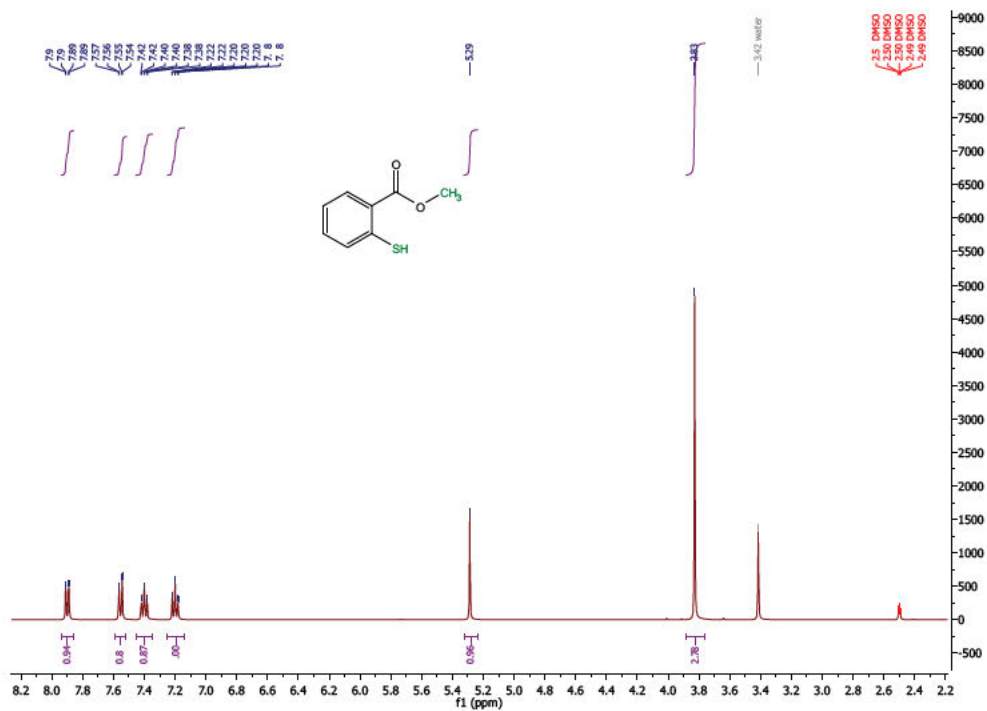


Figure C.2.: <sup>1</sup>H-NMR spectrum of L3a

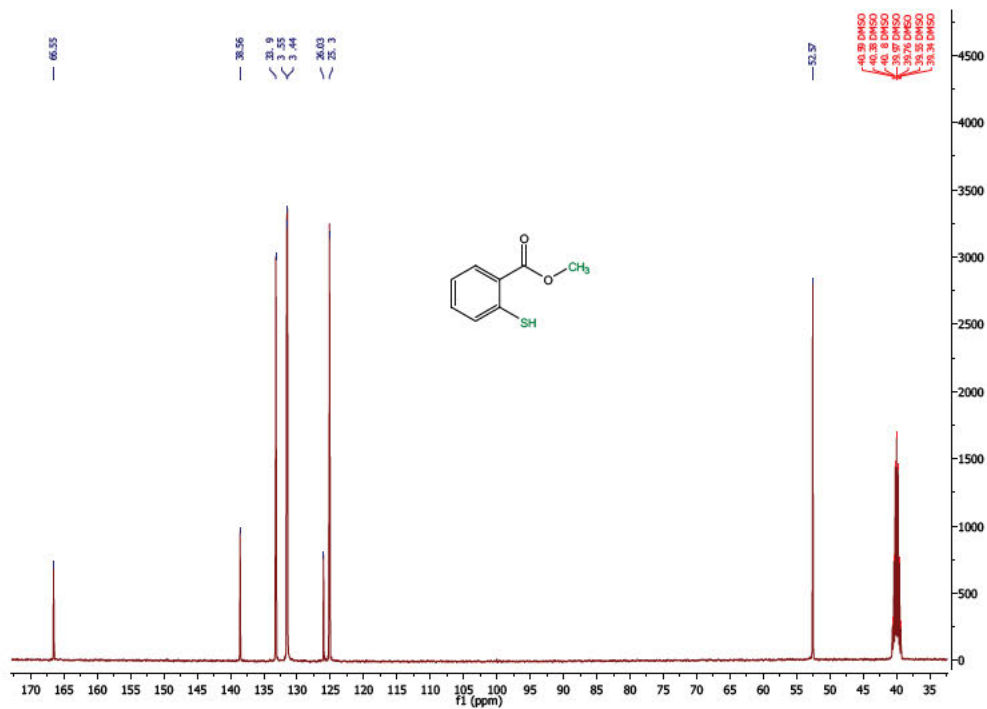
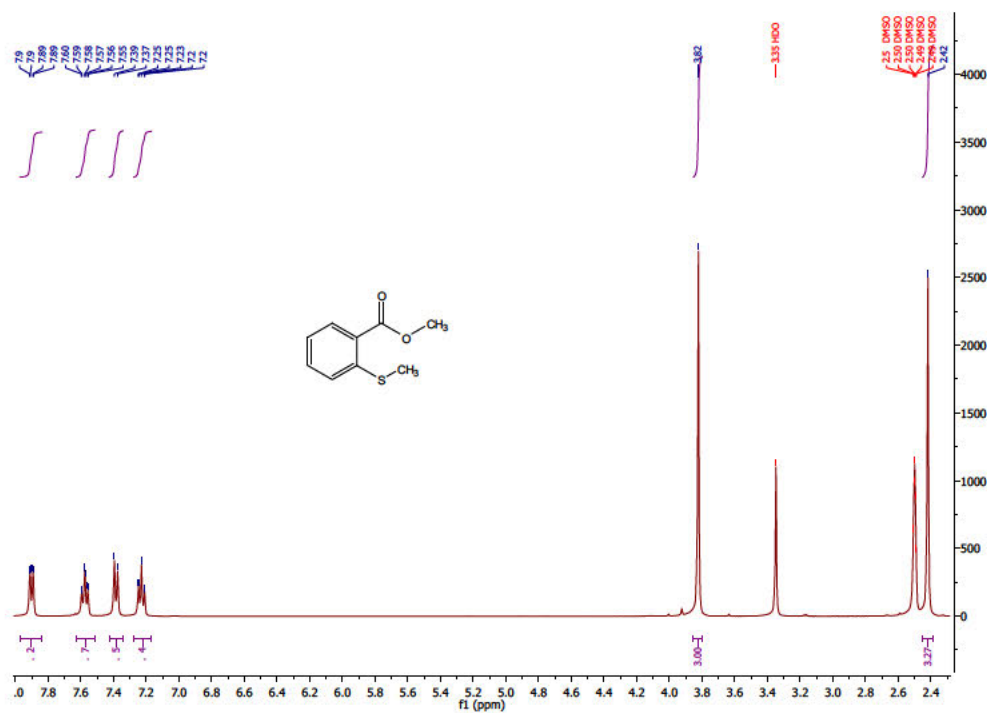
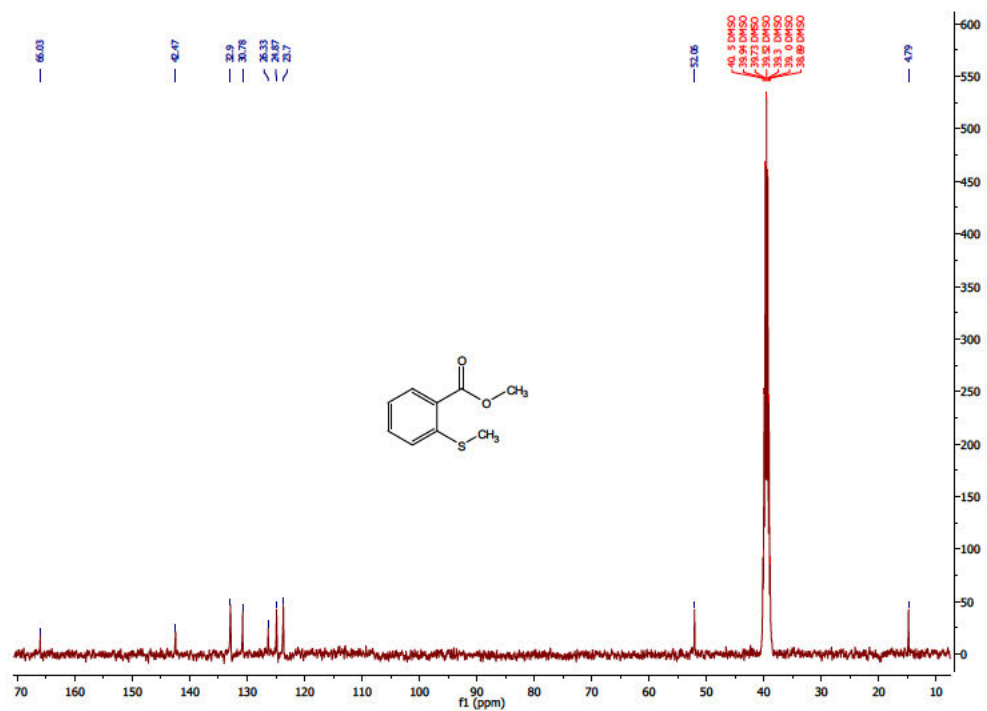


Figure C.3.: <sup>13</sup>C-NMR spectrum of L3a

Figure C.4.:  $^1\text{H-NMR}$  spectrum of L3bFigure C.5.:  $^{13}\text{C-NMR}$  spectrum of L3b

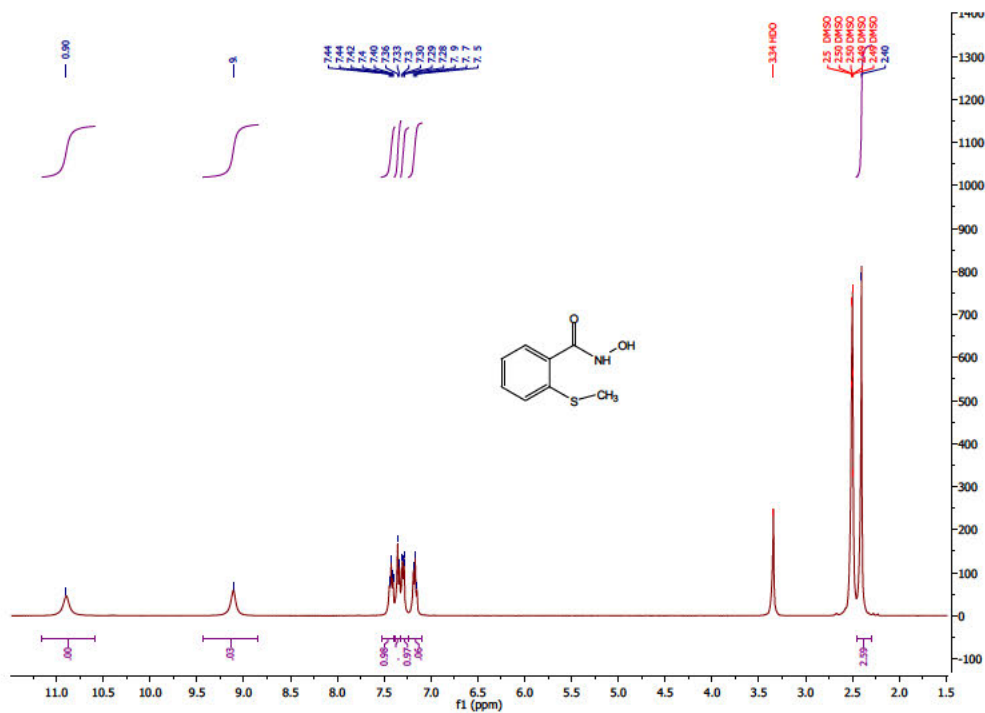


Figure C.6.:  $^1\text{H}$ -NMR spectrum of L3

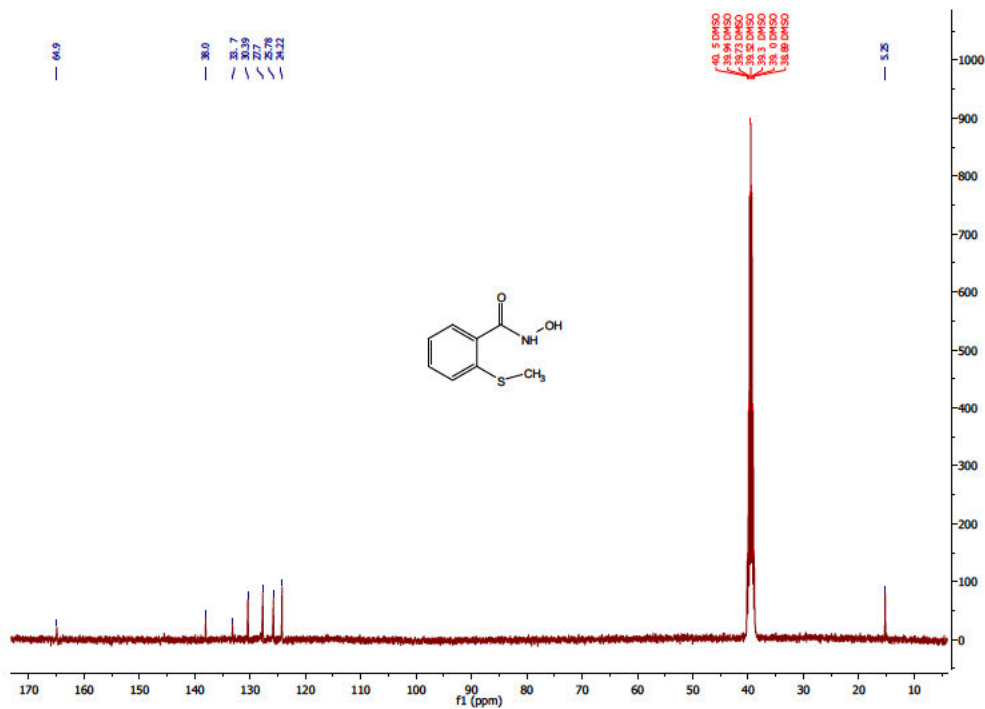
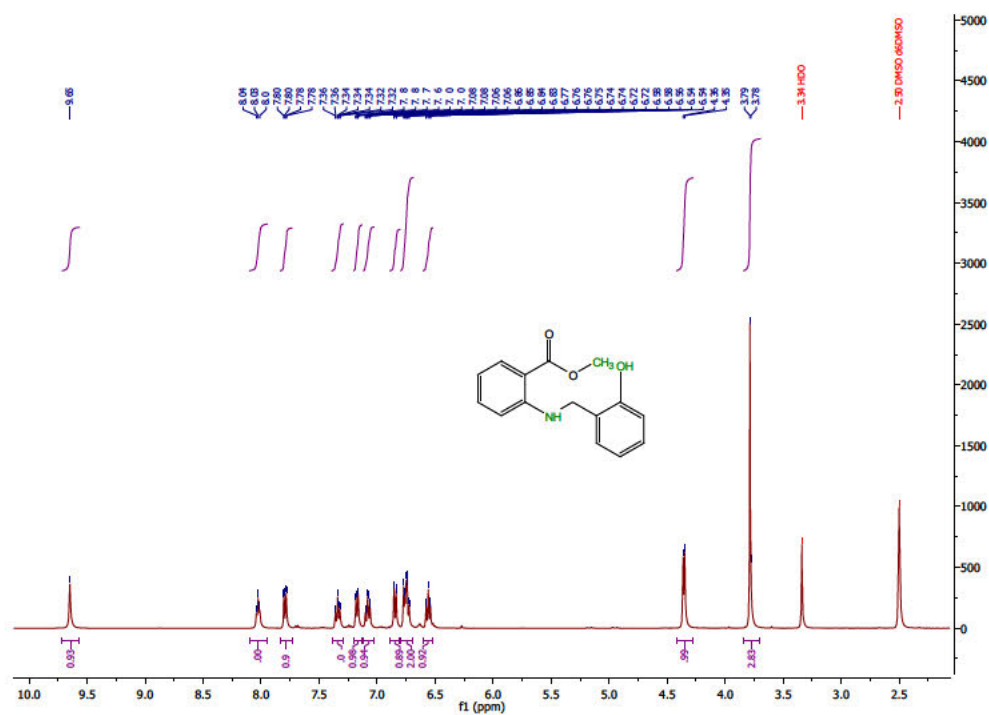
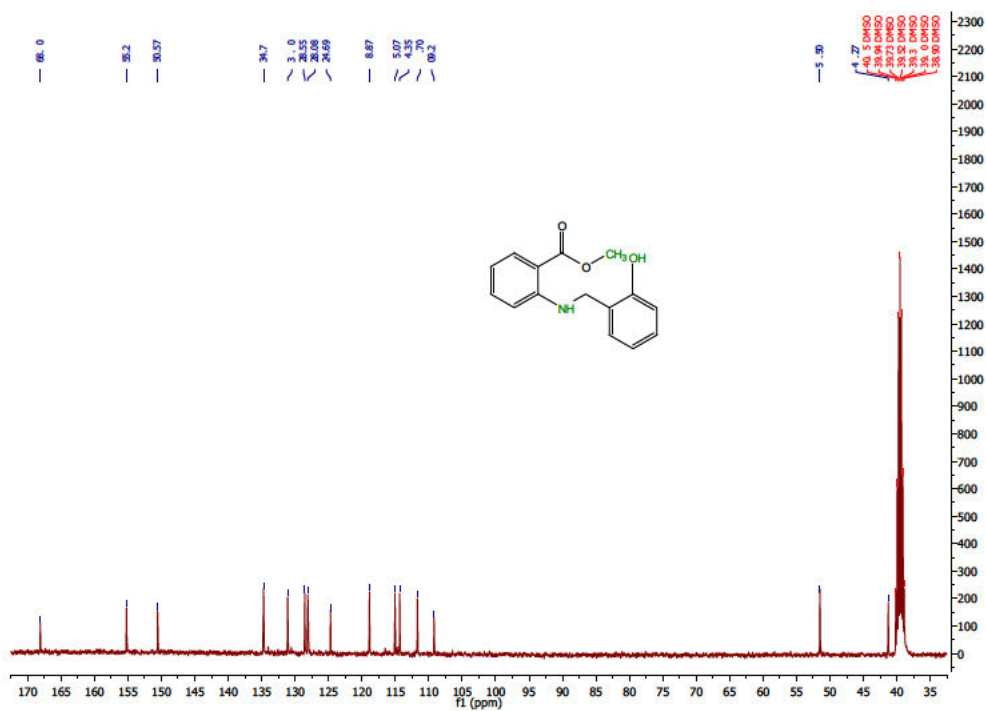


Figure C.7.:  $^{13}\text{C}$ -NMR spectrum of L3

Figure C.8.:  $^1\text{H-NMR}$  spectrum of L5aFigure C.9.:  $^{13}\text{C-NMR}$  spectrum of L5a

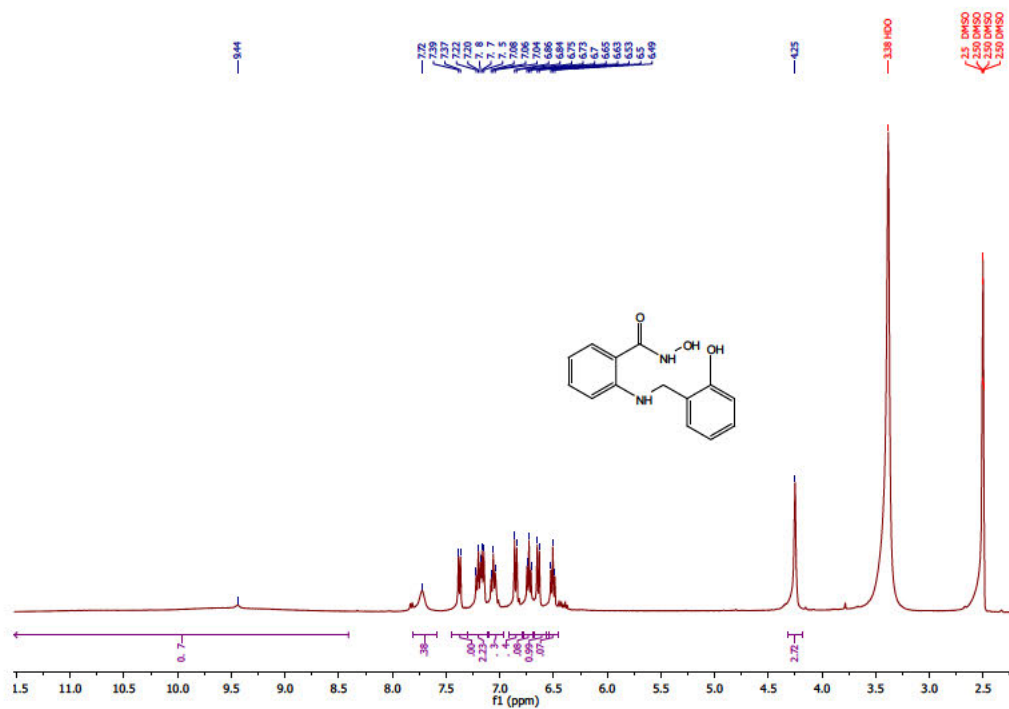


Figure C.10.: <sup>1</sup>H-NMR spectrum of L5

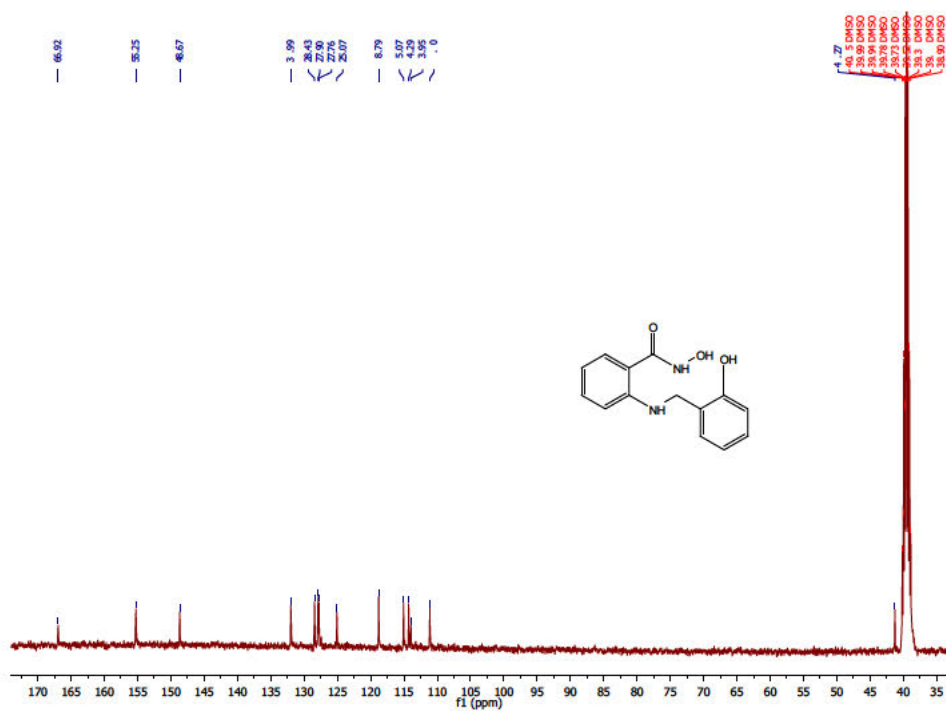
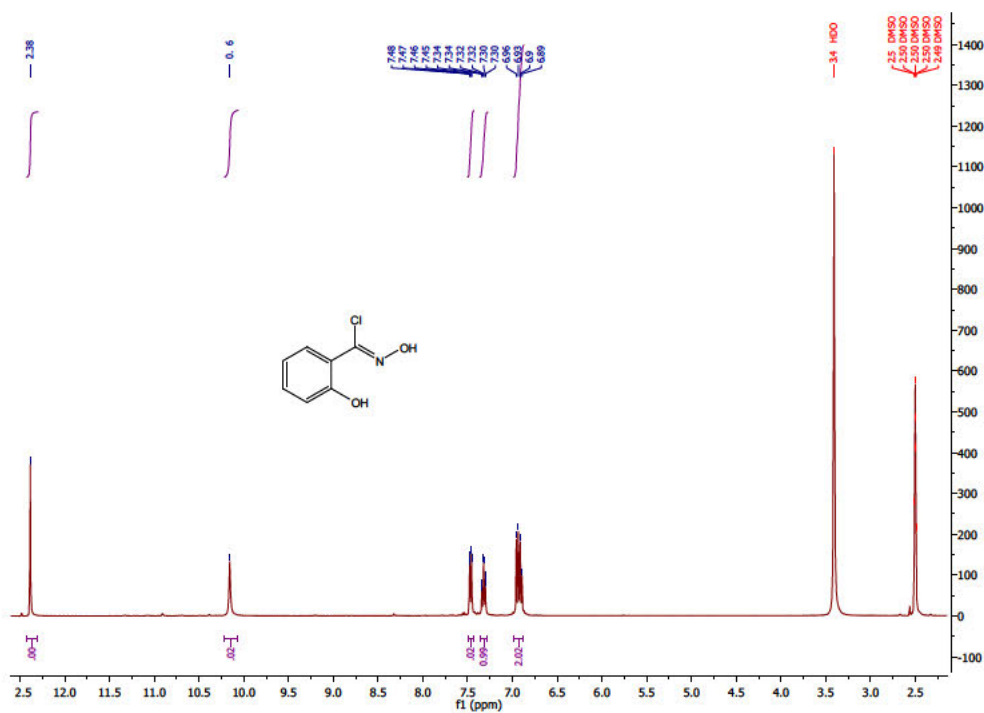
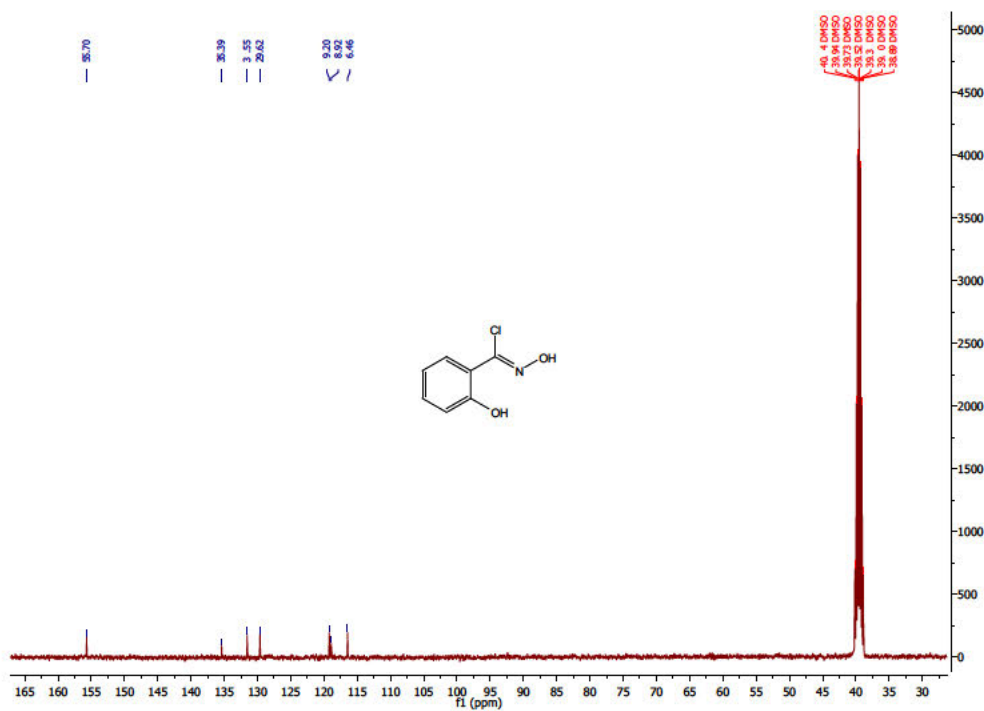


Figure C.11.: <sup>13</sup>C-NMR spectrum of L5



Figure C.12.:  $^1\text{H-NMR}$  spectrum of P1Figure C.13.:  $^{13}\text{C-NMR}$  spectrum of P1

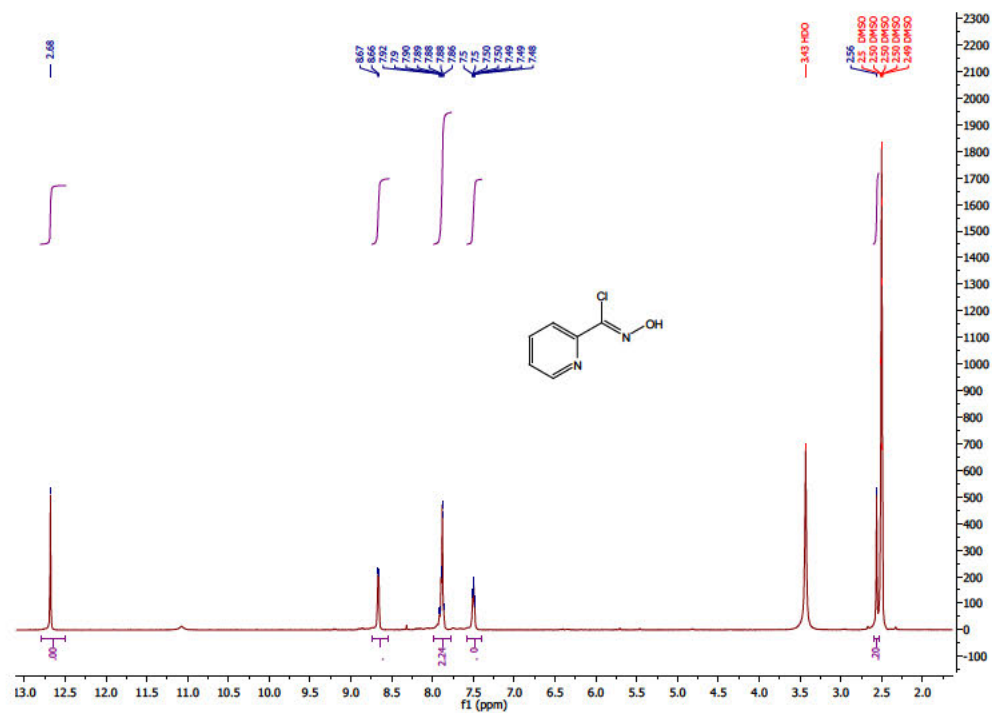


Figure C.14.:  $^1\text{H}$ -NMR spectrum of P2

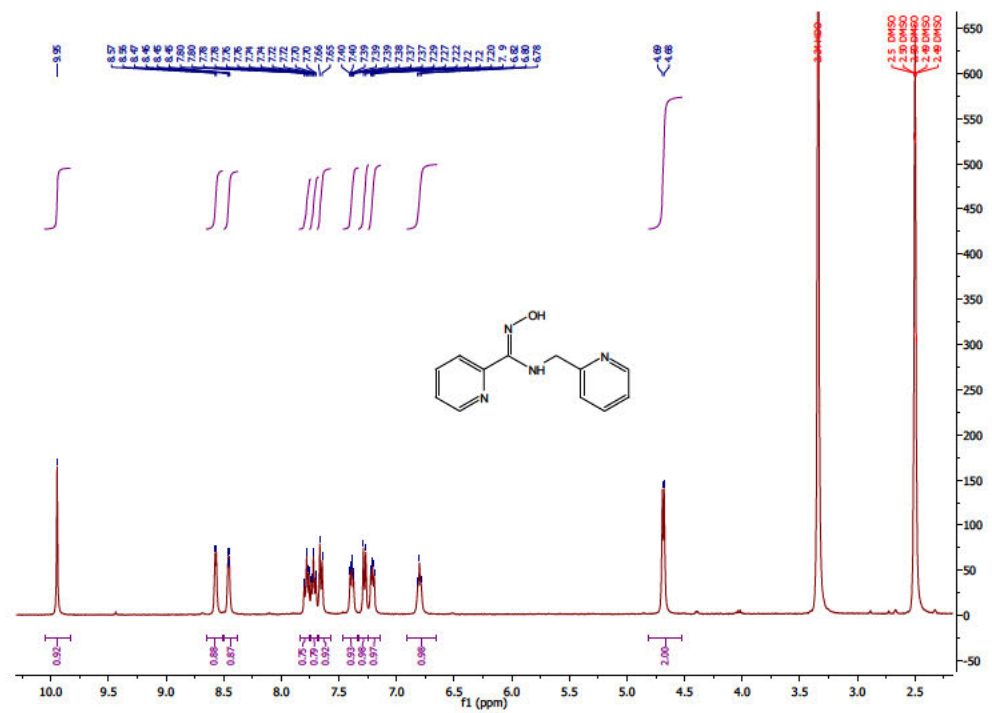
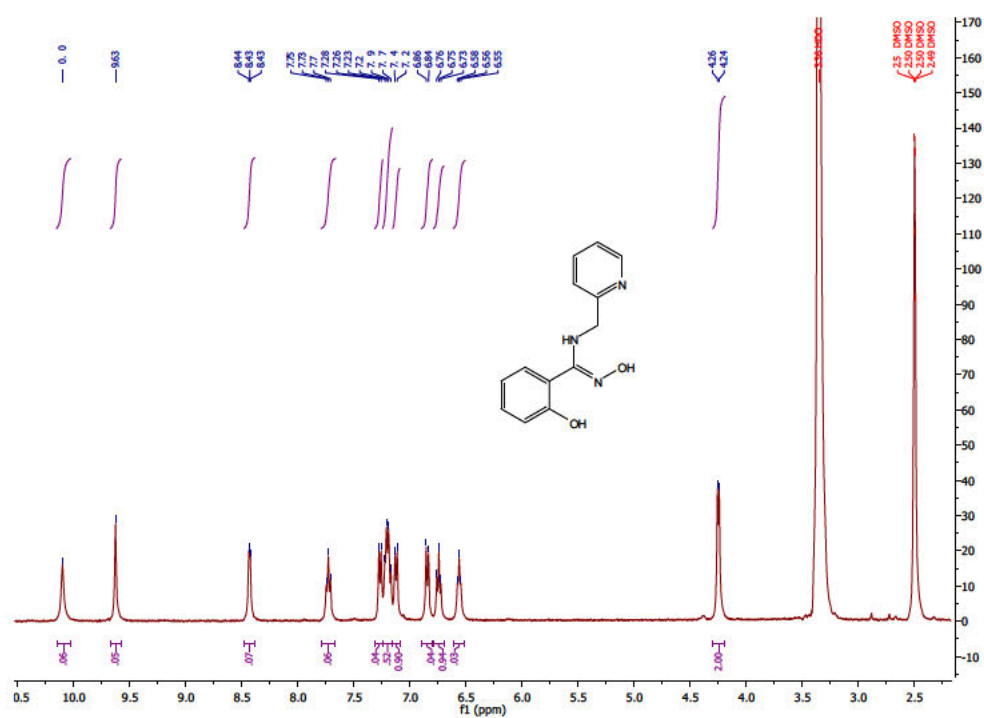
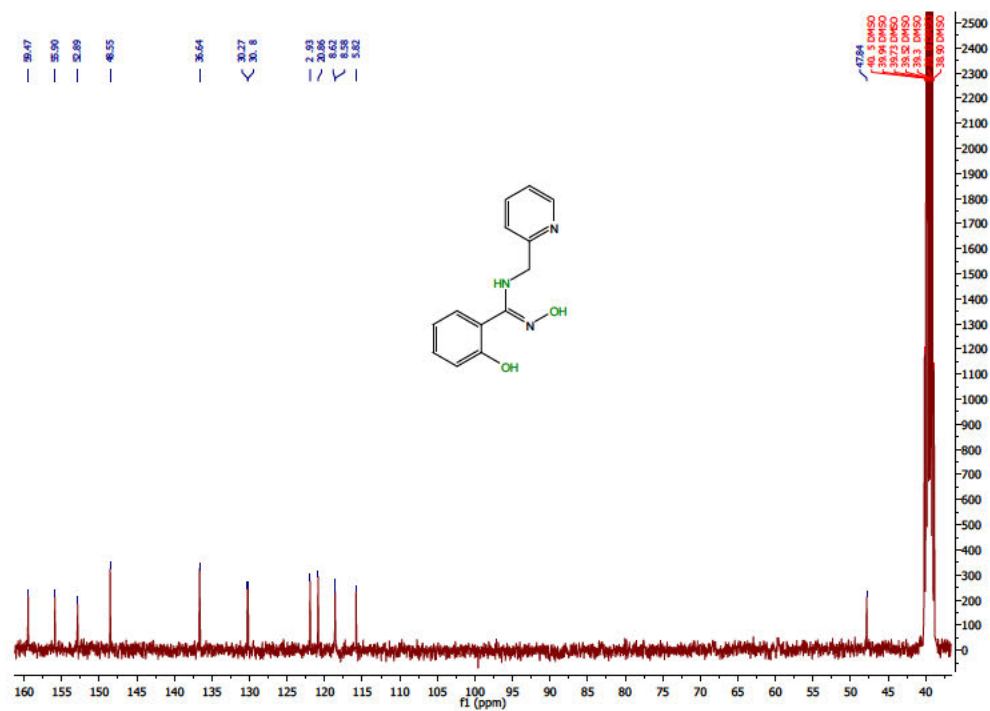
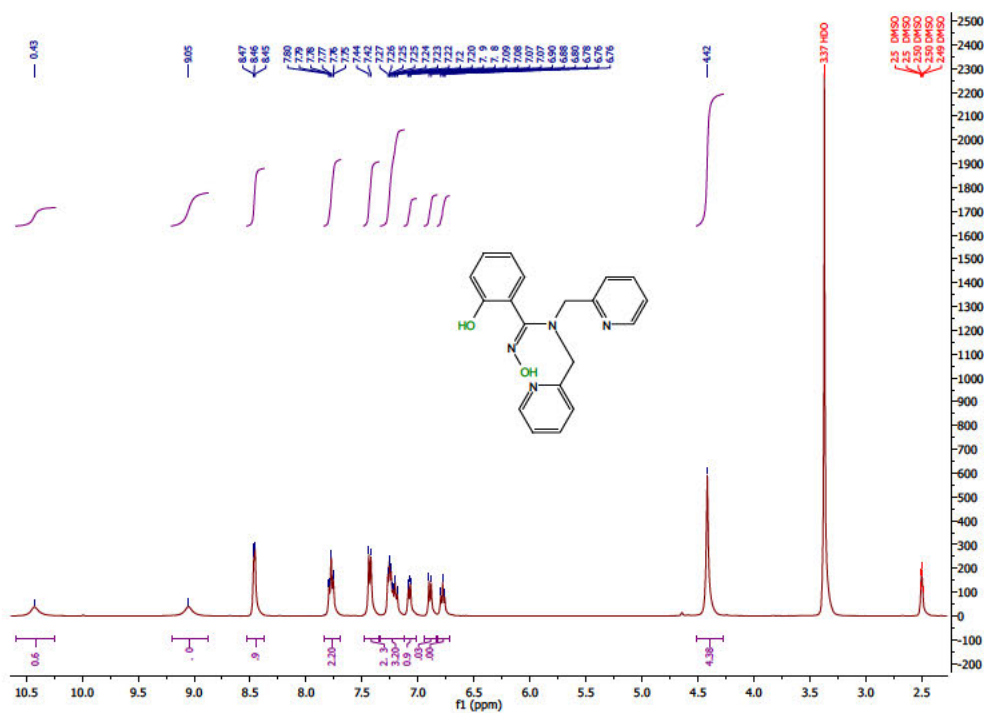
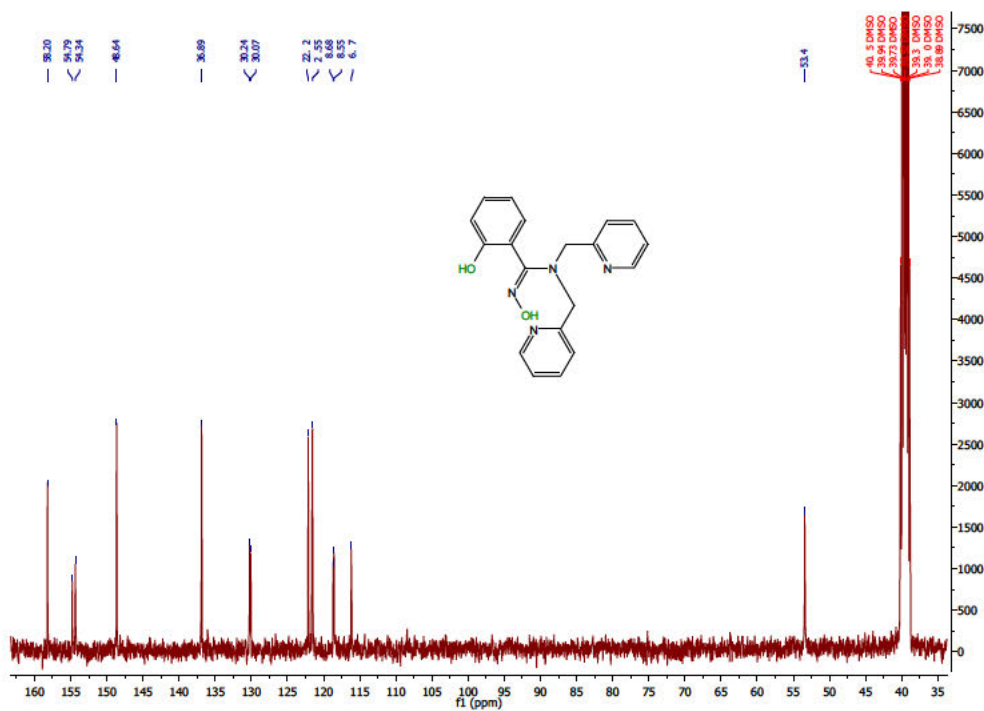


Figure C.15.:  $^1\text{H}$ -NMR spectrum of L6

Figure C.16.:  $^1\text{H-NMR}$  spectrum of L7Figure C.17.:  $^{13}\text{C-NMR}$  spectrum of L7



Figure C.20.:  $^1\text{H}$ -NMR spectrum of L9Figure C.21.:  $^{13}\text{C}$ -NMR spectrum of L9

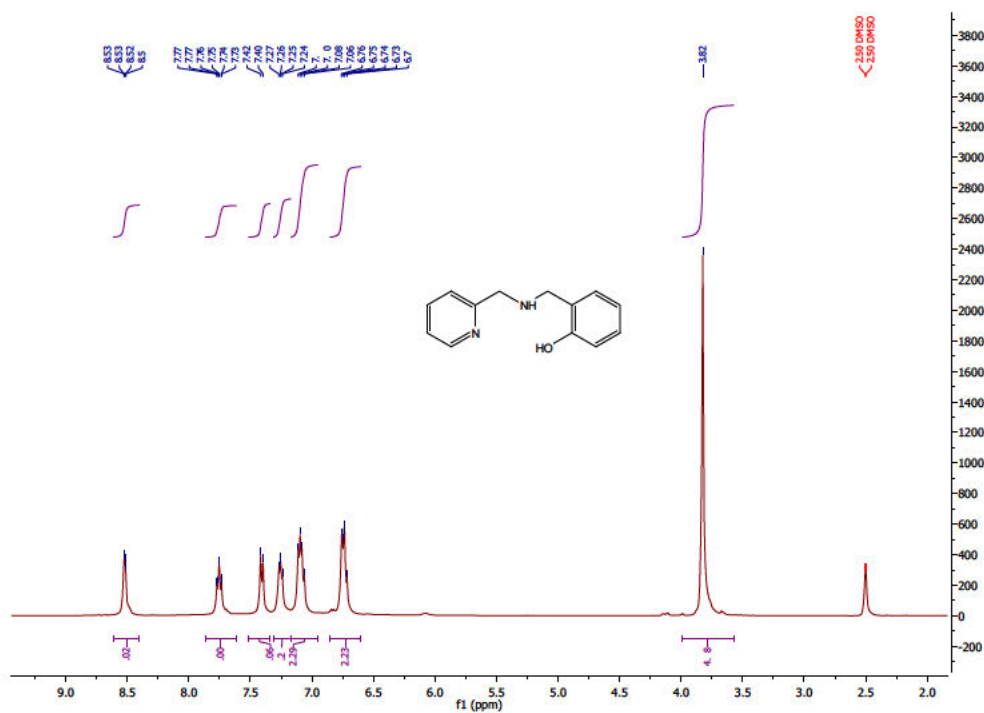


Figure C.22.:  $^1\text{H}$ -NMR spectrum of L10a

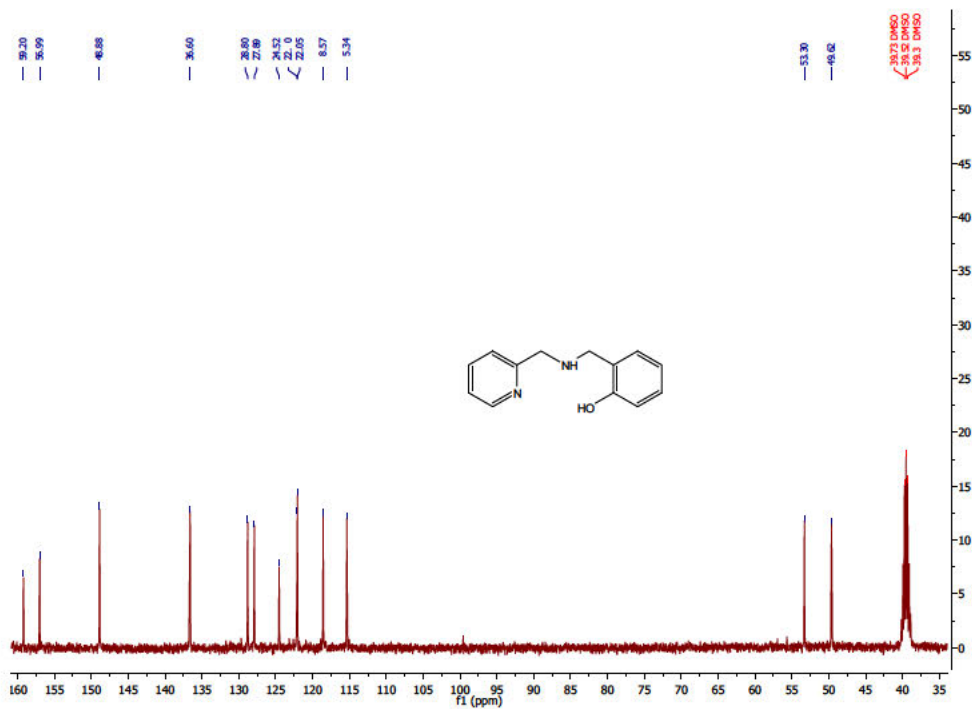
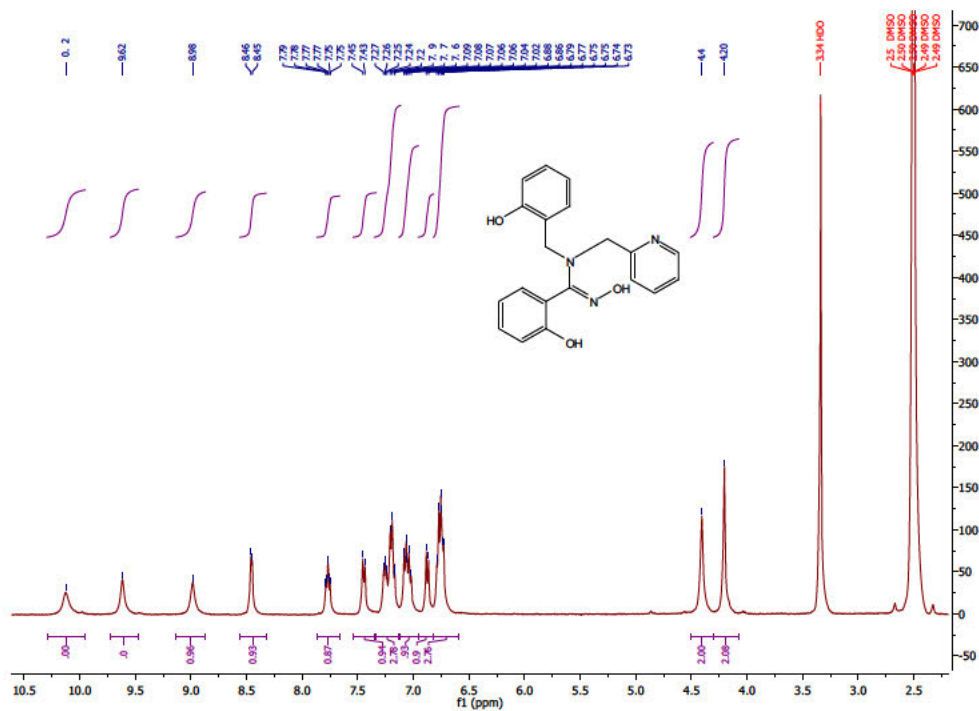
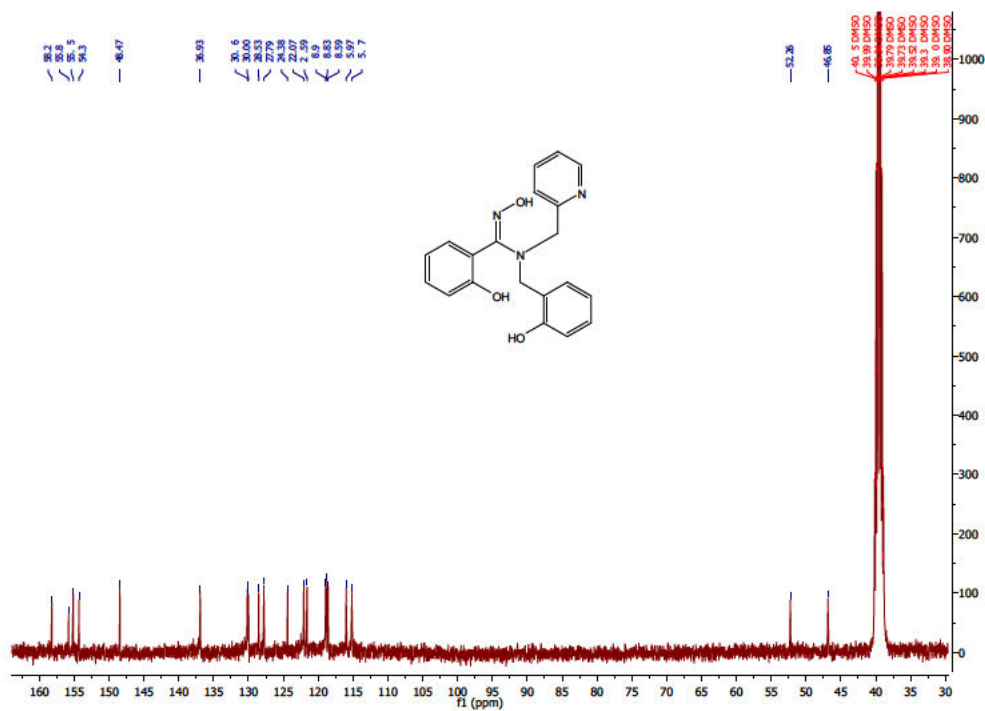


Figure C.23.:  $^{13}\text{C}$ -NMR spectrum of L10a

Figure C.24.:  $^1\text{H-NMR}$  spectrum of L10Figure C.25.:  $^{13}\text{C-NMR}$  spectrum of L10

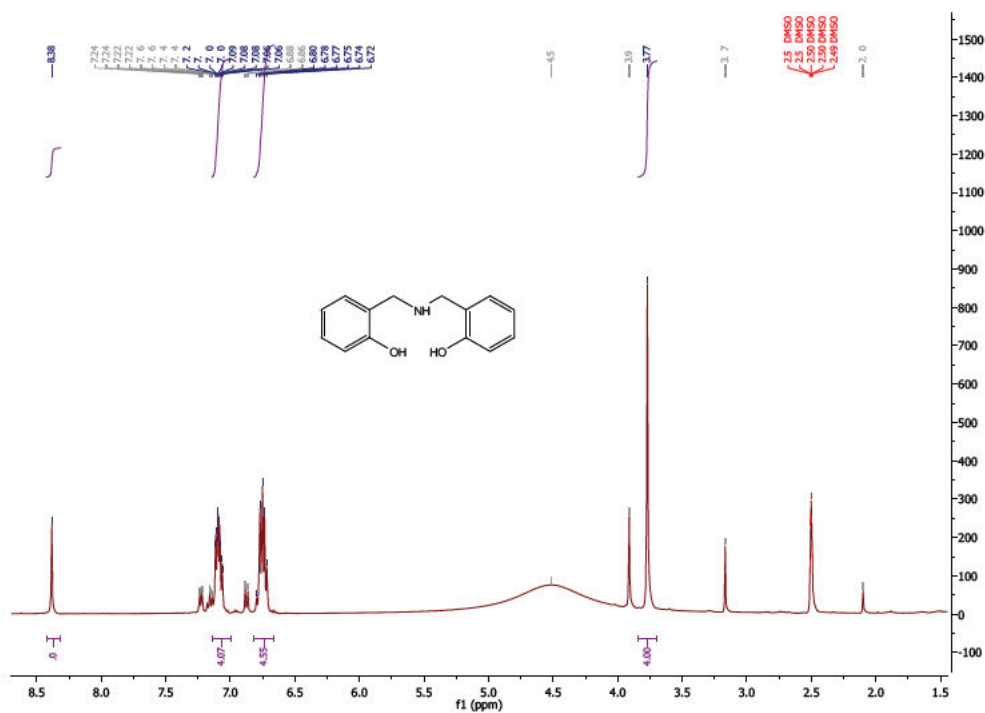


Figure C.26.: <sup>1</sup>H-NMR spectrum of 2,2'-dihydroxydibenzylamine

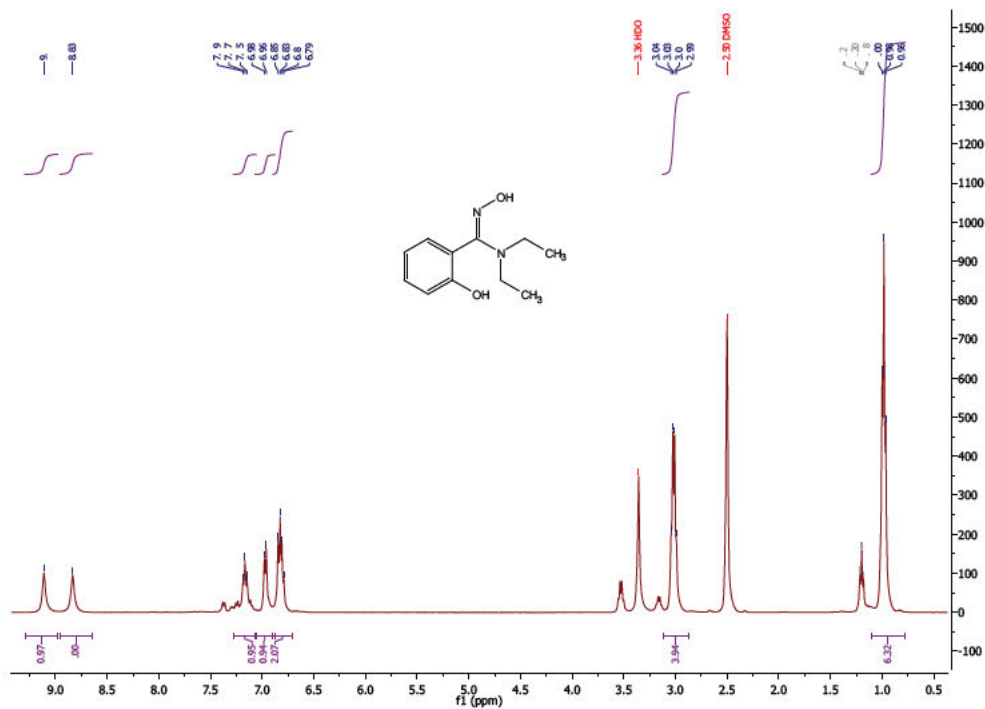
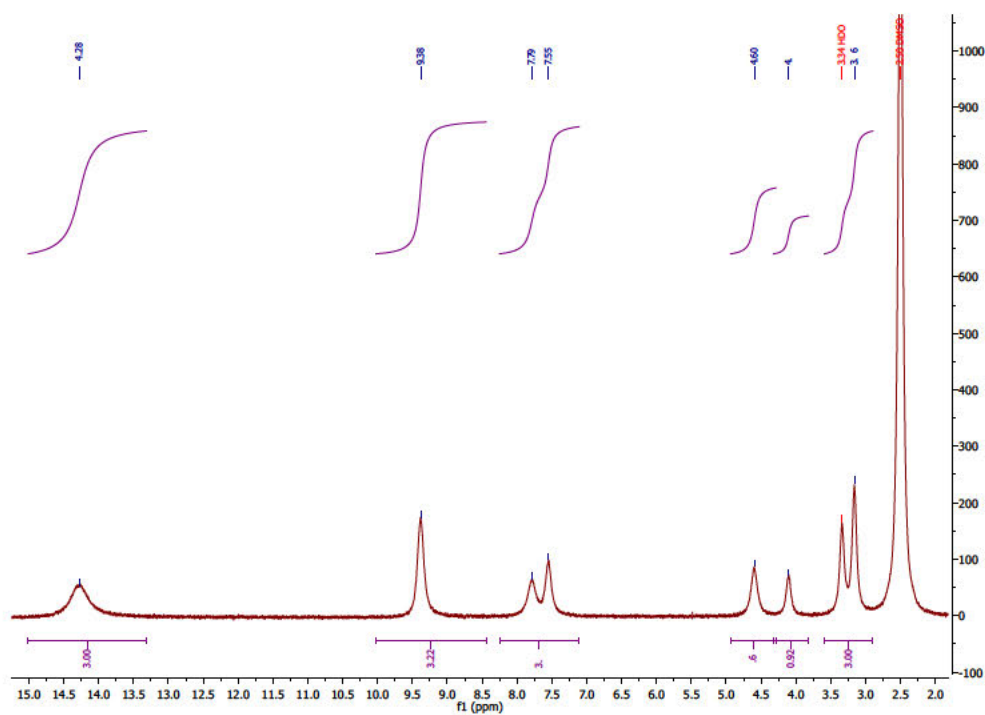
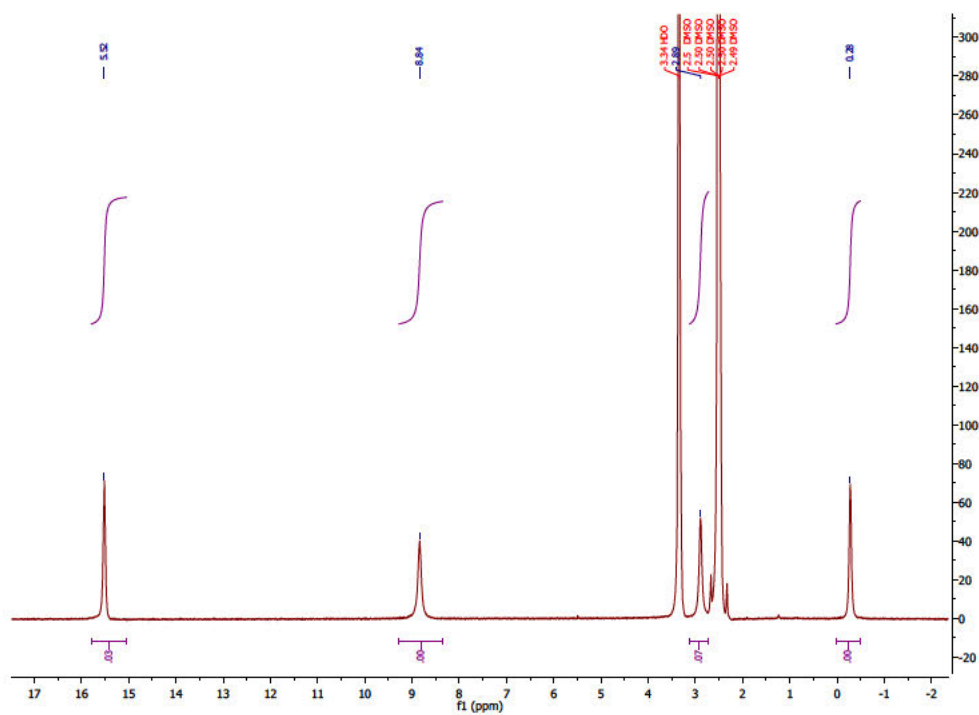


Figure C.27.: <sup>1</sup>H-NMR spectrum of L11



Figure C.28.:  $^1\text{H-NMR}$  spectrum of C4Figure C.29.:  $^1\text{H-NMR}$  spectrum of C7



## D. X-ray diffraction

Table D.1.: Crystallographic data of **L9** and **C1**.

| Compound                                  | <b>L9</b>   | <b>C1</b>   |
|---|---|---|
| Empirical formula                         | C <sub>38</sub> H <sub>36</sub> N <sub>8</sub> O <sub>4</sub> | C <sub>48</sub> H <sub>48</sub> Fe <sub>2</sub> N <sub>6</sub> O <sub>12</sub> S <sub>6</sub> |
| Formula weight / g mol <sup>-1</sup>      | 668.75  | 1204.98   |
| Crystal size / mm                         | 0.2 x 0.18 x 0.05   | not determined  |
| Crystal system                            | orthorhombic  | triclinic   |
| Space group                               | <i>P</i> 2 <sub>1</sub> 2 <sub>1</sub> 2 <sub>1</sub>         | <i>P</i> $\bar{1}$  |
| Unit cell dimensions                      |   |   |
| a / Å                                     | 8.535(2)  | 10.661  |
| b / Å                                     | 11.710(3)   | 10.599  |
| c / Å                                     | 16.918(4)   | 13.236  |
| $\alpha$ / °                              | 90  | 84.14   |
| $\beta$ / °                               | 90  | 73.36   |
| $\gamma$ / °                              | 90  | 63.30   |
| Volume / Å <sup>3</sup>                   | 1691.0(7)   | 1279.6  |
| Z   | 2   | 1   |
| $\rho_{\text{calc.}}$ /g cm <sup>-3</sup> | 1.313   | 1.564   |
| $\mu$ /mm <sup>-1</sup>                   | 0.088   | 0.880   |
| F(000)                                    | 704   | 622   |
| Temperature / K                           | 293(2)  | 293(2)  |
| Diffractometer                            | Bruker SMART APEX2  | Test device at STOE   |
| Radiation                                 | MoK $\alpha$  | MoK $\alpha$  |
| $\theta$ -range for data collection / °   | 2.115 < $\theta$ < 27.944                                     | 1.607 < $\theta$ < 25.999   |
| Index ranges                              | -9 < h < 11<br>-15 < k < 15<br>-22 < l < 22                   | -13 < h < 13<br>-13 < k < 12<br>-16 < l < 16  |
| Collected reflections                     | 11412   | 14701   |
| Independent reflections                   | 4043  | 5006  |
| Completeness                              | 0.994   | 0.997   |
| Max. and min. transmission                | no abs. corr.   | no abs. corr.   |
| $R_{\text{int}}$                          | 0.0695  | 0.0506  |
| $R_{\text{sigma}}$                        | 0.1108  | 0.0928  |
| Data/restraints/parameters                | 4043 / 0 / 229  | 5006 / 0 / 348  |
| Goodness-of-fit on $F^2$                  | 0.774   | 0.921   |
| Final $R_1$ [ $I \geq 2\sigma(I)$ ]       | 0.0390  | 0.0410  |
| Final $wR_2$ [ $I \geq 2\sigma(I)$ ]      | 0.0620  | 0.0724  |
| Final $R_1$ [ <i>all data</i> ]           | 0.1087  | 0.0722  |
| Final $wR_2$ [ <i>all data</i> ]          | 0.0733  | 0.0768  |

Table D.2.: Crystallographic data of **C2** and **C3**.

| Compound                                   | <b>C2</b>   | <b>C3</b>  |
|--|---|--|
| Empirical formula                          | C <sub>35</sub> H <sub>40</sub> Cl <sub>2</sub> Cu <sub>5</sub> N <sub>4</sub> O <sub>11</sub> S <sub>4</sub> | C <sub>36.50</sub> H <sub>34</sub> Cl <sub>1.50</sub> Cu <sub>5</sub> N <sub>4</sub> O <sub>18</sub> S <sub>4.50</sub> |
| Formula weight / g mol <sup>-1</sup>       | 1209.55   | 1331.82  |
| Crystal size / mm                          | 0.09 x 0.07 x 0.04  | 0.14 x 0.1 x 0.06  |
| Crystal system                             | triclinic   | triclinic  |
| Space group                                | <i>P</i> $\bar{1}$  | <i>P</i> $\bar{1}$   |
| Unit cell dimensions                       |   |  |
| a / Å                                      | 12.7041(6)  | 12.1824(9)   |
| b / Å                                      | 13.4344(6)  | 15.4456(11)  |
| c / Å                                      | 14.4133(6)  | 15.5627(12)  |
| $\alpha$ / °                               | 63.284(3)   | 110.916(2)   |
| $\beta$ / °                                | 79.170(3)   | 91.639(2)  |
| $\gamma$ / °                               | 76.138(3)   | 113.295(2)   |
| Volume / Å <sup>3</sup>                    | 2124.20(17)   | 2462.7(3)  |
| Z  | 2   | 2  |
| $\rho_{\text{calc.}}$ / g cm <sup>-3</sup> | 1.891   | 1.796  |
| $\mu$ / mm <sup>-1</sup>                   | 2.848   | 2.470  |
| F(000)                                     | 1218  | 1335   |
| Temperature / K                            | 193   | 173.0  |
| Diffractometer                             | STOE IPDS 2T  | Bruker SMART APEX2   |
| Radiation                                  | MoK $\alpha$  | MoK $\alpha$   |
| $\theta$ -range for data collection / °    | 2.103 < $\theta$ < 28.484   | 1.429 < $\theta$ < 25.000  |
| Index ranges                               | -16 < h < 16<br>-17 < k < 16<br>-19 < l < 19  | -14 < h < 14<br>-18 < k < 17<br>0 < l < 18   |
| Collected reflections                      | 20724   | 8686   |
| Independent reflections                    | 10616   | 8686   |
| Completeness                               | 0.987   | 1.000  |
| Max. and min. transmission                 | 0.8714 and 0.7686   | 0.7456 and 0.6450  |
| $R_{\text{int}}$                           | 0.0469  | merged   |
| $R_{\text{sigma}}$                         | 0.0756  | 0.0763   |
| Data/restraints/parameters                 | 10616 / 3 / 562   | 8686 / 281 / 783   |
| Goodness-of-fit on $F^2$                   | 1.021   | 1.026  |
| Final $R_1$ [ $I \geq 2\sigma(I)$ ]        | 0.0449  | 0.0605   |
| Final $wR_2$ [ $I \geq 2\sigma(I)$ ]       | 0.1062  | 0.1325   |
| Final $R_1$ [ <i>alldata</i> ]             | 0.0938  | 0.1065   |
| Final $wR_2$ [ <i>alldata</i> ]            | 0.1424  | 0.1572   |

Table D.3.: Crystallographic data of **C4** and **C5**.

| Compound                                   | <b>C4</b>   | <b>C5</b>   |
|--|---|---|
| Empirical formula                          | C <sub>54</sub> H <sub>56</sub> Cl <sub>2</sub> Cu <sub>5</sub> N <sub>8</sub> O <sub>18</sub> S <sub>4</sub> | C <sub>77</sub> H <sub>82</sub> Co <sub>8</sub> N <sub>9</sub> O <sub>27</sub> S <sub>8</sub> |
| Formula weight / g mol <sup>-1</sup>       | 1621.90   | 2293.43   |
| Crystal size / mm                          | 0.72 x 0.7 x 0.36   | 0.34 x 0.27 x 0.1   |
| Crystal system                             | tetragonal  | triclinic   |
| Space group                                | <i>I</i> $\bar{4}$  | <i>P</i> $\bar{1}$  |
| Unit cell dimensions                       |   |   |
| a / Å                                      | 17.857  | 14.8344(8)  |
| b / Å                                      | 17.857  | 15.2968(9)  |
| c / Å                                      | 9.970   | 25.6912(14)   |
| $\alpha$ / °                               | 90  | 104.996(2)  |
| $\beta$ / °                                | 90  | 92.579(2)   |
| $\gamma$ / °                               | 90  | 113.046(2)  |
| Volume / Å <sup>3</sup>                    | 3179.2  | 5111.2(5)   |
| Z  | 2   | 2   |
| $\rho_{\text{calc.}}$ / g cm <sup>-3</sup> | 1.694   | 1.490   |
| $\mu$ / mm <sup>-1</sup>                   | 1.936   | 1.500   |
| F(000)                                     | 1646  | 2334  |
| Temperature / K                            | 120.15  | 173.15  |
| Diffractometer                             | STOE IPDS 2T  | Bruker SMART APEX2  |
| Radiation                                  | MoK $\alpha$  | MoK $\alpha$  |
| $\theta$ -range for data collection / °    | 2.281 < $\theta$ < 28.186   | 0.832 < $\theta$ < 27.934   |
| Index ranges                               | -23 < h < 15<br>-20 < k < 23<br>-11 < l < 13  | -19 < h < 19<br>-20 < k < 20<br>-33 < l < 33  |
| Collected reflections                      | 5184  | 56062   |
| Independent reflections                    | 3382  | 24453   |
| Completeness                               | 0.867   | 0.997   |
| Max. and min. transmission                 | 0.5043 and 0.3197   | no abs. corr.   |
| $R_{\text{int}}$                           | 0.0276  | 0.1095  |
| $R_{\text{sigma}}$                         | 0.0168  | 0.1662  |
| Data/restraints/parameters                 | 3382 / 15 / 251   | 24453 / 3 / 1164  |
| Goodness-of-fit on $F^2$                   | 1.099   | 0.949   |
| Final $R_1$ [ $I \geq 2\sigma(I)$ ]        | 0.0310  | 0.0633  |
| Final $wR_2$ [ $I \geq 2\sigma(I)$ ]       | 0.0860  | 0.1800  |
| Final $R_1$ [ <i>alldata</i> ]             | 0.0313  | 0.1396  |
| Final $wR_2$ [ <i>alldata</i> ]            | 0.0864  | 0.2119  |

Table D.4.: Crystallographic data of **C6** and **C7**.

| Compound                                   | <b>C6</b>  | <b>C7</b>  |
|--|--|--|
| Empirical formula                          | C <sub>144</sub> H <sub>196</sub> Cd <sub>14</sub> Cl <sub>2</sub> N <sub>28</sub> O <sub>49</sub> S <sub>12</sub> | C <sub>30</sub> H <sub>32</sub> Cl <sub>2</sub> Cu <sub>5</sub> N <sub>8</sub> O <sub>18</sub> |
| Formula weight / g mol <sup>-1</sup>       | 5132.50  | 1181.23  |
| Crystal size / mm                          | 0.14 x 0.097 x 0.02  | 0.24 x 0.18 x 0.05   |
| Crystal system                             | monoclinic   | triclinic  |
| Space group                                | <i>P</i> 2 <sub>1</sub> / <i>c</i>   | <i>P</i> $\bar{1}$   |
| Unit cell dimensions                       |  |  |
| a / Å                                      | 18.1706(5)   | 7.8738(3)  |
| b / Å                                      | 17.2534(3)   | 14.2712(5)   |
| c / Å                                      | 30.5506(7)   | 17.3303(6)   |
| $\alpha$ / °                               | 90   | 102.4505(8)  |
| $\beta$ / °                                | 105.688(2)   | 91.6027(9)   |
| $\gamma$ / °                               | 90   | 92.4221(10)  |
| Volume / Å <sup>3</sup>                    | 9221.0(4)  | 1898.51(12)  |
| Z  | 2  | 2  |
| $\rho_{\text{calc.}}$ / g cm <sup>-3</sup> | 1.849  | 2.066  |
| $\mu$ / mm <sup>-1</sup>                   | 1.826  | 2.988  |
| F(000)                                     | 5092   | 1182   |
| Temperature / K                            | 193(2)   | 173  |
| Diffractometer                             | STOE IPDS 2T   | Bruker SMART APEX2   |
| Radiation                                  | MoK $\alpha$   | MoK $\alpha$   |
| $\theta$ -range for data collection / °    | 1.658 < $\theta$ < 25.999  | 1.681 < $\theta$ < 27.986  |
| Index ranges                               | -22 < h < 21<br>-21 < k < 21<br>-37 < l < 37   | -10 < h < 10<br>-18 < k < 12<br>-22 < l < 22   |
| Collected reflections                      | 38914  | 21181  |
| Independent reflections                    | 18092  | 9145   |
| Completeness                               | 0.998  | 0.999  |
| Max. and min. transmission                 | 0.9472 and 0.7877  | 0.7456 and 0.6415  |
| $R_{\text{int}}$                           | 0.0328   | 0.0252   |
| $R_{\text{sigma}}$                         | 0.0455   | 0.0359   |
| Data/restraints/parameters                 | 18092 / 116 / 1230   | 9145 / 15 / 577  |
| Goodness-of-fit on $F^2$                   | 1.115  | 1.036  |
| Final $R_1$ [ $I \geq 2\sigma(I)$ ]        | 0.0510   | 0.0308   |
| Final $wR_2$ [ $I \geq 2\sigma(I)$ ]       | 0.0901   | 0.0744   |
| Final $R_1$ [ <i>alldata</i> ]             | 0.0844   | 0.0406   |
| Final $wR_2$ [ <i>alldata</i> ]            | 0.1044   | 0.0782   |

Table D.5.: Crystallographic data of **C8** and **C9**.

| Compound                                   | <b>C8</b>   | <b>C9</b>  |
|--|---|--|
| Empirical formula                          | C <sub>30</sub> H <sub>33</sub> Cu <sub>3.40</sub> N <sub>5</sub> Na <sub>2</sub> O <sub>12</sub> | C <sub>259</sub> H <sub>202.67</sub> N <sub>40</sub> O <sub>81</sub> V <sub>20</sub> |
| Formula weight / g mol <sup>-1</sup>       | 917.63  | 6190.07  |
| Crystal size / mm                          | 0.4 x 0.25 x 0.04   | 0.090 x 0.380 x 0.450  |
| Crystal system                             | triclinic   | triclinic  |
| Space group                                | <i>P</i> $\bar{1}$  | <i>P</i> $\bar{1}$   |
| Unit cell dimensions                       |   |  |
| a / Å                                      | 9.4830(6)   | 7.8738(3)  |
| b / Å                                      | 13.2730(9)  | 14.2712(5)   |
| c / Å                                      | 14.8487(10)   | 17.3303(6)   |
| $\alpha$ / °                               | 103.283(5)  | 102.4505(8)  |
| $\beta$ / °                                | 96.821(5)   | 91.6027(9)   |
| $\gamma$ / °                               | 103.033(5)  | 92.4221(10)  |
| Volume / Å <sup>3</sup>                    | 1743.2(2)   | 1898.51(12)  |
| Z  | 2   | 2  |
| $\rho_{\text{calc.}}$ / g cm <sup>-3</sup> | 1.748   | 2.066  |
| $\mu$ / mm <sup>-1</sup>                   | 2.145   | 2.988  |
| F(000)                                     | 929   | 1182   |
| Temperature / K                            | 293(2)  | 173  |
| Diffractometer                             | Bruker P4   | Bruker SMART APEX2   |
| Radiation                                  | MoK $\alpha$  | MoK $\alpha$   |
| $\theta$ -range for data collection / °    | 1.432 < $\theta$ < 25.321   | 1.681 < $\theta$ < 27.986  |
| Index ranges                               | -11 < h < 11<br>-15 < k < 15<br>-17 < l < 17  | -10 < h < 10<br>-18 < k < 12<br>-22 < l < 22   |
| Collected reflections                      | 26326   | 21181  |
| Independent reflections                    | 6032  | 9145   |
| Completeness                               | 0.948   | 0.999  |
| Max. and min. transmission                 | 0.8823 and 0.6487   | 0.7456 and 0.6415  |
| $R_{\text{int}}$                           | 0.1402  | 0.0252   |
| $R_{\text{sigma}}$                         | 0.0863  | 0.0359   |
| Data/restraints/parameters                 | 6032 / 36 / 496   | 9145 / 15 / 577  |
| Goodness-of-fit on $F^2$                   | 1.088   | 1.036  |
| Final $R_1$ [ $I \geq 2\sigma(I)$ ]        | 0.1338  | 0.0308   |
| Final $wR_2$ [ $I \geq 2\sigma(I)$ ]       | 0.3405  | 0.0744   |
| Final $R_1$ [ <i>alldata</i> ]             | 0.1823  | 0.0406   |
| Final $wR_2$ [ <i>alldata</i> ]            | 0.3717  | 0.0782   |

Table D.6.: Crystallographic data of **C10** and **C11**.

| Compound  | <b>C10</b>  | <b>C11</b>  |
|---|---|---|
| Empirical formula   | C <sub>168</sub> H <sub>64</sub> Mn <sub>20</sub> N <sub>24</sub> O <sub>93</sub> | C <sub>70</sub> H <sub>76</sub> Mn <sub>9</sub> N <sub>10</sub> O <sub>31</sub> |
| Formula weight / g mol <sup>-1</sup>                      | 5005.23   | 2047.86   |
| Crystal size / mm   | 0.36 x 0.13 x 0.09  | not determined  |
| Crystal system  | tetragonal  | monoclinic  |
| Space group   | <i>I4</i>   | <i>C2/c</i>   |
| Unit cell dimensions                                      |   |   |
| a / Å   | 20.056(2)   | 15.6568(8)  |
| b / Å   | 20.056  | 23.2877(11)   |
| c / Å   | 16.878(2)   | 22.8095(10)   |
| α / °   | 90  | 90  |
| β / °   | 90  | 98.163(2)   |
| γ / °   | 90  | 90  |
| Volume / Å <sup>3</sup>                                   | 6789.3(18)  | 8232.3(7)   |
| Z   | 1   | 4   |
| ρ <sub>calc.</sub> /g cm <sup>-1</sup>                    | 1.224   | 1.652   |
| μ/mm <sup>-1</sup>  | 0.970   | 1.421   |
| F(000)  | 2484  | 4156  |
| Temperature / K   | 173.15  | 293(2)  |
| Diffractometer  | Bruker SMART APEX2  | Bruker SMART APEX2  |
| Radiation   | MoK α   | MoK <i>alpha</i>  |
| θ-range for data collection / °                           | 1.577 < θ < 27.875  | 1.578 < <i>theta</i> < 27.900   |
| Index ranges  | -26 < h < 22<br>-26 < k < 22<br>-22 < l < 22                                      | -20 < h < 20<br>-30 < k < 30<br>-28 < l < 29                                    |
| Collected reflections                                     | 33431   | 38303   |
| Independent reflections                                   | 8042  | 9843  |
| Completeness  | 0.992   | 0.998   |
| Max. and min. transmission                                | 0.7456 and 0.5334   | no abs. corr.   |
| <i>R</i> <sub>int</sub>                                   | 0.0605  | 0.0608  |
| <i>R</i> <sub>sigma</sub>                                 | 0.0544  | 0.0460  |
| Data/restraints/parameters                                | 8042 / 88 / 395   | 9843 / 10 / 552   |
| Goodness-of-fit on <i>F</i> <sup>2</sup>                  | 1.006   | 1.101   |
| Final <i>R</i> <sub>1</sub> [ <i>I</i> ≥ 2σ( <i>I</i> )]  | 0.0864  | 0.0486  |
| Final <i>wR</i> <sub>2</sub> [ <i>I</i> ≥ 2σ( <i>I</i> )] | 0.2275  | 0.1475  |
| Final <i>R</i> <sub>1</sub> [ <i>alldata</i> ]            | 0.1225  | 0.0615  |
| Final <i>wR</i> <sub>2</sub> [ <i>alldata</i> ]           | 0.2650  | 0.1559  |



Table D.7.: Crystallographic data of **C12** and **C13**.

| Compound  | <b>C12</b>  | <b>C13</b>  |
|---|---|---|
| Empirical formula   | C <sub>74</sub> H <sub>76</sub> Co <sub>4</sub> N <sub>12</sub> O <sub>20</sub> | C <sub>74</sub> H <sub>88</sub> Cl <sub>4</sub> Cu <sub>6</sub> N <sub>14</sub> O <sub>26</sub> |
| Formula weight / g mol <sup>-1</sup>                      | 1689.18   | 2112.62   |
| Crystal size / mm   | 0.15 x 0.14 x 0.045   | 0.26 x 0.25 x 0.07  |
| Crystal system  | monoclinic  | monoclinic  |
| Space group   | <i>P2</i> <sub>1</sub> / <i>c</i>   | <i>P2</i> <sub>1</sub> / <i>a</i>   |
| Unit cell dimensions                                      |   |   |
| a / Å   | 12.3964(18)   | 15.1149(8)  |
| b / Å   | 16.215(2)   | 17.4454(9)  |
| c / Å   | 19.868(3)   | 16.8149(10)   |
| α / °   | 90  | 90  |
| β / °   | 99.817(5)   | 100.3534(18)  |
| γ / °   | 90  | 90  |
| Volume / Å <sup>3</sup>                                   | 3935.1(10)  | 4361.7(4)   |
| Z   | 2   | 2   |
| ρ <sub>calc.</sub> /g cm <sup>-1</sup>                    | 1.426   | 1.609   |
| μ/mm <sup>-1</sup>  | 0.906   | 1.642   |
| F(000)  | 1744  | 2160  |
| Temperature / K   | 203   | 293(2)  |
| Diffractometer  | Bruker SMART APEX2  | Bruker SMART APEX2  |
| Radiation   | MoK α   | MoK α   |
| θ-range for data collection / °                           | 1.631 < θ < 28.0  | 1.697 < θ < 27.993  |
| Index ranges  | -15 < h < 16<br>-21 < k < 20<br>-24 < l < 26                                    | -19 < h < 19<br>-23 < k < 21<br>-22 < l < 22  |
| Collected reflections                                     | 28772   | 32133   |
| Independent reflections                                   | 9468  | 10481   |
| Completeness  | 0.991   | 0.997   |
| Max. and min. transmission                                | 0.7456 and 0.6265   | 0.8298 and 0.6801   |
| <i>R</i> <sub>int</sub>                                   | 0.0861  | 0.1139  |
| <i>R</i> <sub>sigma</sub>                                 | 0.1083  | 0.1545  |
| Data/restraints/parameters                                | 9468 / 25 / 524   | 10481 / 0 / 567   |
| Goodness-of-fit on <i>F</i> <sup>2</sup>                  | 1.011   | 0.831   |
| Final <i>R</i> <sub>1</sub> [ <i>I</i> ≥ 2σ( <i>I</i> )]  | 0.0588  | 0.0504  |
| Final <i>wR</i> <sub>2</sub> [ <i>I</i> ≥ 2σ( <i>I</i> )] | 0.1282  | 0.0930  |
| Final <i>R</i> <sub>1</sub> [ <i>alldata</i> ]            | 0.1288  | 0.1291  |
| Final <i>wR</i> <sub>2</sub> [ <i>alldata</i> ]           | 0.1566  | 0.1105  |

Table D.8.: Crystallographic data of **C14** and **C15**.

| Compound                                   | <b>C14</b>  | <b>C15</b>  |
|--|---|---|
| Empirical formula                          | C <sub>76</sub> H <sub>92</sub> Cl <sub>4</sub> Cu <sub>6</sub> N <sub>20</sub> O <sub>32</sub> | C <sub>80</sub> H <sub>64</sub> Cl <sub>4</sub> Cu <sub>4</sub> N <sub>12</sub> O <sub>12</sub> |
| Formula weight / g mol <sup>-1</sup>       | 2320.73   | 1781.39   |
| Crystal size / mm                          | 0.253 x 0.241 x 0.142   | 0.26 x 0.14 x 0.06  |
| Crystal system                             | triclinic   | monoclinic  |
| Space group                                | <i>P</i> $\bar{1}$  | <i>C</i> 2/ <i>c</i>  |
| Unit cell dimensions                       |   |   |
| a / Å                                      | 11.617(2)   | 20.4189(10)   |
| b / Å                                      | 13.737(3)   | 9.1780(3)   |
| c / Å                                      | 16.387(3)   | 20.5860(10)   |
| $\alpha$ / °                               | 113.07(3)   | 90  |
| $\beta$ / °                                | 96.45(3)  | 110.651(4)  |
| $\gamma$ / °                               | 102.83(3)   | 90  |
| Volume / Å <sup>3</sup>                    | 2287.1(10)  | 3610.0(3)   |
| Z  | 1   | 2   |
| $\rho_{\text{calc.}}$ / g cm <sup>-3</sup> | 1.685   | 1.639   |
| $\mu$ / mm <sup>-1</sup>                   | 1.581   | 1.386   |
| F(000)                                     | 1186  | 1816  |
| Temperature / K                            | 120(2)  | 293(2)  |
| Diffractometer                             | Bruker APEX II CCD area<br>det.   | STOE IPDS 2T  |
| Radiation                                  | MoK $\alpha$  | MoK $\alpha$  |
| $\theta$ -range for data collection / °    | 1.844 < $\theta$ < 28.000   | 2.114 < $\theta$ < 28.301   |
| Index ranges                               | -15 < h < 15<br>-18 < k < 18<br>-21 < l < 21  | -27 < h < 23<br>-10 < k < 12<br>-27 < l < 27  |
| Collected reflections                      | 26720   | 9077  |
| Independent reflections                    | 11027   | 4458  |
| Completeness                               | 1.000   | 0.994   |
| Max. and min. transmission                 | 0.8623 and 0.7860   | 0.9305 and 0.7644   |
| $R_{\text{int}}$                           | 0.0881  | 0.0311  |
| $R_{\text{sigma}}$                         | 0.1215  | 0.0410  |
| Data/restraints/parameters                 | 11027 / 4 / 632   | 4458 / 0 / 254  |
| Goodness-of-fit on $F^2$                   | 0.972   | 1.135   |
| Final $R_1$ [ $I \geq 2\sigma(I)$ ]        | 0.0566  | 0.0507  |
| Final $wR_2$ [ $I \geq 2\sigma(I)$ ]       | 0.1158  | 0.1304  |
| Final $R_1$ [ <i>alldata</i> ]             | 0.1226  | 0.0856  |
| Final $wR_2$ [ <i>alldata</i> ]            | 0.1447  | 0.1610  |

Table D.9.: Crystallographic data of **C16** and **C17**.

| Compound                                   | <b>C16</b>  | <b>C17</b>   |
|--|---|--|
| Empirical formula                          | C <sub>20</sub> H <sub>15</sub> CoN <sub>3</sub> O <sub>3</sub> | C <sub>98</sub> H <sub>128</sub> N <sub>12</sub> Ni <sub>6</sub> O <sub>32</sub> |
| Formula weight / g mol <sup>-1</sup>       | 404.28  | 2338.38  |
| Crystal size / mm                          | 0.320 x 0.210 x 0.160   | not determined   |
| Crystal system                             | triclinic   | monoclinic   |
| Space group                                | <i>P</i> $\bar{1}$  | <i>P</i> 2 <sub>1</sub> / <i>c</i>   |
| Unit cell dimensions                       |   |  |
| a / Å                                      | 12.813(3)   | 13.1333(3)   |
| b / Å                                      | 13.334(3)   | 19.7509(5)   |
| c / Å                                      | 14.761(3)   | 20.3532(4)   |
| $\alpha$ / °                               | 113.23(3)   | 90   |
| $\beta$ / °                                | 107.96(3)   | 102.488(2)   |
| $\gamma$ / °                               | 96.42(3)  | 90   |
| Volume / Å <sup>3</sup>                    | 2124.4(9)   | 5154.6(2)  |
| Z  | 4   | 2  |
| $\rho_{\text{calc.}}$ / g cm <sup>-3</sup> | 1.264   | 1.507  |
| $\mu$ / mm <sup>-1</sup>                   | 0.830   | 1.160  |
| F(000)                                     | 828   | 2448   |
| Temperature / K                            | 120(2)  | 100.0  |
| Diffractometer                             | Bruker APEX II CCD area<br>det.                                 | Test device at STOE  |
| Radiation                                  | MoK $\alpha$  | MoK $\alpha$   |
| $\theta$ -range for data collection / °    | 1.627 < $\theta$ < 28.999                                       | 2.526 < $\theta$ < 25.999  |
| Index ranges                               | -17 < h < 17<br>-18 < k < 18<br>-20 < l < 20                    | -16 < h < 14<br>-21 < k < 24<br>-16 < l < 25                                     |
| Collected reflections                      | 25713   | 24264  |
| Independent reflections                    | 11287   | 9803   |
| Completeness                               | 0.998   | 0.968  |
| Max. and min. transmission                 | 0.862 and 0.733   | no abs. corr.  |
| $R_{\text{int}}$                           | 0.0734  | 0.0350   |
| $R_{\text{sigma}}$                         | 0.1153  | 0.0654   |
| Data/restraints/parameters                 | 11287 / 0 / 487   | 9803 / 7 / 689   |
| Goodness-of-fit on $F^2$                   | 0.987   | 0.972  |
| Final $R_1$ [ $I \geq 2\sigma(I)$ ]        | 0.0566  | 0.0539   |
| Final $wR_2$ [ $I \geq 2\sigma(I)$ ]       | 0.1187  | 0.1523   |
| Final $R_1$ [ <i>alldata</i> ]             | 0.1201  | 0.0871   |
| Final $wR_2$ [ <i>alldata</i> ]            | 0.1444  | 0.1643   |

## E. Curriculum Vitae

[REDACTED]

[REDACTED]  
[REDACTED]  
[REDACTED]  
[REDACTED]

[REDACTED]

[REDACTED]

[REDACTED] [REDACTED]  
[REDACTED]  
[REDACTED]  
[REDACTED]  
[REDACTED]

[REDACTED] [REDACTED]  
[REDACTED]  
[REDACTED]  
[REDACTED]  
[REDACTED]

[REDACTED] [REDACTED]  
[REDACTED]

[REDACTED] [REDACTED]

[REDACTED]

[REDACTED]

[REDACTED]

[REDACTED]

[REDACTED]

[REDACTED]

[REDACTED]

[REDACTED]

[REDACTED]

[REDACTED]

[REDACTED]

[REDACTED]

[REDACTED]

[REDACTED]

[REDACTED]

[REDACTED]

[REDACTED]

[REDACTED]

[REDACTED]

[REDACTED]

[REDACTED]

[REDACTED]

[REDACTED]

[REDACTED]

[REDACTED]

[REDACTED]

[REDACTED]

[REDACTED]

[REDACTED]

[REDACTED]

[REDACTED]

[REDACTED]

[REDACTED]

[REDACTED]

[REDACTED]

[REDACTED]

[REDACTED]

[REDACTED]

[REDACTED]

[REDACTED]